Multiscale modeling of polymer dynamics under equilibrium and non-equilibrium conditions

by

Indranil Saha Dalal

A dissertation submitted in partial fulfillment
of the requirements for the degree of
Doctor of Philosophy
(Chemical Engineering)
in the University of Michigan
2013

Doctoral Committee:

Professor Ronald G. Larson, Chair
Professor Michael J. Solomon
Professor Alan Wineman
Professor Robert M. Ziff

Acknowledgements

Throughout the past few years of my life leading to this dissertation, there are several people within the university and outside of it, who have contributed to my development – both professional and personal. First and foremost, I would like to express my deepest gratitude to my advisor, Prof. Ronald Larson, who provided lots of encouragement and freedom all along, apart from patiently working with me all along in my research. I would also like to thank my committee members – Professor Michael Solomon, Professor Robert Ziff and Professor Alan Wineman, who were always available to provide valuable guidance and suggestions in my research. I consider myself fortunate to receive high quality education in varied topics at the university, and would like to thank all the teachers I have met here. A special thanks also goes to Professor Ronald Larson, Professor Michael Solomon and Professor Joerg Lahann for mentoring me during teaching in the different courses that I served as graduate student instructor. I would also like to thank the extremely cordial staff in the Chemical Engineering department, especially Susan Hamlin, for helping me on numerous occasions.

The past few years were not only a time for academic interactions, but social ones as well. I would like to thank my classmates in the department – especially Sameer Parvathikar, Steven Morris and Kanako Okada, who were always there when I needed them. I would like to thank few other close friends in Ann Arbor – Vivek Vichare, Raghavendra Chivukula and Marimuthu Andiappan, interactions with whom further enriched my social life. I would like to thank all postdoctoral scholars and graduate students in the Larson group whom I have worked with at various times – especially Zuowei Wang, Susan

Duncan, Senthil Kandasamy, Semant Jain, Nazish Hoda, Nobuhiko Watari, Xue Chen, Shi Yu, Shihu Wang, Xueming Tang, Lei Jiang, Jun Liu, Thomas Juhl and Priyanka Desai, for making my stay in the group a memorable one. I would like to thank all the undergraduate students whom I have worked with over the past few years – especially Nicholas Orichella, Meredith Bailey, Alex Albaugh and Mahesh Ganesan (who is presently a graduate student in the university), for all the help in my research. Finally, I would like to thank my family and close friends for their support during all these years, without which this would not be possible.

Table of Contents

Acknowledgements. ii

List of Figures. v

List of Tables. xxiii

List of Appendices. xxiv

Abstract. xxv

CHAPTER I Introduction 1

CHAPTER II Explaining the "missing" high-frequency viscoelastic relaxation modes in the relaxation spectrum of polymers in dilute solutions. 20

CHAPTER III Multiple regimes of deformation in shearing flow of isolated polymers. 60

CHAPTER IV Tumbling and deformation of isolated polymer chains in shearing flow. 112

CHAPTER V Effects of excluded volume and hydrodynamic interactions on the behavior of isolated polymer chains in shearing flow. 139

CHAPTER VI Conclusions and future directions. 177

APPENDICES. 189

List of Figures

Figure 2.1: Comparison of the C-C radial distribution functions in a melt of short (10 monomer) polystyrene chains obtained from experiment (earlier work, data taken from Ref. [44]), all-atom MD simulations (earlier work, data taken from Ref. [44]) and united-atom MD simulations performed in this study. The legend 'all-atom simulation' refers to the results obtained in Ref. [44], 'original UA parameters' refers to results obtained in this work with the united-atom potential provided in Ref. [26] and 'tuned UA parameters' refers to those obtained using a potential in which we introduced several modifications, as discussed in text. Note that the experimental results correspond to a melt of shorter chains (8 monomers) at a lower temperature (323 K). 51

Figure 2.2: Relaxation of backbone bonds from MD simulations (solid blue lines) and corresponding fits to a single exponential decay (dash-dot red lines) for a polystyrene chain of 30 monomers (59 backbone bonds) using different models and solvent baths - (a) United-atom model in benzene at 293 K, (b) MARTINI model in benzene at 293 K, (c) MARTINI model in 2-oligostyrene at 480 K and (d) MARTINI model in 5-oligostyrene at 680 K. t_1 denotes the time scale of the exponential decay and τ is the relaxation time for the end-to-end vector of the chain. 52

Figure 2.3: Relaxation of the backbone bonds from MD simulations (solid blue lines) and the corresponding fits to a sum of two exponential decay terms (dash-dot red lines) for a polystyrene chain of 100 monomers (199 backbone bonds), using the MARTINI

model in solvent baths of (a) benzene at 293 K, (b) 2-oligostyrene at 480 K and (c) 5-oligostyrene at 680 K. t_1 and t_2 denote the time scales of the two exponential decay terms. 53

Figure 2.4: Comparison of the relaxation dynamics of individual chain backbone bonds of a polystyrene chain (30 monomers) and benzene rings in the solvent bath from UA MD simulations. Inset shows the same for CGMD simulations using the MARTINI model. For the relaxation dynamics of benzene rings, the autocorrelation function of the unit vector normal to each benzene ring is computed and then averaged over all benzene molecules in the system. 54

Figure 2.5: Comparison of radial distribution functions between different atom types on the polystyrene chain (30 monomers) obtained from MD simulations (solid blue line) and the ACWS model in continuum solvent (dash-dot red line). The radial distribution functions are shown between the following united-atom types: (a) CH groups on phenyl rings in the side groups with other such CH groups in the phenyl rings, (b) CH_2 groups on the chain backbone with other such groups, (c) CH groups on the chain backbone with other such groups, (d) CH groups in side groups with CH_2 groups in the chain backbone, (e) CH groups in side groups with CH groups in the chain backbone and (f) CH_2 groups in the chain backbone with CH groups in the chain backbone. 55

Figure 2.6: Comparison of the relaxation dynamics for the backbone bonds of a polystyrene chain of 30 monomers from UA MD simulation (in benzene bath) and

different united-atom representations of the same in a continuum solvent. Inset compares the relaxation dynamics for backbone bonds for the ACWS and PSG chain models. For details of the models, see text and Table 2.2. In this and following figures, the time is made dimensionless using the factor D/R_g^2, where D and R_g are the diffusivity of the center of mass and the average radius of gyration of the chain, respectively. 56

Figure 2.7: Comparison of the relaxation dynamics for the backbone bonds of a polystyrene chain of 30 monomers from UA MD simulation (in benzene bath) and chain models with varying degrees of simplification, in a continuum solvent without hydrodynamic interaction (HI). The details of the models are given in text and Table 2.2. The grey dash-dot line shows the single-exponential fit to the relaxation dynamics of the bonds from the UA MD simulation. Inset compares the bond relaxation dynamics for the 'spr+ben+tor' and 'spr+ben+tor+side groups' models, thus showing that the additional effect due to inclusion of side groups is negligible at long times. 57

Figure 2.8: Comparison of the relaxation dynamics for the backbone bonds of a polystyrene chain of 30 monomers from UA MD simulation (in benzene bath) and chain models with varying degrees of simplification (all models without side groups are only considered here), in a continuum solvent, with and without hydrodynamic interaction (HI). The details of the models are given in text and Table 2.2. Two levels of HI ($h^* = 0.15$ and $h^* = 0.5$) are considered here. 58

Figure 2.9: Mean square displacements (MSD) versus time for chain backbone atoms for the following models: (a) spr, (b) spr+ben, (c) spr+ben+tor, (d) spr+ben+tor+side groups, (e) ACWS and (f) a polystyrene chain of 30 monomers in benzene bath from MD simulations. Inset to (f) shows the results from the MD simulation at short times for atoms on the chain backbone and those on the benzene rings constituting the solvent bath. Note that (a)-(e) are for models in a continuum solvent, while the solvent molecules are treated explicitly for (f). Details of the models used for (a)-(e) are provided in text and Table 2.2.....59

Figure 3.1: (a) Variation of $\sqrt{\frac{R_{gx}^{\ 2}}{R_{gx0}^{\ 2}}-1}$ with Weissenberg number for bead-rod polymer chains of various lengths for weaker flows. Inset shows the estimated Weissenberg numbers for the onset of Regime 2 for different chains (Wi_{c2}). (b) Comparison of the behavior of $\sqrt{\frac{R_{gx}^{\ 2}}{R_{gx0}^{\ 2}}-1}$ in Regime 1 with the theoretical solution given by Eq. (21). Inset gives the variation of the approximate Weissenberg numbers for the end of Regime 1 (Wi_{c1}) with chain length. (c) Comparison with the theoretical model given by Eq. (23) that incorporates finite extensibility.....96

Figure 3.2: Variation of R_{gx} with Peclet number for bead-rod chains of various lengths. Regimes 2 and 3 are indicated by solid black lines with the corresponding scaling exponents of 0 and -0.15, respectively.....97

Figure 3.3: Variation of the end-to-end distance of a polymer chain (consisting of 100 rods) with strain (which is time multiplied by strain rate, or $t\dot{\gamma}$) at Pe=3×10^{11}. The plot shows the tendency of the chain to remain in the fully stretched state for a prolonged duration at high shear rates. 98

Figure 3.4: Variation of $R_{end\text{-}end}$ with Peclet number for a polymer chain of 60 rods at shear rates in regime 4 with two different time step sizes. The qualitative behavior is independent of the choice of the time step size although there are some quantitative differences. 99

Figure 3.5: (a) Variation of Rgy with Peclet number for polymer chains of various lengths. The solid lines indicate Regimes 2 and 3 for bead-rod chains. The scaling law for R_{gy} with Peclet number for a single rod (i.e., a rigid dumbbell) is also shown. (b) Variation of the R_{gy} with Weissenberg number at low shear rates, showing the transition from Regime 1 to Regime 2. The solid line roughly marks the end of Regime 1. 100

Figure 3.6: Variation of the ensemble average of R_{gz} with Peclet number for polymer chains of various lengths. The solid lines indicate Regimes 2 and 3. 101

Figure 3.7: Snapshots from simulation trajectories, time ordered from top to bottom, showing representative sequences of events transitioning a flattened coil to a stretched chain and back to a coiled state again, at shear rates of (a) 10, (b) 10^4 and (c) 10^6, corresponding to Peclet numbers of 0.3, 300 and 30000 respectively, the latter two of which are in Regime 3. 102

Figure 3.8: Variation of the end-to-end distance of a polymer chain (consisting of 100 rods) with time (time is represented by strain=t$\dot{\gamma}$) at Peclet numbers of 0.3, 300 and 30000, corresponding to shear rates of 10, 10^4 and 10^6 respectively, the latter two of which are in Regime 3. 103

Figure 3.9: Probability distributions of the end-to-end distance of the polymer chain (of 100 rods) at various shear rates in Regimes 2 and 3. Peclet numbers of 0.03 and 0.3 lie in Regime 2 whereas 300 and 30000 lie in Regime 3. A Peclet number of 3, corresponding to a shear rate of 100, lies in the transition region from Regime 2 to Regime 3. 104

Figure 3.10: Variation of the time-averaged extent of the polymer chain in the gradient direction with Peclet number. The average y-extent shows no dependence on Peclet number in Regime 3, where it is approximately one Kuhn step. 105

Figure 3.11: Probability distributions of rod orientation angles relative to the shear flow direction for single rods and individual rods in a chain of 100 rods. (a) Regime 2, (b) Regime 3. 106

Figure 3.12: Bond angles for an individual rod in a chain of 100 rods. (a) An example log-log plot for the probability distribution of angles at *Pe* = 30, where the solid line shows the convection-controlled regime and has a slope of -2, (b) Variation of the estimated critical angle separating convective and diffusive regimes with Peclet number, which approximately follows a power law with an exponent of -1/3..... 107

Figure 3.13: Variation of the estimated characteristic chain tumbling time (normalized with number of rods in the chain) with Peclet number for various chain lengths. The solid line indicates that our data approximately follows a power law with an exponent of -0.8. 108

Figure 3.14: Comparison of chain tumbling times t_{tumble} (for a chain of 100 rods) and the total time $50t_{flip}$ taken to flip 50 rods. The chain tumbling times are estimated using a power law that approximately predicts the data presented in Figure 3.13. The rod flipping times are calculated using the estimates of the critical angles that are shown earlier. Note that the cross-over of the tumbling time and total flipping time occurs at roughly the Peclet number at the transition between Regimes 2 and 3. The analysis shows that the chain tumbling might restrict the maximum stretch that is attainable by flipping of individual rods in Regime 3. 109

Figure 3.15: (a) Comparison of Weissenberg number dependence of R_{gx} (normalized with the chain contour length) of a bead-rod chain of 500 rods and with chains coarse-grained to varying degrees, using the Cohen Padé approximation as the force law for the springs. The legend for each coarse-grained model has two numbers, the first representing the number of springs and the second one denotes the number of Kuhn lengths in each spring. The product of the two numbers in each case is approximately 500, implying that all the coarse-grained chains represent roughly the same fine-grained one. (b) Same as (a), except that the Underhill-Doyle model is used as the force law for the springs. 110

Figure 3.16: Comparison of Weissenberg number dependence of of R_{gy} a bead-rod chain of 500 rods and with chains coarse-grained to varying degrees, using the (a) Cohen Padé approximation as the force law for the springs, and (b) the Underhill-Doyle model as the force law for the springs. The legends used have similar significance as in Figure 3.15, and the solid lines indicate the approximate scaling law followed by the results for R_{gy} using the coarse-grained models. 111

Figure 4.1: (a) Variation of R_{gx}/L with Pe_K for chains of varying length and resolution. Legends indicate the type of model used (BR, CG or FG) followed by the number of Kuhn lengths in the chain. (b) Variation of R_{gx}/L vs. Wi, for various chain lengths, at shear rates in the transition to stretch saturation. The approximate scaling laws are indicated for all chain lengths considered. (c) A schematic of the FG model. Here L denotes the contour length of the chain ($L = N_K b_K$), where b_K is the length of one Kuhn step. Note, all results shown here are obtained without HI and EV.....135

Figure 4.2: (a) Variation of R_{gy}/b_K with Pe_K for chains of varying length and resolution. The solid black line indicates the scaling of the BR chains at high shear rates. The grey line shows the region where an exponent of approximately -1/4 is obtained for R_{gy} for the CG model for 5000 Kuhn steps (with 200 springs). The green line indicates that the exponent for the CG model (with 20 springs) is about -1/3, at high shear rates. (b) The Peclet number variation of the average Y-extent of the chain. Legends in (a) apply to (b), and indicates the type of model used (BR, CG or FG) followed by the number of Kuhn lengths in the chain. (c) Variation of R_{gy} with Wi for a BR chain of 100 rods for various combinations of HI and EV being present ('+' sign

in the legend indicates which mechanism is active). Here b_K denotes the length of one Kuhn step. Note, all results shown here, except those in (c), are obtained without HI and EV.....136

Figure 4.3: (a) Average x-y trajectory for the bead at the end of a BR chain of 300 beads, relative to the center of mass. (b) Time variation of the MSD in the y-direction for various beads in a chain of 300 rods. The lines show the exponents of the scaling laws in the different regions. (c) Four different examples of loops formed at chain ends during the end-over-end tumbling of a chain of 100 rods when $Pe_K = 0.15$. Red and orange mark the end beads. For each case, two different views are given – one is in the x-y plane that shows the conformation of the chain along the flow direction, and the other zooms into the loop formed at one end. 137

Figure 4.4: Variation of the tumbling times (normalized by N_K) with Pe_K. The solid black line shows the power law for BR chains of different lengths, which agree well with the scaling law in Eq. 4. The light blue line indicates that the power law exponent for the CG model is about -2/3, which deviates from the more resolved BR chains at high shear rates. Inset (i) shows a sketch of the zones used to count the tumbling events, as described in the text. Inset (ii) shows the approximate scaling (with Wi) of the tumbling time for BR chains of different lengths at shear rates prior to stretch saturation. The error bars are all smaller than the sizes of the symbols.....138

Figure 5.1: Dependence of relaxation time for polymer chains on the number of Kuhn steps, for cases where only excluded volume (EV) and only hydrodynamic

interactions (HI) is included. The '+' sign and 'no' indicate the mechanism that is active and not present, respectively. Note that, for results with EV, only the repulsive part of the LJ potential with $\sigma^* = 1$ is used for results presented here. The solid lines indicate that the results follow power laws with exponents of approximately 2 and 1.5 for cases with EV and HI, respectively. The inset shows the variation of the coil radius of gyration at equilibrium with chain length when EV is active. The solid line indicates a power law with an exponent of about 0.6. Note that all these results are obtained using the BR model. 166

Figure 5.2: Dependence of the chain elongation normalized by chain contour length L on shear rate for chains of different length, when only EV is active between beads. For all results shown here, EV is modeled by the repulsive part of the LJ potential with $\sigma^* = 1$. The inset shows the dependence of the coil thickness R_{gy} on shear rate for chains of different length, when only EV is present. The solid line marks the region of shear rates where R_{gy} follows a power law with an exponent of approximately -1/4. 167

Figure 5.3: Dependence of chain elongation on Peclet number for varying strength of EV, modeled by different values of σ^*, where EV is modeled by the repulsive part of the LJ potential. The results show that chain shrinkage at high shear rates occurs only for $\sigma^* = 0.1$, but the exponent (-0.058) is much smaller than in the case reported in earlier simulations in Chapter III (-0.15) without EV or HI. The inset shows the time variation of the end-to-end distance of a chain of 100 rods at high shear rates, with $\sigma^* = 1$. The 'strain' is the dimensionless time $t\dot{\gamma}$. The plot shows increasing levels of

orientational locking at a stretched state at shear rates of $\dot{\gamma} = 10^3$, 10^4 and 10^5, corresponding to Pe = 33.8, 338 and 3380 respectively. 168

Figure 5.4: (a) Probability distributions of the chain end-to-end distance for a BR chain of 100 rods at different shear rates, denoted by Peclet numbers, calculated using a bin size of 5. The inset shows the same for highly stretched states, using a bin size of 0.5. (b) The Peclet number variation of the average residence time for a chain in a highly stretched state, normalized by the chain length. Inset shows the shear rate dependence fraction of time that the chain spends in a highly stretched state over the whole trajectory. For more details and the definitions of the quantities, see text.....169

Figure 5.5: Shear rate dependence of the chain elongation R_{gx} normalized by chain contour length L for BR chains of different length, when only hydrodynamic interaction (HI) is active between beads. For all results shown here, the hydrodynamic diameter of beads is equal to one Kuhn length (represented by one rod in the BR model). Inset (i) shows the shear rate dependence of the coil thickness, represented by R_{gy}, for chains of different lengths, when only HI is present. The solid line marks the region of shear rates where R_{gy} follows a power law with an exponent of approximately -1/4. Inset (ii) shows that the chain forms a coil with R_{gx} of roughly one Kuhn length at high shear rates, for all chain lengths considered. 170

Figure 5.6: (a) The probability distribution of chain end-to-end distance at different shear rates for a BR chain of 100 rods, when only HI is present between beads with a hydrodynamic diameter of one Kuhn length ($h^* = 0.5$). (b) The time variation of the

end-to-end distance of a BR chain of 100 rods from a stretched state, with only HI present, at a shear rate with Pe = 3.38 ($\dot{\gamma}$ = 100). Inset shows the corresponding sequence of chain configurations to form a coiled state starting from a stretched state, where time increases from top to bottom. Note that the chain shows negligible stretching once a coiled state is attained. 171

Figure 5.7: Weissenberg number dependence of the chain elongation for varying levels of HI, modeled by different values of the bead hydrodynamic diameter (controlled by the parameter h^* in the simulation). All results shown here are for a BR chain of 100 rods. The inset shows the Weissenberg number dependence of the coil thickness (R_{gy}) for varying levels of HI. The solid line marks the region of shear rates where R_{gy} follows a power law with an exponent of approximately -1/4.....172

Figure 5.8: Shear rate dependence of the coil elongation normalized by chain length for chains of different length, when both EV and HI are active between beads. EV is modeled in two ways - by the repulsive part of the LJ potential with $\sigma^* = 1$ (denoted by 'EV') and by the full LJ potential with the value of ε^* tuned such that the size of the chain at equilibrium is similar to a theta coil (denoted by 'EV-theta'). The bead hydrodynamic diameter is taken as one Kuhn length for all cases. The inset shows the dependence on Peclet number of the coil thickness R_{gy} for chains of different length, when both EV and HI are active between beads. The solid line marks the region of Peclet numbers where R_{gy} shows a power law with an exponent of approximately -1/4.....173

Figure 5.9: Shear rate dependence of (a) the chain elongation and (b) the tumbling time (normalized by the end-to-end relaxation time of the chain) for a BR chain of 100 rods, when EV-theta and HI between beads are present or absent. The '+' sign and 'no' indicate the mechanism that is present and not present, respectively. For all results shown here, EV-theta is modeled by the full LJ potential with $\sigma^* = 1$ and the value of ε tuned such that the coil size at zero shear rate is same as that of a theta coil without excluded volume interactions. The bead hydrodynamic diameter is taken as one Kuhn length for all cases here. The solid lines indicate the different power laws shown in the different cases. 174

Figure 5.10: Variation of the coil elongation (normalized by the contour length L) with shear rates (represented by Weissenberg numbers) for a chain that consists of 25 Kuhn steps, at different levels of resolution, using the BR and FG models, including EV (no HI). Inset shows the dependence of the coil thickness, normalized by the Kuhn length, on shear rates for the same cases. The solid line indicates the region of shear rates where R_{gy} approximately follows a power law with an exponent of -1/4. The legends indicate the type of model used followed by the number of Kuhn steps. For the FG chains, the number of rods that constitute one Kuhn step is also provided in the legend. For all models used, ε^* is fixed at 1.0 and σ^* is varied so that the coil sizes are similar in the absence of shear flow ($\sigma^* = 0.6$ for the BR chain). 175

Figure 5.11: Variation of the coil elongation (normalized by the contour length L) with shear rates (represented by Weissenberg numbers) for a chain that consists of 12

Kuhn steps, at different levels of resolution, using the BR and FG models, including HI (without any bead-bead excluded volume interactions). Inset shows the dependence of the coil thickness, normalized by the Kuhn length, on shear rates for the same cases. The solid line indicates the region of shear rates where R_{gy} approximately follows a power law with an exponent of -1/4. As in Figure 5.10, the legends indicate the type of model used followed by the number of Kuhn steps. For the FG chains, the resolution is indicated in the legend by the number of rods that constitute one Kuhn step. For all models used, h^* is fixed at 0.5. 176

Figure 6.1: (a) The model with the optimal resolution to represent the polymer chain at various regions of shear rates. The dashed lines roughly indicate the zones where each model is expected to be valid. (b) The variation of the Pe for the onset of Regime 3 (Pe_{crit}) for a given model resolution (n_{res}). The green line indicates that the results show a power law exponent of about 4.....188

Figure A.1: Variation of the viscosity with the amplitude of periodic perturbation for the UA (Errington-Panagiotopoulos) and the CG (MARTINI) models for benzene. The extrapolation to zero amplitude represents the viscosity prediction for the system. Note that the predictions from the UA model agrees well with the experimental value at 293 K, whereas that from the CG model is about four times larger. 192

Figure A.2: Variation of computed density with number of benzene molecules in the bath for the Errington-Panagiotopoulos potential. Note that the predicted density for sufficiently large solvent bath is about 2% lower than the experimental value.....193

Figure A.3: The relaxation dynamics of the chain backbone bonds and the corresponding fits to a single exponential decay for the following models: (a) spr, (b) spr+ben, (c) spr+ben+tor, (d) spr+ben+tor+pot, (e) spr+ben+tor+side groups and (f) ACWS from BD simulations. Details of the models used for (a)-(f) are provided in text and Table 2.2.....194

Figure B.1: An example of a tumbling pathway where the beads at one end reach the critical y distance ahead of those at the other end, and are then carried away by convection to reach the other end. The simulations are for a BR chain of 100 rods in the absence of HI and EV, with a $Pe_K = 0.15$, which represents a shear rate in Regime 2. Note that the two end beads on the chain are colored red and yellow, whereas all other beads are colored blue.....197

Figure B.2: An example of a tumbling pathway where the motion of the beads at the two ends of the chain are almost synchronized. The simulations are for a BR chain of 100 rods in the absence of HI and EV, with a $Pe_K = 0.15$, which represents a shear rate in Regime 2. Note that the two end beads on the chain are colored red and yellow, whereas all other beads are colored blue.....198

Figure B.3: An example of a tumbling pathway where a group of internal beads reach the critical y distance ahead of those at the ends, and are then dragged away by convection to reach the other end. The simulations are for a BR chain of 100 rods in the absence of HI and EV, with a $Pe_K = 0.15$, which represents a shear rate in Regime

2. Note that the two end beads on the chain are colored red and yellow, whereas all other beads are colored blue.....199

Figure C.1: Comparison of the variation of R_{gx}/L with Wi obtained from the self-consistent method using the fractional extension based on the pre-averaged contour length of the whole chain and those obtained from BD simulations. The first term in the legend denotes either the model used for BD simulations or the method used for the self-consistent algorithm, which is followed by the chain length in terms of the number of Kuhn steps and the number of Kuhn steps mimicked by each spring. 'BR' and 'CG' denote bead-rod and bead-spring chains in BD simulations, respectively. The term 'UD' indicates the case where the Underhill-Doyle spring force law is used. The inset compares the results obtained from an analytical model given in Ref. [3] (implementation is discussed in details in Chapter III) and BD simulations with the bead-rod chain model.....218

Figure C.2: Comparison of the variation of R_{gx}/L with Wi obtained from the self-consistent method using the fractional extension based on the maximum average spring length in the chain (i.e. the length of the central spring, see Eq. (11)) and those obtained from BD simulations. The legends have similar meaning as those in Figure C.1. Note that the results from the self-consistent method agree well with those from simulations for the chain lengths considered here. 219

Figure C.3: Comparison of the shear rate variation of R_{gy} obtained from the self-consistent method using the fractional extension given in Eq. (11) and those obtained from BD

simulations. The legends have usual meanings (as described in the caption of Figure C.1). The solid gray line indicates a power law with an exponent of -1/3 at high shear rates. 220

Figure C.4: Comparison of the shear rate dependence of R_{gx} from the self-consistent method with different spring force laws and different number of Kuhn steps mimicked by one single spring, for chain lengths of 500 and 5000 Kuhn steps. Inset shows the same for R_{gy}. The legends have usual meanings. 221

Figure C.5: The variation of chain stretch (R_{gx}) normalized by the chain length (number of Kuhn steps) with Wi for widely varying chain lengths, from the self-consistent method and from the model for Gaussian chains without the effects of finite extensibility (see text for details). The gray dotted line indicates the values of Wi where the results from the two models start to deviate (i.e. end of Regime 1). Note that, for all chain lengths investigated here, this deviation starts when R_{gx} attains a value of about 7% of the chain length. The inset highlights the universality in the variation of the quantity $\frac{\left(R_{gx,plat} - R_{gx}\right)}{N_K^{1.35}}$ with Wi in the transition Regime, between Regime 1 and Regime 2. Here $R_{gx,plat}$ is the saturation value of R_{gx} at high shear rates (i.e. at the plateau, about 0.2L). The solid line indicates a power law with an exponent of -0.7. 222

Figure C.6: The Peclet number dependence of R_{gy} for widely varying chain lengths from the self-consistent method. The Peclet number is defined as Wi/N_K^2. The solid line

indicates a power law with an exponent of -1/3 at high shear rates. Note that the results are independent of chain length at high shear rates of Regime 2, consistent with the simulation and theoretical predictions in Chapters III and IV. Insets (i) and (ii) show the variation of the crossover Peclet numbers Pe_{c1} (denotes the end of Regime 1) and Pe_{c2} (denotes the onset of Regime 2) with chain length. In both cases, the solid line indicates a power law with an exponent of -3/2. 223

List of Tables

Table 2.1: List of the MD simulations of polystyrene chains and the number and time scales of the modes fitted to the bond orientation autocorrelation function. 'UA' and 'MARTINI' refer to the united-atom and MARTINI models respectively..... 48

Table 2.2: Chain models with continuum solvent studied. In all cases, there are 60 backbone beads (59 rods). Stiff Fraenkel springs are used to mimic 'rods' for all models. 49

Table 2.3: Diffusivities of the center of mass of the polymer chain (with 60 beads), in the absence and presence of HI. The diffusivity values reported here are in terms of characteristic length and time scales used in Ref. [54]. Note that, in the absence of HI, Rouse theory gives $D_{cm} = \frac{1}{N_{beads}}$ in the characteristic length and time units, where N_{beads} is the total number of beads in the chain. In this case, $N_{beads} = 60$ and hence $D_{cm} = 1/60 = 0.0167$, which is consistent with our simulation results given in the table. In the presence of HI, D_{cm} is higher than that without HI and decreases with the increase of the coil size (the average radius of gyration increases with the inclusion of additional mechanisms of bending, torsion and potential). 50

Table 4.1: Values of Kb used and the corresponding number of rods per Kuhn step for the FG chain model. 134

List of Appendices

APPENDIX A: Additional details on the molecular dynamics and Brownian dynamics simulations of polystyrene in benzene bath. 189

APPENDIX B: Sequences of chain configurations during tumbling in shear flow. 195

APPENDIX C: A self-consistent method for the prediction of the deformation behavior of isolated polymer chains in shear flows. 200

Abstract

In this dissertation, we have explored various aspects of polymer dynamics in dilute solutions, at equilibrium and non-equilibrium conditions, with computational models ranging over multiple length and time scales, using both molecular dynamics and Brownian dynamics (BD) simulations. Our investigations on equilibrium polymer dynamics helps resolve the puzzle of the absence of high frequency modes in the relaxation spectrum of the chain, reported decades ago by Schrag and coworkers. For this, we systematically introduce the various mechanisms acting on the atoms of a short polystyrene chain. Our simulations clearly show that, in terms of a re-scaled time that is based on the chain size and diffusivity of the center of mass, each additional detail causes a slow-down in the relaxation dynamics of the chain backbone bonds. Finally, when all mechanisms are present, including the explicit solvent molecules, the bond relaxation dynamics shows a single exponential decay for a short polystyrene chain with a time scale that is temporally indistinguishable from that of the end-to-end relaxation dynamics, in excellent agreement with the earlier experiments.

Next, we investigate the conformational and dynamic behavior of polymer chains in shear flows using BD simulations with chain models encompassing widely varying resolutions. Our simulations reveal multiple regimes for chain deformation as the flow rates range from weak to ultra-high. We show that, in the absence of any excluded volume (EV), the chain compression obtained at high shear rates in several earlier simulations is an artifact of

insufficient chain discretization. In the presence of EV, an orientational "locking" at the fully extended state is observed at extremely high shear rates. We show that the chain tumbling at strong shear rates occurs by the formation of loops whose length is limited by the time required to stretch them, and derive scaling laws from a balance of convection and diffusion of monomers in those loops. Our model and results presented here corrects the previously reported scaling laws obtained by using coarse-grained bead-spring models, which fails to capture the correct physics at strong shear rates that can excite a single spring away from equilibrium.

CHAPTER I

Introduction

The dynamics of polymers, both in solutions and in a melt, has been investigated for decades through viscoelastic experiments [1-4] and Optical Flow Birefringence (OFB) measurements [5-11]. The earliest analytical model for a polymer chain in a dilute solution is provided by Rouse [12] to which corrections for hydrodynamic effects, using pre-averaged hydrodynamics, is incorporated by Zimm [13]. Essentially, these models represent the polymer chain by a series of beads connected by Hookean springs, where each bead experiences a Brownian force from the solvent molecules. These simple models beautifully illustrate how the polymer relaxation dynamics consists of processes at multiple length and time scales – each corresponding to a "mode" in the chain, and thus provides a strong analytical foundation over which further details can be analyzed and interpreted. Surprisingly, in spite of using such simplistic assumptions, experiments have confirmed that these models adequately describe the chain dynamics at equilibrium over a wide range of frequencies, even at high enough frequencies when the basic assumption of these models to represent a sub-section of the chain by a linear (Hookean) spring is supposed to break down!

Apart from these mechanical bead-spring models that provide an analytical foundation, for highly detailed theoretical and computational studies, especially in conditions that are far

away from equilibrium as well as in more complicated environments, there is always a need for detailed knowledge of the evolution of conformations of individual polymer molecules, which requires more sophisticated models for the chain. Experimentally, direct studies for the chain conformational dynamics began little more a decade ago, through the imaging of individual DNA molecules in extensional and shear flows [14, 15]. This is followed and massively supplemented by information from computer simulations of polymer molecules, which are enabled by the increase in computing power. Throughout the past decade, Brownian dynamics (BD) and molecular dynamics (MD) simulations, in addition to other techniques like the Dissipative Particle Dynamics (DPD) and Stochastic Rotation Dynamics (SRD), have been instrumental in extracting molecular-level insights for polymer molecules in both solutions and melts. For polymer solutions, Brownian dynamics simulations have been significantly useful to understand the behavior of polymer molecules in flow fields. Extensive investigations utilizing Brownian dynamics have been performed to understand the dynamics of polymer molecules in various flow fields – few examples include extensional [16], shear [17, 18] and mixed flows with varying amounts of extension and shear [19]. These typically employ bead-rod [18] or less refined bead-spring [16, 19] models for polymer chains of sufficient length to understand the underlying physics. Molecular Dynamics simulations have also been applied to study polymer dynamics in various environments. This technique has been used quite frequently by researchers to study dynamics in melts - one of the earliest examples being the study by Kremer and Grest [20], which involved system of several model polymer chains of simple spherical beads connected by springs. Despite the power to provide a highly detailed

picture, the use of MD for polymer solutions has been confined to studying the chain dynamics at equilibrium for relatively small chain sizes, owing to the significantly high computational requirements to track an enormous number of degrees of freedom of all solvent molecules in the system. However, few researchers did employ MD simulations to investigate the dynamics of polymers in dilute solutions, and some of the studies consisted of using a model chain with spherical beads connected by springs immersed in a bath of simple spherical solvent molecules [21-23]. The interaction between the beads and solvent particles is modeled using simple LJ potentials [21, 22] or hard-sphere interactions [23]. However, these simulations are expected to provide only a qualitative picture as they neglect the exact structure of the monomers as well as the solvent. Others include MD simulations of polyisoprene in toluene [24, 25], polyisoprene in cyclohexane [26], polystyrene in benzene [27, 28] and poly(ethylene oxide) in water [29] and toluene [30, 31]. These studies provide valuable information on the variation of dynamic properties with changes in concentration [27-29] as well as the relaxation of different bonds and the cooperativity of conformal transitions [24]. It was shown that the cooperation needed for conformal transitions is provided mostly by the immediate neighbors – an observation consistent with that of an earlier Brownian dynamics study of polyisoprene [32].

Despite the phenomenal increase in computing power, a fully atomistic study of large polymer molecules will still not be practically feasible for some more years ahead. The reason behind this is not only the length scales involved due to bigger molecules but also the time scales required for the simulation. For macromolecules, simulation time scales increase by orders of magnitude with modestly increasing length scales, both because the

larger molecules need bigger simulation boxes to contain them and because the relaxation time increases rapidly with the size of the molecule. Hence, the simulation needs to be run for longer duration so that the system is equilibrated and properties can be calculated. At the same time, the timestep size needs to be small (~1 fs) to perform numerically accurate simulations of an atomistically detailed system. Thus, it will take about 10^6 timesteps to just reach a nanosecond for such a system. For a reasonably large system, the huge number of interactions that needs to be computed in each timestep results in a prohibitive computational cost.

The philosophy of coarse-graining attempts to provide a practical solution to this problem. In general, all coarse-graining procedures combine a group of interaction sites to one effective interaction site. From the point of view of an atomistic picture, it means that a group of atoms are combined to form a single "super-atom". The total interaction between two different groups of atoms can now be represented by the interaction between just two super-atoms – resulting in a massive reduction in the number of pair interactions to be computed. The information and distribution functions required to enable this reduction usually comes from atomistic simulations. It is implicitly assumed that all the faster processes occurring at finer length scales are at equilibrium and only the slower processes are considered to describe the time evolution of the system. It is to be emphasized here that the terms "fast" and "slow" depends on the "resolution" (or degree of coarse-graining) chosen to describe the system. From the simulation standpoint, usage of softer coarse-grained potentials presents another advantage – the size of the timestep can be increased by one or two orders of magnitude (for usual coarse-grained models of atomistic systems).

Combined with the savings from reducing the number of degrees of freedom, the overall simulation speed is increased by 3-4 orders of magnitude. The degree of coarse-graining can be varied and is typically selected based on the processes to be investigated. However, coarse-graining at any level inevitably leads to some loss of information about the system and this loss is expected to increase with increasing degrees of coarse-graining. Selecting the appropriate level of coarse-graining is critical to the accuracy and relevance of the final results obtained from the simulation. From this viewpoint, Brownian dynamics simulations of dilute polymer solutions also represent an extreme level of coarse graining, where usually bead-spring or bead-rod models are employed which neglect the exact structure of the polymer chain, in addition to replacing the explicit solvent molecules by a continuum.

Among coarse graining methods used in recent studies, the structure-based coarse-graining provides a procedure for hopping between length scales while staying as close as possible to the chemical structure. This approach usually starts with the molecule with atomistic details and systematically moves to larger length scales. This method has been quite successful for various macromolecules [33-36]. Structure-based coarse-graining involves two important steps. First, an atomistic model of the system is mapped to “beads” or “super-atoms”. Despite being an important step, there is no set of well-established rules to execute the mapping for any given system. The mapping scheme involves selecting the “mapping ratio” (number of atoms or groups to be combined into one bead or super-atom) and the location of the centers of mapped beads or super-atoms. Thus, there can be a multitude of viable mapping schemes for any given system and the selection of any one scheme also involves the next step of structure-based coarse-graining, where the potentials

for the CG model are determined. It involves the computation of distribution functions of bond lengths, bond angles, torsions and the radial distribution function for the CG beads from the atomistic simulations. For simplicity, it is assumed that the distribution functions for the intra-molecular degrees of freedom are independent of each other. This assumption can sometimes be used as a condition to be fulfilled by the CG model, which helps in the selection of an appropriate mapping scheme, as in Ref. [37]. Once the distributions are computed, the CG interaction potentials are obtained by Boltzmann inversion. The potentials thus obtained represent the first guess to the actual potential that would produce the correct structure. If it doesn't, these potentials need to be optimized so that the final distributions obtained from CG simulations match with those calculated by the simulation of atomistic models. This optimization has been carried out using simplex algorithm in some earlier studies [38, 39]. Although mostly this approach is used to arrive at a mesoscale model, the same philosophy is valid for modeling at any length scale and systematic coarse-graining starting from atomistic model can lead to a macroscopic model that still retains some information about the atomistic one. Following the same guiding principles, a soft ellipsoid model to describe an entire polymer chain has also been obtained [40].

As discussed earlier, the coarse graining techniques mostly focus on obtaining the correct structural correlations of the actual system by matching the same with the results obtained from higher resolution simulations. For polymer solutions, with the available methods, starting from a MD system that consist of a polymer chain and solvent molecules, successive coarse graining steps can be performed to finally obtain a bead-spring model for

BD simulation for a given chain, while passing through varying degrees of resolution in the intermediate stages that may use either MD or BD simulations. Even with this seemingly tremendous loss of information while traversing such widely different length scales, the structural correlations are expected to be preserved at equilibrium. However, nothing is known about the loss in the accuracy in the dynamics of the processes that occur in the system, especially when such models are applied to study chains in strong flows, far from equilibrium. Large flow rates are expected to excite the motions at the short length scales, the absence of which, in highly coarse grained models, can lead to an incorrect understanding of the physics. At this point, it is also not known if the absence of such finer details is significant for studies of equilibrium polymer dynamics as well. In this thesis, we will explore how these finer details influence the physics for dilute polymer solutions, both at equilibrium and non-equilibrium conditions. In the process, we will also clarify and correct results from several earlier studies and approximately evaluate the flow rates at which different coarse-grained models, at varying degrees of resolutions, break down to provide incorrect predictions for the dynamics. This knowledge will enable future studies to select the appropriate model (i.e. the correct length scale for resolution of the chain) for the theoretical/computational study of a given problem. In what follows, we list down the specific problems and issues that will be investigated in this thesis, both at equilibrium and non-equilibrium conditions, for dilute polymer solutions.

Equilibrium polymer dynamics

As mentioned earlier, the dynamics of polymer chains in dilute solutions and melts, both at equilibrium and non-equilibrium conditions, have been thoroughly investigated by theory

[12, 13], experiments [1-11] and simulations [16-19, 24-32, 41, 42] over several decades. Viscoelastic [1-4] and Optical Flow Birefringence (OFB) measurements [5-11] have established the success of the decades-old Rouse-Zimm theory [12, 13] in predicting the chain dynamics in dilute solutions over a wide range of frequencies. The Rouse-Zimm theory treats the polymer chain as a set of beads connected by Hookean (linear) springs, where each spring represents a sub-section of the chain. Although relevant for the dynamics at low frequencies (or large time scales), where the sub-section represented by the spring is not perturbed far away from equilibrium, this model is not expected to capture the dynamics of the chain at high frequencies (or short time scales) that excite polymer segments that are smaller than the sub-section represented by a Hookean spring. At very high frequencies, the chain dynamics are likely to be governed by the local motions of a few bonds on the chain backbone, which will be influenced by the bending, torsional and non-bonded potentials (typically described by Lennard-Jones interactions). At such length scales (a few bonds) and time scales (high frequencies), the assumption of an elastic spring is expected to break down, as it fails to exhibit fast modes that are controlled by these highly local interactions. However, quite surprisingly, as mentioned earlier, experiments by various researchers [5, 8, 9, 10] have shown that the Rouse-Zimm theory can be used to describe the chain dynamics over the entire frequency range studied for polystyrene and polyisoprene chains in dilute solutions, where the highest frequencies accessed should excite a response at length scales smaller than that of a single spring. Even more surprising is the fact that the best fits of the Rouse-Zimm theory to the data are obtained if each spring is chosen to represent an amazingly long sub-molecule of approximately 100

backbone bonds, corresponding to a molecular weight of about 5000 and 2400 for polystyrene and polyisoprene, respectively, as summarized in Ref. [10]. In sharp contrast, analogous experimental measurements in melts for both of these polymers have shown the existence of higher modes, which are only poorly fit by the bead-spring model, even when the smallest sub-chain size is chosen to be an order of magnitude smaller than that needed for an excellent fit in the case of dilute solutions [3, 4, 10]. The results in melts are not surprising: we expect small-scale motions of the chain to affect the high-frequency viscoelastic spectrum and the smallest-scale (highest frequency) modes, involving only a few bonds, to be poorly predicted by a coarse-grained bead-spring model. What is puzzling is that these higher modes don't appear in the viscoelastic spectrum of dilute solutions.

Despite several prior studies, the mystery of vanishing high frequency modes in dilute solutions, leading to an abrupt cut-off in the relaxation spectrum, is still unresolved. Schrag and coworkers [10] suggested that this cut-off is an effect of the hindrance of the solvent molecules to local motions. They argued that since a group of few solvent molecules have to diffuse away to allow the exploration of the local conformational space at short times, the relaxation of localized modes is hindered to such an extent that they don't appear in the relaxation spectrum of the chain. Others [41, 43] also suggested that the torsional barriers to bond rotations might slow down the relaxation of faster modes to an extent that their rates become similar to those of the end-to-end relaxations of short polymer chains. This idea was tested by Jain and Larson [42], who used Brownian dynamics on a polyethylene model chain that included bending and torsional potentials between the backbone bonds.

They showed that the bending and torsional rigidities suppress the local modes of motion such that for a chain of 60 backbone bonds the relaxation dynamics of the backbone bonds deviates strongly from that predicted by the Rouse theory and is closer to that of the end-to-end vector of the chain. However, even with the inclusion of torsional and bending potentials, the relaxation spectrum for this 60-bond chain did not show a single exponential decay, which was observed in viscoelastic and OFB experiments for chains of such length.

In Chapter II of this thesis, using multi-scale modeling, including Molecular Dynamics simulations, with both united-atom and coarse-grained force fields, as well as Brownian dynamics simulations with still higher levels of coarse-graining, we explain this long-mysterious absence of high frequency modes in the viscoelastic spectrum of isolated polymer chains in good solvents at equilibrium. The relaxation spectrum we obtain for a chain of 30 monomers at atomistic resolution is, remarkably, a single exponential, while that of a coarse-grained chain of 100 monomers is well fit by only two modes, in perfect agreement with experimental observations of Schrag and co-workers mentioned earlier (summarized in Ref. [10]). We also performed Brownian Dynamics (BD) simulations in which the explicit solvent molecules are replaced by a viscous continuum, using chain models of varying degrees of resolution, both in the presence and absence of hydrodynamic interactions (HI). Although the local dynamics is suppressed by the addition of bending, torsion, side groups and excluded volume interactions, none of the BD simulations predict a single exponential relaxation for a short polymer chain. The comparison of the relaxation of the bond vectors from different models indicates an additional slow-down in the presence of explicit solvent molecules, which is critical to

obtain a single exponential relaxation for short chains. These results indicate that the chain dynamics at small length scales (down to a few Kuhn steps) are significantly different from the predictions of models based on a continuum solvent, and finally help explain the experimental results showing an abrupt cut-off in the relaxation spectrum of the polymer chain. In other words, we show that, even at equilibrium conditions, the chain dynamics is correctly predicted only when all the explicit solvent molecules and the chain rigidities are retained.

Non-equilibrium polymer dynamics

In this study, steady shear flows form the basis of all investigations in non-equilibrium conditions. Shear flows are ubiquitous in nature, since the flow near any boundary can be approximated as a shear flow, and represents a very interesting case of the class of mixed flows, one where the extensional and rotational rates are equal. The behavior of isolated long, flexible polymers in shearing flow is thought to be relatively well understood, as a result of single-molecule imaging of long DNA polymers [15, 44-45], rheological measurements on dilute polymer solutions [46-49], and Brownian dynamics simulations of isolated bead-rod and bead-spring models of such polymers [17-18, 50-52]. These studies have firmly established that a single molecule in shear flow undergoes a repeated succession of stretching and coiling events without ever reaching a steady state conformation – consistent with the fact that a shear flow is composed of equal amounts of extensional and purely rotational flows. The conformational transitions and probability distributions of the stretch of the molecule computed from Brownian dynamics simulations on a multi-bead Kramer's chain agree well with the experimental results obtained by

tracking single DNA polymers [17]. These studies show that at low shear rates the distribution of chain stretch is strongly peaked at low values of stretch. As the shear rate increases, the distribution of stretch gradually broadens, and at high shear rates, a nearly uniform distribution of stretch, ranging from nearly coiled to nearly fully extended, is attained. Thus, at high shear rates, the average molecular stretch saturates at a value of around 40% of the contour length of the chain. This roughly uniform distribution, with its corresponding plateau value of the mean stretch, has been thought to represent the asymptotic high-shear-rate state of isolated, flexible polymers under steady shearing.

In light of this seemingly settled picture, it is rather surprising that a recent simulation study by Sendner and Netz [53] of a polymer chain composed of stiff Fraenkel springs showed a highly non-monotonic dependence of mean stretch on shear rate, with a maximum stretch, followed by a decrease at very high shear rates. This non-monotonic dependence of stretch on shear rate was observed in the absence of hydrodynamic interactions (HI) and excluded volume (EV), but became more pronounced in the presence of HI, and almost vanished when EV interactions were considered. While these results might seem inconsistent with earlier studies, most of the earlier studies either used coarse-grained flexible spring chains, or did not investigate the behavior at the very large shear rates at which the non-monotonic stretch was observed by Sendner and Netz [53]. To the best of our knowledge, only three earlier studies have noted a decrease in chain stretch at very high shear rates. In one of these, Liu [50] observed a decrease in the average chain end-to-end distance at high shear rates for a Kramer's chain of 20 beads. In the other, Petera and Muthukumar [51] observed a non-monotonic chain stretch in a bead-rod chain

of 20 beads when hydrodynamic interactions and excluded volume interactions were neglected. Another recent study observed a non-monotonic dependence of stretch on shear rate when attractive interactions were introduced between beads of a 20 and 40-bead bead-spring chain [54]. Additionally, the study by Doyle et al. [18] notes a "region III" at ultra-high shear rates in the viscosity measurements from BD simulations of the bead-rod model for a chain of 20 rods. Much longer chains were studied in ref. [53] and a decrease in chain stretch at high shear rate without HI and EV was reported for a chain composed of 101 beads connected by stiff Fraenkel springs that mimic rods. For a Gaussian chain, the root mean square of the stretch increases linearly with shear rate [55], which suggests that the decrease in chain stretch at high shear rates observed in simulations results from the finite extensibility of the chain.

These studies, especially those of Sendner and Netz [53], suggest that the plateau in stretch observed in early studies does not represent the asymptotic high-shear-rate limit, and that the behavior of isolated polymer chains over the entire range of shear rate is still not well understood, even for the case in which both excluded volume and hydrodynamic interactions are neglected. The overall aim of this thesis is to map out thoroughly the polymer chain dynamics over the widest possible range of shear rates for finitely extensible chains of different numbers of Kuhn steps. In the process, we will investigate the chain deformation regimes and the corresponding scaling laws over a wide range of shear rates and chain lengths. Our results with highly resolved chains will correct the previously reported scaling laws of chain tumbling dynamics - both at weak and high shear rates. We also formulate a simple physical model that predicts the correct scaling laws to

explain our simulation results. We also explore the inaccuracies and numerical artifacts that occur in such computations when an insufficient chain resolution is employed, thereby finally completely, and accurately, explaining chain dynamics in shear flows, including the surprising non-monotonic stretch behavior observed in the earlier studies. Note that all studies in this thesis for non-equilibrium polymer dynamics is performed using BD simulations, over a wide range of chain model resolutions.

In Chapter III, we use Brownian dynamics simulations without excluded volume and hydrodynamic interactions, on single polymer molecules represented by bead-spring models with stiff Fraenkel springs mimicking a single Kuhn step, similar to that used in the study by Sendner and Netz [53]. We explore, in details, the multiple nonlinear regimes of deformation in shear flows that are controlled by the Peclet number (*Pe*), which is the shear rate times the relaxation time of a Kuhn step. We show that, for all chain lengths investigated using the bead-rod model, the average stretch in the flow direction initially increases with increasing *Pe*, followed by saturation in chain stretch, as observed in previous studies. At even higher *Pe*, the stretch begins to decrease with increasing shear rate, in accordance with the results of similar simulations mentioned earlier. Our analysis of the trajectories at these rates reveal "premature" recoiling of the chain before attaining a fully extended state during the phase of the "tumbling orbit" in which the chain is stretching. At even higher *Pe*, orientation "locking" effects lead to an increasing stretch. We also show that the predictions of coarse-grained bead-spring models agree well with those of the fine-grained chains until high shear rates are reached, where the flow perturbs the individual springs from equilibrium.

In Chapter IV, we use BD simulations of polymer chains modeled over a wide range of resolution to find universal scaling laws for polymer coil dimensions and tumbling time. At high shear rates (denoted by $\dot{\gamma}$), our results show that the coil thickness in the gradient direction becomes independent of chain length (also shown in the results of Chapter III using the bead-rod model), scaling as $N_K^0\dot{\gamma}^{-1/4}$, where N_K denotes the numbers of Kuhn steps, and the tumbling time scales as $N_K\dot{\gamma}^{-3/4}$, correcting scaling laws presented in prior studies [19, 45]. We find this to be a consequence of the formation of loops whose length is limited by the time required to stretch them, and derive scaling laws from a balance of convection and diffusion of monomers. We find that, in the absence of HI and EV, for wormlike chains, the shrinkage in chain stretch observed at ultra-high shear rates (shown in Chapter III and in the recent study by Sendner and Netz [53]) is pushed out to arbitrarily high shear rates if the chain is resolved increasingly finely below the Kuhn length. Finally, scaling laws in the presence of excluded volume and hydrodynamic interactions are derived that are expected to be valid for long chains at high shear rates.

In Chapter V, we extend the analysis in Chapters III and IV to polymer chains in the presence of EV and HI, over a wide range of model resolution. Our results reveal that the decrease in chain stretch at high shear rates, in the presence of HI but absence of EV, is an artifact of resolution, similar to the case of chains without either EV or HI. However, the response in the presence of EV (in the absence of HI) at high shear rates is similar across all model resolutions studied, including the orientational "locking" behavior at high shear rates. Even with the presence of both HI and EV, the deformation behavior of the chains is

similar and small amounts of EV interactions are sufficient to hinder the chain compression at high shear rates.

Thus, in this thesis, we present computational studies of various aspects of polymer dynamics in dilute solutions, using models that retain all details on the chain as well as explicit solvent molecules (MD) and those which replace the solvent degrees of freedom by a continuum (BD) while describing the chain over a wide range of resolutions, all the way down to a relatively crude bead-spring model. However, the study of non-equilibrium polymer dynamics using MD simulations, with explicitly treated solvent molecules, is beyond the scope of this study, owing to enormous computational cost. Besides resolving different aspects of polymer dynamics in dilute solutions, these studies constitute a platform for understanding the differences between the performances of various models and serves to highlight the importance of the various details and their contributions to chain dynamics. Our results also provide estimates of the appropriate level of resolution to be used to investigate the physics correctly for a given rheological problem.

References:

[1] Lamb, J; Matheson, A. J. *Proc. Roy. Soc., Ser. A*, 1964, 281, 207-222.
[2] Massa, Dennis J.; Schrag, John L.; Ferry, John D. *Macromolecules,* 1971, 4, 2, 210-214.
[3] Inoue, T.; Okamoto, H.; Osaki, K. *Macromolecules*, 1991, 24, 5670–5675.
[4] Gray, R. W.; Harrison, G.; Lamb, J. *Proceedings Royal Society (London)*, 1977, A356, 77.
[5] Sammler, R. L.; Landry, C. J. T.; Woltman, G. R.; Schrag, J. L. *Macromolecules*, 1990, 23, 2388.
[6] Yoshizaki, T.; Yamakawa, H. *J. Chem. Phys.* 1988, 88, 1313.
[7] Bird, R. B.; Curtiss, C. F.; Amstrong, R. C.; Hassager, O. *Dynamics of Polymeric*

Fluids,
Vol. 2: Kinetic Theory; Wiley: New York, 1987.
[8] Sammler, R. L.; Schrag, J. L. *Macromolecules*, 1989, 22, 3435.
[9] Amelar, S.; Eastman, C. E.; Morris, R. L.; Smeltzly, M. A.; Lodge, T. P.; Meerwall, E. D.
V. *Macromolecules*, 1991, 24, 3505–3516.
[10] Peterson, S. C.; Echeverria, I.; Hahn, S. F.; Strand, D. A.; Schrag, J. L. J. *Polym. Sci.: Part B: Polym. Phys.*, 2001, 39, 2860–2873.
[11] Lodge, Timothy P.; Miller, James W.; Schrag, John L. *Journal of Polymer Science*, 1982, 20, 1409-1425.
[12] Rouse, P. E., Jr. *J. Chem. Phys*., 1953, 21, 1272-1280.
[13] Zimm, B. H. *J. Chem. Phys*., 1956, 24, 269-278.
[14] Perkins, T. T.; Smith, D.E.; Larson, R. G.; Chu, S. *Science*, 1995, 268, 5207, 83-87.

[15] Smith, D. E.; Babcock, H. P.; Chu, Steven *Science*, 1999, 283, 5408, 1724-1727.
[16] Larson, R. G.; Hu, Hua; Smith, D. E., Chu, S. *Journal of Rheology*, 1999, 43, 2, 267-304.

[17] Hur, J. S.; Shaqfeh, E. S. G.; Larson, R. G. *Journal of Rheology*, 2000, 44, 4, 713-742.

[18] Doyle, P. S.; Shaqfeh, E. S. G.; Gast, A. P. *Journal of Fluid Mechanics*, 1997, 334, 251-291.

[19] Lee, Joo Sung; Shaqfeh, Eric S. G.; Muller, Susan J. *Physical Review E.* 2007, 75, 040802-1-4.

[20] Kremer, Kurt; Grest, Gary S. *J. Chem. Phys*., 1990, 92, 8, 5057-5086.

[21] Kremer, Kurt; Grest, Gary S.; Carmesin, I. *Physical Review Letters*, 1988, 61, 5, 566-569.

[22] Bruns, W.; Bansal, R. *J. Chem. Phys*., 1981, 74, 3, 2064-2072.

[23] Rapaport, D. C. *J. Chem. Phys*., 1979, 71, 8, 3299-3303.

[24] Moe, Neil E.; Ediger, M. D. *Macromolecules*, 1995, 28, 2329-2338.

[25] Moe, Neil E.; Ediger, M. D. *Macromolecules*, 1996, 29, 5484-5492.

[26] Faller, Roland *Phys. Chem. Chem. Phys*., 2002, 4, 2269-2272.

[27] Muller-Plathe, Florian *Macromolecules*, 1996, 29, 4782-4791.

[28] Muller-Plathe, Florian *Chemical Physics Letters*, 1996, 252, 419-424.

[29] Borodin, Oleg; Bedrov, Dmitry; Smith, Grant D. *Macromolecules*, 2001, 34, 5687-5693.

[30] Fuson, Michael M.; Ediger, M. D. *Macromolecules* 1997, 30, 5704-5713.

[31] Fuson, Michael M.; Hanser, Kent H.; Ediger, M. D. *Macromolecules* 1997, 30, 5714-5720.

[32] Adolf, David B.; Ediger, M. D. *Macromolecules*, 1991, 24, 5834-5842.

[33] Tschop, W; Kremer, K.; Batoulis, J.; Burger, T., Hahn, O. *Acta Polymer*, 1998, 49, 61-74.

[34] Harmandaris, V. A.; Adhikari, N. P.; van der Vegt, N. F. A.; Kremer, K. *Macromolecules*, 2006, 39, 6708-6719.

[35] Harmandaris, V. A.; Reith, D.; van der Vegt, N. F. A.; Kremer, K. *Macromolecular Chemistry and Physics*, 2007, 208, 2109-2120.

[36] Milano, G.; Muller-Plathe, F. *J. Phys. Chem. B*, 2005, 109 (39), 18609-18619.

[37] Harmandaris, V. A.; Reith, D.; van der Vegt, N. F. A.; Kremer, K. *Macromolecular Chemistry and Physics*, 2007, 208, 2109-2120.

[38] Faller, R.; Schmitz, H.; Biermann, O.; Muller-Plathe, F. *Journal of Computational Chemistry*, 1999, 20, 10, 1009-1017.

[39] Reith, D.; Meyer, H.; Muller-Plathe, F. *Macromolecules*, 2001, 34, 2335-2345.

[40] Murat, M.; Kremer, K. *Journal of Chemical Physics*, 1998, 108, 10, 4340-4348.

[41] Fixman, M. *J. Chem. Phys.* 1978, 69 (4), 1538–1545.
[42] Jain, Semant; Larson, Ronald G. *Macromolecules* 2008, 41, 3692-3700.

[43] Larson, R. G. *Macromolecules* 2004, 37, 5110–5114.

[44] Hur, J. S.; Shaqfeh, E. S. G.; Babcock, H. P.; Smith, D. E.; Chu, S. *J. Rheol.* **45**, 421-450 (2001).

[45] Schroeder, C. M.; Teixeira, R. E.; Shaqfeh, E. S. G.; Chu, S. *Phys. Rev. Lett.* **95**, 018301 (2005).

[46] Link, A.; Springer, J. *Macromolecules* **26**, 464-471 (1993).

[47] Lee, E. C.; Solomon, M. J.; Muller, S. J. *Macromolecules* **30**, 7313-7321 (1997).

[48] Lee, E. C.; Muller, S. J. *Polymer* **40**, 2501-2510 (1999).

[49] Bossart, J.; Öttinger, H. C. *Macromolecules*, **30**, 5527-5540 (1997).

[50] Liu, T. W. *J. Chem. Phys.* **90**, 5826-5842 (1989).

[51] Petera, D.; Muthukumar, M. *J. Chem. Phys.* **111**, 7614-7623 (1999).

[52] Hsieh, C.-C.;Larson, R. G. *J. Rheol.* **48**, 995-1021 (2004).

[53] Sendner, C.; Netz, R. R. *Eur. Phys. J. E* **30**, 75-81 (2009).

[54] Hoda, N.; Larson, R. G. *J. Rheol.,* **54**, 1061-1081 (2010).

[55] Bruns, Wolfgang; Carl, Wilfried *Macromolecules* **26**, 557-558 (1993).

CHAPTER II

Explaining the "missing" high-frequency viscoelastic relaxation modes in the relaxation spectrum of polymers in dilute solutions

1. Introduction

As discussed in Chapter I, equilibrium and non-equilibrium polymer dynamics, in dilute solutions and melts, have been extensively studied by means of theory [1, 2], experiments [3-13] and computational investigations [14-17, 19-24] over several decades. The foundation for the analysis of the dynamics of polymer chains in dilute solutions is provided by the rather simplified Rouse model [1], whereas the Zimm model [2] adds the effect due to hydrodynamic interactions. The Rouse model simplifies the chain as a series of beads connected by Hookean springs, where each spring represents a sub-section of the chain and the thermal motion of the solvent molecules provides a Brownian force to each bead. The resulting picture consists of a series of relaxation processes over different length scales of the chain, each called a "mode" and each associated with a time scale. These originate from the normal modes, which are defined for such a chain after a transformation of the coordinates of each bead (in the solution of the Rouse model [1]), where each normal mode is representative of a chain segment that contains one or several springs. The

relaxation of each of these normal modes is independent of others, and all of them show a single exponential relaxation with a characteristic time scale. Hence, after transforming back to Cartesian coordinates, the relaxation dynamics of one single spring in the chain have contributions due to the relaxation of all modes – consisting of one, two etc. upto N springs (if the polymer chain consists of N springs). Thus, the Rouse theory (and the Zimm theory as well) predicts the relaxation of one spring to be a sum of N exponential decay terms, with each term corresponds to a normal mode in the chain. It is reasonable to expect that such a highly simplified model will not capture the chain dynamics at high frequencies, which is likely to be governed by the local motions of a few bonds on the chain backbone, which will in turn be influenced by the bending, torsional and excluded volume interactions (typically described by Lennard-Jones potentials at these small length scales) in the real chain. However, quite surprisingly, viscoelastic [7, 8] and Optical Flow Birefringence (OFB) measurements [3-6, 9, 10] by various researchers have shown that the Rouse-Zimm theory can be applied successfully to describe the chain dynamics over a wide range of frequencies, spanning several orders of magnitudes, for dilute solutions of polystyrene and polyisoprene, where the highest frequencies accessed should excite a response at length scales smaller than that represented by a single Hookean spring. Even more puzzling is the fact that Rouse-Zimm model fits the experimental data quite well if each spring represents an amazingly long subsection consisting of molecular weights of about 5000 and 2400 for polystyrene and polyisoprene, respectively (all these observations are summarized in Ref. [10]), which approximates to 100 backbone bonds in each case. In contrast, the same experimental measurements in melts for both of these polymers have

shown the existence of higher modes, the highest being roughly an order of magnitude smaller in size than that obtained in dilute solutions [7, 8, 10]. These results in melts are consistent with our expectation that the chain motions at small length scales will affect the high-frequency viscoelastic spectrum, and hence are not as surprising as those in dilute solutions. The fact that these modes are "missing" in the viscoelastic spectrum of dilute solutions constitutes the key mystery emerging out of these experimental results.

As discussed in Chapter I, these puzzling results in dilute solutions are still not resolved, in spite of several earlier studies by various researchers [14, 15, 18]. The question was partly answered earlier in the simulation study of Jain and Larson [15], where they showed that the time scales of higher modes shift to larger values with the addition of bending and torsion, thus not showing up in the spectrum. However, for the short chain that they investigated, the relaxation spectrum was still not single exponential, which is expected from the viscoelastic and OFB measurements.

In this Chapter, we find that an atomistically resolved model of a short polystyrene chain that couples the motion of solvent molecules with that of the atoms on the polymer chain, while also including bending and torsional potentials, side groups and excluded volume interactions on the chain, is able to predict single exponential relaxation in a dilute solution with a good solvent. Our results show sensitivity to all these mechanisms and prove that each of them is needed to obtain a single exponential relaxation for a short chain, especially the inclusion of solvent molecules explicitly – a detail that was not considered in the earlier study by Jain and Larson [15]. By using both Molecular dynamics (MD) and Brownian dynamics (BD) simulations of realistic chains, our results reveal that the

presence of small-molecule solvent molecules provides an additional suppression of the local modes of motion. The total slow-down of the relaxation of the individual backbone bonds occurs to such an extent that the time scales of local motions and chain end-to-end dynamics are comparable and thus cannot be distinguished in viscoelastic measurements. Also, significantly, our study indicates a minimum sub-chain size (approximately 50 repeat units, or 100 backbone bonds) for polystyrene chains in baths of benzene and short oligostyrenes that is similar to that implied by experiments, in which Aroclor was the solvent. As highlighted later in the article, since the same smallest sub-chain size is obtained for polystyrene in benzene and the oligostyrenes, as was observed experimentally in Aroclor, and all these solvent molecules have different sizes and thus relax over varying amounts of time, it is unlikely that the shortest relaxation time is due simply to the finite solvent relaxation time as suggested in Ref. [10]. Additionally, we examine the variation of the different scaling law regimes of the mean square displacement (MSD) of the atoms on the polymer backbone with the addition of different mechanisms.

2. Models and computational details

2.1. Selection of polymer and solvent

While often applied to polymer melts, atomistically detailed MD simulations have rarely been applied to dilute polymer solutions. However, few examples where atomistic MD simulations have been used to study various aspects of physics in dilute solutions include polyisoprene in a bath of toluene [19, 20], polyisoprene in cyclohexane [21], polystyrene

in benzene [22, 23] and poly(ethylene oxide) in water [24] and toluene [55, 56]. Among these, polystyrene and polyisoprene are the best studied. However, for polyisoprene most studies have used proprietary software packages such as CFF91 [19, 20] and COMPASS [25], for which the simulation parameters are not published. For polystyrene, the united-atom force field used by Mondello *et al.* [26], which is based on the published united-atom AMBER force field [27], has been used by several researchers for MD simulations [28-30]. Additionally, for polystyrene, this force field uses united-atoms to avoid simulation of hydrogen atoms, and so is more efficient than other force fields, which include hydrogens explicitly. Hence, we choose polystyrene for our study, with interaction potentials slightly changed from the original ones given in Ref. [26], as explained later in section 2.2.

Among the good solvents for polystyrene, many force fields for MD simulations are available for benzene, starting from the one of the earliest by Evans and Watts [31]. These include united-atom (UA) [32, 33], asymmetric united-atom (AUA) models [31, 34-37] and all-atom (AA) [38] models. Only UA and AUA models are considered for this study, since an all-atom solvent model is incompatible with the united-atom representation of the polystyrene chain. We computed the viscosity and radial distribution functions for several UA and AUA benzene models and compared these with experiments. We calculated the viscosity using the periodic perturbation method for non-equilibrium MD simulations in GROMACS [39, 40], which was shown to have superior efficiency and accuracy in an earlier comparative study [41]. All of our MD simulations are carried out in the NPT ensemble at T = 293 K and P = 1 atm, for a total of 100 ns with a timestep size of 2 fs. The Nose-Hoover and the Parrinello-Rahman algorithms are used to fix the temperature and

pressure, respectively. Unless otherwise mentioned, a cut-off distance of 1.5 nm is used for all non-bonded interactions. From these simulations, we observe that the united-atom Errington-Panagiotopoulos potential [33], which has been used in several studies involving benzene [42, 43], reproduces the experimental viscosity (at 293K, the viscosity predicted from MD simulations using the Errington-Panagiotopoulos potential is 0.655 cP and the experimental value is 0.652 cP) and the CH-CH radial distribution function of benzene and is thus selected for this study. To the best of our knowledge, there are no earlier studies that computed viscosity using this model. We also observe that the density predicted from MD simulations in the NPT ensemble varies with the number of benzene molecules present in the system, even if the long-range corrections are included. However, the predicted density becomes system size independent and is in good agreement with the experimental value for benzene for a simulation box of 800 molecules. (At 293 K, the density predicted from MD simulations is 869 kg/m^3 and the experimental value is 876 kg/m^3.) The results for the calculation of viscosity of the benzene bath and the variation of density of the bath with the number of benzene molecules are provided in Appendix A.

2.2. Tuning the interaction potential for the polymer

The radial distribution function for a melt of short polystyrene chains was computed in Ref. [44] using an AA model, and found to be in good agreement with the corresponding experimental result, which was obtained for somewhat smaller chains and a different temperature (all conditions are mentioned in Ref. [44]). Before starting simulations for our

polymer-solvent system, we need to further tune the original interaction potential parameters obtained from Ref. [26] to obtain a closer agreement with the results in Ref. [44]. For this, we matched the simulation conditions of Ref. [44], specifically taking 48 chains of polystyrene, each 10 monomers long, at 500 K and 1 atm. For all cases, an initial NVT run of 20 ns at a low density is performed at 500 K so that all chains are in well-relaxed configurations. This is followed by a NPT run of 20 ns at 500 K and 1 atm so that the system gets compressed and equilibrated to the corresponding melt state. The final state from this run is used to perform a production run in the NVT ensemble for 20 ns to compute the averages of the various properties for the melt system. All simulations are performed using the GROMACS package [39, 40], using a timestep size of 2 fs and the Nose-Hoover and the Parrinello-Rahman algorithms to control the temperature and pressure, respectively.

A couple of small changes are systematically introduced to the original potential from ref. [26] to judge the effects of each on the final melt structure for the system mentioned earlier. The interactions between polystyrene side-groups (phenyl rings) are modeled by the Errington-Panagiotopoulos potential [33] for compatibility with the force field we chose for the benzene bath in the final simulation model, while retaining the interaction potentials between the ring and backbone atoms given in Ref. [26]. The periodic torsional potential for the C-C backbone in Ref. [26] is replaced by a Ryckaert-Bellemans potential used earlier for united-atom polyethylene [45]; the Ryckaert-Bellemans potential has more realistic energy barriers for gauche-gauche and gauche-trans transitions than does the potential in Ref. [26]. Our results for the melt structure with these two changes remain

almost the same as those obtained with the original potential given in Ref. [26]. After these tweaks, we change the Lennard-Jones diameter (denoted by σ) for the CH_2 and the CH united-atoms to 0.55 nm and 0.5 nm, respectively, to obtain a melt structure in closer agreement with that obtained using an atomistic model in Ref. [44], than was obtained using the original potential in Ref. [26]. Figure 2.1 shows the radial distribution functions obtained from experiment, from MD simulations using the atomistic model in Ref. [44], from MD simulation using the original potential by Mondello and Yang [26] and from the final potential with the changes mentioned above. Note that the experiments were performed on a melt of shorter chains (8 monomers) at a lower temperature (323 K). Although not significantly different, the values of the second, third and fourth peaks for the final tuned potential are in better agreement with the results of the atomistic model [44], which are at the same conditions as our simulations. However, the first peak is observed to be lower than the corresponding value obtained in Ref. [44] for all cases. This difference in packing at short distances is probably due to the absence of H atoms in the united-atom model, which uses an 'average' excluded volume diameter of CH and CH_2 groups that is larger than that of the actual C atoms in an atomistic model. Additionally, note here that our radial distribution functions are for the CH and CH_2 groups and hence can be slightly different from that between bare C atoms (as in Ref. [44]).

2.3. Methodology for polymer-solvent and isolated chain simulations

Using the potentials discussed above, simulations were carried out for one polystyrene chain of 30 monomers (which has 59 backbone bonds and is similar in length to the chain considered in Ref. [15]) in a bath of 1500 benzene molecules. The simulation is performed using GROMACS [39, 40] for a total of 1100 ns with a timestep of 2 fs, where the final 1000 ns is used as the production run for averaging data and computing the autocorrelation functions. The temperature (293 K) and pressure (1 atm) are controlled by the Nose-Hoover and the Parrinello-Rahman algorithms, respectively. A cut-off of 1.5 nm is used for all non-bonded interactions and the neighbor lists are updated after every 10 timesteps.

Coarse-grained MD (CGMD) simulations of dilute solutions of polystyrene in benzene are also performed for the MARTINI model for the same system, which is developed in Ref. [46], using GROMACS. The CGMD systems consist of polystyrene chains of either 30 or 100 monomers immersed in baths of benzene molecules and of oligomers of styrene with 2 and 5 repeat units. The files for the coordinates and run parameters of one example CGMD system were downloaded from the website http://md.chem.rug.nl/cgmartini/index.php/downloads/example-applications/151-ps. The CGMD simulations for chains with 30 and 100 monomers are each run for a total of 6000 ns, using a timestep size of 20 fs for all cases. The other parameters used for the MD simulation are same as given in Ref. [46]. The final 5000 ns are used as the production run for computing averages of quantities and autocorrelation functions for systems with polystyrene chains of 30 and 100 monomers. The temperature is controlled at 293 K for all simulations with benzene. However, higher temperatures are used for the systems with styrene oligomers, so that the viscosity of the resulting solvent bath is of a similar order of

magnitude to that of benzene at 293 K and the total simulation time represents a sufficiently large number of end-to-end relaxation times for the polymer chains. For all MD simulations, the chain end-to-end relaxation time (τ) is obtained by an exponential fit to the autocorrelation function for the end-to-end vector.

Simulations with a united-atom polystyrene chain with 30 monomers are also performed in a continuum solvent, with different level of details present in the chain, as discussed later in Section 3.2. For all these continuum solvent simulations, the stochastic dynamics (SD) technique in GROMACS is used, which is essentially Brownian dynamics (BD) with an inertial term included in the integration. It is to be noted that these SD simulations using GROMACS do not include the effects due to hydrodynamic interactions (HI). The timestep size for integration, cut-off for non-bonded interactions and the frequency of updating the neighbor list are kept similar to the corresponding values used in the MD simulations. The models with and without side groups are run for a total time of 1500 and 2000 ns respectively, out of which the trajectory excluding the first 100 ns is considered as the production run.

To evaluate the effects of the inclusion of HI, several BD simulations are performed on a chain consisting of only the backbone (no side groups) in the presence of HI. For those simulations, the details of the stochastic differential equation and simulation parameters are provided in Ref. [47]. Briefly, the chain consists of beads connected by stiff Fraenkel springs, which mimic inextensible rods, and which hereafter are typically referred to as "rods" [48, 54]. Even though they are actually nearly inextensible springs, the notation "spr" is used to designate models containing this kind of "rod." A harmonic bending

potential is introduced between consecutive rods with a large bending stiffness to fix the angle between consecutive rods at about 109.5 degrees [48]. The HI between beads is calculated by the Rotne-Prager-Yamakawa (RPY) tensor [47]. The torsional potential used for groups of three backbone bonds is same as that imposed on the backbone atoms of the united-atom polystyrene chain for MD simulations. The implementation of torsional interactions in the simulations is similar to that discussed in Ref. [49]. Lennard-Jones potentials are used to compute the excluded volume interactions between the beads on the chain, where such interactions are only calculated for pairs of beads separated by 4 or more rods, which is consistent with the MD and SD simulations in GROMACS, where the non-bonded interactions are excluded between any pair of atoms separated by up to three bonds. All simulations with HI use an explicit integration scheme with a timestep size that is small enough to ensure good convergence of the results.

3. Results and discussion

3.1. Local relaxation dynamics from MD simulations

The Rouse and Zimm theories predict that in a bead-spring chain with many springs, the relaxation of a single spring (corresponding to a subsection of the polymer chain) is given by a summation of several exponential decay terms, where the total number of terms is equal to the number of modes of relaxation in the entire polymer chain [15]. This, in turn, is equal to the number of springs in the bead-spring representation of the chain. Thus, a fit of the local relaxation (i.e. bond relaxation) dynamics to a sum of exponential decay terms

should show the total number of modes of relaxation for the polymer chain, as well as the time scales of all such processes. Figure 2.2 shows the autocorrelation function for the bond vectors in the polystyrene chain of 30 monomers (59 backbone bonds), for the united-atom and MARTINI models, in baths of benzene and styrene oligomers. It must be noted here that one individual backbone bond in the CGMD (MARTINI) model represents two C-C backbone bonds in the real chain. Remarkably, the local relaxation dynamics for all cases show an excellent fit by a single exponential, with a time scale that is fairly similar to the end-to-end relaxation time (denoted as τ; the values are given in the legends of the subplots) for the entire chain! The CGMD simulations show a steeper relaxation at short times compared to the exponential fit, whereas the relaxation from the united-atom model is fairly consistent with the single exponential fit even at short times. This can perhaps be attributed to the reduced number of interaction sites in the coarse-grained model, which provides more free space to each bead to undergo a faster motion at short times relative to the united-atom model, thereby generating a faster initial relaxation of the bond vectors. This behavior in dilute solutions with benzene and styrene oligomers is consistent with experimental findings summarized by Schrag and coworkers [10], who showed that the relaxation spectrum of the polystyrene chain exhibits an abrupt cut-off with the highest mode representing a sub-chain of about 50 monomers.

In this context, it is worth mentioning that the average radius of gyration for a polystyrene chain of 30 monomers obtained from the MD simulations with the united-atom model is about 1.28 nm, which is in good agreement with the experimental results reported for polystyrene chains of similar average molecular weight in solutions with cyclohexane

(1.28 nm) and toluene (1.39 nm) [53]. This further highlights the validity of the united-atom model used in this study. The corresponding value obtained for the MARTINI model is about 1.55 nm, which is somewhat higher than reported in Ref [53].

Note that in all cases in Fig. 2.2, the single exponential fit is of the form ae^{-t/t_1} to the autocorrelation function of the bonds excluding the steep initial decay. The final 85% and 50% of the relaxation are considered for the fit for the united-atom and MARTINI models, respectively, owing to a steep initial decay for CGMD as discussed earlier. The exponential pre-factor $a < 1$ is less than unity in the fits, highlighting that the initial decrease at short times is steeper than the single exponential decay shown at longer times. However, differences are minor with the united-atom model, which is perhaps a more accurate description than the coarse-grained MARTINI model but requires computational times that are about two orders of magnitude higher. Accordingly, a fit of the form $a\left(e^{-t/t_1}+e^{-t/t_2}\right)$ is attempted for chains that are 100 monomers long, as discussed in the following paragraph.

Figure 2.3 show the relaxation dynamics of the bonds in chains that are 100 monomers long and immersed in different solvent baths, using the MARTINI model for CGMD simulations. Interestingly, for the chain with 100 monomers, the bond relaxation shows an excellent fit to a sum of two exponential decay terms (as discussed earlier), where the longer time scale is similar to the end-to-end relaxation of the chain and the shorter time scale is similar to the bond relaxation time for the chain with 30 monomers, for all solvent baths considered. Although not shown here, a single exponential fit is in poor agreement

with the relaxation dynamics. The different cases investigated and the values of the time scales of the modes are listed in Table 2.1. To summarize, these simulation results clearly indicate that there is only one relaxation time for chains of 30 monomers while two relaxation times are required to fit the relaxation of chains of 100 monomers. These results are consistent with earlier experimental observations, in which the highest mode of relaxation corresponds to a sub-chain of 50 monomers. Note that an even larger polystyrene chain in benzene, namely 150 monomers, will probably have a relaxation timescale of about 1000 ns for the longest mode of the relaxation spectrum, and hence extremely long MD simulations (at least 40000 - 50000 ns of total simulation time) would be needed to resolve the relaxation at large times (~ 1000-2000 ns) sufficiently well to clearly distinguish such a mode from the others that have relatively shorter time scales. Even with a coarse-grained force field like MARTINI, such a simulation is beyond the reach of the computer resources deployed for this study. Also, note in Fig. 2.2 that the time scales from the united-atom and MARTINI models (in benzene bath) differ roughly by a factor of 4, which is consistent with a similarly larger viscosity of the benzene bath from the MARTINI model relative to the corresponding united-atom model (shown in Appendix A).

Figure 2.4 compares the relaxation dynamics of the backbone bond vectors for a polystyrene chain of 30 monomers with that of a single benzene molecule (averaged over all benzene molecules) in the solvent bath, using the UA model discussed earlier. The inset shows the same from CGMD simulations using the MARTINI model. Clearly, from both simulations, the relaxation time of benzene is approximately three orders of magnitude

smaller than the relaxation time of the polymer backbone bonds, whereas that of Aroclor is roughly two orders of magnitude smaller than that of the shortest chain relaxation time, as reported in Ref. [10]. Thus, following the analysis presented in Ref. [10], the minimum sub-chain of polystyrene in benzene should be smaller than that predicted for polystyrene in Aroclor, if the rate of local motions is the principal cause for the cut-off in the relaxation spectrum. The fact that the same size of the shortest sub-chain is obtained for solvents that relax at different time scales shows that such a cut-off in the spectrum is not caused solely by supposedly "slow" solvent dynamics blocking the exploration of local conformation space.

3.2. Effect of different mechanisms on the relaxation dynamics

To understand the role of the presence of solvent molecules, excluded volume interactions between chain beads, side groups, and torsional and bending rigidities on relaxation dynamics of the lowest and the highest modes, we next simplify our model systematically. Firstly, the solvent molecules are removed to model the chain in a continuum solvent, while retaining the side groups and the torsional and bending interactions between the various atoms on the chain. Due to the absence of the solvent molecules, the non-bonded interaction potential between the chain atoms needs to be tuned further to ensure that the radius of gyration of the chain is similar to that in the MD simulation, where the solvent molecules are modeled explicitly. We do this by uniformly reducing the coefficient for the attractive part of the potential (coefficient C_6 for the Lennard-Jones potential) between all

pairs of atoms to the same percentage of its original value, which turns out to be 44% of the original value. This results in a more repulsive overall intra-chain potential, which we denote as 'ACWS' as an abbreviation for 'Atomistic Chain Without Solvent'. In principle, the inter-atomic potential on the chain can also be changed iteratively such that the resulting radial distribution functions between the different pairs of atoms are similar to those obtained from the MD simulation, using the Iterative Boltzmann Inversion technique [50, 51, 52] that is typically used to construct coarse-grained models. However, in this case, the final potential for ACWS captures the chain size correctly and produces a radial distribution function between the different atoms that is in fairly close agreement with the corresponding values from the MD simulation. Figure 2.5 shows a comparison of the radial distribution functions obtained from the MD simulation and the ACWS model for different pairs of atom types on the chain. Additionally, as noted later in this article, the relaxation dynamics are not very sensitive to the exact details of non-bonded interaction potentials used, as long as the overall chain size agrees well. Thus, we regarded the ACWS implicit-solvent model to be sufficiently accurate for our purposes.

The model is then further simplified by removing all non-bonded potentials, while retaining the side groups and torsional and bending interactions (denoted by 'spr+ben+tor+side groups'). In successive simplifications, (i) the side groups are cleaved off while retaining the torsional and bending interactions along the chain backbone (denoted by 'spr+ben+tor'), (ii) the torsional interactions are removed between chain backbone atoms (termed as 'spr+ben') and (iii) the bending potentials are removed to result in a freely-jointed bead-rod chain (denoted by 'spr'). Two additional models with

intra-chain potential are included in the analysis – (i) a model without the side groups but with a tuned non-bonded potential between the atoms so that the resulting chain has the same radius of gyration as that in the MD simulation (termed as 'spr+ben+tor+pot') and (ii) a chain with side groups and a non-bonded potential that acts only between the atoms on the chain backbone (denoted by 'PSG' that serves as an abbreviation for 'Phantom Side Groups'). As done earlier to construct the ACWS model, the potential for these latter two models is tuned such that the chain size matches that from the MD simulation. A summary of all the models with a continuum solvent discussed here is given in Table 2.2. Overall, the models considered can be classified in two broad categories – a group where the side groups are retained and another where the side groups are cleaved off.

Figure 2.6 compares the relaxation dynamics of the backbone bond vectors from the UA MD simulation to the ACWS and the 'spr+ben+tor+side groups' models, for a chain of 30 monomers. Unless otherwise specified, the time scale is made dimensionless using the characteristic time R_g^2/D_{cm} for each model, where R_g and D_{cm} are the radius of gyration and the center of mass diffusivity of the chain for the specific model considered, respectively. The results clearly indicate that the relaxation of the chain backbone bonds becomes faster as the simulation model gets more simplified. Similar trends are observed for the end-to-end relaxation as well (not shown here), although the differences between the various models are much less for the end-to-end vector than for the bond vectors. The inset to Fig. 2.6 compares the bond relaxation dynamics from the ACWS and PSG models. These results are very close to one another, which shows that the dynamics are not very sensitive to the exact details of the non-bonded potentials when the average chain sizes are similar.

Note that bond relaxation from the UA MD simulation is described by a single exponential, as discussed earlier, while none of the models using a continuum solvent show a single exponential relaxation for the backbone bond vectors. (For the quality of the fits to a single exponential decay of the bond relaxation dynamics for the various cases using BD simulations, see Appendix A.)

Figure 2.7 extends the comparison presented in Figure 2.6 to include chain models without the side groups. Note that all the results for the chains in a continuum solvent shown in Fig. 2.7 are from BD simulations without HI. As observed for the different models in Figure 2.7, starting from the full MD simulation with explicit solvent (black line), the relaxation of bonds become progressively faster when one successively removes first the explicit solvent and side groups (yellow line), then the interaction potentials (blue line), then the torsional potential (red line), and finally also the bending potential (green line), leaving only a freely jointed bead-rod chain model whose behavior is close that of Rouse theory. The trends are similar for the end-to-end relaxation dynamics (not shown here), although with much smaller differences than those observed for the relaxation of the bond vectors. The relaxation behaviors for the chain models consisting of beads, rods and bending and torsional potentials are qualitatively similar to those of equivalent models considered by Jain and Larson [15]. Note that only the MD simulation predicts a single exponential relaxation for the bond vectors (an exponential fit is shown here for the bond relaxation from MD simulation). The inset to Fig. 2.7 compares the bond relaxation dynamics for the 'spr+ben+tor+side groups' and the 'spr+ben+tor' models. These results show that the inclusion of side groups slows down the relaxation of bond vectors at short

times, but has negligible effect at long times. Thus, the results presented in Figs. 2.6 and 2.7 predict an additional slow down of the local relaxation dynamics for a short chain in the presence of explicitly treated solvent molecules such that it behaves as a single exponential decay.

Figure 2.8 shows the effect of inclusion of HI on the bond relaxation dynamics for the chain models without side groups. The strength of hydrodynamic interactions is controlled by the hydrodynamic interaction parameter h^*, which is defined as $h^* = \sqrt{\frac{3}{\pi}} \frac{r_H}{l_{rod}}$ for a bead-rod chain with spherical beads, where r_H is the hydrodynamic radius of the beads and l_{rod} is the length of one "rod" (mimicked by a stiff Fraenkel spring) in the chain (more details are given elsewhere [47]). Starting with the model with only spring forces, which is the freely jointed chain, if one adds hydrodynamic interactions (HI) with HI parameter $h^* = 0.15$ (corresponding to a bead hydrodynamic diameter approximately equal to 30% of the length of one rod) and $h^* = 0.50$ (corresponding to a bead hydrodynamic diameter approximately equal to the length of one rod), the relaxation slows down dramatically (see the green curves in Fig. 2.8). Note that this slow-down of the relaxation dynamics is only in terms of the rescaled time that we consider here for our results. In absolute units, the dynamics of the chain, including the center of mass diffusivity, is faster in the presence of HI. This is highlighted in Table 2.3, where the center of mass diffusivities are listed in characteristic length and time units (as described in Ref. [54]). This behavior (in terms of the rescaled time) is consistent with the predictions of the Zimm theory, where the spacing between the time scales of the modes is smaller than those in the Rouse theory, owing to scaling law

exponents of 1.5 and 2 for the mode relaxation times from the Zimm and Rouse theory, respectively. Further suppression of the bond relaxation is obtained with the addition of bending, torsional and non-bonded Lennard-Jones potentials in the presence of HI, although none of them predict a single exponential decay for the bond relaxation dynamics (note that the results for the 'spr+ben' model is not shown here for clarity). As mentioned earlier, the torsional interactions used in all these simulations are same as those acting between the backbone atoms of the polystyrene united-atom chain. The non-bonded Lennard-Jones potential between the beads is tuned so that the chain shows the same average radius of gyration as that in the MD simulation. Note that the value of $h^* = 0.15$ used here for simulations with HI is typically used in BD simulations with coarse-grained bead-spring models for polystyrene [47]. Also, note that, even with the additional slow-down in the presence of HI, the local dynamics is faster than that obtained from MD simulations with explicit solvent molecules. The end-to-end relaxation dynamics in the presence of HI also show an additional slow down relative to those obtained without HI (not shown here), but the differences are much smaller than the bond relaxation dynamics.

Although the dynamics becomes slower with the inclusion of HI for all cases shown in Fig. 2.8, it is evident that the additional slow-down in the bond relaxation becomes weaker as more mechanisms are included, such that the dynamics with HI is not significantly different from that without HI when the non-bonded potentials are included. The presence of HI also has a negligible effect on the end-to-end relaxation when all the mechanisms i.e. bending, torsion and non-bonded potentials are acting along the chain (results not shown). This reduction in the slow-down due to HI is expected since the number of rods in one

Kuhn step, or equivalently the Kuhn length itself, increases with the addition of those mechanisms, thereby further reducing the ratio of the bead hydrodynamic diameter to the Kuhn length (for a given h^*) and hence weakening the effect of HI on the dynamics. Also, it is worth noting that the RPY tensor used here to compute the effect of HI between beads is only correct for beads that don't overlap, whereas there can be a significant amount of bead overlaps in all cases where the non-bonded potential is not present. The amount of bead-bead overlap is also expected to decrease with the addition of bending and torsion interactions, which prevents local bending of the chain at length scales of a few rods.

3.3. Effect of different mechanisms on the bead MSD

The scaling law exponents and different regimes for the variation of bead mean square displacement (MSD) with time are known from the Rouse and Zimm models for a simple chain model that consists of Hookean springs and frictional beads, without and with HI, respectively. However, these descriptions are too simplistic for a real polymer-solvent system, which has bending and torsional interactions between bonds, non-bonded excluded volume interactions, side groups and interactions with solvent molecules. To the best of our knowledge, a systematic study of the effect of these mechanisms on the bead MSD has not yet been carried out. Figures 2.9(a)-(f) highlight the effect of each interaction on the bead MSD for a united-atom polystyrene chain model of 30 monomers. All simulations are done with a continuum solvent, except the MD study in Figure 2.9(f) that includes the

solvent molecules explicitly. Note that HI is not included for the results presented in Figure 2.9.

Figure 2.9(a) shows the time dependence of bead MSD for the simplest case, where the chain consists of beads connected by rods (60 beads in this case). The presence of three dynamic regimes with the corresponding scaling law exponents of about 1, 0.5 and 1 at short, intermediate and long times, respectively, agrees well with the predictions of the Rouse theory. For convenience, the regimes at short, intermediate and long times will henceforth be denoted by Regimes I, II and III respectively. Since the chain as a whole behaves diffusively at long times, the corresponding exponent for Regime III is expected to be 1, irrespective of the interactions included in the simulations. However, notable changes are observed in the exponents of Regimes I and II upon inclusion of other interactions. Starting with only stiff spring interactions, upon addition of bending potentials between the rods, the scaling exponent of Regime I decreases from unity to about 0.92 and that of Regime II increases from 0.5 to roughly 0.6 (Figure 2.9(b)). Further addition of a torsional potential to the spring and bending potentials further reduces the exponent of Regime I to 0.85 and increases that of Regime II to about 0.7 (Figure 2.9(c)). Further addition of side groups affects the bead dynamics in Regime I, decreasing the exponent to about 0.8, but the exponent of Regime II remains unchanged (Figure 2.9(d)). Inclusion of a potential to all of these other interactions leads to the ACWS model, and while this doesn't further change the exponent of Regime I, that of Regime II is significantly increased to approximately 0.85 (Figure 2.9(e)). Although not shown here, the behavior for the PSG and 'spr+ben+tor+pot' models are in close agreement with the

ACWS model. Thus, in a continuum solvent, each additional interaction decreases the exponent of Regime I, step by step, from around unity to approximately 0.8 but increases that of Regime II from 0.5 (corresponding to the Rouse theory) to about 0.85, thereby almost entirely removing the difference in exponents between Regimes I and II predicted by the Rouse theory.

In the presence of solvent molecules, one additional sub-diffusive regime appears at fairly short times (< 10 ps, but > 1 ps) with a scaling law exponent of about 0.65 (denoted by Regime 0 henceforth), followed by Regimes I and II with power law exponents of approximately 0.94 and 0.76, respectively (Figure 2.9(f)). The MSD at short times is shown in more detail in the inset of Figure 2.9(f), where the MSD of atoms on the solvent benzene rings is also shown for comparison. At very short times (< 1 ps), one additional dynamic regime ("Regime -1") is observed for the polymer backbone atoms with a power law scaling of about 0.8. The MSD for the atoms on the benzene molecules show three distinct regimes with scaling law exponents of about 1, 0.57 and 1, where the intermediate sub-diffusive regime occurs at similar times (1 – 10 ps) as that of Regime 0 for the chain atoms (and also has a similar power law exponent). This suggests that Regime 0 in the polymer probably occurs due to the solvent molecules hindering the motion of chain atoms at times between 1 and 10 ps. However, this time scale is about 3 orders of magnitude lower than that of the bond relaxation time for the PS chain in benzene, and thus most of the local relaxation dynamics occur at larger times i.e. in Regimes I and II. The variations in the range of Regime 0 and its implications on the bond relaxation dynamics with increasing sizes of solvent molecules will be discussed in a future work. Also, note that the

scaling law exponents of Regimes I and II are significantly different for a continuum solvent and explicit solvent molecules - the addition of explicit solvent molecules increases the exponent of Regime I from 0.8 to 0.94 and lowers that of Regime II from 0.85 to 0.76, relative to the exponents for ACWS (Figure 2.9(e)).

4. Summary

In this Chapter, the relaxation dynamics of the individual bond vectors of short polystyrene chains were investigated, using both MD and BD simulations. The parameters of the united-atom model of the polystyrene chain, presented in Ref. [26], were further tuned to provide a closer agreement with the structural correlations in a melt of short polystyrene chains [44], before being used for MD simulations with benzene. The results from the MD simulations for chains of 30 and 100 monomers, using both the united-atom and MARTINI models with solvent baths of benzene and short chain oligostyrenes, show that the relaxation dynamics consist of one and two modes, respectively, for the 30 monomer and 100 monomer chains, which agrees remarkably well with the experiments of Schrag and co-workers [10]. BD simulations were also performed for the polystyrene chain of 30 monomers by replacing the explicit solvent molecules with a viscous continuum, where the different mechanisms of bending, torsion, side groups and non-bonded interaction potentials were added one at a time to understand the cumulative effect of each on the relaxation dynamics. In general, each added mechanism contributed to an additional slow-down of the local relaxation dynamics, but without an explicit solvent, even inclusion of

all of them failed to produce a single exponential relaxation of the bonds for 30-monomer chains. The inclusion of HI in the BD simulations further suppressed the local dynamics, but also failed to produce a single exponential relaxation spectrum. Overall, all of our BD simulations predicted faster relaxation of the backbone bonds relative to the MD simulations, which treat the solvent molecules explicitly. This highlights that the additional slow-down obtained in the presence of explicit solvent molecules is critical to obtain a single exponential relaxation spectrum. The changes in the different regimes of the bead mean square displacement (MSD) due to the inclusion of the mechanisms mentioned above were also investigated. The simulations indicate that the dynamics at length scales extending up to around 50 monomers is only adequately captured when the motion of explicit solvent molecules are coupled with that of the beads on the chain, as in the MD simulations, and cannot be predicted accurately even using resolved chains when the solvent bath is substituted by a continuum, as in BD simulations. Remarkably, however, the behavior is captured by the crudest model of all - a simple bead spring chain in which 50 monomers are represented by a single flexible spring, as the experiments of Schrag and coworkers showed years ago.

References

[1] Rouse, P. R. *J. Chem. Phys.* 1953, 21 (7), 1272–1280.

[2] Zimm, B. H. *J. Chem. Phys.* 1956, 24 (2), 269–278.

[3] Sammler, R. L.; Landry, C. J. T.; Woltman, G. R.; Schrag, J. L. *Macromolecules*, 1990, 23, 2388.

[4] Yoshizaki, T.; Yamakawa, H. *J. Chem. Phys.* 1988, 88, 1313.

[5] Bird, R. B.; Curtiss, C. F.; Amstrong, R. C.; Hassager, O. *Dynamics of Polymeric Fluids, Vol. 2: Kinetic Theory*; Wiley: New York, 1987.

[6] Sammler, R. L.; Schrag, J. L. *Macromolecules*, 1989, 22, 3435.

[7] Inoue, T.; Okamoto, H.; Osaki, K. *Macromolecules*, 1991, 24, 5670–5675.

[8] Gray, R. W.; Harrison, G.; Lamb, *J. Proceedings Royal Society (London)*, 1977, A356, 77.

[9] Amelar, S.; Eastman, C. E.; Morris, R. L.; Smeltzly, M. A.; Lodge, T. P.; Meerwall, E. D. V. *Macromolecules*, 1991, 24, 3505–3516.

[10] Peterson, S. C.; Echeverria, I.; Hahn, S. F.; Strand, D. A.; Schrag, J. L. J. *Polym. Sci.: Part B: Polym. Phys.*, 2001, 39, 2860–2873.

[11] Smith, D. E.; Babcock H. P.; Chu S. *Science* 1999, 283, 1724-1727.

[12] Teixeira, Rodrigo E.; Babcock, Hazen P.; Shaqfeh, Eric S. G.; Chu, Steven

Macromolecules 2005, 38, 581-592.

[13] Hur, J. S.; Shaqfeh, E. S. G.; Babcock, H. P.; Smith, D. E.; Chu, S. *J. Rheol.* 2001, 45, 421-450.

[14] Fixman, M. *J. Chem. Phys.* 1978, 69 (4), 1538–1545.

[15] Jain, Semant; Larson, Ronald G. *Macromolecules* 2008, 41, 3692-3700.

[16] Doyle, P. S.; Shaqfeh, E. S. G.; Gast, A. P. *J. Fluid. Mech.* 1997, 334, 251-291.

[17] Hur, J. S.; Shaqfeh, E. S. G.; Larson, R. G. *J. Rheol.* 2000, 44, 713-742.

[18] Larson, R. G. *Macromolecules* 2004, 37, 5110–5114.

[19] Moe, Neil E.; Ediger, M. D. *Macromolecules* 1995, 28, 2329-2338.

[20] Moe, Neil E.; Ediger, M. D. *Macromolecules* 1996, 29, 5484-5492.

[21] Faller, Roland *Phys. Chem. Chem. Phys.* 2002, 4, 2269-2272.

[22] Müller-Plathe, Florian *Macromolecules* 1996, 29, 4782-4791.

[23] Müller-Plathe, Florian *Chemical Physics Letters* 1996, 252, 419-424.

[24] Borodin, Oleg; Bedrov, Dmitry; Smith, Grant D. *Macromolecules* 2001, 34, 5687-5693.

[25] Doxastakis, M.; Theodorou, D. N.; Fytas, G.; Kremer, F., Faller, R.; Muller-Plathe, F.; Hadjichristidis, N. *J. Chem. Phys.* 2003, 119, 13, 6883-6894.

[26] Mondello, M.; Yang, Hyung-Jin; Furuya, Hidemine; Roe, Ryong-Joon *Macromolecules* 1994, 27, 3566-3574.

[27] Weiner, S. J.; Kollman, P. A.; Case, D. A.; Singh, U. C.; Chio, C.; Alagona, G.; Profeta, S. Jr.; Weiner, P. *J. Am. Chem. Soc.* 1984, 106, 765.

[28] Lyulin, Alexey V; Michels, M. A. J. *Macromolecules* 2002, 35, 4, 1463–1472.

[29] Roe, R. J. *Journal of Non-Crystalline Solids* 1998, 235-237, 308-313.

[30] Bernardin III, Frederick E.; Rutledge, Gregory C. *Polymer* 2007, 48, 24, 7211-7220.

[31] Evans, D. J.; Watts, R. O. *Molecular Physics* 1976, 32, 1, 93-100.

[32] Cleassens, M.; Ferrario, M.; Ryckaert, J. P. *Molecular Physics* 1983, 50, 1, 217-227.

[33] Errington, J. R.; Panagiotopoulos, A. Z. *J. Chem. Phys* 1999, 111, 21, 9731-9738.

[34] Hoheisel, C. *J. Chem. Phys.* 1988, 89, 12, 7457-7461.

[35] Friedrich, A.; Lustig, R. *Journal of Molecular Liquids* 2002, 98-99, 241-259.

[36] Contreras-Camacho, R. O.; Ungerer, P.; Boutin, A.; Mackie, A. D. *J. Phys. Chem. B* 2004, 108, 37, 14109-14114.

[37] Bonnaud, P.; Nieto-Draghi, C.; Ungerer, P. *J. Phys. Chem.* B 2007, 111, 14, 3730-3741.

[38] Cacelli, Ivo; Cinacchi, Giorgio; Prampolini, Giacomo; Tani, Alessandro *J. Am. Chem. Soc.* 2004, 126, 43, 14278-14286.

[39] Van der Spoel, D.; Lindahl E.; Hess B.; Groenhof G.; Mark A. E.; Berendsen H. J. *Journal of Computational Chemistry* 2005, 26(16), 1701-1718.

[40] Hess B.; Kutzner C.; Van Der Spoel D.; Lindahl E. *Journal of Chemical Theory and Computation* 2008, 4(3), 435-447.

[41] Hess, Berk *J. Chem. Phys.* 2002, 116, 1, 209-217.

[42] Carrero-Mantilla, J. *The Journal of Chemical Thermodynamics* 2008, 40, 2, 271-283.

[43] Moghaddam, S.; Panagiotopoulos, A. Z. *Fluid Phase Equilibria* 2004, 222-223, 221-224.

[44] Qian, Hu-Jun; Carbone, Paola; Chen, Xiaoyu; Karimi-Varzaneh, Hossein Ali;

Liew, Chee Chin; Muller-Plathe, Florian *Macromolecules* 2008, 41, 9919-9929.

[45] Pant, P. V. Krishna; Han, Jie; Smith, Grant D.; Boyd, Richard H. *J. Chem. Phys*. 1999, 99 (1), 597-604.

[46] Rossi, Giulia; Monticelli, Luca; Puisto, Sakari R.; Vattulainen, Ilpo; Ala-Nissila, Tapio *Soft Matter*, 2011, 7, 698–708.

[47] Hsieh, Chih-Chen; Li, Lei; Larson, Ronald G. *J. Non-Newtonian Fluid Mech.* 2003, 113, 22, 147-191.

[48] Saha Dalal, Indranil; Albaugh, Alex; Hoda, Nazish; Larson, Ronald G. *Macromolecules* 2012, 45, 9493-9499.

[49] Bekker, H; Berendsen, H. J. C.; van Gunsteren, W. F. *Journal of Computational Chemistry* 1995, 16 (5), 527-533.

[50] Müller-Plathe, Florian *ChemPhysChem* 2002, 3, 9, 754-769.

[51] Reith, Dirk; Pütz, Mathias; Müller-Plathe, Florian *Journal of Computational Chemistry* 2003, 24, 13, 1624-1636.

[52] Peter, Christine; Kremer, Kurt *Soft Matter* 2009, 5, 4357–4366.

[53] Huber, Klaus; Bantle, Siegfried; Lutz, Pierre; Burchard, Walther *Macromolecules* 1985, 18, 1461-1467.

[54] Saha Dalal, Indranil; Hoda, Nazish; Larson, Ronald G. *J. Rheol* **56**, 305 (2012)

[55] Fuson, Michael M.; Ediger, M. D. *Macromolecules* 1997, 30, 5704-5713.

[56] Fuson, Michael M.; Hanser, Kent H.; Ediger, M. D. *Macromolecules* 1997, 30, 5714-5720.

Table 2.1: List of the MD simulations of polystyrene chains and the number and time scales of the modes fitted to the bond orientation autocorrelation function. 'UA' and 'MARTINI' refer to the united-atom and MARTINI models respectively.

Number of monomers	**Solvent bath**	**Model for MD**	**T (K)**	**Number of modes**	**Time scales of modes (ns)**	**End-to-end relaxation time, τ (ns)**
30	Benzene	UA	293	1	$t_1 = 4.82$	7.56
30	Benzene	MARTINI	293	1	$t_1 = 34.6$	36.7
30	2-oligostyrene	MARTINI	480	1	$t_1 = 10.65$	11.23
30	5-oligostyrene	MARTINI	680	1	$t_1 = 4.9$	5.4
100	Benzene	MARTINI	293	2	$t_1 = 22.88$, $t_2 = 230$	340
100	2-oligostyrene	MARTINI	480	2	$t_1 = 4.15$, $t_2 = 62.78$	107
100	5-oligostyrene	MARTINI	680	2	$t_1 = 1.9$, $t_2 = 21.9$	38.9

Table 2.2: Chain models with continuum solvent studied. In all cases, there are 60 backbone beads (59 rods). Stiff Fraenkel springs are used to mimic 'rods' for all models.

Name	Side group included?	Mechanisms included in the model
spr	No	Beads connected by rods
spr+ben	No	Bending interactions between rods
spr+ben+tor	No	Bending and torsional interactions
spr+ben+tor+side groups	Yes	Bending and torsional interactions between beads in backbone and side groups
spr+ben+tor+pot	No	Bending, torsional interactions and non-bonded potential between beads
PSG (phantom side groups)	Yes	Bending and torsional interactions between beads in backbone and side groups, non-bonded potential only between beads on backbone
ACWS (atomistic chain without solvent)	Yes	Bending, torsional interactions and non-bonded potential between beads in backbone and side groups

Table 2.3: Diffusivities of the center of mass of the polymer chain (with 60 beads), in the absence and presence of HI. The diffusivity values reported here are in terms of characteristic length and time scales used in Ref. [54]. Note that, in the absence of HI, Rouse theory gives $D_{cm} = \frac{1}{N_{beads}}$ in the characteristic length and time units, where N_{beads} is the total number of beads in the chain. In this case, N_{beads} = 60 and hence D_{cm} = 1/60 = 0.0167, which is consistent with our simulation results given in the table. In the presence of HI, D_{cm} is higher than that without HI and decreases with the increase of the coil size (the average radius of gyration increases with the inclusion of additional mechanisms of bending, torsion and potential).

	No HI ($h^* = 0$)	**$h^* = 0.15$**	**$h^* = 0.5$**
spr	0.0168	0.0735	0.195
spr+ben	0.0168	0.06	0.164
spr+ben+tor	0.0161	0.051	0.131
spr+ben+tor+pot	0.0163	0.043	0.101

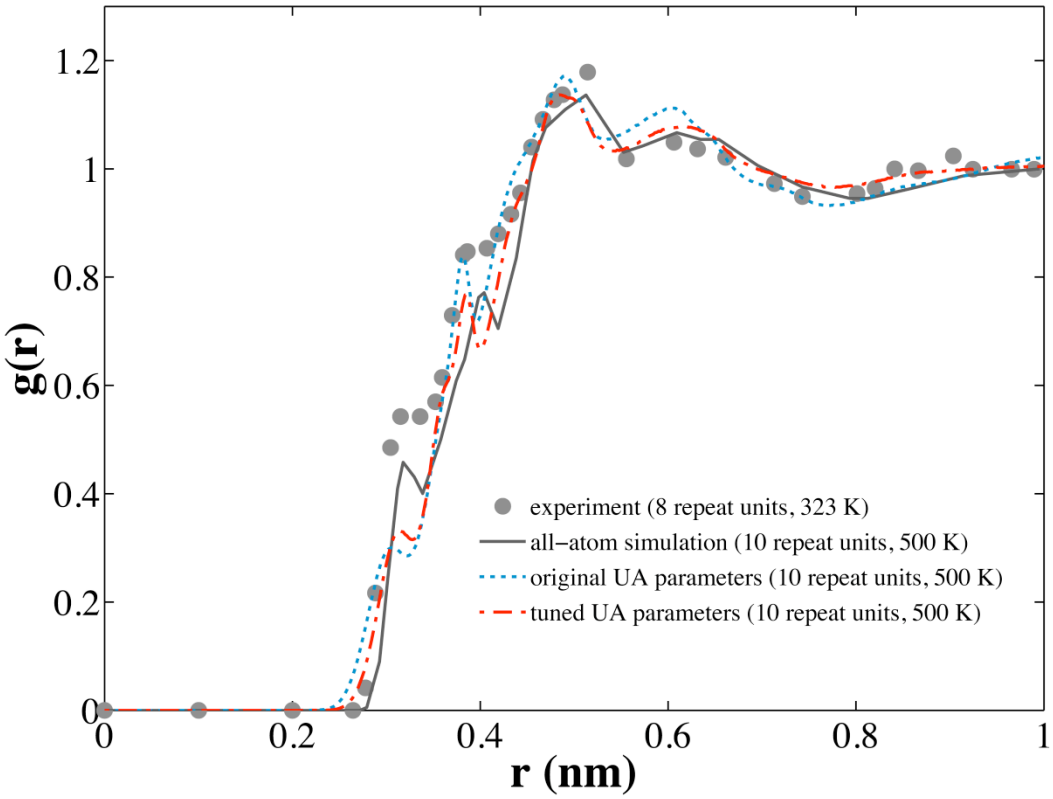

Figure 2.1: Comparison of the C-C radial distribution functions in a melt of short (10 monomer) polystyrene chains obtained from experiment (earlier work, data taken from Ref. [44]), all-atom MD simulations (earlier work, data taken from Ref. [44]) and united-atom MD simulations performed in this study. The legend 'all-atom simulation' refers to the results obtained in Ref. [44], 'original UA parameters' refers to results obtained in this work with the united-atom potential provided in Ref. [26] and 'tuned UA parameters' refers to those obtained using a potential in which we introduced several modifications, as discussed in text. Note that the experimental results correspond to a melt of shorter chains (8 monomers) at a lower temperature (323 K).

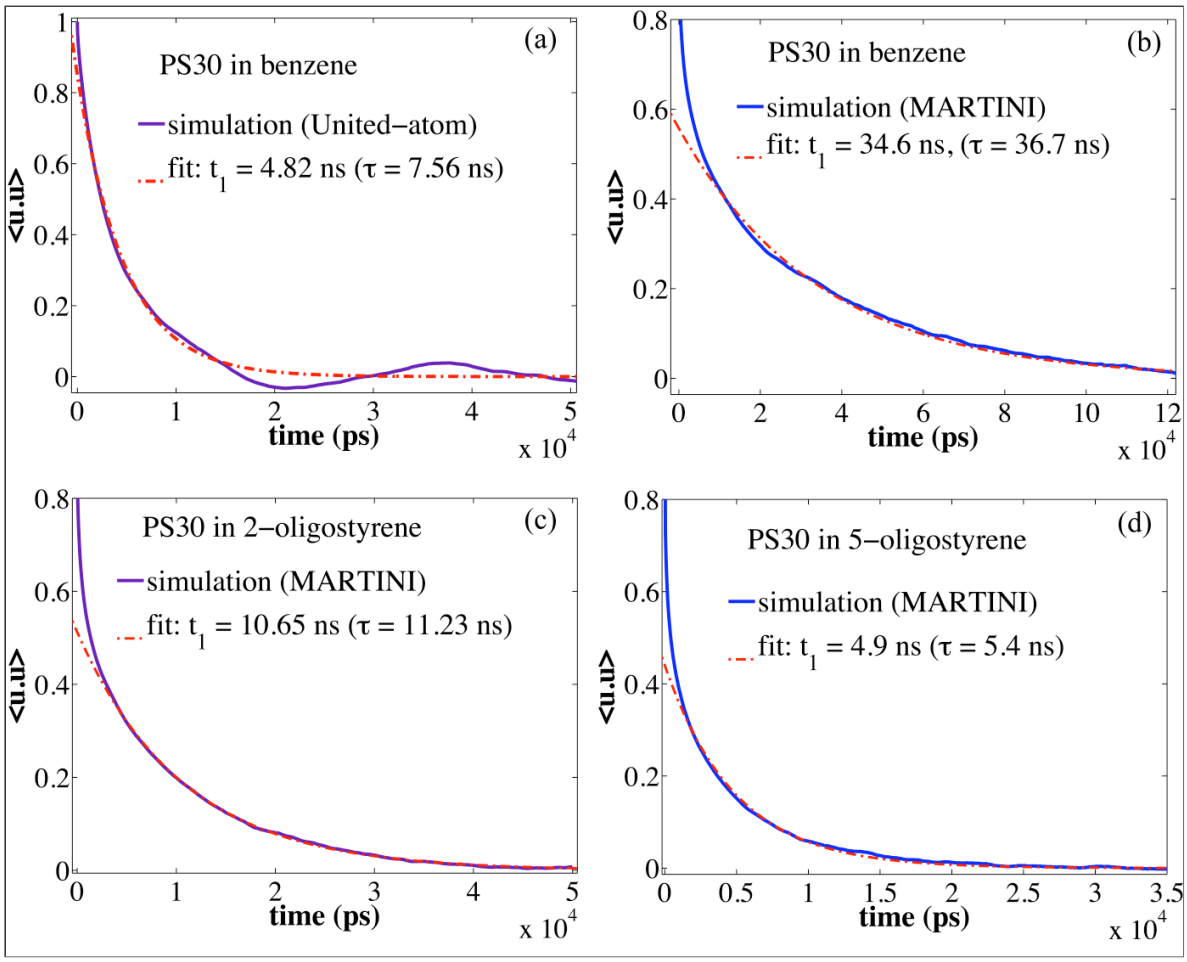

Figure 2.2: Relaxation of backbone bonds from MD simulations (solid blue lines) and corresponding fits to a single exponential decay (dash-dot red lines) for a polystyrene chain of 30 monomers (59 backbone bonds) using different models and solvent baths - (a) United-atom model in benzene at 293 K, (b) MARTINI model in benzene at 293 K, (c) MARTINI model in 2-oligostyrene at 480 K and (d) MARTINI model in 5-oligostyrene at 680 K. t_1 denotes the time scale of the exponential decay and τ is the relaxation time for the end-to-end vector of the chain.

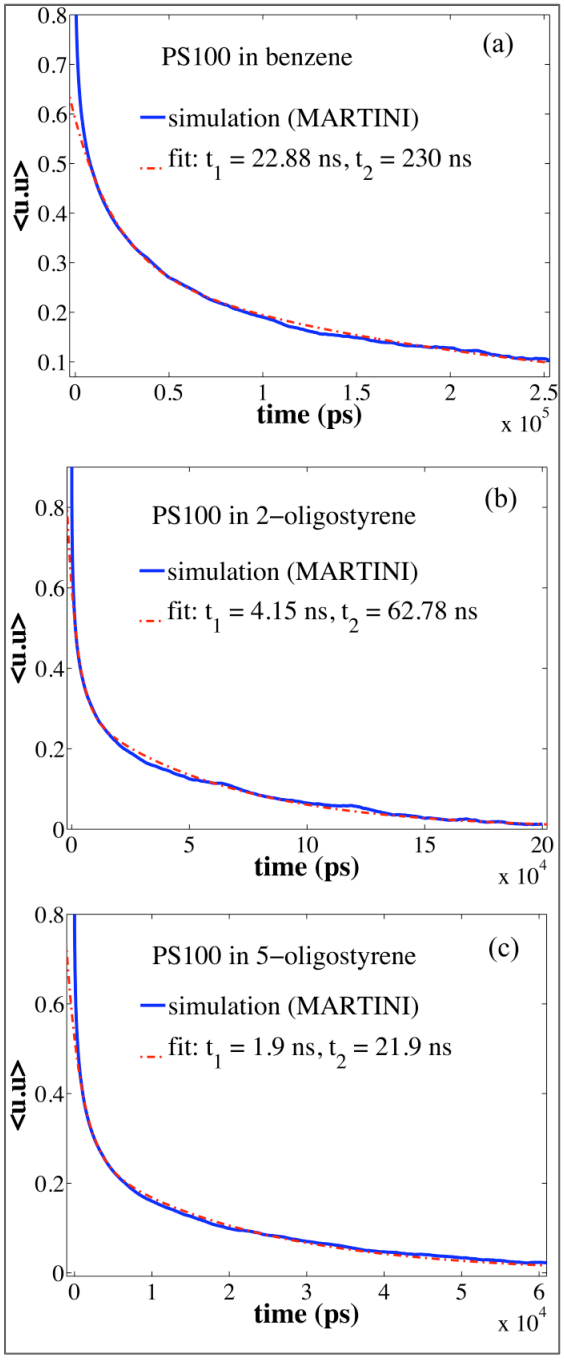

Figure 2.3: Relaxation of the backbone bonds from MD simulations (solid blue lines) and the corresponding fits to a sum of two exponential decay terms (dash-dot red lines) for a polystyrene chain of 100 monomers (199 backbone bonds), using the MARTINI model in solvent baths of (a) benzene at 293 K, (b) 2-oligostyrene at 480 K and (c) 5-oligostyrene at 680 K. t_1 and t_2 denote the time scales of the two exponential decay terms.

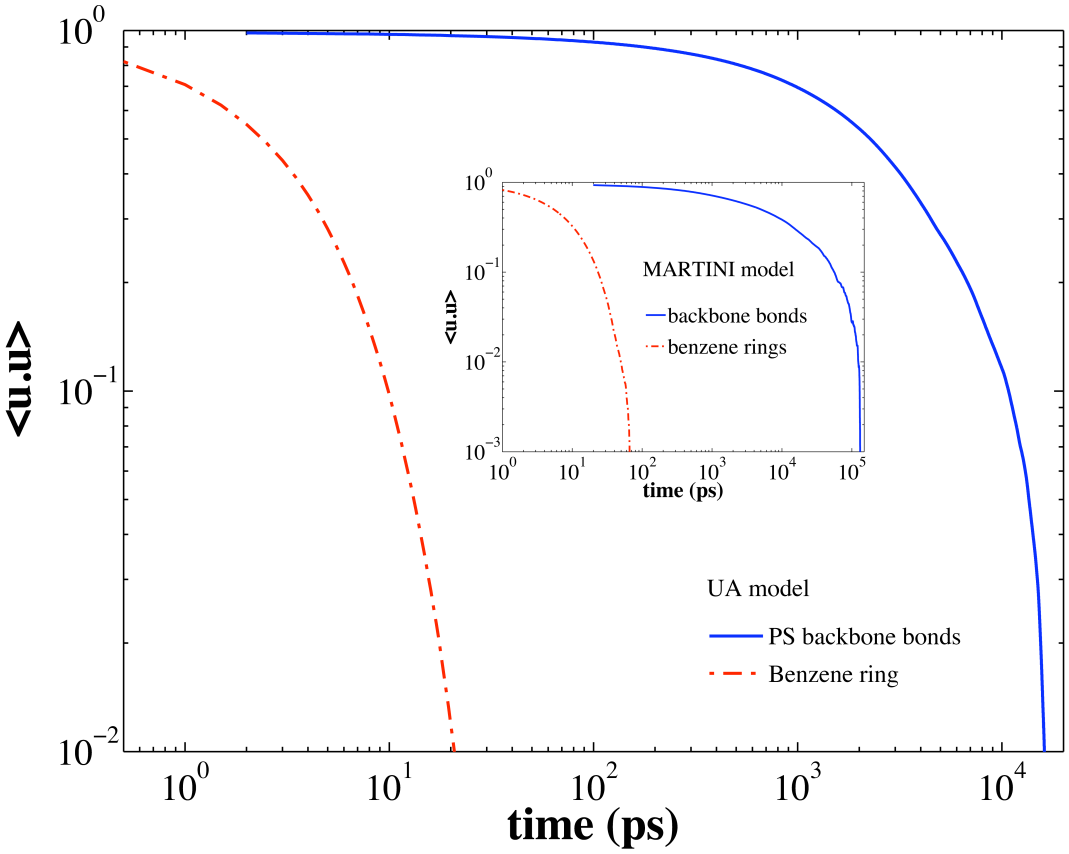

Figure 2.4: Comparison of the relaxation dynamics of individual chain backbone bonds of a polystyrene chain (30 monomers) and benzene rings in the solvent bath from UA MD simulations. Inset shows the same for CGMD simulations using the MARTINI model. For the relaxation dynamics of benzene rings, the autocorrelation function of the unit vector normal to each benzene ring is computed and then averaged over all benzene molecules in the system.

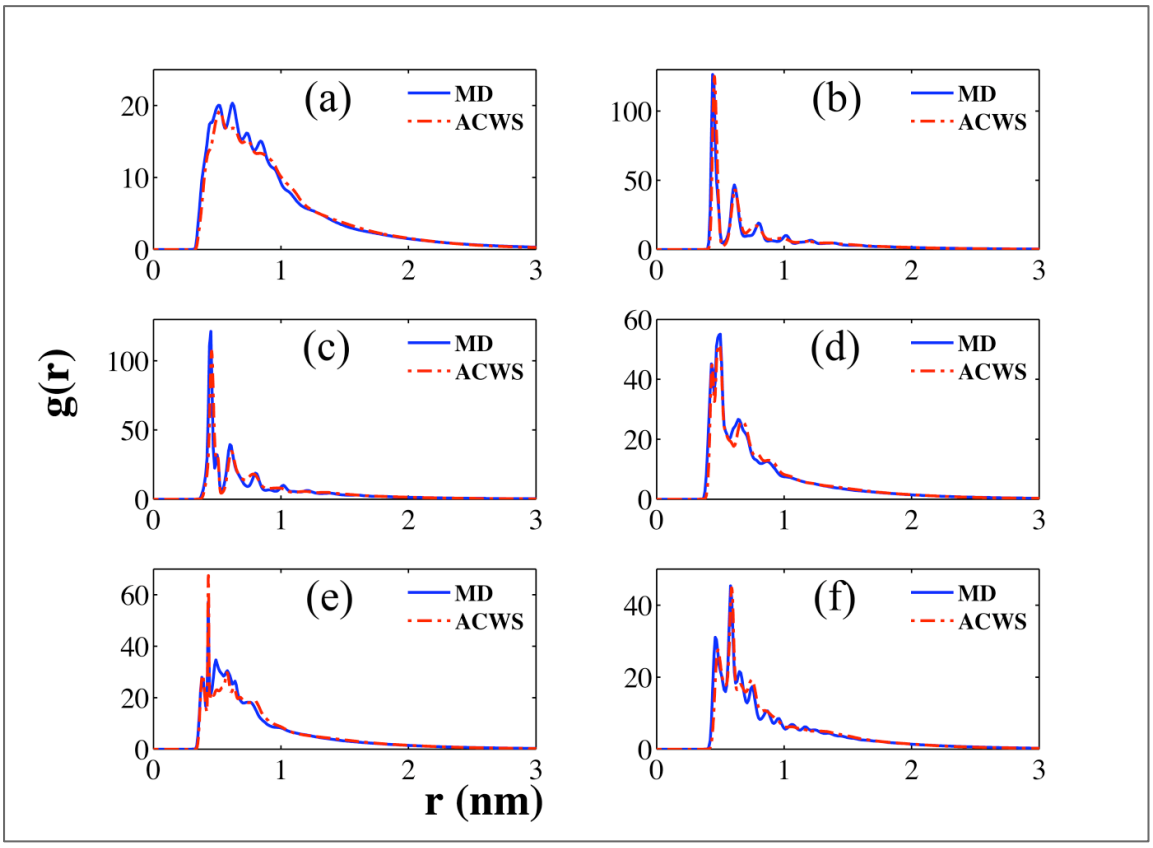

Figure 2.5: Comparison of radial distribution functions between different atom types on the polystyrene chain (30 monomers) obtained from MD simulations (solid blue line) and the ACWS model in continuum solvent (dash-dot red line). The radial distribution functions are shown between the following united-atom types: (a) CH groups on phenyl rings in the side groups with other such CH groups in the phenyl rings, (b) CH_2 groups on the chain backbone with other such groups, (c) CH groups on the chain backbone with other such groups, (d) CH groups in side groups with CH_2 groups in the chain backbone, (e) CH groups in side groups with CH groups in the chain backbone and (f) CH_2 groups in the chain backbone with CH groups in the chain backbone.

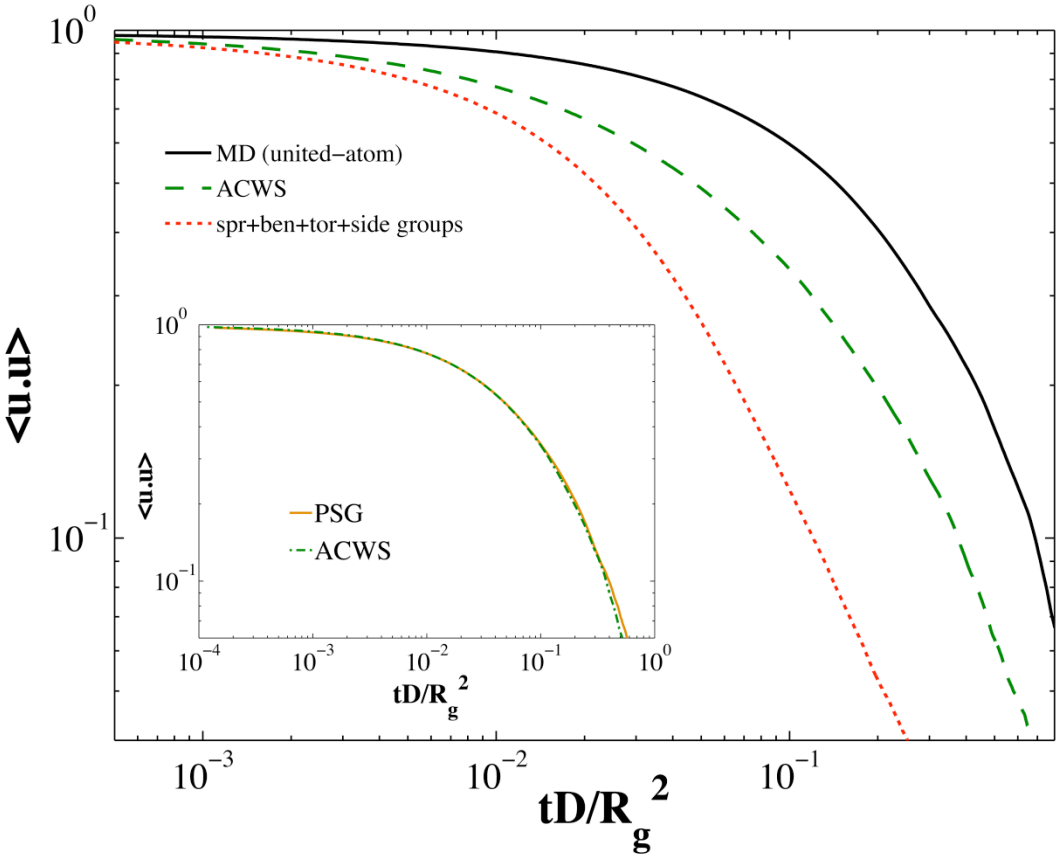

Figure 2.6: Comparison of the relaxation dynamics for the backbone bonds of a polystyrene chain of 30 monomers from UA MD simulation (in benzene bath) and different united-atom representations of the same in a continuum solvent. Inset compares the relaxation dynamics for backbone bonds for the ACWS and PSG chain models. For details of the models, see text and Table 2.2. In this and following figures, the time is made dimensionless using the factor D/R_g^2, where D and R_g are the diffusivity of the center of mass and the average radius of gyration of the chain, respectively.

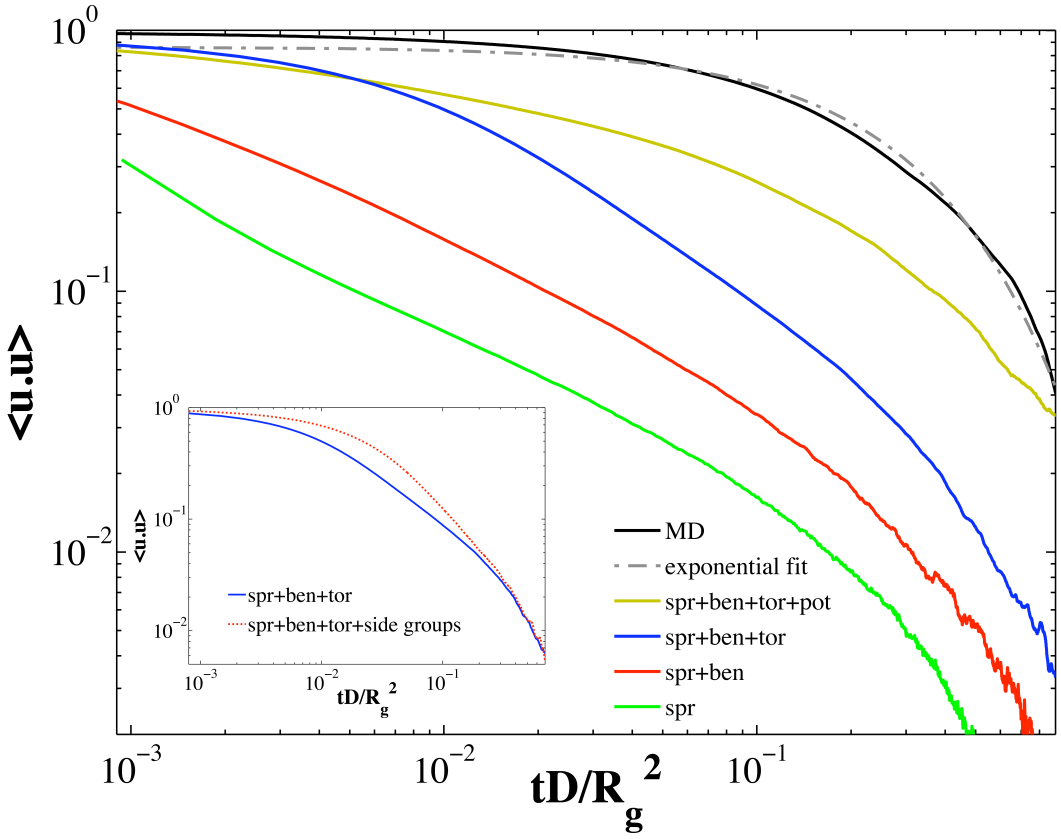

Figure 2.7: Comparison of the relaxation dynamics for the backbone bonds of a polystyrene chain of 30 monomers from UA MD simulation (in benzene bath) and chain models with varying degrees of simplification, in a continuum solvent without hydrodynamic interaction (HI). The details of the models are given in text and Table 2.2. The grey dash-dot line shows the single-exponential fit to the relaxation dynamics of the bonds from the UA MD simulation. Inset compares the bond relaxation dynamics for the 'spr+ben+tor' and 'spr+ben+tor+side groups' models, thus showing that the additional effect due to inclusion of side groups is negligible at long times.

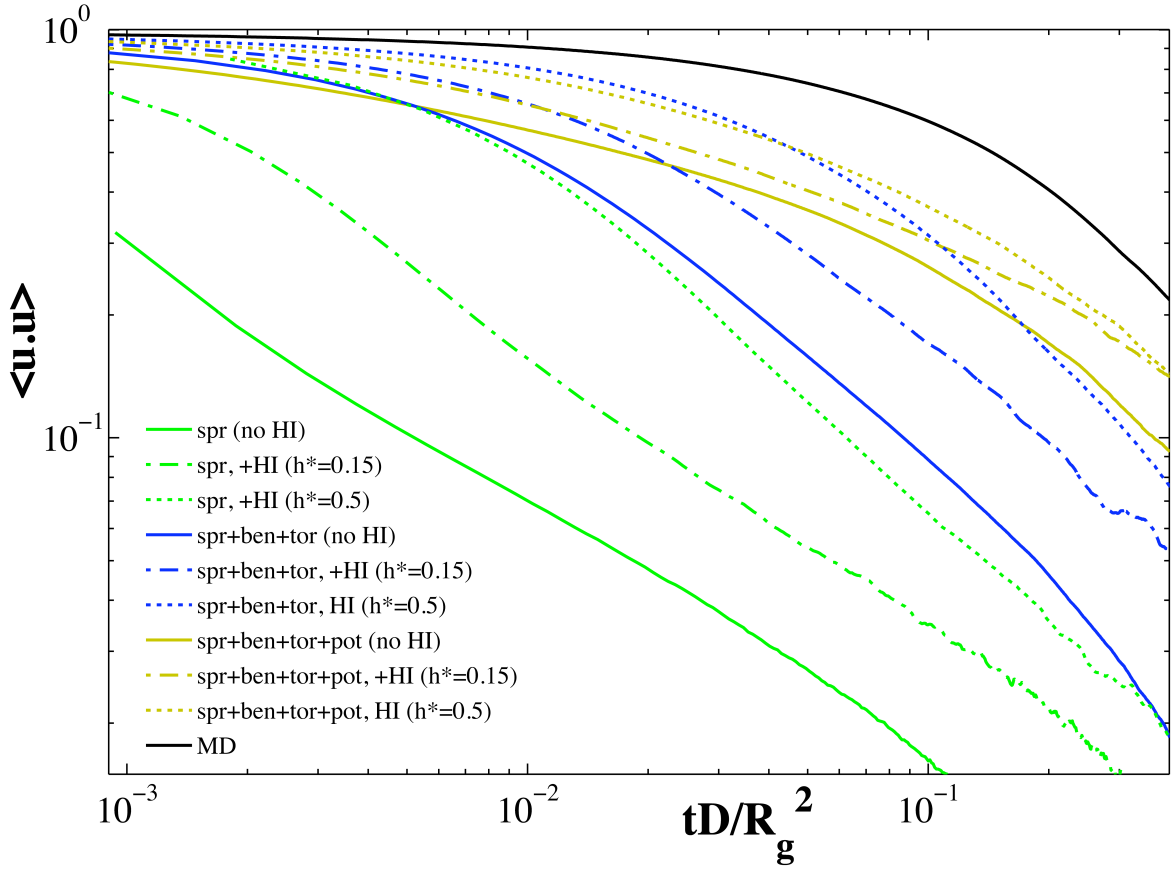

Figure 2.8: Comparison of the relaxation dynamics for the backbone bonds of a polystyrene chain of 30 monomers from UA MD simulation (in benzene bath) and chain models with varying degrees of simplification (all models without side groups are only considered here), in a continuum solvent, with and without hydrodynamic interaction (HI). The details of the models are given in text and Table 2.2. Two levels of HI ($h^* = 0.15$ and $h^* = 0.5$) are considered here.

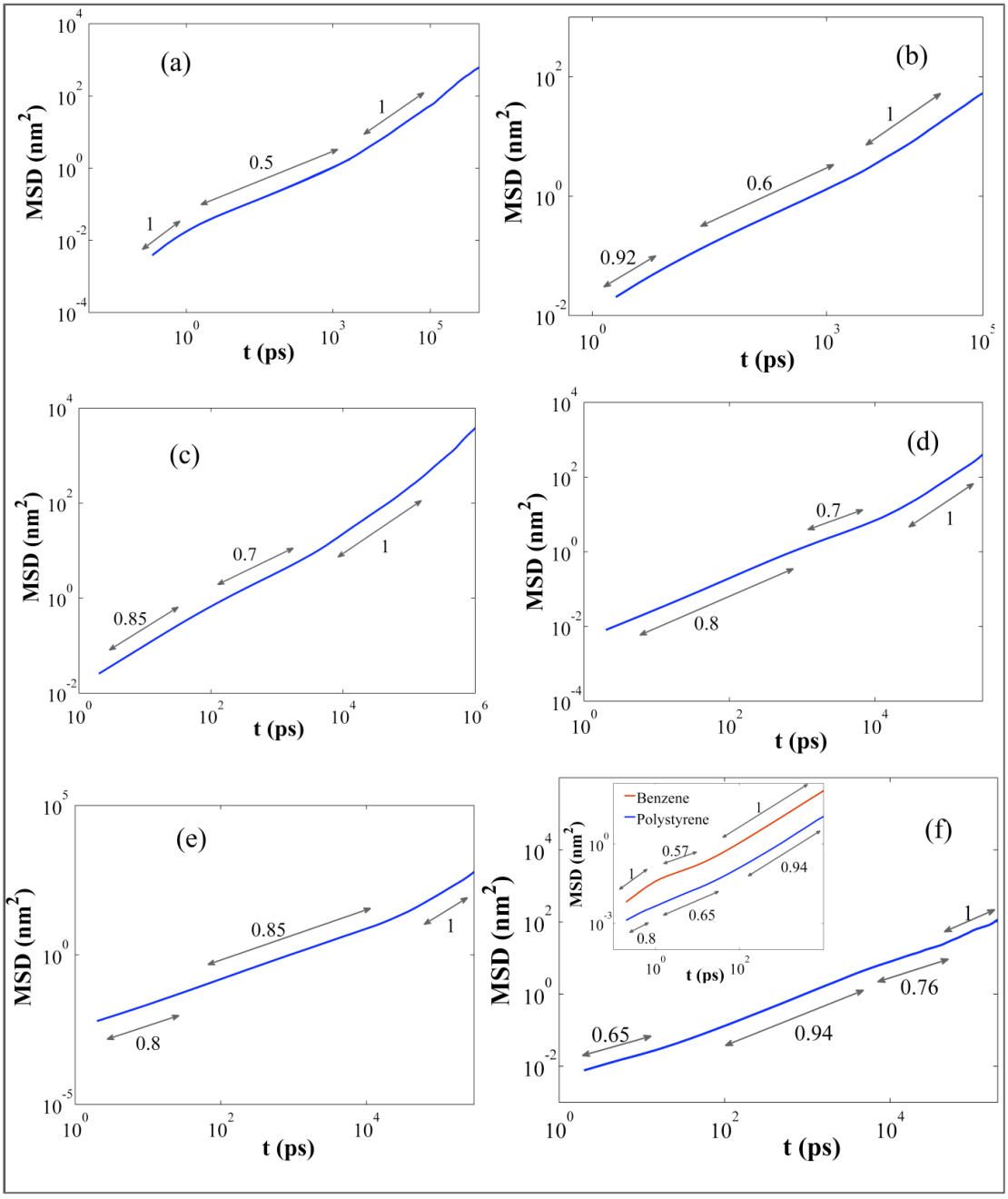

Figure 2.9: Mean square displacements (MSD) versus time for chain backbone atoms for the following models: (a) spr, (b) spr+ben, (c) spr+ben+tor, (d) spr+ben+tor+side groups, (e) ACWS and (f) a polystyrene chain of 30 monomers in benzene bath from MD simulations. Inset to (f) shows the results from the MD simulation at short times for atoms on the chain backbone and those on the benzene rings constituting the solvent bath. Note that (a)-(e) are for models in a continuum solvent, while the solvent molecules are treated explicitly for (f). Details of the models used for (a)-(e) are provided in text and Table 2.2.

CHAPTER III

Multiple regimes of deformation in shearing flow of isolated polymers

1. Introduction

As discussed in Chapter I, the behavior of isolated polymer chains in shear flow is thought to be well understood, as a consequence of extensive investigations by experiments, ranging from rheological measurements to single-molecule imaging [1-7], and Brownian dynamics simulations of isolated polymer chains [8-12]. However, quite surprisingly, a highly non-monotonic behavior emerges from a recent simulation study by Sendner and Netz [13] of a polymer chain formed of beads connected by stiff Fraenkel springs, with a decreasing chain size at high shear rates. This phenomenon of chain compression became more pronounced in the presence of HI, and almost vanished with the inclusion of EV interactions. As mentioned in Chapter I, few earlier studies do exist [8, 9, 10, 14] that investigated such high shear rates and reported observations that are consistent with those suggested by the simulations of Sendner and Netz [13], which considered much longer chains. Since the root mean square of the stretch increases linearly with shear rate for a Gaussian chain [15], this decrease in chain stretch at high shear rates observed in simulations most probably results from the finite extensibility effects.

These seemingly puzzling observations, especially those of Sendner and Netz [13], imply that the behavior of isolated polymer chains over a wide range of shear rate is still not well understood, even for a relatively simple case where both excluded volume and hydrodynamic interactions are neglected. In this Chapter, we present a detailed investigation of this particular case, without excluded volume (EV) and hydrodynamic interaction (HI), and our results here form the foundation to investigate the changes in the response due to those additional mechanisms. More insights into the dynamics of tumbling will be presented in Chapter IV, while the effects of excluded volume and hydrodynamic interactions will be discussed in details in Chapter V. Here, we will seek to frame universal scaling laws for the mean dimensions of the deformed chain along the flow, gradient, and vorticity directions and try to explain the nature of the chain dynamics in different shear-rate regimes. A comparison of the behavior of a bead-rod chain with coarse-grained chains using the Cohen Padé approximation and the spring law developed by Underhill and Doyle (2005) is also provided, which will highlight the inadequacy of current methods of coarse-graining at very high shear rates.

This Chapter is organized in the following manner. In Sec. 2, we discuss the Brownian dynamics simulation method and numerical scheme. The simulation results for bead-rod as well as coarse-grained chains, an analytical model for the dynamics of a single rod, and its relevance to the response of chains at high shear rates are presented in Sec. 3. Finally, the key findings are summarized in Sec. 4.

2. Simulation Method

Here, we explain the basic set-up and the numerical scheme that is relevant to all BD simulations that we present in this thesis. Note that, we only use the "bead-rod" and coarse-grained "bead-spring" chain models in this Chapter (described in the following section), whereas finer resolution models are also used for several studies in the following Chapters. Also, note that the "bead-rod" and the "bead-spring" models are referred to as 'BR' and 'CG', respectively, in the following Chapters.

A. Simulation setup and models

The polymer chain is modeled as a series of N+1 beads (numbered 0 to N) connected to each other by a set of springs (numbered 1 to N). In the absence of excluded volume interactions, the following form of Langevin equation describes the motion of each bead of a bead-spring chain:

$$\frac{d\vec{r}_i}{dt} = \frac{1}{\zeta}\vec{F}_i^{flow} + \frac{1}{\zeta}\left[\vec{F}_{i+1}^{S} - \vec{F}_i^{S}\right] + \frac{1}{\zeta}\vec{F}_i^{R} \qquad (1)$$

where $\vec{r}_i$ is the position vector of the i^{th} bead, ζ is the drag coefficient, $\vec{F}_i^{R}$ represents the Brownian force, $\vec{F}_i^{flow}$ is the drag force due to the flow, and $\vec{F}_i^{S}$ and $\vec{F}_{i+1}^{S}$ denote the forces due to the i^{th} and $(i+1)^{th}$ springs, respectively. In the absence of hydrodynamic interactions, the force due to flow is:

$$\vec{F}_i^{flow} = \zeta\kappa\cdot\vec{r}_i$$

The tensor κ is given as:

$$\kappa = (\nabla \vec{u})^T$$

where ∇ is the gradient operator and $\vec{u}$ is the unperturbed solvent velocity. The Brownian force is given by:

$$\vec{F}_i^R = \sqrt{\frac{6k_B T\zeta}{\Delta t}}\,\vec{n}_i$$

where k_B is Boltzmann's constant, T is the absolute temperature, and $\vec{n}_i$ is a vector whose components are distributed randomly in the interval [-1,1].

If the variables are made dimensionless by scaling length with b_k (Kuhn length), force with k_BT/b_k and time with $\zeta b_k^{\,2}/k_BT$, the following dimensionless form of the equation of motion is obtained:

$$\frac{d\vec{r}_i^*}{dt^*} = \kappa^* \cdot \vec{r}_i^* + \left[\vec{F}_{i+1}^{S*} - \vec{F}_i^{S*}\right] + \sqrt{\frac{6}{\Delta t^*}}\vec{n}_i \qquad (2)$$

where $\vec{r}_i^*, t^*$ and $\vec{F}_i^{S*}$ denote the dimensionless variables. For a simple shear flow with the shear directed along the x-axis and the gradient along the y-axis, κ^* is given by:

$$\kappa^* = \begin{pmatrix} 0 & \dot{\gamma} & 0 \\ 0 & 0 & 0 \\ 0 & 0 & 0 \end{pmatrix}$$

where $\dot{\gamma}$ is the dimensionless shear rate.

As mentioned earlier, in this Chapter, simulations are performed using three different types of chain models – (1) a "bead-rod" chain that uses beads connected by stiff Fraenkel springs that approximate inextensible rods, (2) a coarse-grained "bead-spring" chain that uses the Cohen Padé approximation to the inverse Langevin function [16] to approximate the entropic spring force produced by a fixed, limited number of rods that are represented by each spring, and (3) a bead-spring chain where the spring forces are modeled using the potential developed by Underhill and Doyle [17]. (Note that the "bead-rod" and the "bead-spring" models are also referred to as "BR" and the "CG" in the following Chapters, as mentioned earlier) The former "bead-rod" model represents a freely jointed chain of nearly inextensible "rods" at a resolution of a single Kuhn step, although each "rod" is actually represented by a stiff Fraenkel spring with the following expression for the spring force:

$$\vec{F} = K\left(\left|\vec{Q}\right| - 1\right)\frac{\vec{Q}}{\left|\vec{Q}\right|} \tag{3}$$

where $\vec{Q}$ and K are the end-to-end vector and stiffness constant of the spring, respectively. Using this expression for the spring force in Eq. (2) gives the following:

$$\frac{d\vec{r}_i^*}{dt^*} = \kappa.\vec{r}_i^* + K^*\left[\left\{\left(\left|\vec{Q}_{i+1}^*\right| - 1\right)\frac{\vec{Q}_{i+1}^*}{\left|\vec{Q}_{i+1}^*\right|}\right\} - \left\{\left(\left|\vec{Q}_i^*\right| - 1\right)\frac{\vec{Q}_i^*}{\left|\vec{Q}_i^*\right|}\right\}\right] + \sqrt{\frac{6}{\Delta t^*}}\vec{n}_i \tag{4}$$

where $\vec{Q}_i^* = \vec{r}_i^* - \vec{r}_{i-1}^*$, and the parameter $K^* = \frac{Kb_k^{\,2}}{k_B T}$ is used to adjust the stiffness of the springs in the simulation. To prevent overstretching, a value of K^*=10^4 is used for $\dot{\gamma}$ <=10

and $K^* = 1000\dot{\gamma}$ is used for $\dot{\gamma}$ >10. For the semi-implicit algorithm, described in Sec. 2B, used for solving the stochastic differential algorithm given in Eq. (2), a timestep size $\Delta t^* \leq (1/K^*)$ is found to be sufficient to ensure good convergence.

The coarse-grained chain models use springs that obey a force law of the following general form:

$$F^{S*} = \frac{F^S b_K}{k_B T} = \frac{\alpha \hat{r} - \beta \hat{r}^3}{1 - \hat{r}^2} \tag{5}$$

where F^{S*} represents the spring force in dimensionless units and $\hat{r}$ denotes the fractional spring extension with respect to the fully extended length. For springs that use the Cohen Padé approximation, the parameters are independent of the level of coarse graining: $\alpha = 3$ and $\beta = 1$. For the spring potential developed by Underhill and Doyle [17] for freely jointed bead-rod chains, the parameters α and β are given by:

$$\begin{aligned} \alpha &= 3 - \frac{10}{3\nu} + \frac{10}{27\nu^2} \\ \beta &= 1 + \frac{2}{3\nu} + \frac{10}{27\nu^2} \end{aligned} \tag{6}$$

where ν represents the number of Kuhn lengths per spring, where the Kuhn length is the length of a rod in a freely jointed chain of rods. It is to be noted here that the Cohen and Underhill-Doyle spring potentials are almost identical at high degrees of coarse graining (i.e. large values of ν).

Using these force laws, a single spring gives a force-extension curve very similar to that of a bead-rod sub-chain with ν rods, as long as the sub-chain represented by the spring contains a substantial number of rods (6 rods for the Underhill-Doyle spring). In our simulations, different values of ν (≥ 6) are used to represent the same bead-rod chain at different levels of coarse graining.

B. Numerical Scheme

The Langevin equation (viz. Eq. (1)) for each bead in the bead-rod chain is solved using a single-step semi-implicit time stepping scheme described below. For a polymer chain of N rods, the beads are numbered from 0 to N and the rods are numbered from 1 to N – with the i^{th} rod connecting i-1$^{\text{th}}$ and i^{th} beads.

Subtracting the equation of motion for bead i from that for bead i-1 yields the equation of deformation for the i^{th} spring:

$$\zeta \frac{d\vec{Q}_i}{dt} = \left(\vec{F}_i^{R} - \vec{F}_{i-1}^{R}\right) + \left(\vec{F}_{i+1}^{S} + \vec{F}_{i-1}^{S}\right) - 2\vec{F}_i^{S} + \left(\vec{F}_i^{flow} - \vec{F}_{i-1}^{flow}\right) \tag{7}$$

For small Δt, the above equation can be approximated by:

$$\vec{Q}_i^{t+\Delta t} = \vec{Q}_i^{t} + \frac{\Delta t}{\zeta}\left(\vec{F}_i^{R} - \vec{F}_{i-1}^{R}\right) + \frac{\Delta t}{\zeta}\left(\vec{F}_{i+1}^{S} + \vec{F}_{i-1}^{S}\right) + \frac{\Delta t}{\zeta}\left(\vec{F}_i^{flow} - \vec{F}_{i-1}^{flow}\right) - \frac{2\Delta t}{\zeta}\vec{F}_i^{S} \tag{8}$$

In the above equation, if the term containing the force due to spring i is evaluated at time $t+\Delta t$ instead of t, an implicit equation in time is obtained to solve for $Q_i^{t+\Delta t}$. For a

Fraenkel spring, if the moduli (or absolute values) of the vectors are taken on both sides, the equation can be written as:

$$\left|\vec{Q}_i^{t+\Delta t}\right|\left[1+\frac{2\Delta t}{\zeta}\frac{K\left(\left|\vec{Q}_i^{t+\Delta t}\right|-1\right)}{\left|\vec{Q}_i^{t+\Delta t}\right|}\right]=\left|\vec{Y}_i\right| \tag{9}$$

where $\vec{Y}_i$ is given by:

$$\vec{Y}_i=\vec{Q}_i^t+\frac{\Delta t}{\zeta}\left(\vec{F}_i^R-\vec{F}_{i-1}^R\right)+\frac{\Delta t}{\zeta}\left(\vec{F}_{i+1}^S+\vec{F}_{i-1}^S\right)+\frac{\Delta t}{\zeta}\left(\vec{F}_i^{flow}-\vec{F}_{i-1}^{flow}\right) \tag{10}$$

If we define $B=\frac{2K\Delta t}{\zeta}$, the equation for spring *i* can be solved as:

$$\left|\vec{Q}_i^{t+\Delta t}\right|=\frac{B+\left|\vec{Y}_i\right|}{B+1} \tag{11}$$

Once the modulus $\left|\vec{Q}_i^{t+\Delta t}\right|$ for the spring *i* is known, the components are calculated using the equation:

$$\vec{Q}_i^{t+\Delta t}\left[1+\frac{2\Delta t}{\zeta}\frac{K\left(\left|\vec{Q}_i^{t+\Delta t}\right|-1\right)}{\left|\vec{Q}_i^{t+\Delta t}\right|}\right]=\vec{Y}_i \tag{12}$$

For the coarse-grained spring potentials shown in Eq. (5), the following cubic equation for $\left|\vec{Q}_i^{t+\Delta t}\right|$ is obtained:

$$\left(1+B\beta''\right)\left|\vec{Q}_i^{t+\Delta t}\right|^3-\left|\vec{Y}_i\right|\left|\vec{Q}_i^{t+\Delta t}\right|^2-\left(\nu^2+B\right)\left|\vec{Q}_i^{t+\Delta t}\right|+\left|\vec{Y}_i\right|\nu^2=0 \tag{13}$$

where $B = 2\nu^2\alpha\Delta t$, $\beta'' = \dfrac{\beta}{\nu^2\alpha}$ and $\vec{Y}_i$ is given by Eq. (10).

A similar formulation for the springs at the ends of the chain yields a slightly different expression for $\vec{Y}_i$. For the 1st spring:

$$\vec{Y}_1 = \vec{Q}_1^t + \frac{\Delta t}{\zeta}\left(\vec{F}_1^R - \vec{F}_0^R\right) + \frac{\Delta t}{\zeta}\vec{F}_2^S + \frac{\Delta t}{\zeta}\left(\vec{F}_1^{flow} - \vec{F}_0^{flow}\right) \tag{14}$$

and for the Nth spring:

$$\vec{Y}_N = \vec{Q}_N^t + \frac{\Delta t}{\zeta}\left(\vec{F}_N^R - \vec{F}_{N-1}^R\right) + \frac{\Delta t}{\zeta}\vec{F}_{N-1}^S + \frac{\Delta t}{\zeta}\left(\vec{F}_N^{flow} - \vec{F}_{N-1}^{flow}\right) \tag{15}$$

For any given polymer chain and a given shear flow rate, to obtain good statistics, long simulations are performed with five different starting states. For $\dot{\gamma} > 1$, each starting configuration of the bead-rod chain is simulated for a total strain of 10^6. For lower shear rates, the total run time for each case varied with the number of rods in the chain and is usually chosen to be about 150 times the longest relaxation time for chains with $N \leq 100$ and about 20 times this for larger chains. For all simulations with the bead-rod chains, the data collected in the final 50% of the trajectory is used to calculate the average of any property.

The method described above represents an implicit integration scheme employing a single predictor step, with no further corrections. For simulations with the coarse-grained chains, where the spring force is a non-linear function of the stretch and diverges sharply as it approaches a fully extended state, further corrections to the initial predictor step are

necessary at every time step. Hence, the simulations with the coarse-grained chains are performed using the semi-implicit algorithm described by Somasi *et al.* [18], which refines the results from the predictor step iteratively until the total chain length converges to within a specified tolerance. In these simulations, each starting state is run for a total strain of 3×10^4 when $\dot{\gamma} > 1$. Similar to the bead-rod chains, the total simulation time for each case at lower shear rates is at least 150 times the longest relaxation time. For all runs, only the data collected over the final 80% of the simulation is used to calculate the average of any property. For the bead-rod chains, calculations using this iterative semi-implicit algorithm produced results that are consistent with those using a single step implicit predictor algorithm.

3. Results and Discussion

The components of the radius of gyration of the polymer chain provide a measure of its dimensions in different directions. When a single polymer molecule is subjected to a shear flow, the average stretch in the shear direction is increased while those in the gradient and the vorticity directions are decreased relative to the mean values at equilibrium. The radius of gyration of the polymer chain is defined as:

$$R_g = \sqrt{\frac{\left\langle \sum_i \left| \vec{r}_i - \vec{r}_{c.m.} \right|^2 \right\rangle}{N}} \tag{16}$$

where $\vec{r}_{c.m.}$ is the position of the center of mass of the chain and $\langle ... \rangle$ represents an ensemble average. The radius of gyration along the x-axis can be similarly defined as:

$$R_{gx} = \sqrt{\frac{\left\langle \sum_i \left(x_i - x_{c.m.}\right)^2 \right\rangle}{N}} \tag{17}$$

where x_i and $x_{c.m.}$ denote the positions of the i^{th} bead and the center of mass of the chain along the x-axis, respectively. Similarly, the y- and z-components of the position vector, respectively, are used to define R_{gy} and R_{gz}.

The ability of a shear flow to deform the polymer chain is characterized using the Weissenberg and Kuhn Peclet numbers. The Weissenberg number characterizes the ability of shear to deform the chain as a whole and is defined as:

$$Wi = \dot{\gamma}\tau \tag{18}$$

where τ is the longest relaxation time of the chain. The relaxation time is calculated by fitting the decay of the autocorrelation function of the end-to-end vector to an exponential over the last 70% of the relaxation, where a single exponential function shows an excellent fit. Note that this yields a relaxation time (referred to as the Rouse reorientation time) that is twice the Rouse stress relaxation time for the chain. The (Kuhn) Peclet number is roughly the product of the rod re-orientation time and the shear rate:

$$Pe = \frac{\dot{\gamma}\tau}{N^2} \tag{19}$$

Note that, since we don't consider effects due to HI and EV in this Chapter, the relaxation spectrum is given by the Rouse theory and hence the rod reorientation time is estimated as τ/N^2. For $Pe > 1$, the shear is fast enough to impose orientation on individual isolated rods (or Kuhn steps), while for $Pe < 1$, it is not strong enough to do so. Chains of rods can, however, become oriented at $Pe < 1$ because of tension transmitted along the chain. Stretching of the chain as a whole along with orientation of the rods in the chain occurs when $Wi = PeN^2 = \dot{\gamma}\tau > 1$.

A. Bead-rod simulations

We have performed simulations of bead-rod chains with varying number of rods and over a wide range of shear rates, without excluded volume and hydrodynamic interactions. As discussed earlier, these results for bead-rod chains with non-interacting beads, that provide the foundations for the understanding of various additional effects, are discussed in detail in this Chapter and the effects of including excluded volume and hydrodynamic interactions will be discussed Chapter V. The results for the mean stretch are presented in two parts: Figure 3.1 shows the Weissenberg number dependence of the square root of the fractional deviation of R_{gx}^2, the mean square radius of gyration in the flow direction, from its equilibrium value, and Figure 3.2 shows the variation of R_{gx} normalized by the contour length, L, as a function of the Kuhn Peclet number. Figure 3.1(a) shows the results up to shear rates where a plateau is reached whereas Figure 3.1(b) focuses on relatively low shear rates and compares the simulation results with the analytical solution

for Gaussian chains (discussed in ref. [15]) given in Eq. (21). Inset to Figure 3.1(a) shows the approximate Weissenberg numbers (denoted by Wi_{c2}) at which the plateau in R_{gx} is reached for different chain lengths. Inset to Figure 3.1(b) shows the Weissenberg numbers (denoted by Wi_{c1}) up to which the analytical solution given in Eq. (21) is valid for different chain lengths. These are estimated from the Wi values at which R_{gy} begins to decrease with increasing Wi for different chain lengths, which are shown later in Figure 3.5(b) and mark the onset of the transition more clearly than the results presented in Figure 3.1(b). At low shear rates, universal trends are obtained as a function of the Weissenberg number rather than the Peclet number, and so these results are shown separately in Figure 3.1. The analytical solution for Gaussian chains is given as (using the results in ref. [15]):

$$\frac{R_g^{\,2}}{R_{g0}^{\,2}} - 1 = 0.103(Wi)^2 \tag{20}$$

where $R_{g0}^{\,2}$ denotes the mean square radius of gyration at equilibrium. If we assume that R_{gy} and R_{gz} remain constant at their equilibrium value at low shear rates where Eq. (20) is applicable, we get the following result:

$$\sqrt{\frac{R_{gx}^{\,2}}{R_{gx0}^{\,2}} - 1} = 0.556(Wi) \tag{21}$$

where $R_{gx0}^{\,2}$ denotes the equilibrium value of $R_{gx}^{\,2}$. It is shown later that R_{gy} and R_{gz} are in fact unperturbed from their equilibrium values at low shear rates.

Since our chains are finite in length and the springs are rod-like (i.e., nearly inextensible), the analytical result for Gaussian chains is not expected to agree well with the simulation results except at very low shear rates. Hence, we also compared the simulation results with that of a simple analytical model that incorporates finite extensibility [19]. For a polymer chain in simple shearing flow, the model adjusts the value of the spring constant by imposing the constraint of a constant contour length. In terms of the dimensionless variables, the tuned spring constant is obtained for shear flow by solving the following equation:

$$\sqrt{K^*} = \sqrt{3}\int_0^1 du\left[1+\frac{Wi^2\pi^4}{2NK^*}u^2(1-u)^2\right]^{1/2} \tag{22}$$

This adjusted value of the spring constant is then used in the following equation to calculate R_g:

$$\frac{R_g^2}{R_{g0}^2} = \frac{3}{K^*}\left[1+0.928\left(\frac{Wi}{K^*}\right)^2\right] \tag{23}$$

Knowing R_g, we can calculate R_{gx} by assuming that R_{gy} and R_{gz} are unperturbed from their equilibrium values at low shear rates. Figure 3.1(c) compares the simulation results for $\sqrt{\frac{R_{gx}^{\ 2}}{R_{gx0}^{\ 2}}-1}$ for chains of different sizes with those predicted from the model that incorporates the effect of finite extensibility. It shows that the model qualitatively captures the trends observed in the simulations, but quantitative agreement is good only

at low Wi. Overall, the numerical predictions of Eq. (23) do not seem to provide any advantage over the model for Gaussian chains (Eq. 21).

Figure 3.2 shows the results over the entire range of shear rates investigated. The highly non-monotonic behavior of R_{gx} is in agreement with the observations reported in the study by Sendner and Netz [13] for a chain of 100 rods. However, the results presented in Figure 3.2 also highlight the universality in the behavior of R_{gx}/L for all chain lengths at high shear rates, which has not been reported earlier. At low shear rates, universal scaling is observed in the variation of R_{gx}/R_{gx0} (R_{gx} normalized with the corresponding value at equilibrium) with Weissenberg number (Figure 3.1).

For $Pe \ll 1$, individual isolated rods are unable to orient in the flow direction, but a chain of them can be highly oriented and stretched, as long as $Wi > 1$. At $Wi < 1$, the deformation of the chain as a whole can be treated as a perturbation from equilibrium. (This regime of $Wi < 1$ might be considered as a "Regime 0," where the chain is only slightly deformed from its equilibrium configuration. Since this regime of linear viscoelasticity has been well studied already, we do not consider it further here.) For $Pe \ll 1$, the relevant length and time scales are the unperturbed, equilibrium radius of gyration R_{gx0} and the relaxation time τ, respectively. At higher shear rates, where individual rods in the chain are excited directly by the flow, and not just indirectly through the tension on the whole chain, the chain becomes approximately one-dimensional (R_{gy}, $R_{gz} \ll R_{gx}$), and it is appropriate to scale results using a length scale of

L, which is the contour length of the chain, and a time scale $\tau_s = \tau/N^2$, which is the relaxation time of a single isolated rod (from Rouse theory).

According to Figures 3.1 and 3.2, the variation of R_{gx} with shear rate encompasses at least three distinct regimes. The approximate ranges and the scaling laws for these regimes are:

Regime 1: ($Wi < Wi_{c1}$): $\sqrt{\frac{R_{gx}^{\ 2}}{R_{gx0}^{\ 2}} - 1} \sim Wi$

Regime 2: ($Pe_{c2} < Pe < 10$): $\frac{R_{gx}}{L} \sim Pe^{0}$

Regime 3: ($100 < Pe < 10^5$): $\frac{R_{gx}}{L} \sim Pe^{-0.15}$

As noted earlier, the Weissenberg number Wi_{c1} denotes the end of Regime 1, where the analytical solution for a Gaussian chain is valid. This is observed in Figure 3.1(b), which shows that our simulation results are consistent with those of a Gaussian chain at low *Wi*, and enter a transition to Regime 2 at $Wi > Wi_{c1}$, whose onset is marked by a Peclet number Pe_{c2} (corresponding to a Weissenberg number Wi_{c2} that is defined earlier). From our results presented in Figures 3.1(a) and 3.1(b), it is apparent that both Wi_{c1} and Wi_{c2} increase with the chain length (as seen from results in Figures 3.1(a) and 3.1(b)), while Pe_{c2} decreases with the length of the chain (observed in Figure 3.2). A simple estimate can be provided for Wi_{c2} by using the dependence of R_{gx} in Regime 1 and noting that $R_{gx} \approx 0.2L$ at the onset of Regime 2 (Figure 3.2):

$$\sqrt{\frac{(0.2N)^2}{R_{gx0}^{\ 2}} - 1} \sim Wi_{c2}$$

As $R_{gx0} \sim N^{1/2}$, we get approximately $Wi_{c2} \sim N^{1/2}$, or $Pe_{c2} \sim Wi_{c2}/N^2 \sim N^{-3/2}$. The observed variation of Wi_{c2} is somewhat greater than $N^{1/2}$, presumably because near the transition from Regime 1 to Regime 2 the scaling of R_{gx} with Wi is given by:

$$\sqrt{\frac{R_{gx}^{\ 2}}{R_{gx0}^{\ 2}} - 1} \sim Wi^{0.83}$$

Using similar arguments as before, this yields $Wi_{c2} \sim N^{0.6}$ and hence $Pe_{c2} \sim N^{-1.4}$. The estimated values of Wi_{c2} shown in the inset of Fig. 3.1(a) approximately scales as $Wi_{c2} = 11.49N^{0.58}$, validating the above proposed dependence of R_{gx} on Wi. The values of Wi_{c1} shown in the inset of Fig. 3.1(b) are approximately given by:

$$Wi_{c1} = 0.34N^{0.53}$$

In the light of the arguments presented earlier for Wi_{c2}, this variation in Wi_{c1} with an exponent of about 0.5 suggests that Regime 1 ends when R_{gx} becomes some fraction of the contour length of the chain. In fact, a careful inspection of our data reveals that Regime 1 ends when R_{gx} is approximately 5% of the contour length, i.e. $R_{gx} \approx 0.05L$ at the onset of the transition to Regime 2.

Note that in Fig. 3.2, there is a fourth "regime" at very high shear rates beyond Regime 3, where for chains with $N \leq 100$, R_{gx} begins to increase again at a Peclet number that

depends on N. This occurs because the polymer chain exhibits a tendency to get "locked in" to a fully stretched state for prolonged periods of time, as evident from the stretch-time plots presented in Figure 3.3. The duration of the 'locked-in' state also increases with shear rate – hence yielding an increasing R_{gx} with increasing shear rate. Figure 3.4 shows the variation of the mean $R_{end\text{-}end}$ with Peclet number for a chain of 60 rods at high shear rates in Regime 4 with two different timestep sizes differing by an order of magnitude, which indicates that similar results are obtained even with a reduced timestep size. For larger chains with 300 and 500 rods, locking is not observed even at Pe = 10^8 and R_{gx}/L appears to reach a constant value at the end of Regime 3. This implies that for long polymer chains R_{gx}/L may reach a plateau value instead of showing an increase. We do not explore this "ultra-high" shear rate regime, and the "locking" behavior in more detail, since these shear rates are so high that chain scission would likely result well before this regime is attained. The conditions under which chain scission might be attained, and the relevance of our simulations to experimental work, are discussed in Chapter VI.

Figure 3.5(a) shows the variations in the y-component of the radius of gyration (R_{gy}) with Peclet number for different chain lengths. Figure 3.5(b) shows the variation of R_{gy} with Wi, instead of Pe, at low shear rates. As noted earlier, the results indicate the end of Regime 1 to be at a $Wi_{c1} \sim N^{1/2}$. We observe that the scaling behavior of R_{gy} with shear rate varies among the aforementioned regimes, as follows:

Regime 1: $R_{gy} = R_{gy0}$

Regime 2: $R_{gy} \sim Pe^{-0.25}$

Regime 3: $R_{gy} \sim Pe^{-0.03}$

In the weak flows of Regime 1, the chain deforms solely in the shear direction and the chain dimensions in the other directions remain unperturbed from the equilibrium value. (As discussed later, R_{gz} is also constant in Regime 1). In Regime 2, R_{gy} decreases as $Pe^{-0.25}$ until the inception of Regime 3 where the variation with Pe is extremely weak ($R_{gy} \approx Pe^{-0.03}$). The decrease of R_{gy} in Regime 2 with an exponent of -0.25 was also reported in ref. [11] for bead-rod chains with $N = 50$ rods per chain. Here we note that the exponent of the power law decay shows a weak dependence on the length of the chain; an exponent of -0.2 is obtained for N = 10 while the exponent approaches -0.25 for $N \geq 60$. Interestingly, our results show that, for the larger chain sizes, the values of R_{gy} becomes independent of N in Regimes 2 and 3. This deviates from the predictions of a "Graetz-Lèvêque" analysis developed in the earlier study by Hur *et al.* [11], which predicts that R_{gy} depends on the number of rods N as $N^{3/4}$. However, the Graetz-Lèvêque analysis correctly predicts the dependence of R_{gy} on shear rate, as shown in ref. [11], which considered only a single value of N. The Graetz-Lèvêque analysis is based on a competition between lateral diffusion of chain segments in the shear-gradient direction and convection of those segments along the flow direction. The analysis assumes that the time required to convect the segments a distance of the extended chain is comparable to the time needed to diffuse those segments a distance of R_{gy}. Since the time for convection over a distance of the chain length depends on N, the Graetz-Lèvêque analysis yields a

scaling law in which R_{gy} depends on N. Some corrections to this model, leading to a better understanding of the chain dimensions in the gradient direction, will be discussed in Chapter IV. The main focus of this chapter is to understand and contrast the flow-induced stretching behavior of polymer chains in Regimes 2 and 3, for which we probe the dynamics of a single rod. Figure 3.5(a) shows that for a single rod, R_{gy} decreases approximately as $Pe^{-0.18}$. To the best of our knowledge, the origin of this scaling law has not been described elsewhere and hence an explanation for the same is provided in Sec. 3B.

A similar behavior is obtained for the chain size in the vorticity direction (given by R_{gz}) (shown in Figure 3.6):

Regime 1: $R_{gz} = R_{gz0}$

Regime 2: $R_{gz} \sim Pe^{-0.28}$

Regime 3: $R_{gz} \sim Pe^{0}$

The dependence of R_{gz} on Peclet number is very similar to that of R_{gy}. However, the exponent for the power law decay in Regime 2 shows some dependence on the number of rods in the chain and reaches an asymptotic value of about -0.28 for N ≥ 300. An exponent of -0.197 was reported in ref. [11] for a chain of 50 rods, which is fairly close to the exponent of -0.22 obtained in our simulations for a chain of 60 rods. To the best of our knowledge, this dependence of the exponent on the contour length of the chain (for relatively shorter chains) has not been reported earlier.

Although Regimes 1 and 2 have been observed in earlier studies, a detailed investigation of the behavior of bead-rod chains in Regime 3 has not been performed. Hence, we attempt to understand the key differences between Regimes 2 and 3 and the reason for the surprising decrease in R_{gx} in Regime 3. Figure 3.7 depicts typical sequences of chain configurations in Regimes 2 and 3 for a 100-rod chain, and shows that the chain configuration is almost one-dimensional along the direction of shear flow. Since a shear flow can be represented as a combination of an extensional flow and a pure rotational flow of equal magnitude, the overall dynamics at any shear rate consists of a sequence of coiling and stretching events, which has been confirmed by earlier studies [3, 11]. However, the snapshots in Fig. 3.7 highlight some significant differences between the configurations of the chain in Regimes 2 and 3 during the coiling and stretching phases. The polymer chain configurations at shear rates in Regime 3 ($\dot{\gamma} = 10^4$ and 10^6) contain several 'back-folded' segments even in the most stretched state, just prior to tumbling and recoiling, while such back-folds are rare in the most stretched state at lower shear rates in Regime 2 ($\dot{\gamma} = 10$, Figure 3.7(a)). In Regime 3, the chain enters the recoiling phase before all of these back-folds disappear, while in Regime 2, nearly all the back-folds periodically disappear, leading to a nearly fully stretched chain, before the chain begins to recoil. From our snapshots, it is evident that these back-folds are comprised of beads in close proximity to each other. Since the presence of these back-folds are integral to the occurrence of Regime 3, it might be expected that excluded volume interactions would counter the formation of these back-folds and hence weaken the decrease of R_{gx} in Regime 3. Evidence of this is observed in the results of Sendner and Netz [13] for a chain

of 100 rods, which also show that the decrease in stretch is enhanced by the presence of hydrodynamic interactions.

Since in Regime 2, where there are usually no back-folds when the recoiling phase begins, the average chain end-to-end distance $R_{end\text{-}end}$ is approximately an average of that of a fully stretched chain, L, and a coiled (≈ 0) chain, which is about $L/2$. Thus, in this regime $R_{gx} \approx R_{end\text{-}end}/2 \approx L/4$. However, in Regime 3, since the maximum $R_{end\text{-}end}<L$, the time-average of the end-to-end distance is less than that in Regime 2, and decreases with increasing shear rate. The process of chain stretching and recoiling is more clearly illustrated in the temporal variation of the end-to-end distance ($R_{end\text{-}end}$), presented in Figure 3.8. This plot shows that the maximum extension reached by the chain decreases with increasing shear rate in Regime 3. The corresponding probability distributions of $R_{end\text{-}end}$ at various shear rates in Regimes 2 and 3 are shown in Figure 3.9. This further demonstrates that while the probability distributions are similar for different shear rates in Regime 2, an increase in shear rate in Regime 3 reduces the probability of highly stretched states.

Further insights into the occurrence of Regime 3 are obtained by noting the characteristics of the onset point of this Regime. Figure 3.10 shows the variation of the average chain extent in the gradient direction with shear rate, spanning Regimes 2 and 3. Unlike R_{gy}, which represents a characteristic chain dimension in the gradient direction that is computed using the y position of all the beads, the chain extent along the y-axis (or y-extent) is defined as the maximum distance, along the y-axis, between any pair of beads on the chain. For both chains of 100 and 300 rods, the scaling law for the variation of the

time-averaged y-extent shows no dependence on Peclet number when its value is about one Kuhn length (or one rod). For lower shear rates, when the y-extent is larger than one Kuhn length, it follows a similar power law that is observed for R_{gy} in Regime 2, which has an exponent of -0.25. Since one rod is the smallest length scale in the bead-rod chain, it is perhaps not too surprising that this behavior changes after it reaches an average value equal to the length of one rod, hence starting a new Regime with different scaling laws and an almost one-dimensional chain.

B. Dynamics of a single rod and its implications for chain dynamics

For pure convection (no rotary diffusion), an isolated rod rotates in a simple shear flow according to

$$\dot{\theta} = -\dot{\gamma}\sin^2\theta \approx -\dot{\gamma}\theta^2 \text{ for small } \theta \qquad (24)$$

where θ is the angle with respect to the flow direction. According to Eq. (24), the rod rotates rapidly for large θ, and slows down as θ approaches zero. At high Pe, where rotary diffusion is relatively weak, but not entirely absent, the rod rotation is dominated by convection. The rod rotates rapidly for large θ, but when it slows down as θ approaches zero, Brownian motion can compete with convection. For small θ, Brownian motion causes the angle to fluctuate, and for a large enough fluctuation, the angle can pass through zero, and then convection can take over, driving the rod to tumble or "flip"

rapidly almost 180°, and the process repeats. The angle θ_c at which the diffusion can compete with convection can be obtained by equating the convective flux of probability, $\dot{\gamma}\theta^2$, with the diffusive flux, D_r/θ, which gives:

$$Pe \equiv \dot{\gamma}/D_r \sim \theta_c^{-3} \text{ or } \theta_c \sim Pe^{-1/3} \tag{25}$$

Now, $R_{gy} \sim \langle\theta^2\rangle^{1/2}$ for small θ. We can calculate $\langle\theta^2\rangle$ by averaging over the time T required to execute a tumble. The time T is obtained by integrating Eq. (24) from an angle of $\pi/2$ to θ_c, yielding $T \sim 1/(\dot{\gamma}\theta_c)$. Thus, we obtain

$$\langle\theta^2\rangle \sim \frac{1}{T}\int_0^T \theta^2\, dt = \frac{1}{T}\int_{\pi/2}^{\theta_c} \theta^2 \frac{dt}{d\theta} d\theta = \frac{1}{T}\int_{\theta_c}^{\pi/2} \theta^2 \frac{1}{\dot{\gamma}\theta^2} d\theta \approx \frac{1}{T\dot{\gamma}} \approx \theta_c ,$$

and $R_{gy} \sim \langle\theta^2\rangle^{1/2} \sim \theta_c^{1/2} \sim Pe^{-1/6}$, as observed in Fig. 3.5(a).

The power law $R_{gy} \sim Pe^{-1/6}$ could be reduced to $R_{gy} \sim Pe^{-1/3}$ if the rods are able to rotate towards the flow direction, but unable to tumble, for example, because they are part of a stretched chain that is under tension that blocks tumbling. In that case, the chains would spend all their time fluctuating around the angle θ_c and we would have $\langle\theta^2\rangle \sim \theta_c^{\,2}$. This would give $R_{gy} \sim \langle\theta^2\rangle^{1/2} \sim \theta_c \sim Pe^{-1/3}$. At high shear rates of Regime 2, when the chain is stretched by shear flow, it is reasonable to expect the tumbling of the rods to be suppressed, but not completely blocked, due to the tension in the chain. The evidence that

this, in fact, happens in the case for a rod that is a part of a chain, is shown in Figure 3.11(a) that compares the distribution functions for θ for a free rod and a single rod in a chain of 100 rods in Regime 2. It is to be noted here that the slight asymmetry in the probability distributions about $\theta = 0$ is due to the direction of the shear flow that points towards the positive x-direction – it tends to rotate the rods that are oriented at an angle $\theta > 0$ towards $\theta = 0$ and those with $\theta < 0$ away from $\theta = 0$ (and hence tends to decrease θ further). It is clearly observed that the rod in a chain spends much more time in a small region of θ-space about $\theta = 0$ than a free rod, indicating that tumbling is suppressed compared to a free rod in Regime 2. These results for a single rod also hint at a reason for the transition to Regime 3 that occurs at high *Pe*. Note from Fig. 3.5(a), that R_{gy} for chains decreases with a power law of -0.25 in Regime 2 that puts it on a "collision course" with the value of R_{gy} for a single rod, which decreases with a weaker power law of -1/6. As the rods in a chain become nearly as aligned as they would be if isolated from each other, then perhaps further alignment becomes limited by "flips" of single rods through the flow direction, followed by convection-driven tumbling through almost 180°, which creates a period of rod miss-alignment. Thus, in Regime 2, the tension in the chain inhibits tumbling of individual rods, while in Regime 3, the flow is so strong that chain tension is no longer able to inhibit this tumbling. This transition is possible, because the driving force for tumbling for a fixed orientation angle scales as shear rate, while the chain tension scales as shear rate times the average angle of miss-alignment of the chain with respect to the flow direction. (A perfectly aligned chain has no tension, even for arbitrarily high shear rate). Thus, the chain tension eventually cannot compete with

convective tumbling events, which ultimately disrupt chain alignment, leading to a transition to Regime 3. The probability distribution functions for θ for a free rod and a single rod in a chain of 100 rods in Regime 3 are shown in Figure 3.11(b). This plot clearly suggests that while the free rod continues to get more aligned with increasing shear rates, the extent of further alignment is quite limited for the individual rods in a chain of 100 rods.

C. Dynamics of chain tumbling and its consequences on the stretch in Regime 3

As described earlier, Regime 3 arises due to the initiation of chain tumbling before a fully extended state is attained. Since the average y-extent in Regime 3 is approximately the length of 1 rod, it is perfectly reasonable to assume that the flipping of individual rods is the primary mechanism of tumbling in Regime 3. Hence, it is expected that further insights will be obtained by comparing the dynamics of the two processes involved – chain tumbling and rod flipping. Using the results from the previous section, it can be shown that the time required by one rod to flip is $t_{flip} \approx 2/(\dot{\gamma}\theta_c)$. It is to be noted here that this equation was derived for a single rod. However, at higher shear rates, the distribution of angles of individual rods in a chain follow the same scaling law as for an isolated rod. Figure 3.12 shows the log-log plot of the probability distribution of orientation angles for individual rods in a chain of 100 rods when Pe = 30, and the variation in the critical angle θ_c with Peclet number. Two distinct regimes are observed in Figure 3.12(a). The region near $\theta = 0$ is diffusion-controlled and has a relatively "uniform" distribution implying

equal probabilities for all θ, while at larger θ values convection is dominant and the slope is about -2 in accordance with Eq. (24). The approximate angle where convection-effects start to become weaker and diffusion-control sets in, as we approach $\theta = 0$ from higher values of θ, is taken as the critical angle θ_c. Fig. 3.12(b) shows that the critical angle $\theta_c \sim Pe^{-1/3}$ consistent with the scaling theory presented earlier (viz. Eq. (25)).

One way to investigate the tumbling dynamics of the polymer chain in shear flow is through the power spectral density (PSD) [3]. The peak in the PSD curve for a particular shear rate gives a measure of the rate of tumbling of the chain, or, in our case, the frequency of tumbling. It is to be noted here that the peak is not well characterized and can only be determined approximately. The PSD is computed at various shear rates for a polymer chain and the inverse of the frequency at which the maxima occurs gives the characteristic tumbling time t_{tumble}. For high shear rates encompassing Regimes 2 and 3, the tumbling times for chains of various lengths are shown in Figure 3.13, which approximately follow the power law:

$$t_{tumble} \sim NPe^{-0.8}$$

It is to be noted here that an exponent of -2/3 is predicted by a theoretical solution in ref. [20] for the tumbling time in Regime 2 (The tumbling dynamics of the chain in Regime 2 will be discussed in details in Chapter IV.). Now, assuming that chain tumbling occurs by flipping of individual rods, at least N/2 rods have to be flipped from either end of the chain for the end-over-end tumbling to be complete. The total flipping time of N/2 rods is calculated using the critical angles presented earlier in Fig. 3.12(b). Figure 3.14 shows a

comparison of the tumbling and flipping times for a chain of 100 rods. For $Pe > 10$, $(N/2)t_{flip} > t_{tumble}$, which supports our hypothesis that chain tumbling restricts the maximum attainable stretch in Regime 3. Following the same logic, the maximum stretch R_{max} is proportional to the number of rods that undergo flipping before the chain completes one end-over-end tumbling:

$$R_{max} \sim \frac{t_{tumble}}{t_{flip}} \sim \frac{NPe^{-0.8}}{Pe^{-0.66}} = NPe^{-0.14}$$

The above scaling compares well with the scaling for R_{gx} in Regime 3. However, it is important to note here that the scaling law for the chain tumbling time (in Regime 3) is obtained from our simulations, and it seems unlikely that a simple scaling model can be formulated that will simultaneously determine the tumbling time as well as the average stretch in Regime 3.

D. Results for the coarse-grained models

We also performed simulations using coarse-grained polymer chains with springs modeled by the Cohen Padé approximation and the Underhill-Doyle spring law [17]. As discussed in Sec. 2A, these coarse-grained springs can be used to represent a polymer chain at various levels of coarse graining with $\nu \geq 6$. Our objective is to ascertain the accuracy of these coarse-graining approaches for predicting the stretching behavior of a polymer chain in shear flows of widely ranging magnitudes. As a basis for comparing results of the coarse-grained simulations with the fine-grained ones using the bead-rod model, we define the Weissenberg number for the coarse-grained chain using Eq. (18). It

is to be noted here that for any value of ν, the number of coarse-grained springs in the chain (N_s) is given by $N = N_s\nu$, where N represents the total number of rods that is represented by the whole coarse-grained chain.

Figure 3.15(a) compares simulations of coarse-grained chains using the Cohen Padé approximation with different levels of coarse-graining (i.e., different values of ν) with those of a relatively finer bead-rod polymer chain. The finer bead-rod chain contains 500 rods and all the coarse-grained chains contain $N = N_s\nu = 500$ rods. Fig. 3.15(a) shows that the mean stretch predicted by the coarse grained model is in very good agreement with that of the bead-rod chain for shear flows in Regimes 1 and most of Regime 2, but deviates significantly for stronger flows. This can be explained by noting that the deviation occurs at flow rates high enough to perturb individual springs away from equilibrium. Since the spring law is derived by assuming that a sub-section of the chain, represented by a spring, is in equilibrium, this assumption is expected to be incorrect at these high strain rates. Since one spring in the coarse-grained chain represents six or more rods, it is not surprising that coarse-grained chains cannot properly account for the behavior in flows strong enough to excite a portion of the chain smaller than that represented by a single coarse-grained spring. Interestingly, for weaker flows, even a dumbbell (two-bead model) is essentially adequate to represent the stretch of an arbitrarily long bead-rod chain. However, the predictions of the coarse-grained models show systematic deviations from those of the finer bead-rod chain at high shear rates in Regime 2 as the degree of coarse graining is increased (i.e., N_s is decreased below 5), which is probably caused due to a considerable loss in flexibility of the chain for low

values of N_s. Interestingly, as the degree of coarse-graining is decreased, i.e., the number of springs is increased, deviations from the predictions of the bead-rod model also increase, showing an earlier onset of Regime 3 than the models with even higher levels of coarse graining. This is evidently because an increasing number of springs requires that each spring represents fewer rods, and hence less and less adequate representation of the true elastic forces generated by the fewer rods making up that spring. This suggests that each spring should represent a substantial number of rods ($\nu \geq 10$ in this case) to obtain optimal predictions of stretch using this coarse-grained model.

Figure 3.15(b) compares the results of the bead-rod chain with simulations of coarse-grained chains using the Underhill-Doyle model [20] that employs a more sophisticated spring law than the Cohen Padé approximation. The Cohen spring represents the limit of the Underhill-Doyle model at large ν. With adjustments for lower values of ν, the Underhill-Doyle spring force law was designed to model the force-extension behavior of springs that contain a relatively small number of rods ($\nu \geq 6$). The results in Figure 3.15(b) show that for relatively higher degrees of coarse graining ($\nu \geq 10$), this model gives very good predictions for shear flows in Regime 1 and 2, and deviates from the bead-rod results at even higher shear rates which are strong enough to excite a single spring in the chain – a behavior very similar to that obtained with the Cohen Padé approximation. Interestingly, however, like the Cohen Padé approximation, the Underhill-Doyle spring model too predicts an early onset of Regime 3 for small values of ν, that is, for small numbers of rods per spring. Thus, the Underhill-Doyle model does not

seem to provide any advantage over the Cohen Padé approximation for the shear flow phenomena considered here. For a reasonably long bead-rod chain (500 rods in this case), for reasonable degrees of coarse graining with $\nu \geq 10$ and substantial amounts of chain flexibility where $N_s \geq 10$, both the coarse-grained spring laws (Cohen Padé or Underhill-Doyle) be expected to give results for the stretch that are quite consistent to each other. However, as soon as the shear rate becomes high enough that an extremely coarse-grained description fails, only a fully refined bead-rod description can adequately capture the higher shear rate chain dynamics, and the more refined coarse-graining provided by the Underhill-Doyle approach does not seem to provide any advantage over the simplest approach.

Although the stretch behavior of the bead-rod polymer chain is reasonably well represented by the coarse-grained models in most of Regime 2, deviations are observed for the results of R_{gy} in Regime 2. Figure 3.16(a) and (b) show the comparison of the values of R_{gy} calculated using the bead-rod model for a chain of 500 rods and those obtained using springs following the Cohen Padé approximation and the Underhill-Doyle model respectively. Note that the results for the coarse-grained models using more than one spring are shown, since it is observed from Figures 3.15(a) and (b) that the predictions of R_{gx} in Regime 2 for a dumbbell model does not agree well with those obtained using the bead-rod model. The predictions for R_{gy} of both the coarse-grained models, for all degrees of coarse-graining considered, show a slightly steeper decrease with a power law exponent close to -0.33, in contrast to an exponent of -0.25 observed for the decrease of R_{gy} in Regime 2 for the bead-rod model. This difference further

highlights the inadequacies in the coarse-grained models to accurately predict chain dynamics at high shear rates, and further shows that the Underhill-Doyle model does not provide any significant advantage over the Cohen Padé approximation. As we will further note in Chapter IV, this difference in the variation of the coil thickness also leads to an incorrect prediction of the tumbling dynamics of the chain.

4. Summary

In this Chapter, we investigated the non-monotonic stretch behavior and dynamics of polymer chains of varying contour lengths in shear flow with widely varying shear rates. The polymer chain is modeled using stiff Fraenkel springs that mimic inextensible rods, with each spring representing a single Kuhn step. We employed Brownian dynamics simulations with a semi-implicit time-stepping scheme where the effects due to excluded volume and hydrodynamic interactions are not considered. For this system, three distinct regimes of behavior were observed from which a universal scaling law for each regime could be identified. We observed that the stretch is linear in the Weissenberg number in Regime 1 ($Wi < Wi_{c1}$), where the flow is too weak to perturb rods away from equilibrium without the assistance of chain tension. The stretch reaches a plateau in Regime 2 ($Pe_{c2} <$ Pe < 10) and then decreases with shear rate in Regime 3 (Pe > 100); at these high shear rates the individual rods in the chain can be rotated by the flow without the assistance of chain tension. A comparison of the temporal behavior and the probability distributions of the chain end-to-end distances in Regimes 2 and 3 shows that in Regime 3 complete

chain unraveling becomes rare and a significant fraction of the rods remain back-folded even when the chain reaches its highest stretch just before a tumbling event causes it to coil up. It is also shown that, after decreasing in Regime 3, the average chain stretch increases once again at very high shear rates beyond Regime 3 owing to the tendency of the chain to get "locked in" to a fully stretched state for prolonged durations. A qualitative explanation for the behavior in Regime 3 is sought by comparing the chain tumbling time and the flipping time for individual rods in a chain, which indicates that in Regime 3 chain tumbling restricts the stretching process, leading to a decrease in maximum attainable stretch with increasing shear rate. In this regard, it is worth mentioning that Regime 3 is quite sensitive to the presence of both excluded volume and hydrodynamic interactions, as noted by Sendner and Netz [13]. Hence, although this work sets the foundations, a comprehensive understanding of Regime 3 would require systematic mapping of the additional effects due to both excluded volume (EV) and hydrodynamic interactions (HI).

Similar simulations were performed using coarse-grained springs that are modeled by the Cohen Padé approximation and by the Underhill and Doyle model [17] to compare the performance of such models with the corresponding bead-rod model, which was chosen to contain 500 rods. The stretch of the coarse-grained chains at varying degrees of resolution agrees remarkably well with that of the bead-rod chain for shear rates in Regimes 1 and most of Regime 2, for cases when each spring represents a moderately large number of Kuhn lengths ($\nu \geq 10$) and the chain possesses a reasonable degree of flexibility ($N_s \geq 10$). As it might be expected, the results of the coarse grained models

deviate from those of the bead-rod model at high shear rates, where the flow is strong enough to perturb the individual springs away from equilibrium.

References

[1] Smith, D. E.; Babcock, H. P.; Chu, S. *Science* **283**, 1724-1727 (1999).

[2] Hur, J. S.; Shaqfeh, E. S. G.; Babcock, H. P.; Smith, D. E.; Chu, S. *J. Rheol*. **45**, 421-450 (2001).

[3] Schroeder, C. M.; Teixeira, R. E.; Shaqfeh, E. S. G.; Chu, S. *Phys. Rev. Lett.* **95**, 018301 (2005).

[4] Link, A.; Springer, J. *Macromolecules* **26**, 464-471 (1993).

[5] Lee, E. C.; Solomon, M. J.; Muller, S. J. *Macromolecules* **30**, 7313-7321 (1997).

[6] Lee, E. C.; Muller, S. J. *Polymer* **40**, 2501-2510 (1999).

[7] Bossart, J.; Öttinger, H. C. *Macromolecules*, **30**, 5527-5540 (1997).

[8] Liu, T. W. *J. Chem. Phys.* **90**, 5826-5842 (1989).

[9] Doyle, P. S.; Shaqfeh, E. S. G.; Gast, A. P. *J. Fluid. Mech.* **334**, 251-291 (1997).

[10] Petera, D.; Muthukumar, M. *J. Chem. Phys.* **111**, 7614-7623 (1999).

[11] Hur, J. S.; Shaqfeh, E. S. G.; Larson, R. G. *J. Rheol* **44**, 713-742 (2000).

[12] Hsieh, C.-C.;Larson, R. G. *J. Rheol.* **48**, 995-1021 (2004).

[13] Sendner, C.; Netz, R. R. *Eur. Phys. J. E* **30**, 75-81 (2009).

[14] Hoda, N.; Larson, R. G. *J. Rheol.* **54**, 1061-1081 (2010).

[15] Bruns, Wolfgang; Carl, Wilfried *Macromolecules* **26**, 557-558 (1993).

[16] Larson, R. G. *J. Rheol.* **49**, 1-70 (2005).

[17] Underhill, P. T.; Doyle, P. S. *J. Rheol.* **49**, 963-987, (2005).

[18] Somasi, Madan; Khomami, Bamim; Woo, Nathaniel J.; Hur, Joe S.; Shaqfeh, Eric S. G. *J. Non-Newtonian Fluid Mech.* **108**, 227-255 (2002).

[19] Carl, W. *Maromol. Theory Simul.* **3**, 705-713 (1994).

[20] Winkler, Roland G. *Phys. Rev. Lett.* **97**, 128301 (2006).

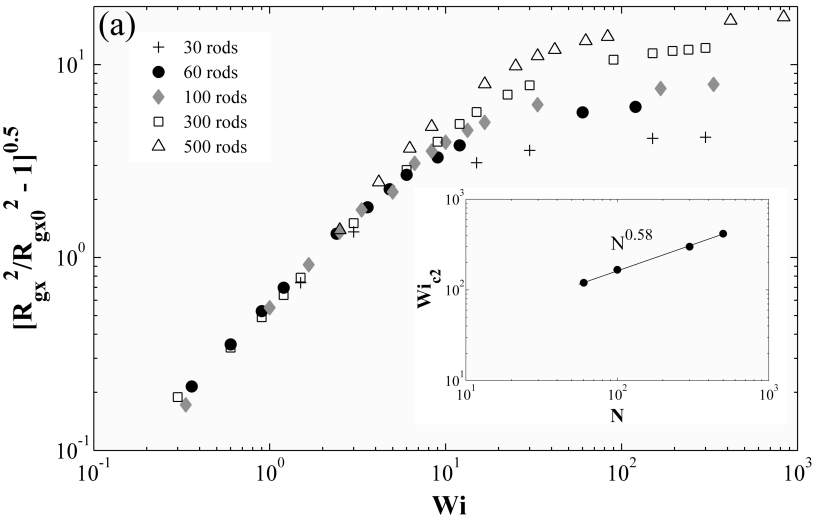
(a)
30 rods
60 rods
100 rods
300 rods
500 rods
$[R_{gx}^2/R_{gx0}^2 - 1]^{0.5}$
Wi
Wi_{c2}
$N^{0.58}$
N

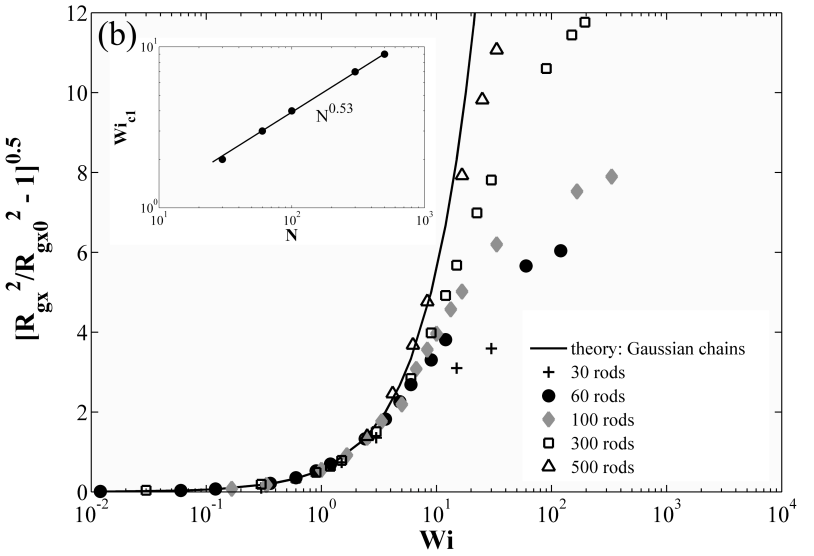
(b)
Wi_{c1}
$N^{0.53}$
N
theory: Gaussian chains
30 rods
60 rods
100 rods
300 rods
500 rods
$[R_{gx}^2/R_{gx0}^2 - 1]^{0.5}$
Wi

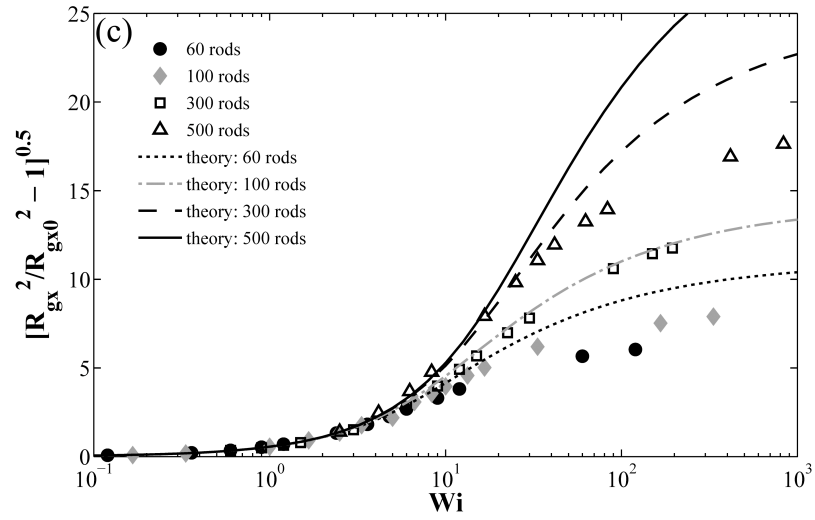
(c)
60 rods
100 rods
300 rods
500 rods
theory: 60 rods
theory: 100 rods
theory: 300 rods
theory: 500 rods
$[R_{gx}^2/R_{gx0}^2 - 1]^{0.5}$
Wi

Figure 3.1: (a) Variation of $\sqrt{\frac{R_{gx}^{\ 2}}{R_{gx0}^{\ 2}}-1}$ with Weissenberg number for bead-rod polymer chains of various lengths for weaker flows. Inset shows the estimated Weissenberg numbers for the onset of Regime 2 for different chains (Wi_{c2}). (b) Comparison of the behavior of $\sqrt{\frac{R_{gx}^{\ 2}}{R_{gx0}^{\ 2}}-1}$ in Regime 1 with the theoretical solution given by Eq. (21). Inset gives the variation of the approximate Weissenberg numbers for the end of Regime 1 (Wi_{c1}) with chain length. (c) Comparison with the theoretical model given by Eq. (23) that incorporates finite extensibility.

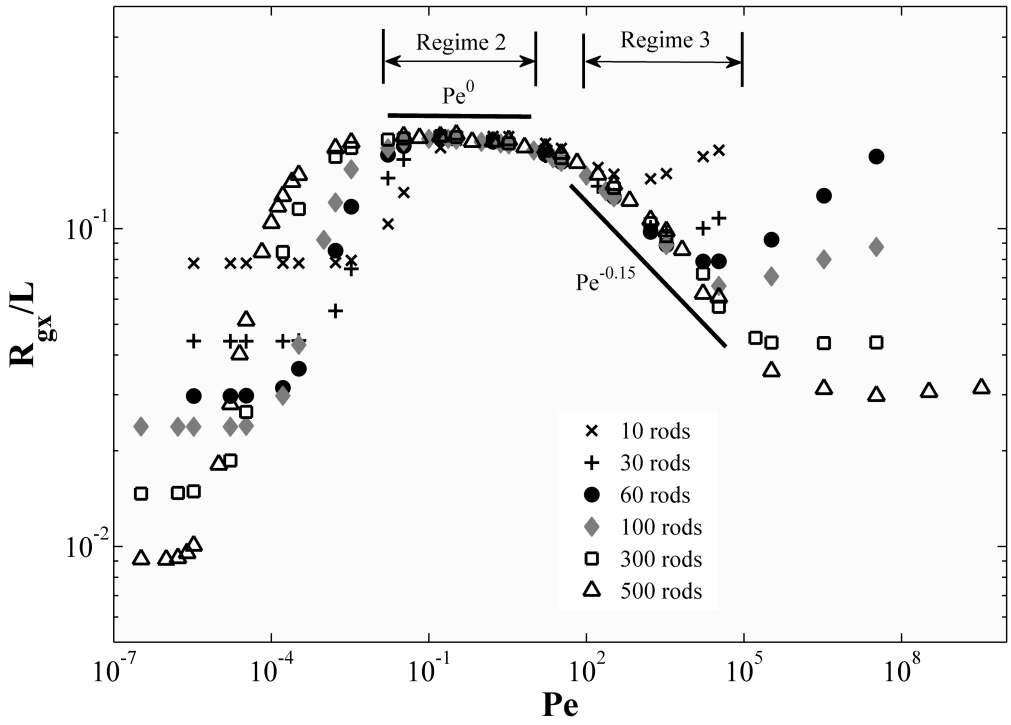

Figure 3.2: Variation of R_{gx} with Peclet number for bead-rod chains of various lengths. Regimes 2 and 3 are indicated by solid black lines with the corresponding scaling exponents of 0 and -0.15, respectively.

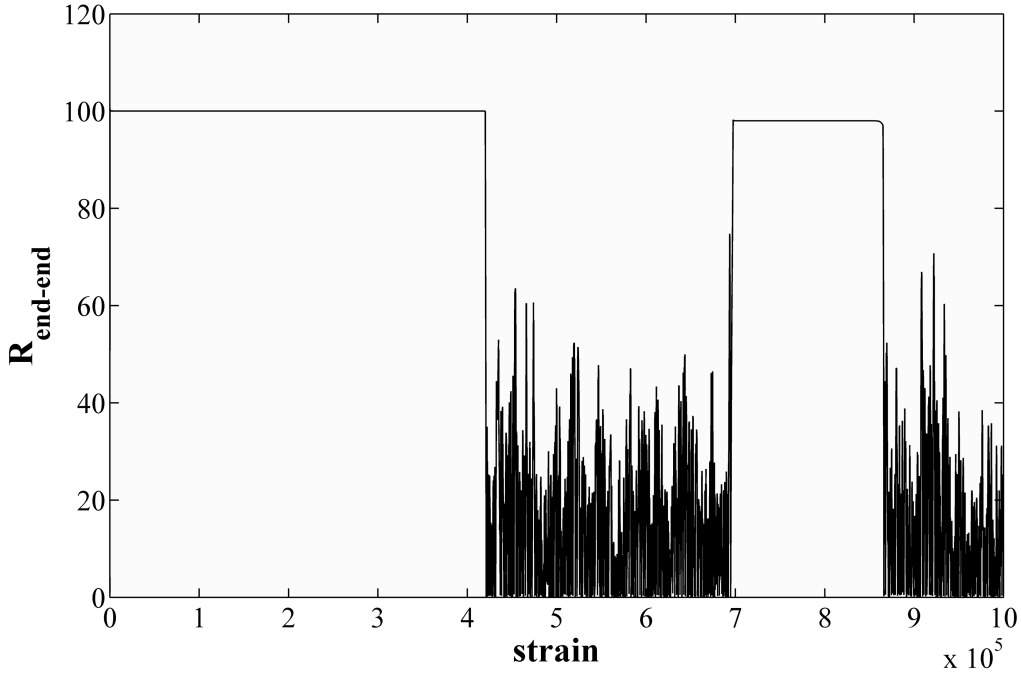

Figure 3.3: Variation of the end-to-end distance of a polymer chain (consisting of 100 rods) with strain (which is time multiplied by strain rate, or $t\dot{\gamma}$) at Pe=3×10^{11}. The plot shows the tendency of the chain to remain in the fully stretched state for a prolonged duration at high shear rates.

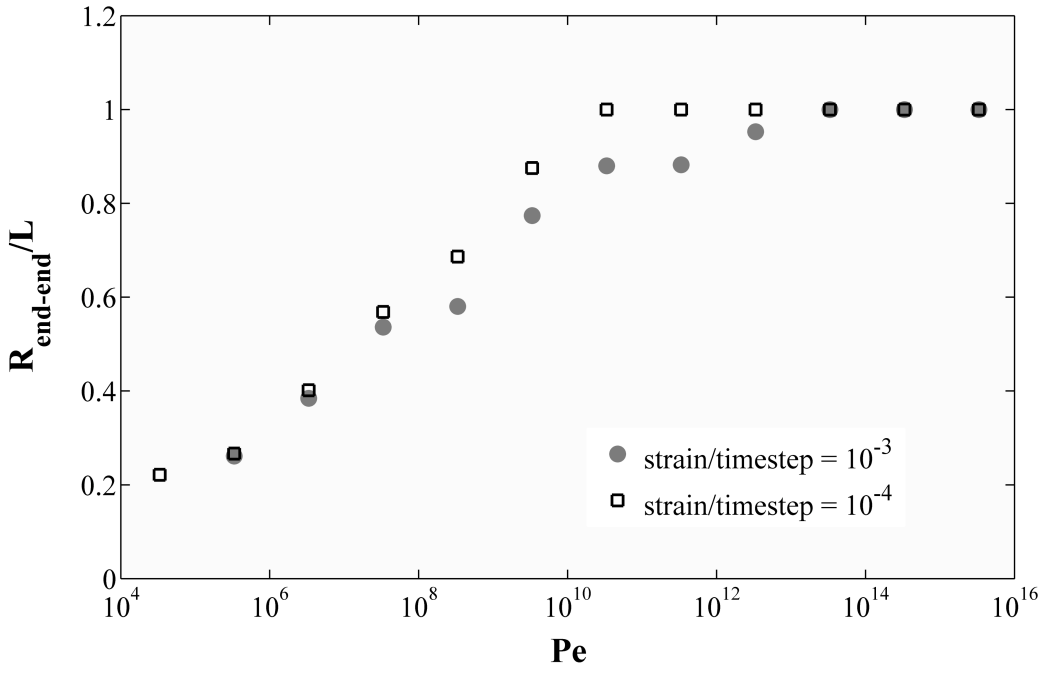

Figure 3.4: Variation of $R_{end\text{-}end}$ with Peclet number for a polymer chain of 60 rods at shear rates in regime 4 with two different time step sizes. The qualitative behavior is independent of the choice of the time step size although there are some quantitative differences.

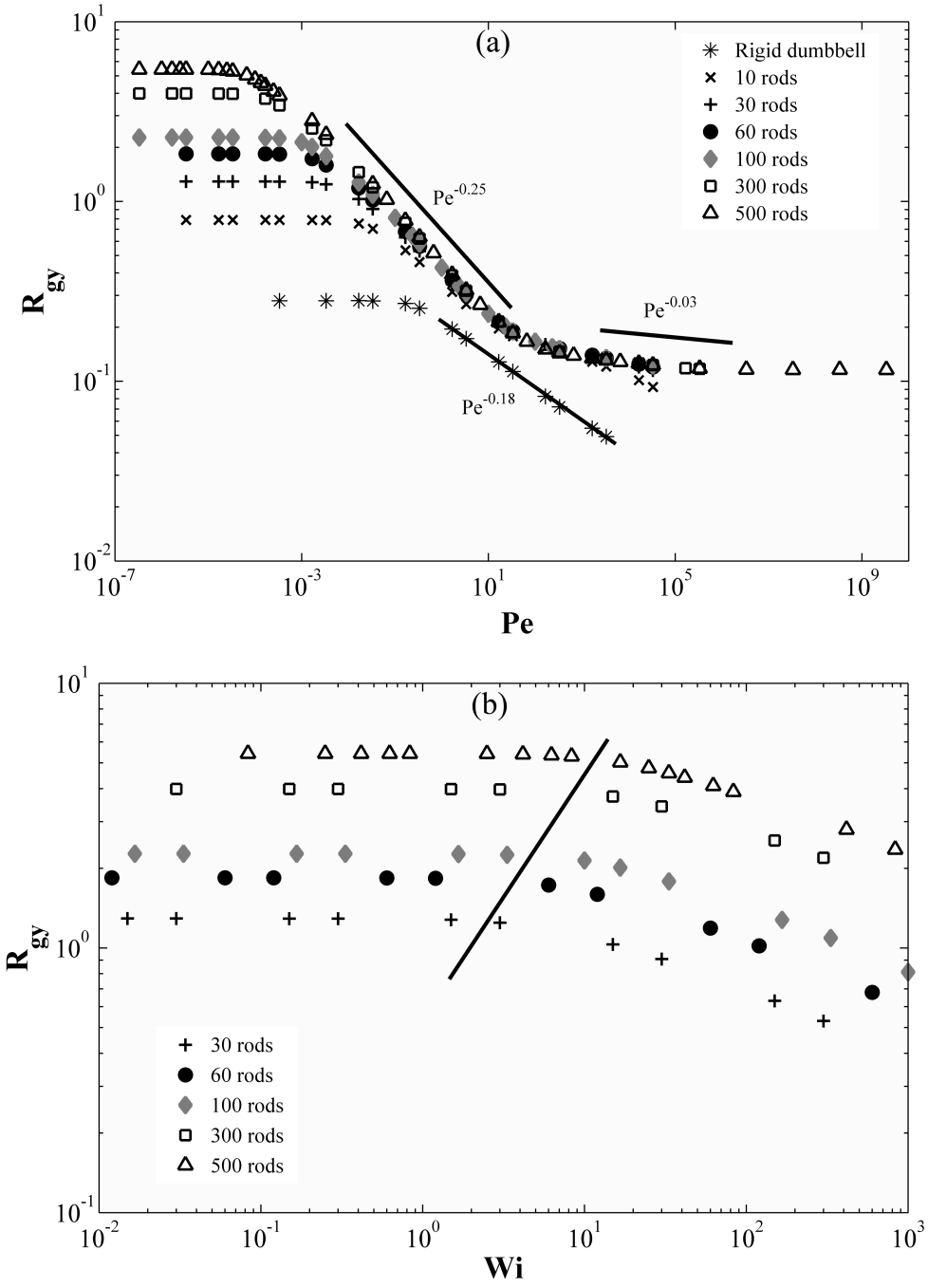

Figure 3.5: (a) Variation of R_{gy} with Peclet number for polymer chains of various lengths. The solid lines indicate Regimes 2 and 3 for bead-rod chains. The scaling law for R_{gy} with Peclet number for a single rod (i.e., a rigid dumbbell) is also shown. (b) Variation of the R_{gy} with Weissenberg number at low shear rates, showing the transition from Regime 1 to Regime 2. The solid line roughly marks the end of Regime 1.

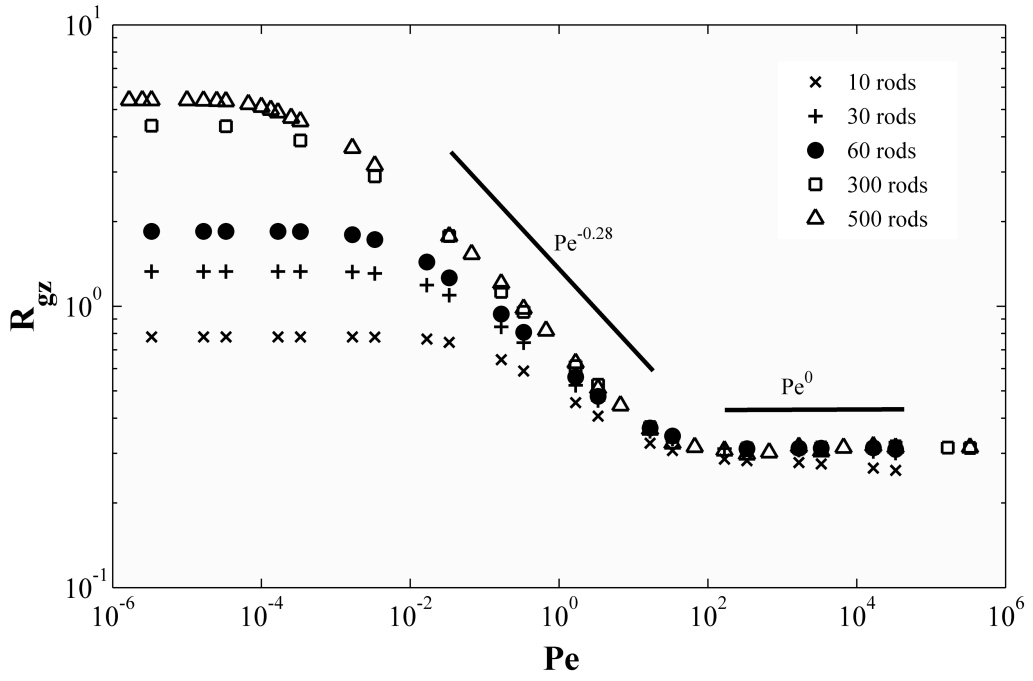

Figure 3.6: Variation of the ensemble average of R_{gz} with Peclet number for polymer chains of various lengths. The solid lines indicate Regimes 2 and 3.

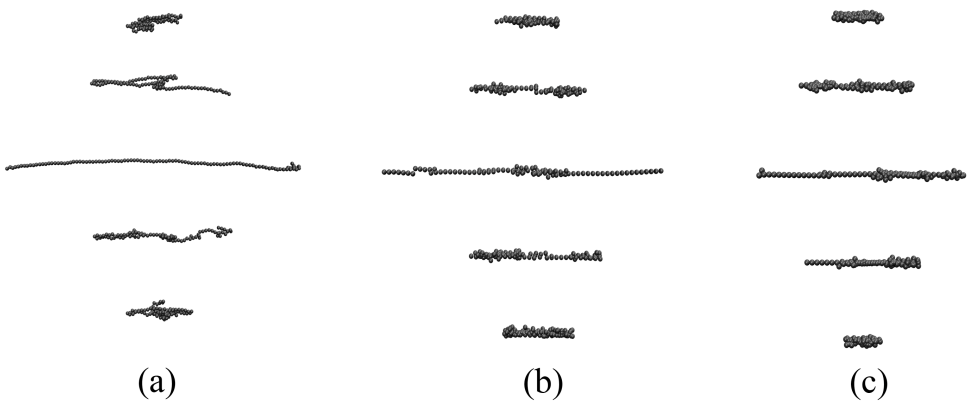

Figure 3.7: Snapshots from simulation trajectories, time ordered from top to bottom, showing representative sequences of events transitioning a flattened coil to a stretched chain and back to a coiled state again, at shear rates of (a) 10, (b) 10^4 and (c) 10^6, corresponding to Peclet numbers of 0.3, 300 and 30000 respectively, the latter two of which are in Regime 3.

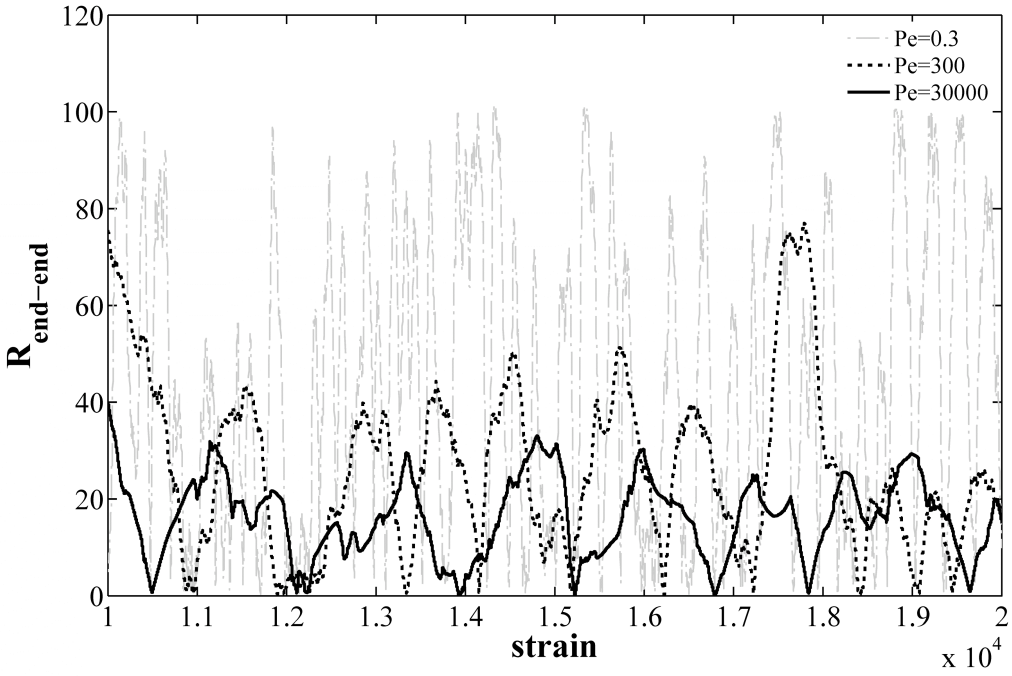

Figure 3.8: Variation of the end-to-end distance of a polymer chain (consisting of 100 rods) with time (time is represented by strain=t$\dot{\gamma}$) at Peclet numbers of 0.3, 300 and 30000, corresponding to shear rates of 10, 10^4 and 10^6 respectively, the latter two of which are in Regime 3.

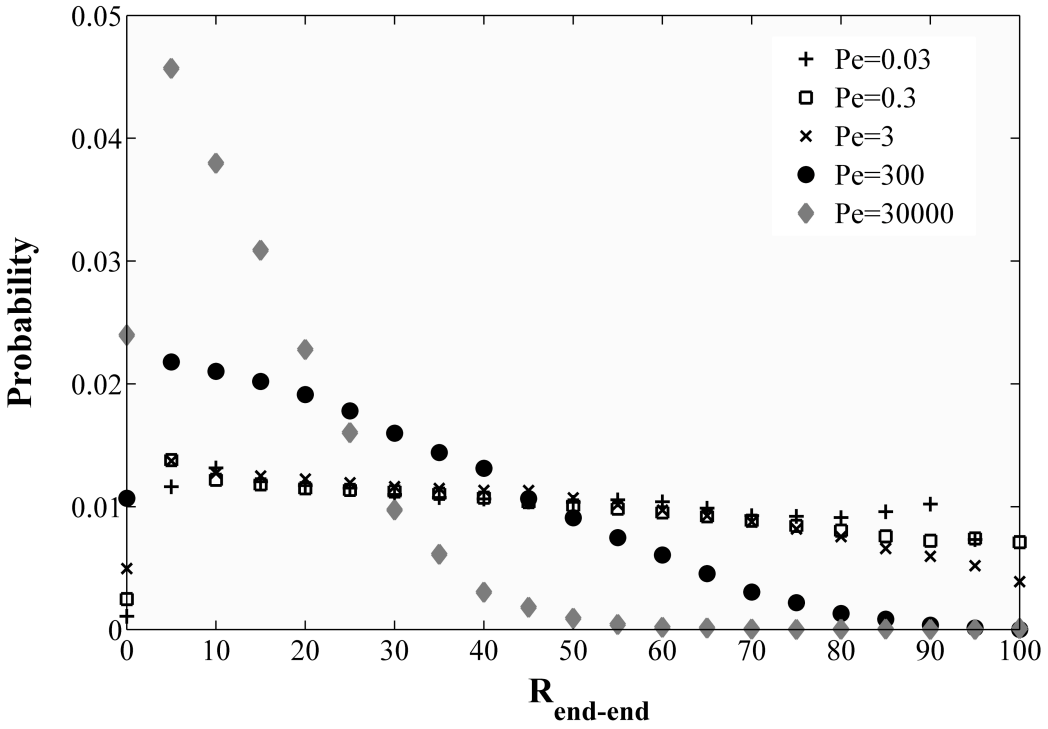

Figure 3.9: Probability distributions of the end-to-end distance of the polymer chain (of 100 rods) at various shear rates in Regimes 2 and 3. Peclet numbers of 0.03 and 0.3 lie in Regime 2 whereas 300 and 30000 lie in Regime 3. A Peclet number of 3, corresponding to a shear rate of 100, lies in the transition region from Regime 2 to Regime 3.

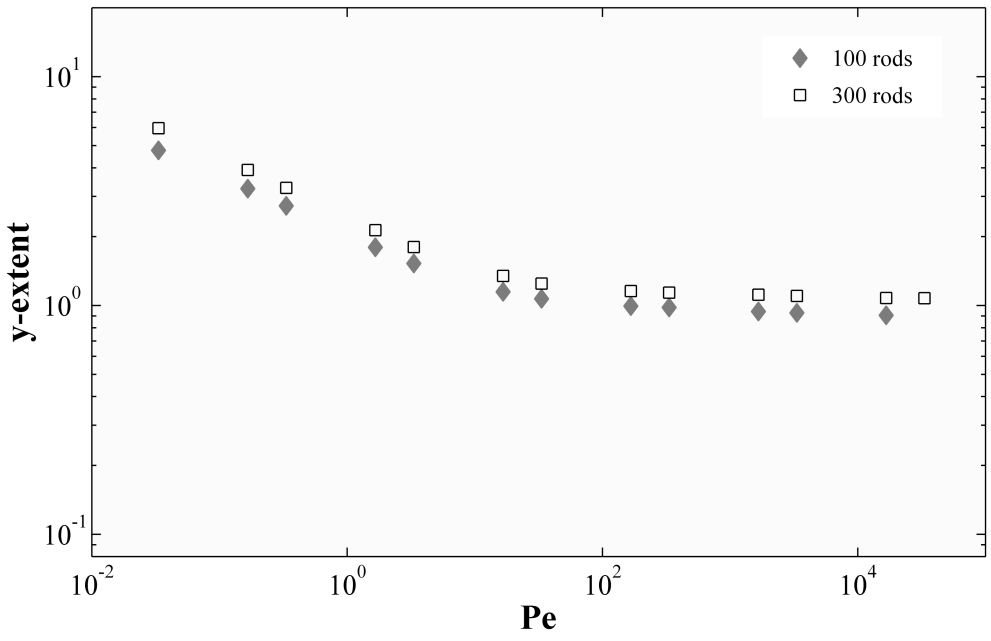

Figure 3.10: Variation of the time-averaged extent of the polymer chain in the gradient direction with Peclet number. The average y-extent shows no dependence on Peclet number in Regime 3, where it is approximately one Kuhn step.

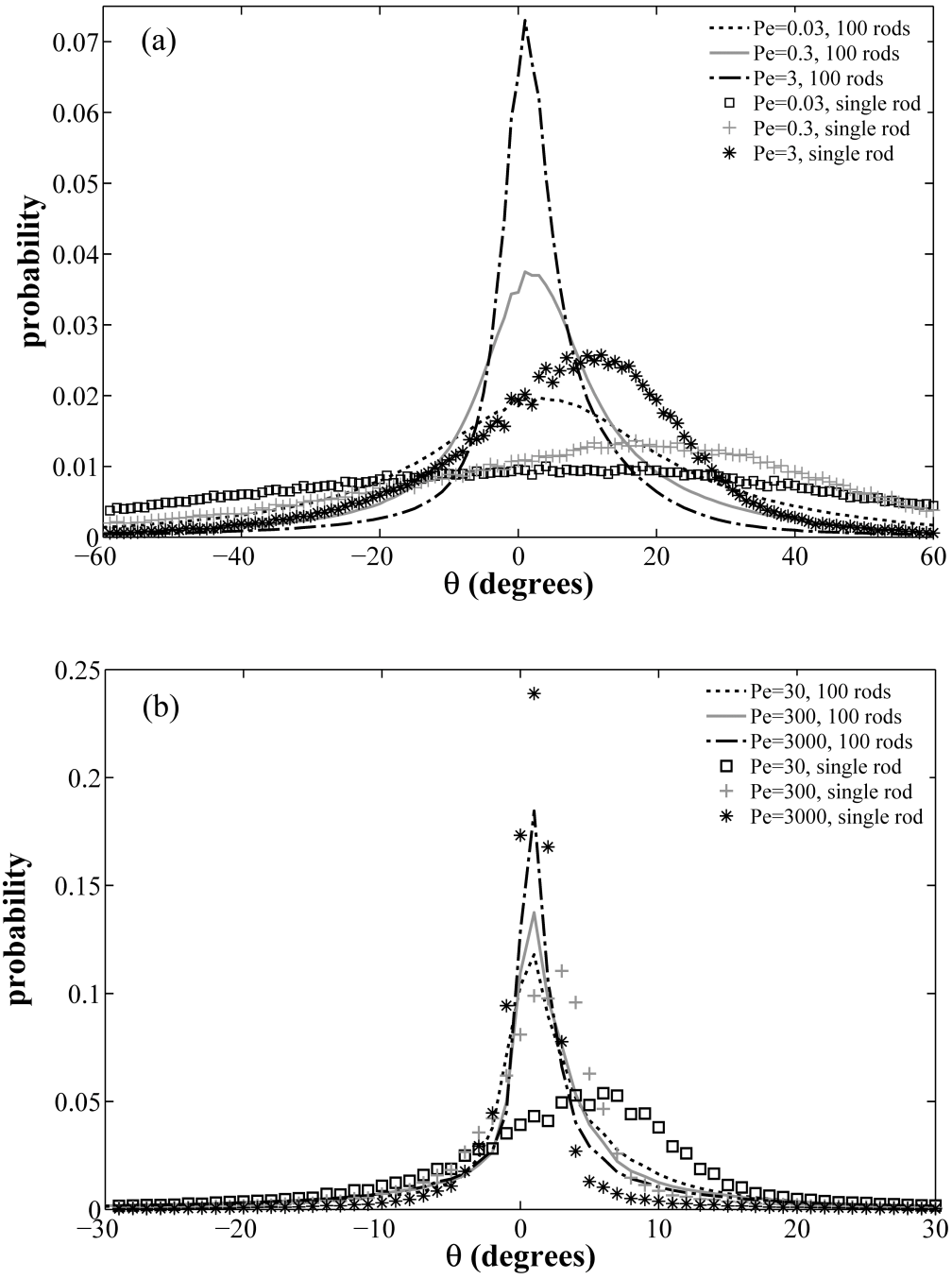

Figure 3.11: Probability distributions of rod orientation angles relative to the shear flow direction for single rods and individual rods in a chain of 100 rods. (a) Regime 2, (b) Regime 3.

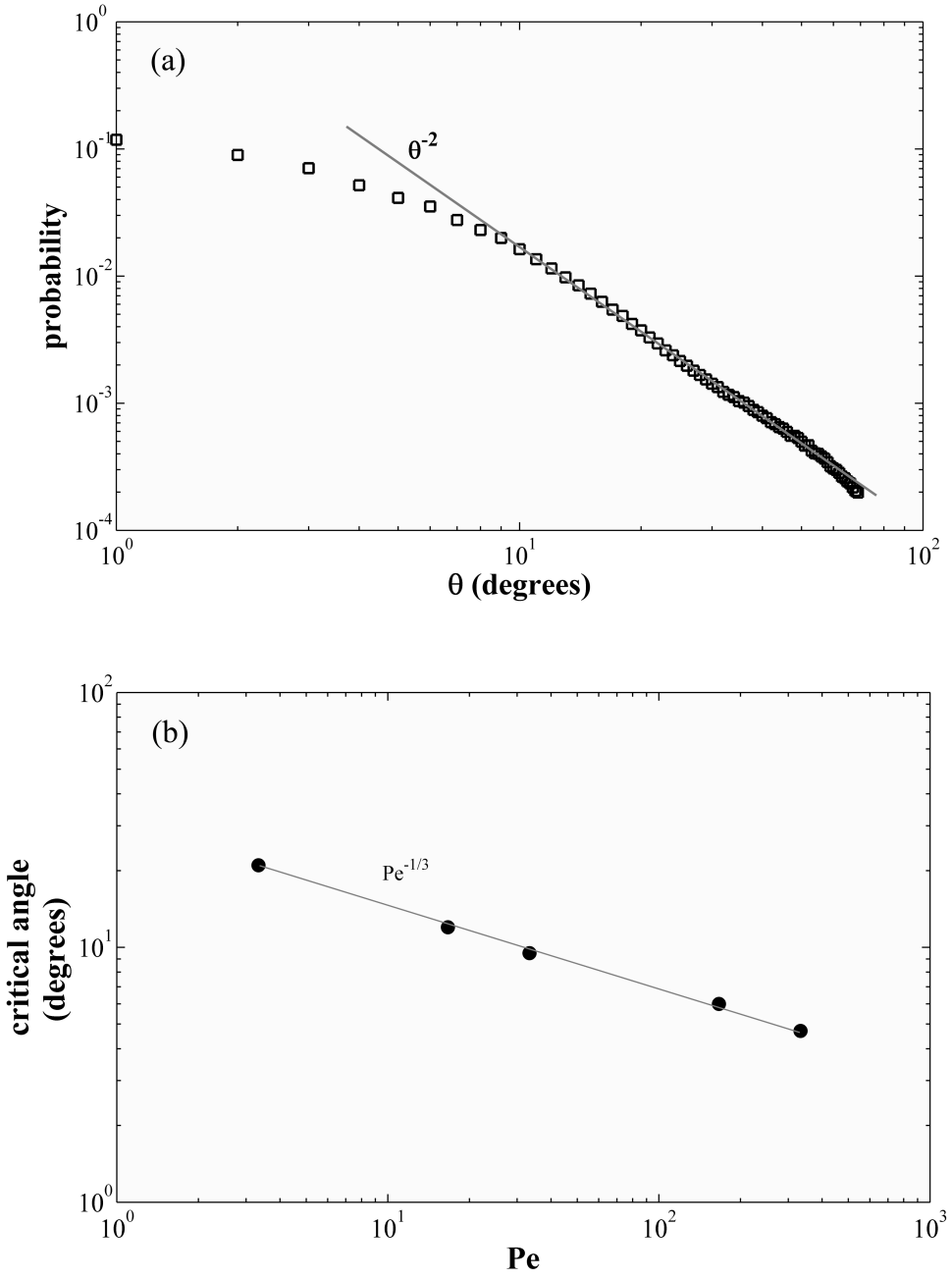

Figure 3.12: Bond angles for an individual rod in a chain of 100 rods. (a) An example log-log plot for the probability distribution of angles at *Pe* = 30, where the solid line shows the convection-controlled regime and has a slope of -2, (b) Variation of the estimated critical angle separating convective and diffusive regimes with Peclet number, which approximately follows a power law with an exponent of -1/3.

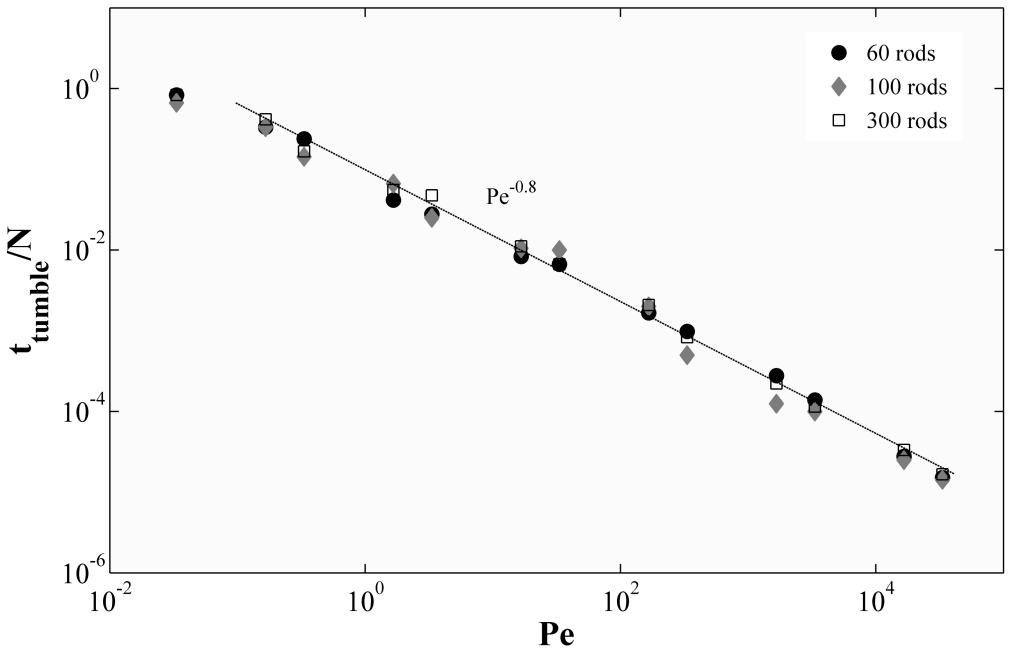

Figure 3.13: Variation of the estimated characteristic chain tumbling time (normalized with number of rods in the chain) with Peclet number for various chain lengths. The solid line indicates that our data approximately follows a power law with an exponent of -0.8.

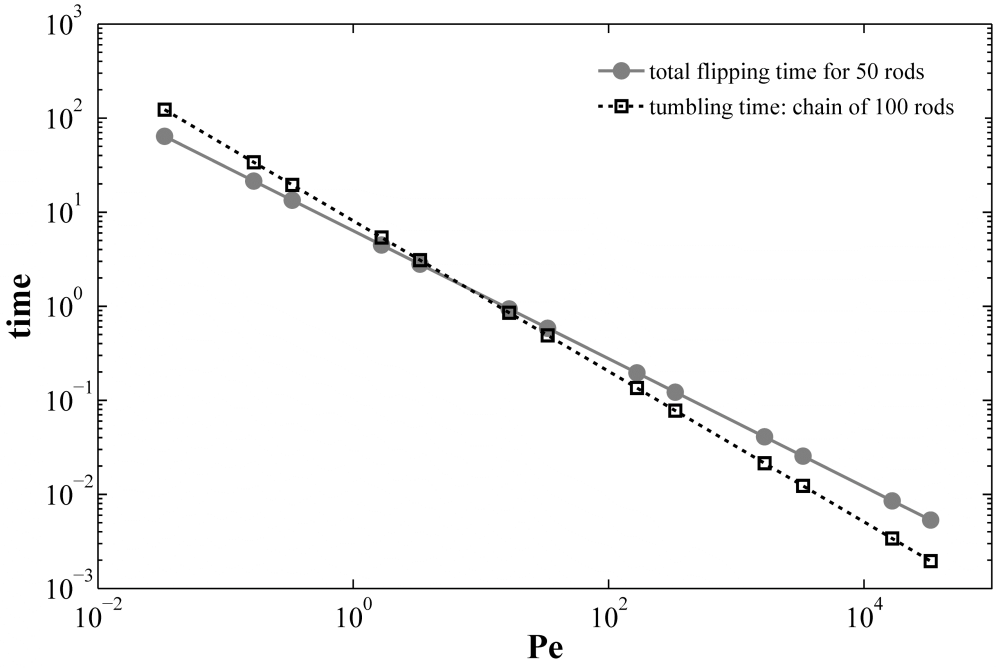

Figure 3.14: Comparison of chain tumbling times t_{tumble} (for a chain of 100 rods) and the total time $50t_{flip}$ taken to flip 50 rods. The chain tumbling times are estimated using a power law that approximately predicts the data presented in Figure 3.13. The rod flipping times are calculated using the estimates of the critical angles that are shown earlier. Note that the cross-over of the tumbling time and total flipping time occurs at roughly the Peclet number at the transition between Regimes 2 and 3. The analysis shows that the chain tumbling might restrict the maximum stretch that is attainable by flipping of individual rods in Regime 3.

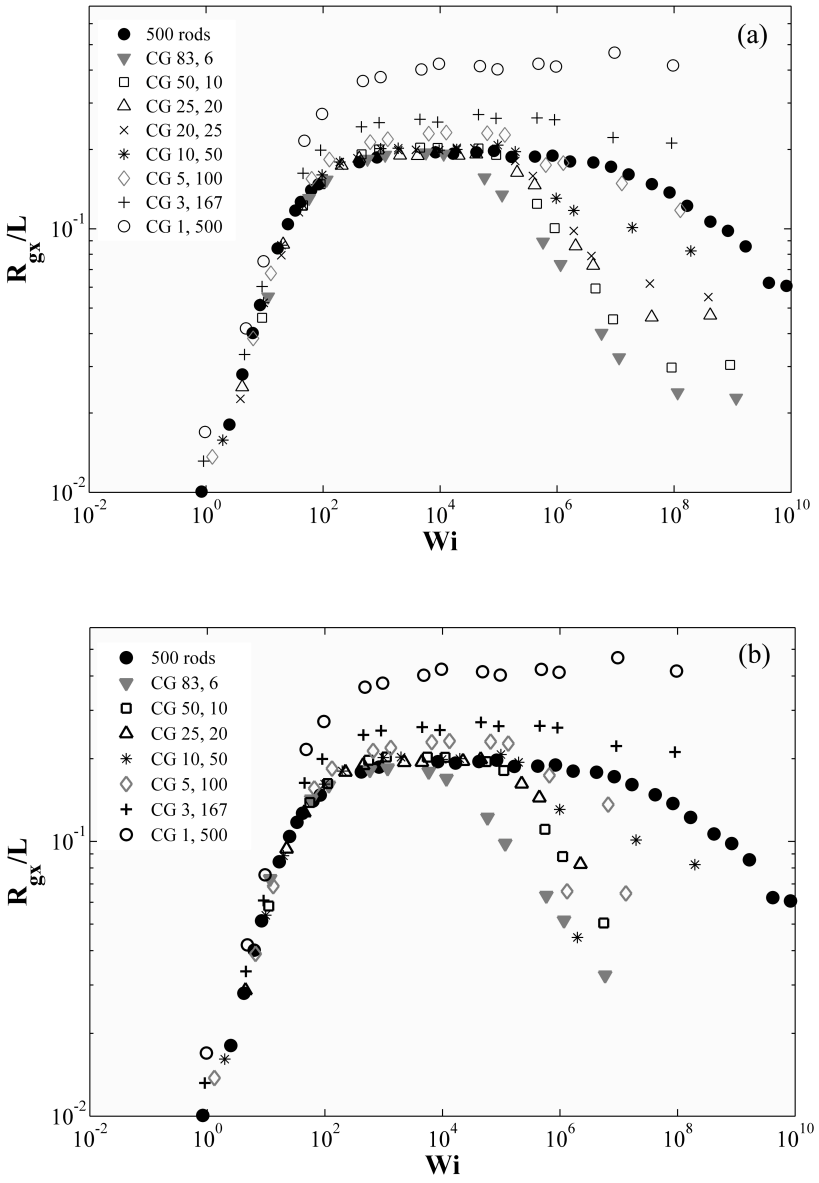

Figure 3.15: (a) Comparison of Weissenberg number dependence of R_{gx} (normalized with the chain contour length) of a bead-rod chain of 500 rods and with chains coarse-grained to varying degrees, using the Cohen Padé approximation as the force law for the springs. The legend for each coarse-grained model has two numbers, the first representing the number of springs and the second one denotes the number of Kuhn lengths in each spring. The product of the two numbers in each case is approximately 500, implying that all the coarse-grained chains represent roughly the same fine-grained one. (b) Same as (a), except that the Underhill-Doyle model is used as the force law for the springs.

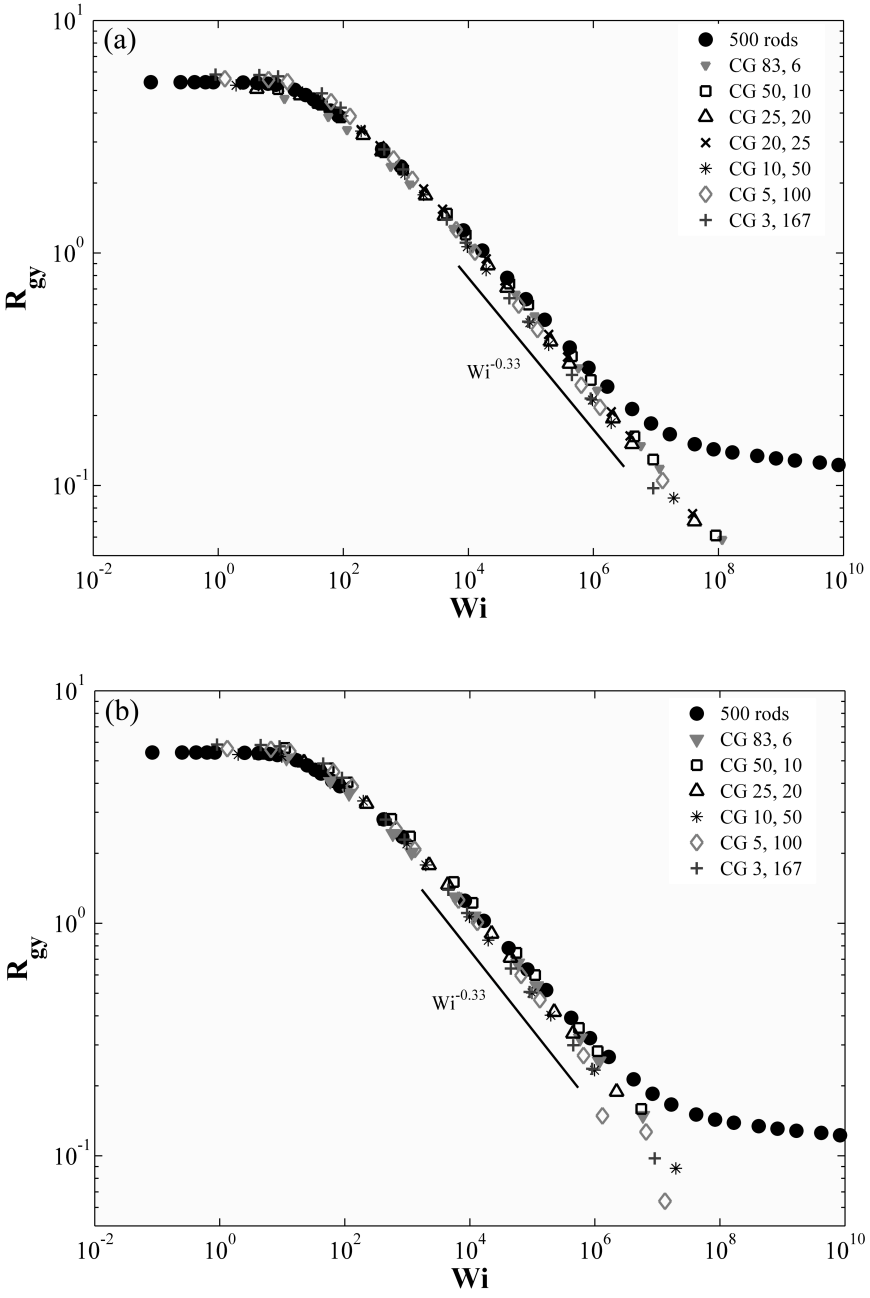

Figure 3.16: Comparison of Weissenberg number dependence of of R_{gy} a bead-rod chain of 500 rods and with chains coarse-grained to varying degrees, using the (a) Cohen Padé approximation as the force law for the springs, and (b) the Underhill-Doyle model as the force law for the springs. The legends used have similar significance as in Figure 3.15, and the solid lines indicate the approximate scaling law followed by the results for R_{gy} using the coarse-grained models.

CHAPTER IV

Tumbling and deformation of isolated polymer chains in shearing flow

1. Introduction

As mentioned in the previous Chapters, the dynamics of isolated flexible and semi-flexible polymer chains in shear flow has attracted considerable attention, and is thought to be well understood as a result of single-molecule imaging of DNA molecules [1, 2, 3] and Brownian dynamics simulations [4, 5]. These studies have shown that the average molecular extension of a polymer chain in the flow direction (x) increases with shear rate ($\dot{\gamma}$) and reaches a plateau at high shear rates. The failure to reach full extension at high shear rates is a consequence of repeated end-over-end tumbling of the polymer molecule, due to the equal strength of the extensional and rotational components in a shear flow. The plateau of polymer extension at high shear rate was assumed to be the asymptotic response at high shear rates, until some recent simulations [6, 9], including those shown in Chapter III, performed over a wide range of shear rates, revealed a highly non-monotonic response in chain stretch. Quite surprisingly, without excluded volume (EV) and hydrodynamic interactions (HI), the average chain stretch was shown to reach a maximum and then decrease at the highest shear rates. (This effect almost vanished in the presence of EV, but became more pronounced again when both HI and EV were included [6].) In this Chapter,

we show that this non-monotonic behavior disappears in the absence of EV and HI when a bending potential is included in the chain model to represent more accurately the behavior of a semi-flexible wormlike chain, such as double-stranded DNA or other biopolymers.

In addition, coarse-grained simulations [7, 8] have indicated that the tumbling time decreases with shear rate as $\dot{\gamma}^{-2/3}$ at high shear rates, which was further confirmed by a theoretical analysis [11]. For a DNA chain, the measured tumbling time approximately followed this power law for shear flows with Wi > 10 [7, 8], where Wi is the Weissenberg number, which is the product of shear rate $\dot{\gamma}$ and the relaxation time of the polymer chain. It seems doubtful, however, that results using coarse-grained chains will be accurate at high shear rates, where small subsections of the chain are excited by the flow and perturbed away from equilibrium. Using a fine-grained bead-rod model, we obtain a more accurate scaling law for the tumbling time, and derive this law theoretically, in what follows. At high shear rates, in the absence of EV and HI, the bead-rod model shows that radius of gyration of the chain in the flow gradient direction (R_{gy}) scales with shear rate as $R_{gy} \sim \dot{\gamma}^{-1/4}$ [5]. A Graetz-Lèvêque analysis in that study was consistent with this shear-rate scaling, but also predicted a scaling with chain length, as $R_{gy} \sim N_K^{1/4}$, where N_K is the number of Kuhn steps in the chain. We show below, however, that this latter prediction is incorrect and derive the correct result from a new physical picture of the chain dynamics under fast shearing flow.

In this Chapter, we resolve the physics for both the deformations and tumbling dynamics of chains over a wide range of chain lengths in steady shear flow using both fine-grained

and coarse-grained models, encompassing both slow and fast shearing. The results are explained using simple balances of diffusion and convection of chain segments. In the absence of HI and EV, at high shear rates, chain deformations depend on the discretization level of the chain model; for insufficiently discretized models there is a decrease in chain stretch with increasing shear rates. The coil dimensions and tumbling time over a wide range of $\dot{\gamma}$ and N_K in the absence of EV and HI are determined. In the region where chain extent in the flow direction shows a plateau, the end-over-end tumbling time (t_{tumble}) actually scales as $t_{tumble} \sim N_K \dot{\gamma}^{-3/4}$ and the width of the chain in the shear-gradient direction scales as $N_K^0 \dot{\gamma}^{-1/4}$, rather than the previously reported $t_{tumble} \sim N_K \dot{\gamma}^{-2/3}$ and $N_K^{1/4} \dot{\gamma}^{-1/4}$ scaling laws, respectively. We will show that the width of the chain in the shear-gradient (y) direction is set by a local transverse diffusion that is cut off by convection at a strain of unity. This, in turn, determines the time scale of tumbling. Additionally, it is shown that the Graetz-Lèvêque analysis, with suitable modifications to the diffusion coefficient, only holds true for relatively low shear rates, where the transverse diffusion is not cut-off in the tumbling orbit. Finally, scaling laws that are expected to be valid in the presence of HI and EV for long chains at high shear rates are derived.

2. Simulation Methods

All results presented here are obtained from Brownian dynamics simulations of an isolated polymer chain, with and without a bending potential, using the semi-implicit algorithm explained in an earlier study [10], as well as in Chapter III. The effects of excluded volume

(EV) and hydrodynamic interactions (HI) are also considered and the implications of these additional mechanisms for longer chains will be discussed after results in the absence of EV and HI are presented. Note, the results without the inclusion of EV and HI in our model are most reasonable for semi-flexible chains such as doubled-stranded DNA of short or moderate length, where EV and HI effects are relatively weak [5, 8]. However, future work will be required to confirm or modify results obtained here, by inclusion of HI and EV. Three levels of chain resolution are employed to probe the numerical effects caused by discretization: (i) The coarse-grained (CG) model uses springs that follow the Cohen-Padé approximation [10], with the parameter ν representing the number of Kuhn steps modeled by one spring. (ii) The more refined bead-rod (BR) model is comprised of stiff Fraenkel springs that mimic inextensible rods, with each "rod" representing one Kuhn step of the chain. (Note that, the details of the Cohen-Padé approximation and the bead-rod model are also provided in Chapter III.) (iii) The fine-grained (FG) model also uses stiff Fraenkel springs (henceforth referred to as "rods"), but with a harmonic bending potential acting between them. The "rods" in a FG model represent a polymer chain segment smaller than the Kuhn length and the stiffness of the bending potential determine the number of rods that constitute a Kuhn length. Figure 4.1(c) shows a schematic of the FG model. The bending potential U_b between two consecutive rods in the chain is given as $U_b = K_b\theta^2$, where K_b represents the angle stiffness parameter and θ is the angle between the two rods. For such a chain, the number of rods per Kuhn step is determined by the value of K_b. For a given value of K_b, the number of rods in one persistence length (defined as half of the Kuhn length) is determined by fitting the correlation of the bond vectors along the chain

contour to an exponential, for a trajectory in the absence of shear. Table 4.1 gives the values of K_b used in the simulations in this article and the corresponding number of rods that represent a single Kuhn step. The FG chain can thus represent any desired level of resolution of a worm-like chain, approaching continuous bending along the chain in the limit of a large number of rods per Kuhn step. It is to be noted that, owing to significantly larger computational requirements, all simulations with the FG model presented in this Chapter are performed without including the effects of HI and EV. Some simulation results using the FG model that include HI and EV will be shown in Chapter V. In this article, the x and y axes represent the flow and the gradient directions, respectively. Unless otherwise mentioned, the chain dimensions reported here are measured in terms of radii of gyration along different axes, which is defined as

$$R_{g\delta} = \sqrt{\frac{\left\langle \sum_i (\delta_i - \delta_{c.m.})^2 \right\rangle}{N_b}}, \qquad \delta \equiv \text{x, y, z}$$

where δ and $\delta_{c.m.}$ denote the components of the position vectors of the beads and the center of mass of the chain along the x, y and z axes, respectively. The total number of beads in the chain is denoted by N_b and $\langle .. \rangle$ represents an ensemble average.

In all cases, the end-to-end relaxation time of the polymer chain, τ, is estimated by fitting the final 70% of the autocorrelation function for the end-to-end vector of the chain (as described in Chapter III). The Peclet number (Pe_K) is defined as the product of the shear rate and the relaxation time of one Kuhn length. (As discussed in Chapter III, this is given

by τ/N_K^2 for cases without HI and EV, where N_K is the chain length in terms of the number of Kuhn lengths.) The Weissenberg number is defined as $Wi = \tau\dot{\gamma}$. Note that since several rods constitute one Kuhn step for the FG model, unlike the BR model, we use the symbols Pe_K and N_K to present results in this Chapter, to signify that these quantities represent the Peclet number defined on one Kuhn step (which may or may not be represented by one rod in the chain, depending on the model used) and the number of Kuhn lengths, respectively.

For the CG and BR models without HI, details about the semi-implicit numerical algorithm and simulation parameters are provided in Chapter III. For FG model with bending potentials, an explicit integration scheme was used. The effects of both HI and EV are modeled as in Ref. [6], using the BR model with stiff Fraenkel springs that mimic inextensible rods. The HI between beads was calculated using the Rotne-Prager-Yamakawa (RPY) tensor [6, 10] (using a hydrodynamic diameter of one Kuhn length for each bead for all simulations in this article). The details of the semi-implicit numerical algorithm used to solve the stochastic differential equation with HI are given in Ref. [10]. The EV is modeled by a pair-wise Lennard-Jones potential acting between beads with a bead diameter equal to the length of one rod. For results shown in this Chapter, the energy parameter of the Lennard-Jones potential, for cases with and without HI, is tuned such that the R_g of the chain at zero shear is same as that of an ideal polymer coil without any EV interactions. In all cases with HI and EV, for a given $\dot{\gamma}$, the stiffness of the Fraenkel springs and the timestep size for integration used in the simulations of Chapter III were observed to be sufficient to attain convergence of the results mentioned here. Unless

otherwise mentioned, the initial 20% of each simulation is kept for equilibration, and the final 80% of the run is used to calculate the average of any quantity.

3. Results and Discussion

Figures 4.1 and 4.2 show the variation of R_{gx} and R_{gy} with Peclet number Pe_K for polymer chains of different lengths and represented by models at varying degrees of resolution. The normalized R_{gx} (normalized by the contour length of the chain $L = N_K b_K$, where b_K is the length of one Kuhn step) for the different models (Figure 4.1(a)) first increases with shear rate, shows a plateau, and then decreases again, consistent with the results in Chapter III and prior observations [6]. The results obtained from the CG and BR models for a chain of 500 Kuhn lengths, and those of the BR and FG models for a chain of 25 Kuhn lengths are consistent with one another, except at high shear rates. Note, results for several other CG representations for a chain of 500 Kuhn lengths are not shown here for clarity (results for several other values of ν are given in Chapter III for a chain of 500 Kuhn lengths). Figure 4.1(b) shows the approximate power law exponents for the transition to the plateau in R_{gx} for the BR model for different chain lengths, which will be used later for the analysis of the tumbling times at these shear rates. However, it is noted from the results that the exponent in this transition regime shows a slow increase with increasing chain lengths, reaching 0.9 for a CG model of 5000 Kuhn lengths. Our results also clearly show that the decrease of R_{gx} starts at different values of Peclet numbers for different levels of chain resolution. The decrease is the earliest in the CG model, which is expected to be inaccurate

at high shear rates when the individual springs are excited away from equilibrium by the flow. This onset occurs at about Pe_K = 10 for the BR model, irrespective of the chain length. However, the Pe_K at this transition is systematically pushed to higher values as the Kuhn length is resolved further in the FG models (in fact, the decrease in R_{gx} for the FG model representing a chain of total 25 Kuhn lengths, with 8 rods per Kuhn length, starts at Pe_K > 7000). It is worth noting here that, for different chains using the FG model, the power law exponent for R_{gx} at high shear rates where it shows a decrease is about -0.15, consistent with the observations presented in Chapter III.

Similar conclusions about the effects of chain resolution are inferred from the results of R_{gy} (normalized by b_K) presented in Figure 4.2(a). Our results show that, for both BR and FG chains, R_{gy} stays constant at the equilibrium value for weak shear flows and follows a power law in Pe_K with an exponent of about -1/4 (0.265 ± 0.015 for a BR chain of 500 Kuhn steps) at high shear rates, consistent with earlier findings [5], as well as the results in Chapter III. For both BR and FG chains, R_{gy} approaches a constant value at ultra-high shear rates, where R_{gx} shows a decrease. Interestingly, the CG models show a steeper decay with an exponent of about -1/3 (0.33 ± 0.01 for a CG model for 500 Kuhn steps with ν = 25), which is also observed in the results of Chapter III and consistent with a similar prediction at higher shear rate in Ref. [11]. However, we also found that the CG model for a chain of 5000 Kuhn steps, with ν = 25, does show an exponent of about -1/4 in the region of shear rates where R_{gx} shows a plateau, but it changes to about -1/3 at higher shear rates. (While the difference between the exponents -1/4 and -1/3 is rather small, the statistical error for best fits to the data in Fig. 4.2(a) is about ± 0.01.)

The CG chains also fail to show the saturation in R_{gy} at high shear rates in the range of Peclet numbers considered in this study, even though the onset of the decrease in R_{gx} is achieved. For the BR and FG chains, a closer inspection reveals that the value of Pe_K at the onset of the decrease in R_{gx} coincides with the value at which R_{gy} reaches saturation. Figure 4.2(b) shows the variation of the average projected length of the chain along the y-axis (denoted as 'Y-extent') with Peclet number. In all cases shown, the saturation value of the Y-extent equals the length of one rod in the BR and FG models (Note, the length of one rod in the FG model depends on the number of rods that constitute a single Kuhn length). Since for the FG chains the length of a single rod shrinks as resolution increases and the power law decay for the Y-extent is the same for all FG representations (representing a BR chain of 25 Kuhn steps), the Pe_K at which Y-extent equals the rod length is pushed to higher values as the chain is resolved more finely. Accordingly, the saturation in R_{gy} and the decrease in R_{gx} occur at higher values of Pe_K for FG chains with higher resolution. This implies that, at least in the absence of HI and EV (i.e. for a wormlike chain), the transitions in R_{gx} and R_{gy} observed at ultra-high shear rates depend on the chain discretization, and will only occur at $Pe_K \rightarrow \infty$ as the chain resolution is pushed to the limit of continuously distributed flexibility. These trends are physically possible, since, as shown in Chapter III, these transitions occur due to a competition between chain end-to-end tumbling and individual rod flipping, one after another, in the absence of HI and EV. Thus, at ultra-high shear rates that show chain compression, one rod flips followed by the next, and these flipping motions propagate along the chain. With the addition of a bending penalty between consecutive rods, these rod flips can only occur at higher shear rates, when the

forces due to the flow overwhelm the forces due to the bending potential. As chain resolution is increased, the stiffness of the bending potential is increased, and thus the shear rates at which such transitions can occur is expected to increase.

We also investigated the variation of chain dimensions for the BR model of 100 Kuhn steps with both HI and EV. The results presented in Figure 4.2(c) show the effects induced by EV and HI on the trends for R_{gy} for the BR chain of 100 Kuhn steps considered here. Clearly, the behavior for all the cases is similar to those obtained without HI and EV, except at the highest shear rates. Since we are comparing values across different mechanisms here and the scaling of the relaxation spectrum of the chain is expected to be different when HI is added, we used the Weissenberg number (Wi) as the basis instead of the Peclet number that was defined earlier. Interestingly, the power law in Wi for R_{gy} in the presence of HI (without EV) shows a slightly steeper exponent (-0.278± 0.015) relative to that in the absence of HI and EV. In the presence of HI and EV, the plateau in R_{gy} is attained at a lower Wi, but this leveling off is likely to be dependent on the chain resolution as discussed earlier. (Note that, more results for chain deformations in the presence of HI and EV will be presented in Chapter V.) Although not shown, the effect on R_{gx} is similar to the observations in Ref. [6], with HI further amplifying the decrease at ultra-high shear rates (after the plateau) and EV suppressing it. This shows that the underlying physics and the corresponding model presented here is generally valid. It is worth noting that the scaling laws for R_{gy} in the presence of EV and HI for long enough chains are expected to be different and are discussed later in this Chapter.

In the regime of shear rates where R_{gx} shows a plateau, results presented in Figure 4.2(a) indicate that R_{gy} is independent of N_K. There is a small dependence on N_K for short chains but the values at a given Pe_K converge rapidly with increasing N_K, such that the predictions from BR chains of 300 and 500 Kuhn steps and the CG chain of 5000 Kuhn steps agree remarkably well with one another. This is in contrast to the predictions of the "Graetz-Lèvêque" analysis in Ref. [5], which indicated that the chain thickness in the flow gradient direction should depend on chain length, following the scaling $R_{gy} \sim N_K^{1/4}\dot{\gamma}^{-1/4}$. The Graetz-Lèvêque analysis assumes that the time required by chain segments to diffuse a distance of R_{gy} in the shear-gradient direction is comparable to the time needed to convect the segments a distance of the extended chain in the flow direction. Since the time needed to convect segments over a distance of the chain length varies with N_K, the Graetz-Lèvêque analysis predicts that R_{gy} depends on N_K. However, no systematic simulations had been performed until now to check the dependence of R_{gy} on N_K.

To motivate what follows, we present in Figure 4.3(a) the average x-y trajectory of the beads at the ends of a BR chain of 300 Kuhn steps with respect to the center of mass of the chain, during the tumbling orbit of the chain at high shear rates where R_{gx} shows a plateau. (Snapshots showing some examples of the sequence of chain configurations during the tumbling process are given in Appendix B.) We show trajectories only of chain ends with positive y-coordinates, which are convected by the flow along the positive x-direction, i.e. from left to right in the figure. These trajectories reveal that the diffusion in the y-direction that occurs during this convection is limited to a distance y_c that decreases with increasing shear rates.

Based on this observation, we now present a simple model that predicts the dependence of the thickness of the chain in the flow gradient direction, R_{gy}, and the end-over-end tumbling time, t_{tumble}, with shear rate. In what follows, "high" shear rates will denote the flow regime where the chain stretch shows a plateau and do not include results from the highest shear rates where an artificial decrease in average stretch occurs due to the limits of chain resolution discussed above. We define the time t_c to be the time needed for a bead to diffuse a distance y_c in the y-direction that equals the distance that the bead is convected along the x-direction over the same time. At this time t_c the chain segment that had diffused laterally by this distance y_c has been stretched to a strain of order unity, which creates tension in the flow direction, and inhibits further lateral diffusion in the y-direction. If D is the diffusion coefficient of this chain segment, this time t_c is then given by $t_c \sim \frac{y_c^2}{D}$. This same t_c can be set to $t_c \sim \frac{y_c}{v_x}$, where v_x is the velocity of a bead in the x-direction. For a shear flow with a shear rate $\dot{\gamma}$, $v_x = \dot{\gamma} y_c$. Thus, $t_c \sim 1/\dot{\gamma}$. Combining the two expressions for t_c for the convective and diffusive processes, now we have the following expression for y_c:

$$y_c^2 \sim \frac{D}{\dot{\gamma}} \qquad (1)$$

A diffusing bead has to drag other beads, which reduces its mobility. Thus, following a similar line of argument as in Ref. [5], the effective diffusivity of a bead will be given as $D \sim \frac{D_0}{n_b}$, where D_0 is a constant and n_b represents the number of beads that are dragged by

a bead during diffusion. Before being stretched, the chain of n_b beads should approximately follow a random walk. Thus, we have $n_b \sim y_c^2$, which gives the scaling:

$$D \sim \frac{D_0}{y_c^2} \tag{2}$$

which we confirm shortly. (We note here that when the number of beads being dragged becomes large enough for excluded volume and/or hydrodynamic interactions to become important, this scaling will change slightly in a well-known way, as discussed later in this article.) Combining this with the expression for y_c, we finally get:

$$y_c \sim D_0^{1/4}\dot{\gamma}^{-1/4} \tag{3}$$

For a large chain at high shear rates, the beads will spend the majority of the tumbling orbit at a mean y-distance of approximately y_c, which implies that the radius of gyration of the chain in the shear-gradient direction, R_{gy}, scales as:

$$R_{gy} \sim y_c \sim N_K^0\dot{\gamma}^{-1/4} \tag{4}$$

This result is consistent with the results presented in Figure 4.2(a), as well as those presented in Chapter III. As mentioned earlier, the Graetz-Lèvêque analysis assumed that diffusion in the gradient direction is limited by convection along the *entire* contour of the chain, thereby implying that R_{gy} should increase as the chain gets longer. Our model corrects this picture and implies that R_{gy} is set by a *local* balance of the time needed to diffuse a loop of chain in the shear-gradient direction against the time needed to stretch it out, thereby removing the dependence on chain length. However, it is important to note

here that the Graetz-Lèvêque analysis will be relevant for all chains at transitional shear rates before the plateau in R_{gx} is reached. It should also apply to short chains at high shear rates, where the beads can reach the other end before diffusion is completely cut-off by convection. These cases where the Graetz-Lèvêque analysis is expected to hold true will be discussed later.

To confirm our model for the diffusivity (Eq. 2), we consider the mean square displacement (MSD) of beads in the y-direction, for an ensemble of chains, each starting from a fully extended initial configuration, subjected to a shear flow for a time long enough for it to undergo approximately one end-over-end tumble. The diffusion distance squared of the beads in the y-direction is given by $y^2 \sim Dt$. As lateral diffusion continues and y increases, more beads must be recruited into the outwardly diffusing random-walk loop, so that D decreases as $D \sim n_b^{-1} \sim y^{-2}$. We therefore expect the scaling $y^4 \sim D_0 t$ in the diffusion-controlled regime before the loop becomes stretched by the flow and y_c is reached. In terms of the mean square displacement (MSD), this becomes

$$\log(\text{MSD}) \sim 0.5\log(t) \qquad (5)$$

Figure 4.3(b) shows the calculated variation of log(MSD) with log(t) for beads at different positions along a BR chain of 300 Kuhn lengths when $Pe_K = 0.03$, where the statistics are averaged over 100 chains. As expected from Eq. (5), an approximate slope of 0.5 is obtained for the inner beads over the entire time for which MSD is calculated. However, for the beads near the chain ends, diffusion to a distance of about one Kuhn length shows a slope of approximately 0.75, while subsequent diffusion to larger distances show a slope

close to 0.5. As we move farther from the chain ends, the slopes of both regimes approach a value of 0.5 and they merge into a single regime for the 50th bead. The slope of 0.75 for diffusion in y-direction was also reported earlier [4] and was used in Ref. [7], but in that study [4] MSD was computed only using a data up to small distances (less than one Kuhn length) and hence the subsequent regime with slope = 0.5 was not reported. Our investigations also show that D_0 depends weakly on the chain length for short chains but is almost a constant for chains with more than 100 Kuhn lengths, which explains the slight chain length dependence of R_{gy} in Figure 4.2(a). Figure 4.3(c) shows snapshots of a few loops formed during the chain tumbling, viewed from different angles. For all cases shown, the upper snapshot shows the x-y view of the chain while the lower snapshot shows the loop formed at the chain end more clearly, and supports our argument that the beads in the loop perform a random walk in the y-direction. Our model also implies that, in the range of shear rates at which y_c is large compared to the length of each spring, a CG model with enough beads will form a Gaussian loop and hence approximately follow Eq. (4). An example of this is shown in Figure 4.2(a), for a CG chain of 5000 Kuhn steps and $\nu = 25$.

As a consequence of this picture, it can be concluded that for long chains, beads have already diffused to a distance y_c early on in the tumbling process at high shear rates, and then get convected by the flow. Using the x-velocity of these beads $v_x = \dot{\gamma} y_c \sim \dot{\gamma}^{3/4}$ and the distance to be convected ~ N_K, the tumbling time (t_{tumble}) at high shear rates is given as:

$$t_{tumble} \sim \frac{N_K}{v_x} \sim N_K \dot{\gamma}^{-3/4} \qquad (6)$$

The exponent of -3/4 represents a steeper decrease with shear rate than the exponent -2/3 reported in earlier studies [7, 8]. However, coarse-grained chain models were used in these studies, similar to the CG results in Figure 4.2(a) (and also to those in Chapter III) that show approximately $R_{gy} \sim \dot{\gamma}^{-1/3}$, deviating slightly from the results of the more finely resolved chain models at high shear rates. This difference in the scaling of R_{gy} affects the scaling of the tumbling time, which from the simple argument based on the aspect ratio will predict $t_{tumble} \sim \dot{\gamma}^{-2/3}$, a result that was observed in Ref. [7]. Next, we explain our new algorithm to calculate the frequency of shear-induced tumbling and present results of the tumbling time at high shear rates that further support our arguments leading to Eq. (6), and also show that the CG model predicts an exponent of -2/3 that is consistent with earlier observations.

The sketch in the inset (i) of Figure 4.4 defines the four zones used for the calculation of tumbling times of the end-to-end vector. The orientation angle of the end-to-end vector is defined such that it becomes positive when that vector rotates in the counterclockwise direction from the x-axis, where the orientation angle is 0. The relevant angle considered in this case is that between the x-axis and the projection of the end-to-end vector in the x-y plane, whose values are taken to lie between $-\pi/2$ and $\pi/2$. For any given shear rate, the positive and negative orientation angles are averaged separately over the whole trajectory, which are denoted as θ_{pos} and θ_{neg} respectively. The zones indicated in the sketch are defined using the angles θ_{pos} and θ_{neg}. The space between the radial vectors of $\theta = 0$ and $\theta = \theta_{neg}$ is defined as zone 0, between $\theta = \theta_{neg}$ and $\theta = \pi/2$ as zone 1, between $\theta = \pi/2$ and θ

= θ_{pos} as zone 2 and between $\theta = \theta_{pos}$ and $\theta = 0$ as zone 3. For the imposed direction of the shear flow in our case, the chain end-to-end vector will have a net average angular rotation in the clockwise direction. Hence, to execute a complete shear-induced tumble starting from zone 0, it must move into zones 1, 2, 3 and return to zone 0 in succession. Due to thermal fluctuations, there will be both clockwise and anticlockwise rotations at small time intervals, with a net clockwise motion over relatively large time intervals. Our algorithm tracks the rotational motion of the end-to-end vector and calculates the number of times a complete tumbling event (rotation through zones 0, 1, 2, 3 and 0 again, in the clockwise sense) occurs for a given total simulation time.

After ignoring the initial 10% of the total run, the counter starts when the angle of the end-to-end vector is in zone 0. Whenever it crosses into zone 1, the number of tumbles is increased by 1/4 (since there needs to be a total of 4 zone crossings in succession to execute a complete tumble). If it crosses into zone 3 instead, the count is decreased by 1/4. Continuing this way, for every zone crossing that is in the clockwise direction (zone 0 to 1, 1 to 2, 2 to 3 and 3 to 0), the count is increased by 1/4. Any zone crossing in the reverse sense decreases the counter by 1/4. If the end-to-end vector remains in the same zone (no zone crossings) after a time step, the counter is not changed. This way, after a large time interval, the counter will give the total number of tumbling events (in the clockwise sense i.e. the shear-induced tumbling) and a division by the total time of counting will yield the tumbling frequency. Inverting the frequency, we get the average tumbling time for the end-to-end vector.

For low shear rates, when the polymer chain is not stretched and exists as a coil, the dynamics of the end-to-end vector is not a good representative of the overall tumbling dynamics of the coil. In such cases, the analysis described above is applied to the position vectors of each bead (relative to the center of mass of the chain) and the results are averaged over all the beads to obtain the tumbling frequency for the whole coil. At high shear rates, tumbling times calculated using this local criterion of using the position vector of each bead agree remarkably well with those obtained using only the tumbling of the end-to-end vector. Our new method for tracking tumbling gives a much more precise measurement of the tumbling frequency than given by the earlier method of using the rather weak maximum in the Fourier transform of the time dependence of the angle of the end-to-end vector [7, 8].

The results for the tumbling time (normalized by N_K) are shown in Figure 4.4 at various shear rates (very low shear rates that hardly deform the chain, with $Wi \leq 4$, were not considered for this analysis) for different chain lengths. At high shear rates, the results for the BR model follow our scaling law (Eq. 6) remarkably well. Note that our model suggests a nearly constant velocity v_x of an end bead relative to the center of mass, throughout most of the tumbling orbit, which should produce a relatively uniform probability distribution for the end-to-end distance of the polymer chain, consistent with prior findings in Ref. [5] and in Chapter III. Results are also shown in Figure 4.4 for the tumbling time variation for CG chains that represent 300 and 500 Kuhn steps (with $\nu = 25$ and $\nu = 50$ respectively) at high shear rates. The scaling exponent obtained from the CG model is about -2/3, which is clearly different from that for the corresponding BR model,

but consistent with the results presented in Ref. [7]. An exponent of about -2/3 is also observed in several other CG chains of varying lengths that we investigated, but are not shown here for clarity.

At the intermediate shear rates, in the transition region before the chain stretch attains a plateau, we expect the transverse diffusion not to be limited by local convection and hence the Graetz-Lèvêque analysis (with D given by Eq. 2) should apply. For the BR model, our simulation data in this region of shear rates shows roughly $R_{gx} \sim \dot{\gamma}^{m}$, where m = 0.5, 0.57, 0.73 and 0.79 for chains with 100, 150, 300 and 500 Kuhn lengths respectively (Figure 4.1(b)). In this case, following the Graetz-Lèvêque analysis and using $R_{gx} \sim \dot{\gamma}^{m}$, and $D \sim \frac{D_0}{R_{gy}^{\,2}}$ (from Eq. 2), the derivation described in [5] yields $R_{gy} \sim \dot{\gamma}^{-(1-m)/5}$. Then, since the Graetz-Lèvêque analysis estimates the tumbling time by equating the time needed for convection of an end bead over a distance $R_{gx} \sim \dot{\gamma}^{m}$ to the time needed for the bead to diffuse a distance $R_{gy} \sim \dot{\gamma}^{-(1-m)/5}$ in the y direction, we obtain $t_{tumble} \sim \frac{R_{gy}^2}{D} \sim \frac{R_{gy}^4}{D_0} \sim \left(\dot{\gamma}^{-(1-m)/5}\right)^4 \sim \dot{\gamma}^{-\frac{4}{5}(1-m)} \sim \dot{\gamma}^{p}$, where p = -4(1-m)/5. The observed values of p = -0.38, -0.34, -0.22 and -0.17, for chains with 100, 150, 300 and 500 Kuhn lengths respectively (shown in inset (ii) of Figure 4.4), agree well with those expected from the values of m observed for these chains. For a long chain, this transition regime can span several orders of magnitude in Wi with m ≈ 1 (as mentioned earlier, m = 0.9 for a CG chain with 5000 Kuhn steps) and subsequently p ≈ 0. The Graetz-Lèvêque analysis is also

likely to hold for short chains at high shear rates, since the beads can reach the other end of the chain before the transverse diffusion is cut-off. Using $R_{gx} \sim N_K$, the Graetz-Lèvêque analysis gives $R_{gy} \sim N_K^{1/5}\dot{\gamma}^{-1/5}$, which has a slightly weaker shear-rate dependence than in Eq. (4) and agrees quite well to the scaling observed for short chains (~ 10 Kuhn lengths) in Figure 4.2(a).

Based on the mechanism presented above, we can estimate the relevant scaling laws for long chains when EV and HI are present. When EV is present, the loop size will be given as $y_c \sim n_b^{\beta}$, where $\beta = 0.5$ for a coil at the theta condition and $\beta = 0.6$ for the same in a good solvent. In the limit of dominant HI (in the absence or presence of EV), Eq. (2) will change to $D \sim \frac{D_0}{y_c}$. Since $R_{gy} \sim y_c$, we get the following scaling laws for the coil thickness and tumbling times at high shear rates for finely resolved chains in the cases given below:

(I) No EV, no HI: $R_{gy} \sim \dot{\gamma}^{-1/4}$, $t_{tumble} \sim N_K\dot{\gamma}^{-3/4}$

(II) EV (good solvent), no HI: $R_{gy} \sim \dot{\gamma}^{-3/11}$, $t_{tumble} \sim N_K\dot{\gamma}^{-8/11}$

(III) Dominant HI, with or without EV: $R_{gy} \sim \dot{\gamma}^{-1/3}$, $t_{tumble} \sim N_K\dot{\gamma}^{-2/3}$

Out of these, case (I) is discussed earlier in this article and provides the foundation for the analysis of the other cases. It is worthwhile to note that the exponent of the tumbling time systematically changes from -3/4 to -2/3 as additional mechanisms of EV and HI are introduced. We expect to observe these scaling laws for very long chains with EV and HI, when relatively large loops will be formed during shearing for either mechanism to have a

significant effect on the dynamics. However, simulations of such large chains with EV or HI are beyond the reach of current computing power, which makes it impossible to directly validate the scaling laws presented above.

4. Summary

In summary, we have presented a new picture of the dynamics of polymer chains at high shear rates, where the chain stretch saturates. We show that lateral diffusion of a growing loop of polymer in the gradient direction ceases when the loop is stretched out by convective flow, and we developed a scaling law $R_{gy} \sim N_K^0 \dot{\gamma}^{-1/4}$ based on this balance, which shows no dependence on the chain length. The tumbling time is given by $t_{tumble} \sim N_K \dot{\gamma}^{-3/4}$ for long chains where the beads spend a substantial amount of time in the convection-controlled regime with a uniform x-velocity. We also showed that a Graetz-Lèvêque analysis holds at lower shear rates when the chain stretch in the flow direction plateaus. In the absence of HI and EV, our results for highly resolved chains indicate that the decrease in chain stretch at ultra high shear rates is not present for wormlike chains that are suitably resolved below the persistence length, implying that the stretch saturation will be the asymptotic response, at least in the absence of HI and EV. Understanding the physics of the tumbling dynamics for the simplest case without HI or EV allows us to make predictions about the corresponding scaling laws for long chains in the presence of HI and EV. Thus, relatively simple physical arguments provide a complete understanding of the variation of chain dimension and tumbling dynamics over the range of shear rates relevant to earlier experimental and simulation studies.

References

[1] Smith, D. E.; Babcock H. P.; Chu S. *Science* **283**, 1724-1727 (1999).

[2] Teixeira, Rodrigo E.; Babcock, Hazen P.; Shaqfeh, Eric S. G.; Chu, Steven *Macromolecules*, **38**, 581-592 (2005).

[3] Hur, J. S.; Shaqfeh, E. S. G.; Babcock, H. P.; Smith, D. E.; Chu, S. *J. Rheol.* **45**, 421-450 (2001).

[4] Doyle, P. S.; Shaqfeh, E. S. G.; Gast, A. P. *J. Fluid. Mech.* **334**, 251-291 (1997).

[5] Hur, J. S.; Shaqfeh, E. S. G.; Larson, R. G. *J. Rheol* **44**, 713-742 (2000).

[6] Sendner, C.; Netz, R. R. *Eur. Phys. J. E* **30**, 75-81 (2009).

[7] Schroeder, C. M.; Teixeira, R. E.; Shaqfeh, E. S. G.; Chu, S. *Phys. Rev. Lett.* **95**, 018301 (2005).

[8] Lee, Joo Sung; Shaqfeh, Eric S. G.; Muller, Susan J. *Physical Review E*. **75**, 040802(R) (2007).

[9] Hoda, Nazish; Larson, Ronald G. *J. Rheol* **54**, 1061 (2010).

[10] Hsieh, Chih-Chen; Li, Lei; Larson, Ronald G. *J. Non-Newtonian Fluid Mech.* 113, 147-191 (2003).

[11] Winkler, Roland G. *Phys. Rev. Lett.* **97**, 128301 (2006)

Table 4.1: Values of Kb used and the corresponding number of rods per Kuhn step for the FG chain model.

K_b/k_BT	Number of rods per Kuhn step
0.35	2
0.96	4
1.95	8
3.95	16

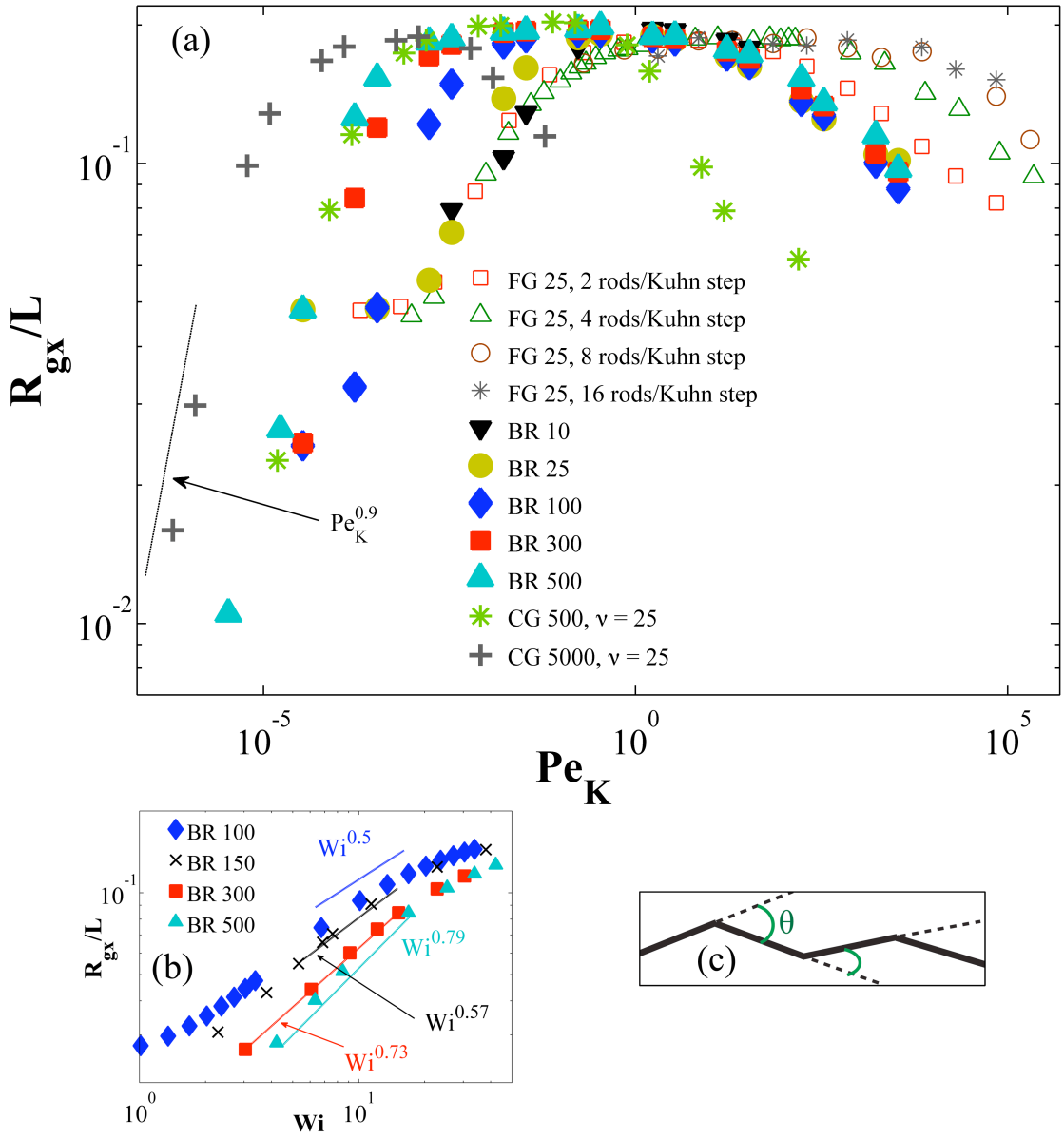

Figure 4.1: (a) Variation of R_{gx}/L with Pe_K for chains of varying length and resolution. Legends indicate the type of model used (BR, CG or FG) followed by the number of Kuhn lengths in the chain. (b) Variation of R_{gx}/L vs. Wi, for various chain lengths, at shear rates in the transition to stretch saturation. The approximate scaling laws are indicated for all chain lengths considered. (c) A schematic of the FG model. Here L denotes the contour length of the chain ($L = N_K b_K$), where b_K is the length of one Kuhn step. Note, all results shown here are obtained without HI and EV.

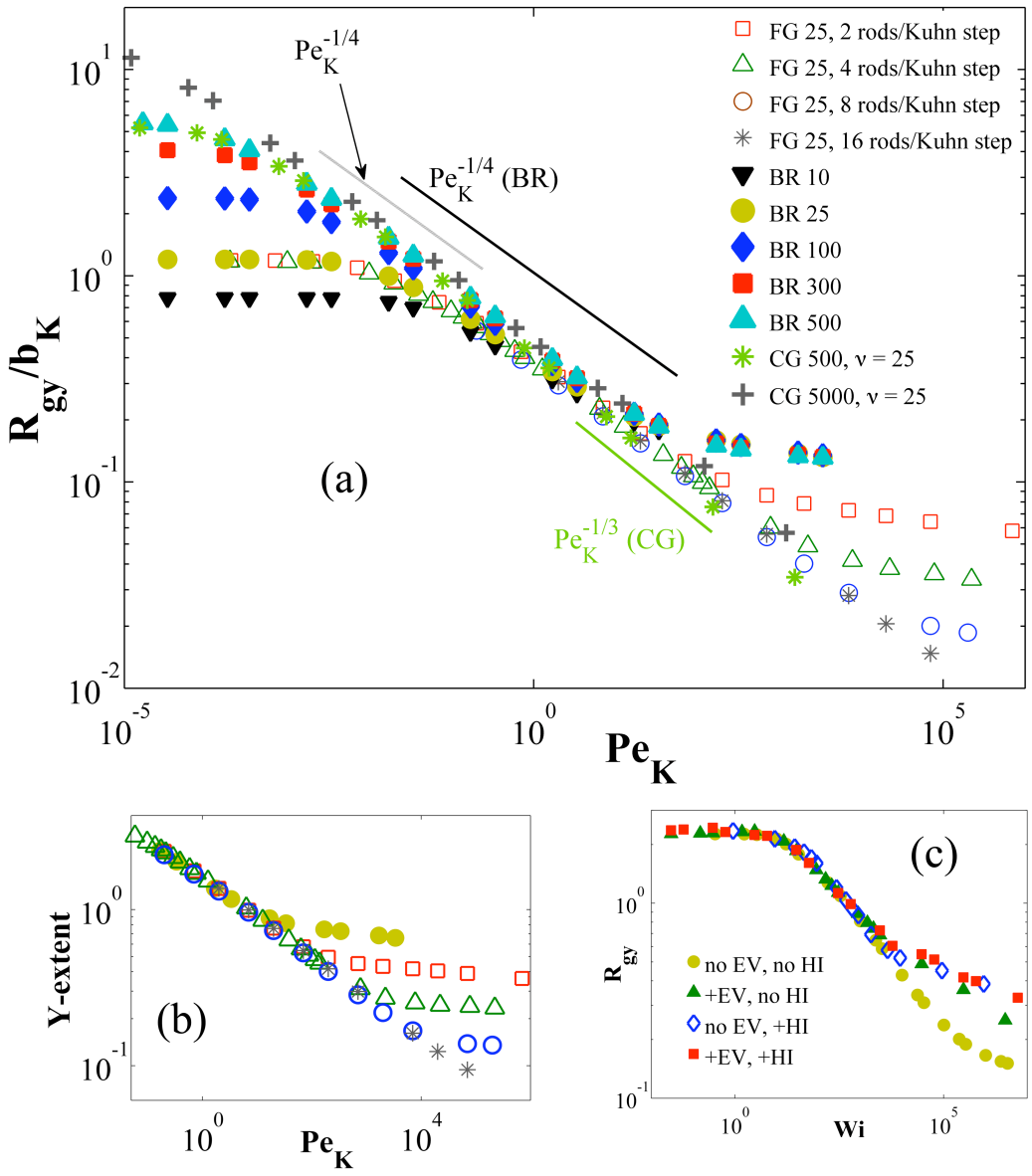

Figure 4.2: (a) Variation of R_{gy}/b_K with Pe_K for chains of varying length and resolution. The solid black line indicates the scaling of the BR chains at high shear rates. The grey line shows the region where an exponent of approximately -1/4 is obtained for R_{gy} for the CG model for 5000 Kuhn steps (with 200 springs). The green line indicates that the exponent for the CG model (with 20 springs) is about -1/3, at high shear rates. (b) The Peclet number variation of the average Y-extent of the chain. Legends in (a) apply to (b), and indicates the type of model used (BR, CG or FG) followed by the number of Kuhn lengths in the chain. (c) Variation of R_{gy} with Wi for a BR chain of 100 rods for various combinations of HI and EV being present ('+' sign in the legend indicates which mechanism is active). Here b_K denotes the length of one Kuhn step. Note, all results shown here, except those in (c), are obtained without HI and EV.

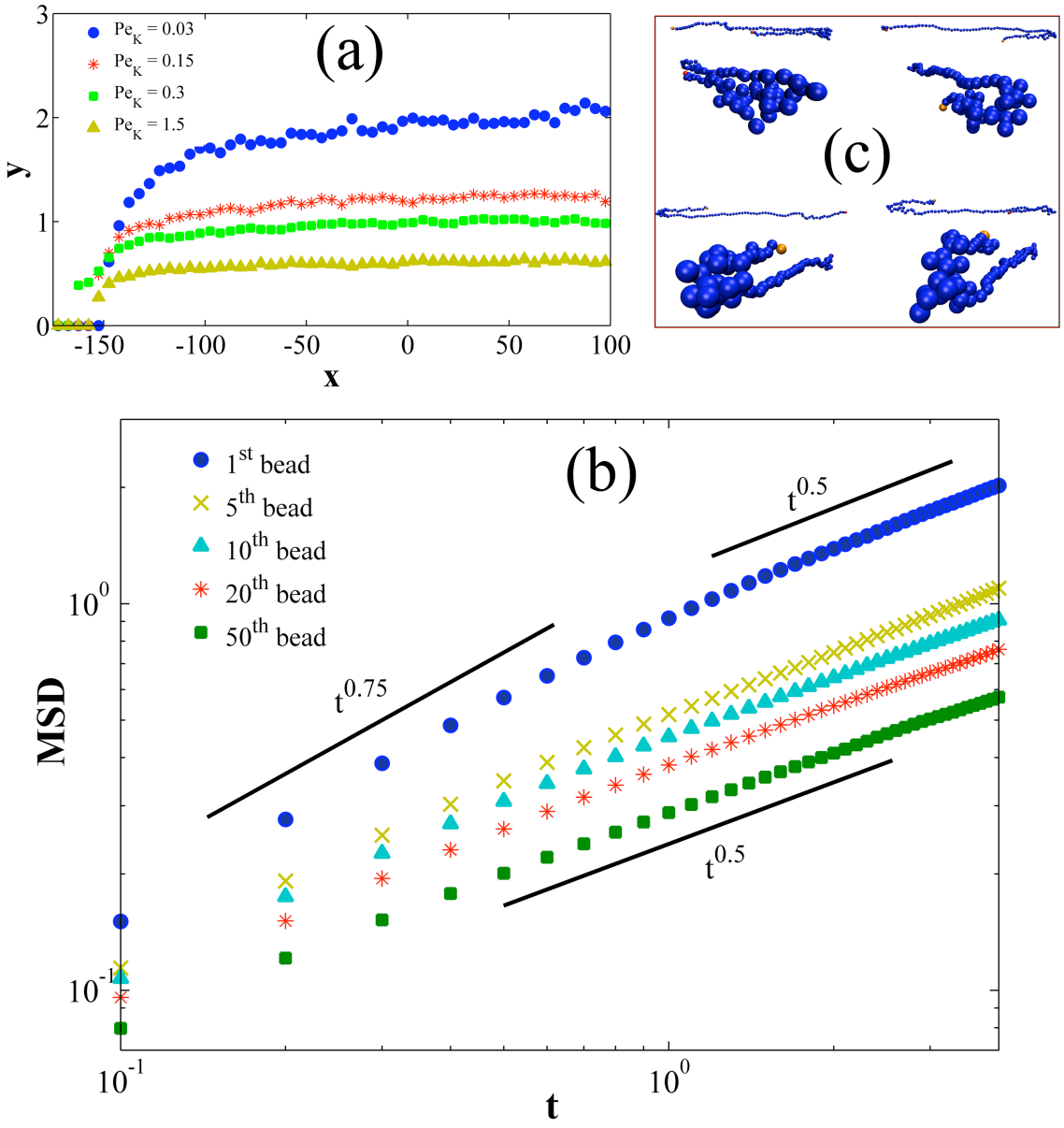

Figure 4.3: (a) Average x-y trajectory for the bead at the end of a BR chain of 300 beads, relative to the center of mass. (b) Time variation of the MSD in the y-direction for various beads in a chain of 300 rods. The lines show the exponents of the scaling laws in the different regions. (c) Four different examples of loops formed at chain ends during the end-over-end tumbling of a chain of 100 rods when $Pe_K = 0.15$. Red and orange mark the end beads. For each case, two different views are given – one is in the x-y plane that shows the conformation of the chain along the flow direction, and the other zooms into the loop formed at one end.

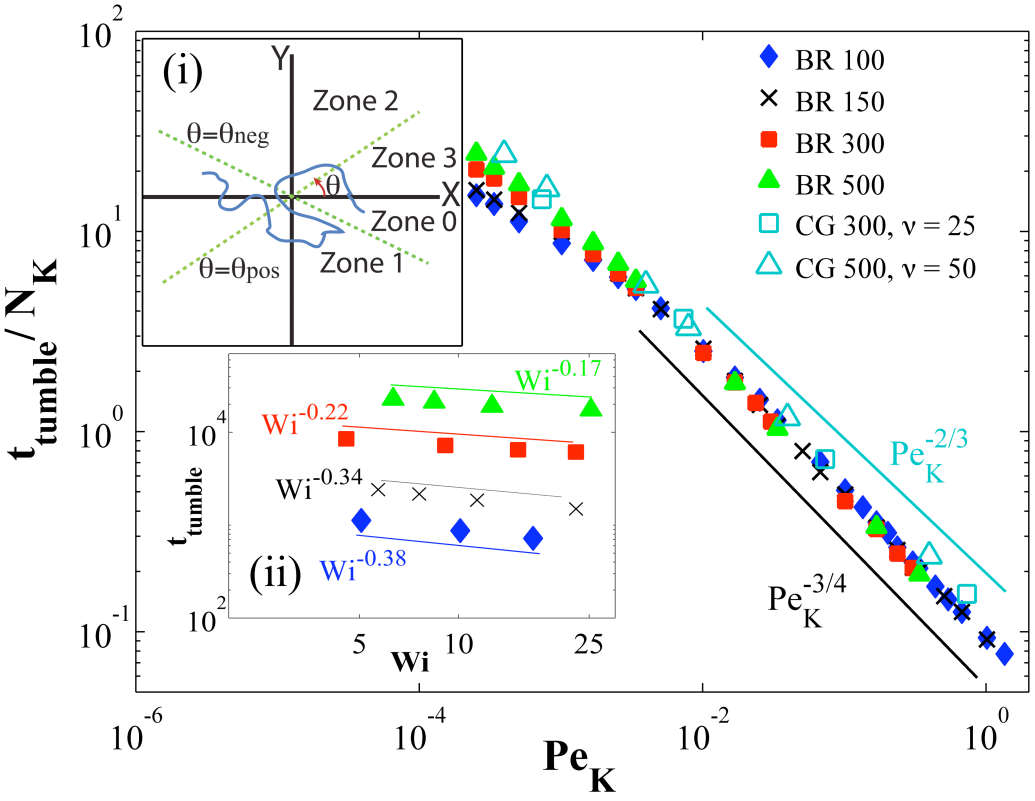

Figure 4.4: Variation of the tumbling times (normalized by N_K) with Pe_K. The solid black line shows the power law for BR chains of different lengths, which agree well with the scaling law in Eq. 4. The light blue line indicates that the power law exponent for the CG model is about -2/3, which deviates from the more resolved BR chains at high shear rates. Inset (i) shows a sketch of the zones used to count the tumbling events, as described in the text. Inset (ii) shows the approximate scaling (with Wi) of the tumbling time for BR chains of different lengths at shear rates prior to stretch saturation. The error bars are all smaller than the sizes of the symbols.

CHAPTER V

Effects of excluded volume and hydrodynamic interactions on the behavior of isolated polymer chains in shearing flow

1. Introduction

As highlighted in the preceding Chapters, the deformation of polymer chains subjected to shear flows has been extensively investigated in the past decade by single-molecule imaging experiments [1-3] and Brownian dynamics simulations of isolated bead-spring and bead-rod chains [4-8] by various researchers. All these studies showed that the stretch increases with shear before reaching a plateau at high flow rates, which is about 40% of the maximum chain extension [7]. This plateau is a consequence of the chain undergoing incessant end-over-end tumbling events, where the end-to-end distance varies from zero to full extension (example of such tumbling events are shown in Appendix B). This plateau was believed to be the asymptotic response of the chain at high shear rates, until some surprising results were observed in a bead-rod simulation study by Sendner and Netz [9] who observed that the dimension in the flow direction started to decrease at extremely high shear rates. Results from the same study also indicated that this chain shrinkage was hindered in the presence of excluded volume interactions between beads, but was

amplified by hydrodynamic interactions (HI). Using BD simulations of long bead-spring and bead-rod chains, the deformation behavior is analyzed in detail in the absence of HI and EV in Chapter III, which showed three distinct regimes. Regime 1 spans weak to moderate shear rates where the chain elongation increases with shear rate. Regime 2 covers intermediate flow rates where the chain stretch shows a plateau. And Regime 3 encompasses extremely high shear rates where a decrease in chain elongation is observed. From the results in Chapter IV, we observe that while the behavior in the first two regimes are insensitive to refinement of the chain, the behavior in the third regime results from insufficient resolution of the chain and can be suppressed in the absence of HI and EV if rods with bending potential are introduced to increase the refinement of the polymer model. The anomalous chain compression in Regime 3 with insufficient chain refinement occurs due to sequential flipping of individual rods, which slows the process of chain stretching to the point that end-over-end tumbling events occur before the chain becomes completely extended. If the rods are replaced by shorter rods with a bending potential, however, full extension is nearly attained before a tumbling event, and the decrease in elongation is avoided, thereby extending Regime 2 and avoiding the onset of Regime 3. Since these investigations in Chapters III and IV are limited to simulations without HI and excluded volume interactions, these effects need to be included to fully resolve the deformation behavior of real chains in the presence of shear.

In this Chapter, we therefore investigate chain deformation in shear when excluded volume interactions and HI are acting between the beads, thus completing the study of chain deformation due to shearing flows presented in the earlier Chapters. We add bead-bead

excluded volume interactions and HI separately and observe the effects of each on chain elongation (in the flow direction) and chain thickness (in the shear-gradient direction), relative to those obtained earlier without either of these additional mechanisms. Although some indications of the elongation behavior with HI and excluded volume interactions were given earlier in Ref. [9], the details and the relevance of those observations to actual systems are not fully clear, since only a single model (the bead-rod model) was used for a single chain length (100 rods). In this Chapter, after explaining our simulation methods in Section 2, we present and discuss our observations in Section 3. Our results with HI and excluded volume interactions for the chain stretch and width can again be categorized using three distinct regimes, but the trends at high shear rates change depending on which mechanism is acting between the beads. In what follows, we show that a rather small strength of bead-bead excluded volume interactions suppresses the chain shrinkage in Regime 3, while increasing HI systematically lowers the elongation, producing a highly coiled state at high shear rates in the absence of any excluded volume interactions. Note that, in Chapter VI, we discuss the range of shear rates in which experiments are possible without chain scission to relate to our results using BD simulations.

2. Simulation Methods

The model of the polymer chain, symbols for variables, and the governing equations used in this article are the same as discussed in Chapter III, unless otherwise mentioned. Briefly, using a characteristic length scale of one rod in a polymer chain model (l_{rod}), consisting of

beads connected by stiff springs that mimic inextensible rods, and a time scale of $\zeta l_{rod}^2 / k_B T$, where ζ is the bead drag coefficient, we arrive at the following equation of motion without HI and EV:

$$\frac{d\vec{r}_i^*}{dt^*} = \kappa^* \cdot \vec{r}_i^* + \left[\vec{F}_{i+1}^{S*} - \vec{F}_i^{S*} \right] + \sqrt{\frac{6}{\Delta t^*}} \vec{n}_i \qquad (1)$$

where all the variables have the same significance as described in Chapter III and the corresponding dimensionless variables are denoted by a '*'. For this study, we use two different types of chain models to understand the numerical artifacts caused due to the level of resolution: (i) the "bead-rod" model used earlier in Chapters III and IV for the polymer chain (henceforth referred to as the 'BR' model), where each "rod" is mimicked by a stiff Fraenkel spring and represents one Kuhn length of the polymer chain (b_K; thus for the BR model $l_{rod} = b_K$), and (ii) the 'fine-grained' (FG) model which also consists of beads connected by 'rods' (mimicked by stiff Fraenkel springs), where a harmonic bending potential acts between consecutive rods in the chain (details given in Chapter IV). The bending stiffness parameter can be tuned to obtain a given level of resolution, i.e. the number of rods that constitute a Kuhn step of the chain (thus for the FG model, $l_{rod} < b_K$). Further details and values of the bending stiffness required to obtain different levels of discretization are provided in Chapter IV. Most of the results in this study use the BR model, and FG models are used to highlight the importance of the inclusion of finer details in the results. In both the BR and FG models, the Fraenkel springs that mimic inextensible "rods" with a force law given as:

$$\vec{F} = K\left(\left|\vec{Q}\right| - 1\right)\frac{\vec{Q}}{\left|\vec{Q}\right|} \tag{2}$$

where K and $\vec{Q}$ are the stiffness constant of the Fraenkel spring and the spring end-to-end vector, respectively. With this spring force expression, Eq. (1) becomes:

$$\frac{d\vec{r}_i^*}{dt^*} = \kappa.\vec{r}_i^* + K^*\left[\left\{\left(\left|\vec{Q}_{i+1}^*\right| - 1\right)\frac{\vec{Q}_{i+1}^*}{\left|\vec{Q}_{i+1}^*\right|}\right\} - \left\{\left(\left|\vec{Q}_i^*\right| - 1\right)\frac{\vec{Q}_i^*}{\left|\vec{Q}_i^*\right|}\right\}\right] + \sqrt{\frac{6}{\Delta t^*}}\vec{n}_i \tag{3}$$

where the value of the parameter $K^* = \frac{Kl_{rod}^2}{k_B T}$ can be tuned to adjust the stiffness of the Fraenkel springs in the polymer chain. Following the approach in Chapter III, a value of $K^* = 10^4$ is used for $\dot{\gamma} < 10$ and $K^* = 10000\,\dot{\gamma}$ for $\dot{\gamma} \geq 10$ to prevent overstretching of the springs, unless otherwise mentioned. For the FG model, an additional force due to the bending potential between consecutive rods will also be present.

To investigate the effects of excluded volume interactions in either the BR or the FG models, the following Lennard-Jones potential (LJ) is introduced for the non-bonded interactions between beads (similar to the approach in Ref. [9]):

$$U_{ij} = 4\varepsilon\left[\left(\frac{\sigma}{\left|\vec{r}_{ij}\right|}\right)^{12} - \left(\frac{\sigma}{\left|\vec{r}_{ij}\right|}\right)^{6}\right] \tag{4}$$

where $\left|\vec{r}_{ij}\right| = \left|\vec{r}_i - \vec{r}_j\right|$ represents the inter-bead distance, σ represents the "diameter" of the beads and ε is the interaction strength. For the BR model, the excluded volume interactions

are only computed between beads that are separated by 2 or more rods, i.e. beads that are not consecutive to each other in the chain. In the FG model, the LJ interactions are excluded for all bonded neighbors within a Kuhn step (i.e. for an FG chain where four rods constitute one Kuhn step, the LJ interactions are excluded between beads that are separated by 4 rods or less), so that the scheme is consistent with that used for the BR model, where the excluded volume interactions are excluded between bonded neighbors (i.e. within one Kuhn step, since every rod in the BR model represents a Kuhn step). If the force due to the excluded volume interactions is included, the equation for the evolution of bead trajectories for the BR model is given as:

$$\frac{d\vec{r}_i^*}{dt^*} = \kappa.\vec{r}_i^* + K^*\left[\left\{\left(\left|\vec{Q}_{i+1}^*\right|-1\right)\frac{\vec{Q}_{i+1}^*}{\left|\vec{Q}_{i+1}^*\right|}\right\}-\left\{\left(\left|\vec{Q}_i^*\right|-1\right)\frac{\vec{Q}_i^*}{\left|\vec{Q}_i^*\right|}\right\}\right]$$
$$+4\varepsilon^*\sum_{j=0,|i-j|\geq 2}^{N}\frac{1}{\left|\vec{r}_{ij}^*\right|}\left[12\left(\frac{\sigma^*}{\left|\vec{r}_{ij}^*\right|}\right)^{12}-6\left(\frac{\sigma^*}{\left|\vec{r}_{ij}^*\right|}\right)^{6}\right]\frac{\vec{r}_{ij}^*}{\left|\vec{r}_{ij}^*\right|}+\sqrt{\frac{6}{\Delta t^*}}\vec{n}_i \qquad (5)$$

where the dimensionless parameters $\varepsilon^* = \frac{\varepsilon}{k_B T}$ and $\sigma^* = \frac{\sigma}{b_K}$ are used to adjust the interaction strength and the bead diameter for the Lennard-Jones interactions, respectively (Note that, for the BR model, we have $l_{rod} = b_K$). Also, for the FG model, there will be an additional force due to the harmonic bending potential between consecutive rods and the excluded volume interactions will only be computed between beads that are separated by a distance larger than one Kuhn step along the chain contour, as mentioned earlier. In the BR model, the excluded volume interactions between beads is modeled in two ways – (i) only

the repulsive part of the LJ potential is retained (thus dropping the attractive part of the interaction involving the $\left(\frac{\sigma}{|\vec{r}|}\right)^6$ term) and (ii) the full LJ potential is used with the value of ε^* tuned such that the radius of gyration of the chain at equilibrium is same as that of a theta coil (i.e. a chain where both HI and bead-bead excluded volume interactions are absent). The first way represents a traditional way of including the excluded volume interactions, which leads to coil expansion, while the second method includes both short-range repulsion and longer-range attraction, in such a way that their effects on equilibrium coil size cancel out. Henceforth, the first way will be denoted by the term 'EV', whereas 'EV-theta' will represent the second method that produces a theta coil at equilibrium. Interaction cut-off radii of $2.5\sigma^*$ and $2\sigma^*$ are used for EV-theta and EV, respectively. For the integrations involving excluded volume interactions, unless otherwise mentioned, a timestep size $\Delta t^* \leq (1/K^*)$ is used. However, for cases with relatively smaller bead 'diameter', i.e. $\sigma^* < 0.5$, a lower timestep size of $\Delta t^* \leq (1/10K^*)$ is needed to ensure good convergence of the results. The implicit numerical algorithm discussed in Chapter III is used for simulations using EV and EV-theta in this study. As described in Chapter III, for lower shear rates ($\dot{\gamma} < 1$), the total run time with EV varies with the number of rods in the chain (N; thus the number of Kuhn steps in the chain N_K = N for the BR model) and is usually chosen to be about 100 and 50 times the longest relaxation time for chains with N ≤ 200 and N > 200, respectively, for the BR model. Since the simulation time scales roughly as N^2 with either EV or EV-theta for computing the pairwise LJ interactions, chains longer than N = 300 are not considered either with the BR or the FG model. For the BR model, at

higher shear rates ($\dot{\gamma} \geq 1$), simulations are run for a total strain (one unit strain is defined as $\dot{\gamma}t$, where t is the simulation time) of at least 10^5 for N ≤ 200 and 5×10^4 for larger chains. Unless otherwise mentioned, the initial 20% of the simulation is kept for equilibration, and the final 80% of the run is used to calculate the average of each quantity.

The hydrodynamic interactions between the beads are modeled by the Rotne-Prager-Yamakawa (RPY) tensor as in earlier studies [8, 9] using the semi-implicit numerical scheme described in Ref. [8]. The selection procedure mentioned earlier for the values of the dimensionless spring stiffness parameter and the timestep size for integration works well even when HI is applied. We observed that, to get accurate results for our case of a BR or a FG chain, where beads are connected by stiff springs that mimic rods, the diffusion tensor (D_{ij}, defined in Ref. [8]) has to be updated after every time step unlike what is done in Ref. [8], where the beads are connected by coarse-grained springs. The hydrodynamic radius of the beads is controlled by the parameter h^* (defined in Ref. [8]), for which a maximum value of 0.5 is used in most of our simulations, representing a hydrodynamic bead diameter equal to the length of one rod, where one rod represents a Kuhn step and a sub-chain smaller than one Kuhn step in the BR and FG chains, respectively. With the introduction of HI, the simulation time scales roughly as N^3, which limits the maximum chain lengths for simulation to N ≤ 150 for any chain model. With the BR model, for lower shear rates ($\dot{\gamma} \leq 1$), the total run time with HI varied with the number of rods in the chain and is usually chosen to be above 100 times the longest relaxation time for chains with N ≤ 100 and about 50 times this for larger chains. At higher shear rates (

$\dot{\gamma} > 1$), simulations are run for a total strain of at least 5000 for N ≤ 100 and 1000 for larger chains. As in the case with excluded volume interactions, the average of any quantity is calculated using the final 80% of the simulation trajectory. These values also apply to cases where both HI and EV (or EV-theta) are present. However, note that for cases where both HI and EV are present, the equilibrium coil size is larger than that of the theta coil and, consequently, the end-to-end relaxation time is also larger. Hence, for most cases considered here, the total run time at weaker shear rates for chains with both HI and EV is much lower than 100 times the longest relaxation time, leading to relatively poorer statistics for weaker shear rates.

For all cases, the rotational relaxation time (τ) of the polymer chain is calculated by fitting the last 70% of the autocorrelation function for the chain end-to-end vector. The Weissenberg number (Wi) is defined as the product of the shear rate and the rotational relaxation time ($\mathrm{Wi} = \tau\dot{\gamma}$). The definitions of the radii of gyration R_{gx} and R_{gy} along the flow and flow-gradient directions, respectively, are given in Chapter III. In this Chapter, the terms "coil elongation" and "coil thickness" will denote R_{gx} and R_{gy}, respectively.

In the investigations in Chapter III with the BR model, the Peclet number (Pe), based on the relaxation time of one single rod, was defined as $\mathrm{Pe} = \mathrm{Wi}/\mathrm{N}_\mathrm{K}^2$ (Here N_K is the number or rods in one Kuhn step. Note, for the BR model N_K = N and $l_{rod} = b_K$). From another viewpoint, this pertains to using a rod relaxation time $\tau_r = \tau/\mathrm{N}_\mathrm{K}^2$, which is sensible to use in the absence of excluded volume interactions and HI when the relaxation spectrum of the modes in the chain scales as N_K^2. Thus, in Chapter III, this value of τ_r is related to the

characteristic time scale of the simulation ($\tau_0 = \zeta b_k^2 / k_B T$) by a prefactor of 0.0338 (equal to $1/3\pi^2$) that is obtained empirically using the values of τ measured for different chain lengths. Since the same characteristic time scale of $\zeta b_k^2 / k_B T$ is used for the simulations in this study using the BR model, for convenience we define $\mathrm{Pe} = 0.0338\dot{\gamma}$, thus using the same definition of the Peclet number as in Chapter III throughout for presenting our results from the BR model.

In this Chapter, we use the same definition of Regimes 1 and 2 as described in Chapter III. Regime 1 represents the range of relatively weak shear rates (or Peclet numbers) where the coil thickness stays constant at its equilibrium value, whereas Regime 2 denotes the intermediate shear rates where the coil elongation approximately reaches a saturation value (about 0.2L in the absence of HI and EV, where L is the contour length of the chain). As we will note later in this article, the variation of coil elongation and thickness at ultra-high shear rates (constituting Regime 3 in Chapter III) is highly sensitive to the mechanisms that are acting on the chain. For the BR model in this study, shear rates with $\mathrm{Pe} \geq 1$ are considered to be in Regime 3 for all cases, unless otherwise specified. As we note later in this Chapter, the chain deformation behavior, in terms of the Weissenberg number, is roughly similar in Regime 1 leading to Regime 2. Hence, the values of Wi for the end of Regime 1 and the onset of Regime 2, given in Chapter III, are still relevant for results shown here.

3. Results and Discussion

3.1. Scaling of relaxation times

To investigate the scaling of the relaxation times, we use the BR model throughout. As mentioned earlier, the rotational relaxation time for long chains scales as N_K^2 in the absence of HI and as $N_K^{1.5}$ in the presence of HI without excluded volume interactions, according to the Rouse and Zimm models, respectively. However, the BR model used here differs from the Rouse and Zimm models in two significant ways. (i) We consider a bead-rod polymer chain, where each "rod" in our chain is actually a stiff Fraenkel spring, mimicking a Kuhn step, which resolves the polymer more finely than does a chain of Hookean springs, where each spring represents several Kuhn steps. (ii) We account for the effects of instantaneous fluctuations of HI in our BD simulations, whereas pre-averaged HI was used in the Zimm theory. Hence, it is worthwhile to compare the scaling of the rotational relaxation times of our chains with those of the Rouse and Zimm analytical theories. To the best of our knowledge, no other study has computed the relaxation times from bead-rod model similar to that used in this study.

Figure 5.1 shows the variation of the relaxation times of chains of different lengths in the presence of only EV (in the absence of HI) and only HI (in the absence of EV), using the BR model. For all cases with EV, the dimensionless energy scale ε^* in the LJ potential and the dimensionless excluded volume diameter of the beads σ^* (in Eq. 5) are both taken to be unity. For the results with HI, the bead hydrodynamic diameter is taken to be equal to the length of one Kuhn step. We observe that, in the presence of EV and without HI, the exponent for the dependence of relaxation time on chain length is about 2 (see Fig. 5.1),

which is similar to that obtained from the Rouse theory. In the presence of HI (without EV), the exponent is approximately 1.5, which is quite consistent with the predictions of the Zimm model. Thus, our results highlight the generality of the Rouse and Zimm theories, despite the differences mentioned earlier. The inset shows the variation of the chain radius of gyration with chain length (in terms of number of Kuhn steps) in the presence of EV (without HI). The exponent of about 0.6 for the power law obtained from our results agrees very well with that expected for polymer chains of different lengths in good solvents.

3.2. Effects of EV (without HI)

The representative values of the LJ parameters used here are $\sigma^* = 1.0$ (i.e. one Kuhn length for the BR model) and $\varepsilon^* = 1.0$ (i.e. 1 k_BT), while accounting for only the repulsive part of the potential. Figure 5.2 and its inset show the Peclet number variation of the average coil elongation and the coil thickness, respectively, for the BR model. The trends obtained for the variation of both R_{gx} and R_{gy} in weak to intermediate shear rates (encompassing Regimes 1 and 2) are quite similar to those in the absence of excluded volume interactions (see Chapters III and IV), with the "plateau" in R_{gx} that characterizes Regime 2 becoming increasingly evident at higher chain lengths. Also, the value of R_{gx}/L at the plateau is similar to that in the absence of EV. However, interestingly, a true "plateau" is not obtained, as the coil elongation increases gradually with shear rates instead of reaching a saturation value, as observed earlier for chains without EV and HI. Also, note that, the

decrease in R_{gx} at high shear rates is absent for all chain lengths considered, as indicated earlier in Ref. [9] for a chain of 100 rods. Instead, Regime 3 is characterized by frequent "orientational locking" in the completely stretched state with all bonds oriented in the flow direction at shear rates much lower than that required for locking to occur in bead-rod chains without excluded volume interactions (for BR chains, locking appears beyond Regime 3 for chains without EV or HI, as noted in Chapter III). Similar to the case of non-interacting beads presented earlier in Chapter III, R_{gy} stays constant at the equilibrium value in Regime 1, and in Regime 2 follows a power law with an exponent of about -1/4 and is independent of the chain length (inset of Figure 5.2). In Regime 3, increasing orientational "lock-up" in the fully extended state causes the average chain dimensions in the shear-gradient direction to decrease with shear rate.

This "locking" behavior is shown more clearly in the inset of Figure 5.3, where the temporal variation of the chain end-to-end distance (for a chain of BR 100 rods with $\sigma^* = 1.0$) is presented at different Peclet numbers. A systematic increase in the duration of orientational locking in the fully stretched state is clearly observed with increasing shear rate, which accounts for the slow increase in R_{gx} at high shear rates, in place of a long plateau or decrease in R_{gx} at high shear rates in Figure 5.2. As noted earlier in Chapter III, Regime 3 is characterized by the presence of back-folds where beads come very close to one another, even in the most stretched states that the chain can attain before tumbling. In the presence of excluded volume interactions, back-folds are likely to be hindered by repulsive forces between beads, and so the chain remains locked in the extended state for a considerable duration before tumbling can start.

Given the fact that a decrease in R_{gx} with shear rate does not occur for beads interacting via a Lennard-Jones potential with $\sigma^* = 1$, the mean coil elongation presented in Figure 5.3, for different values of σ^* with ε^* fixed at 1.0, indicate that the chain behavior for the BR model in strong shear flows is significantly affected by the bead "diameter" (σ^*), with a regime where R_{gx} decreases with increasing shear rate, reminiscent of Regime 3 for ideal bead-rod chains (see Chapter III), re-appearing only when σ^* is reduced to about 10% of the Kuhn length. Even when σ^* is reduced to this degree, the power-law exponent of the dependence of R_{gx} on shear rate is only around -0.058 (± 0.08), instead of the value of -0.15 obtained when bead interactions are neglected entirely (results shown in Chapter III). Thus the coil elongation at high shear rates for the BR model is extremely sensitive to the strength of excluded volume interactions, even when such interactions are still very weak.

More detailed analysis of the properties of the orientational "locking" behavior is presented in the results of Figure 5.4. The probability distributions of the end-to-end distance for a BR chain of 100 rods at different Peclet numbers are shown in Figure 5.4(a). A bin size of 5 is used to calculate the distributions, whereas the inset shows the same calculated with a bin size of 0.5. It is observed that at Pe = 0.00338 ($\dot{\gamma} = 0.1$), the distribution is peaked at low values of coil stretch, which is expected since the polymer chain does not get significantly extended at relatively weaker shear rates. The roughly uniform distribution at Pe = 0.0338 is reminiscent of those obtained in Chapter III, for chains without EV in shear rates of Regime 2. However, at higher shear rates, the probability of the fully extended state becomes positive, which indicates a significant

proportion of highly stretched states at these shear rates. In this context, note that the probability distributions for a BR chain of 100 rods in the same range of shear rates, in the absence of EV, never show a large positive value for such highly stretched states (shown in Chapter III).

The probability distributions in the inset of Fig. 5.4(a) are calculated from the same trajectories, but are much more refined with a bin size that is 10 times smaller. These resolve the peak in the distribution in the region of highly stretched states and show the presence of orientational locking as well. Clearly, the locked states occur only at Pe = 1.69 (i.e. Pe > 1), with a significantly large positive probability for the fully extended state. At lower values of Pe, the peak occurs at highly stretched states but the fully stretched state is not present.

Figure 5.4(b) shows the variation of the average residence time (t_{res}) in the highly stretched state, normalized by the chain length, with shear rates. Note that "time" is calculated here in terms of dimensionless strain units ($\dot{\gamma}t$, consistent with that used in the inset of Fig. 5.3), but we prefer to call it a "residence time" instead of "residence strain". Here, one individual residence time is calculated by the duration in which the chain end-to-end distance is greater than 99.7% of the chain length. Although not shown, the trends are similar if we use 99.9% of the chain length instead of 99.7%. It is clearly observed that the average residence times scale linearly with chain length at high shear rates, thereby producing almost universal results for the normalized residence times. The inset shows the Peclet number variation of the fraction of the total trajectory in which the chain stretch is greater than 99.7% of the chain length (t_{frac}). Note that, for Pe $\geq 10^4$, this fraction is quite

close to 1, which shows the existence of a significant proportion of locked states in the trajectory. Similar to those for t_{res}/N_K, t_{frac} is almost independent of chain length at high shear rates. Thus, the results in Fig. 5.4(b) explain the chain length independence of coil elongation values (normalized by chain length) at high shear rates.

3.3. Effect of HI (without EV)

For most simulations of the BR model with HI discussed in what follows, a bead hydrodynamic diameter equal to one Kuhn length is used (corresponding to $h^* = 0.5$). Figure 5.5 and inset (i) show the variation of R_{gx} and R_{gy}, respectively, with shear rate. The coil elongation (Fig. 5.5) shows an initial increase with shear rates and a decrease at high shear rates. Although these trends in both the coil elongation and thickness are similar to those obtained in the case without HI and EV, the plateau in R_{gx} that constitutes Regime 2 in the earlier studies in Chapters III and IV without HI is reduced to nothing more than a local maximum in R_{gx} for the chain lengths considered in this study. The coil elongation shows a slow decrease after the maximum followed by an abrupt transition to very low values at the highest shear rates. Also, the decrease in R_{gx} depends on chain length and is much steeper (power law exponent about -0.75 for 60 rods and -0.93 for 125 rods) than without HI or EV (power law exponent of -0.15 for all chains Chapter III). Additionally, the maximum occurs at an R_{gx}/L value of about 0.1, which is lower than the corresponding value of 0.2 obtained for the plateau without HI in earlier simulations in Chapter III as well as for the results for EV without HI presented earlier in this Chapter (Fig. 5.2). These

trends are consistent with the simulation results for a chain of 100 rods with HI in the earlier study by Sendner and Netz [9].

In addition to the lower maximum value of R_{gx}/L, another significant difference from chains without HI is that the value of R_{gx} at high shear rates in Regime 3, shown in the inset (ii) to Figure 5.5, is very small, only around one Kuhn length (which is the length of one rod for the BR model). Hence the ratio R_{gx}/L monotonically decreases with chain length at high shear rates in Figure 5.5. The variation of the coil thickness with shear rate (inset (i)) is similar to those observed earlier (see Chapter III), including the appearance of all three regimes. In Regime 1, R_{gy} remains close to the equilibrium (no-flow) value; in Regime 2, where R_{gx} goes through a maximum, R_{gy} decreases with a power law exponent of about -1/4; and in Regime 3, R_{gy} saturates at very high shear rates. Furthermore, the values of R_{gy} become independent of chain length for longer chains at high shear rates, which is consistent with the earlier observations in Chapters III and IV.

The absence of a plateau in chain stretch and the greater tendency of the BR chain to form a coil are also highlighted in the results in Figure 5.6(a). This shows the probability distribution of the chain end-to-end distance for a BR chain of 100 Kuhn steps at different shear rates. Note that at all shear rates the probability distribution shows a maximum at a low value of end-to-end distance, with the highly stretched states being significantly less probable. Also, the probability distribution shows a sudden transition between the shear rates of $\dot{\gamma} = 10$ (Pe = 0.338) to $\dot{\gamma} = 100$ (Pe = 3.38), corresponding to the abrupt transition to very low values of R_{gx} already shown in Fig. 5.5. The absence of the largely uniform probability distribution of coil elongation observed for the shear rates in Regime 2 in the

absence of EV and HI (Chapter III and Ref. [7]) further confirms that HI promotes the clustering of beads and thus significantly reduces the probability of stretched states.

This clustering due to HI at high shear rates with the BR model in Regime 3 is highlighted further in the inset of Figure 5.6(b), which shows the coiling of a BR chain of 100 rods, starting from an initial fully stretched state, at a shear rate of $\dot{\gamma}$ = 100 (Pe = 3.38). The inset presents the sequence of chain configurations leading to a coiled state, where time increases from top to bottom and the snapshots are zoomed in at higher times to show the clustering of beads more clearly. Fig. 5.6(b) shows the corresponding temporal variation of the end-to-end distance, which shows a sharp decrease to a coiled state with no further stretching. This behavior of tumbling in the coiled state with HI contrasts with the behavior in Regime 3 in earlier simulations that omitted HI (discussed in Chapter III), in which the chain tumbles by a sequence of stretched and coiled states, with the maximum stretch decreasing with increasing shear rate, but not to the extent seen when HI is present. We will show later in this Chapter that this extreme clustering and overlapping of beads is unrealistic, and disappears once bead-bead excluded volume interactions are introduced or the chain model is discretized further.

Figure 5.7 and its inset shows the effect of bead hydrodynamic diameter on the variation of the coil elongation and thickness with shear rates, respectively, for a chain of 100 rods in the absence of any excluded volume interactions. As discussed earlier, the hydrodynamic diameter is controlled by the parameter h^*, where h^* = 0.5 represents a hydrodynamic diameter of one rod length (or one Kuhn step for the BR model). The trends in Fig. 5.7 are presented as functions of Weissenberg number Wi, rather than Peclet number. Results in

Fig. 5.7 show that, at any Wi, R_{gx} decreases with increasing bead hydrodynamic diameter, especially at high Wi, indicating an increased clustering of beads at higher HI. As expected for low bead hydrodynamic diameter, $h^* = 0.05$, the elongation approaches that for a 100 rod chain without HI over a wide range of shear rates, although the transition to Regime 3 occurs at a somewhat lower value of Wi, when $h^* = 0.05$ than it does for $h^* = 0$. As h^* increases, this transition becomes more abrupt and occurs at even lower values of Wi. Also, the value of the maximum coil elongation decreases with increasing h^*, and the range of shear rates over which there is a plateau in elongation also decreases systematically. Interestingly, even in Regime 1 the chain deformation decreases with increasing h^*, which might be relevant to the experimental observations presented in the study by Lee *et al.* [10] who observed much smaller chain deformation at modest Wi compared to that predicted by the Rouse or Zimm predictions. The inset presents the variation of R_{gy} with Wi for different values of h^*, which show systematic deviations from the results with no HI only at high shear rates. Similar to the results for R_{gx}, the saturation in R_{gy} at high flow rates occurs at lower Wi, and hence at higher values of R_{gy}, when h^* increases, highlighting an early transition to Regime 3. At lower shear rates, all the results are almost identical with each other.

3.4. Effects of HI, EV and bead-bead attraction (EV-theta)

Figure 5.8 and its inset present the chain deformations along the flow and shear-gradient directions when both hydrodynamic interaction (HI) and bead-bead excluded volume

interactions are included in the BR model. For all these simulations, the bead hydrodynamic diameter is taken as one Kuhn length, and so $h^* = 0.5$. Figure 5.8 presents the Peclet number variation of R_{gx}/L for chains of different lengths using EV and EV-theta. Similar to the case of a chain with HI, chains larger than 150 rods are not considered owing to high computational cost. It is clear from Fig. 5.8 that the results for EV and EV-theta are qualitatively similar over the range of shear rates considered. The overall trends agree well with those obtained for case of chains where only EV acts between beads (Figure 5.2), with an increase in coil elongation followed by a plateau-like region (Regime 2) and a slow increase at extremely high shear rates (Regime 3). However, the value of R_{gx}/L at the plateau is about 0.2 for EV, which is close to that obtained for chains where both HI and any bead-bead LJ interactions are absent, compared to roughly 0.1 for EV-theta, which is similar to the corresponding value for chains where only HI acts between beads, as discussed earlier. The short range repulsive interactions between beads presumably reduce the clustering of beads mentioned earlier and increases the coil elongation at intermediate shear rates where the plateau occurs. For EV-theta, additional long range attractive interactions between beads counter-balances the effect of short range repulsion and reduces the elongation to a value similar to that of a chain without EV. The values of R_{gx}/L show a slow increase at large shear rates (in Regime 3) similar to the case of chains with only EV discussed earlier in this article. As mentioned earlier for chains with only EV, this increase is caused by increased locking in the fully stretched state, similar to what is shown in the inset of Fig. 5.3. In accordance with the results for coil elongation, the results for R_{gy} for EV and EV-theta shown in the inset of Fig. 5.8 are quite

similar to those observed in the earlier case with only EV. Again, there is a low shear rate region of nearly constant R_{gy} (Regime 1), followed by a power-law decrease (exponent around -1/4 for the chains considered) at intermediate shear rates (Regime 2). At extremely high shear rates in Regime 3, increasing orientational locking causes a further decrease of R_{gy}.

3.5. Comparison of effects of different mechanisms

Figure 5.9(a) and (b) presents a comparison of the coil elongation and tumbling behavior for a chain of 100 rods (using the BR model) with increasing shear rates, for different combinations of mechanisms. The results are plotted against Weissenberg number, instead of the Peclet number, to highlight the consistency in the results. In all cases, the bead-bead excluded volume interactions is modeled by EV-theta with $\sigma^* = 1$, whereas the bead hydrodynamic diameter is equal to the length of a single rod (which represents one Kuhn step in the BR model). Figure 5.9(a) shows that R_{gx}/L with only EV-theta approximately agrees with results in the absence of any excluded volume interactions and HI, except at extremely high shear rates of Regime 3, where the LJ potential between the beads hinders the bead overlap that causes chain shrinkage. However, in the intermediate shear rates (in Regime 2), R_{gx}/L shows a gradual increase with shear rates even with EV-theta, instead of a "plateau" obtained for chains in the absence of HI and any excluded volume interactions, similar to the results in Figure 5.2 for chains with EV. The presence of HI ($h^* = 0.5$ in this case), with or without EV-theta, reduces the chain deformation in Regime 1 and lowers the

maximum R_{gx}/L to about 0.1 (relative to 0.2 without EV-theta or HI). Without EV-theta, the coil elongation shows a very short plateau followed by a sharp transition to chain shrinkage, because HI without excluded volume interactions promotes bead clustering, as discussed earlier. With EV-theta and HI, the elongation decreases below the maximum and then increases again and eventually merges with the results obtained with EV-theta only at extremely high shear rates, instead of showing chain shrinkage in Regime 3, presumably due to orientational locking in the extended state at high shear rates, as discussed earlier.

The variation of the chain tumbling times (normalized by the end-to-end relaxation time τ) with Wi in Regimes 1 and 2 is shown in Figure 5.9(b). The tumbling time is the average time needed for an extended chain to rotate through the flow direction, coil up, and then re-extend, as discussed elsewhere [7] and calculated using the algorithm explained in Chapter IV. At high shear rate, the coiling-up process occurs by means of growth of chain loops formed at chain ends, also discussed in Chapter IV. Average chain loop sizes (which set the value of R_{gy}) in this range of shear rates are similar to those reported in Chapter IV (see Figure 4.2(c)). The trends for the tumbling time are consistent with those expected based on the observations for the coil elongation in Fig. 5.9(a). The results for cases without HI, with or without EV-theta, agree with one another and show a power law regime with an exponent of about -3/4 in the range of shear rates where the plateau is observed in R_{gx} (Regime 2), which is explained in Chapter IV. When both HI and EV-theta are present, the tumbling times are reduced below those in the absence of HI, but a similar scaling law is observed, consistent with the fact that the coil elongation roughly follows a plateau in Regime 2. The lower values of the observed tumbling time are expected due to lesser

maximum elongation in this case. When only HI is present, the tumbling time decreases with a steeper with an exponent of about -1.1, owing to the decrease in coil elongation instead of a plateau in this case.

3.6 Effects of Chain resolution

Our results in Chapter IV, in the absence of HI and any excluded volume interactions, have shown that the chain response at ultra-high shear rates in Regime 3 is highly sensitive to the chain resolution, with the onset of the decrease in the coil elongation being pushed to higher shear rates with increasing levels of discretization. In this Chapter, we use the FG model to study the changes in the response of the chain over a wide range of shear rates, in the presence of EV and HI, when the chain resolution is increased systematically. The studies presented here with EV (and without HI) and with HI (in the absence of EV) are performed on chains consisting of 25 and 12 Kuhn steps, respectively, at varying degrees of resolution. The values of the bending stiffness needed to attain a certain number of rods per Kuhn step in the FG chain (i.e. the chain resolution) are shown in Table 4.1.

Figure 5.10 shows the variation of the coil elongation (normalized by L) with the Weissenberg number, for BR and FG chains of different resolutions, all consisting of a total of 25 Kuhn steps. Across all resolutions, we used $\varepsilon^* = 1.0$, while tuning the values of σ^* at each level of resolution such that the coil sizes are similar in the absence of shear flow (Note that $\sigma^* = 0.6$ for the BR model for these simulations. Since there are more beads, and hence more pairwise interactions, in chains with higher levels of resolution, the

same values of ε^* and σ^* will give a larger coil size at equilibrium with increasing resolution.). Interestingly, although minor differences exist between the results at relatively lower shear rates, the behavior at high shear rates is independent of the level of chain discretization, in sharp contrast to the results in Chapter IV for cases without HI and excluded volume interactions. The variation of the coil thickness with Weissenberg number (shown in the inset) is also similarly consistent over varying degrees of chain resolution. These results indicate that our observations presented earlier for BR chains with EV (and similar ones shown for a chain of 100 rods in Ref. [9]) will remain valid over the entire range of shear rates considered in this study.

Figure 5.11 presents a similar study in the presence of HI (without excluded volume interactions), for chains of varying resolutions that consist of 12 Kuhn steps. For all levels of resolution used in this case, we use $h^* = 0.5$. The behavior of R_{gx}/L for different model discretizations is similar to those presented in Chapter IV, with the plateau in coil elongation becoming more prominent with increasing chain resolution, consequently pushing the onset for the decrease in chain stretch to arbitrarily high Wi. A similar behavior is observed for the coil thickness as well (given in the inset), with the onset of saturation in R_{gy} occurring at larger values of Weissenberg numbers with increasing Chain resolution. These results imply that our observations regarding the clustering of beads in the presence of HI, leading to highly compact configurations, is most likely an artifact due to insufficient chain resolution. In the continuous bending limit (i.e. when there are an infinite number of rods to model one Kuhn step), when only HI is acting (without any

excluded volume interactions), the onset of the decrease will be pushed to $\mathrm{Wi} \to \infty$ and only Regimes 1 and 2 will be present, similar to the observations in Chapter IV.

4. Summary

We have presented a detailed study of the effects of hydrodynamic interaction (HI) and excluded volume on the deformation behavior of polymer chains subjected to a wide range of shear rates. For most investigations, we have adopted a bead-rod chain, where each rod is modeled by a stiff, nearly inflexible Fraenkel spring, which mimics a single Kuhn step in the chain. The EV and HI between beads are computed using the Lennard-Jones (LJ) potential and Rotne-Prager-Yamakawa (RPY) tensor, respectively. Our results show three distinct regimes in most cases, just as without HI and excluded volume interactions given in the earlier Chapters. These regimes are distinguished by the shear rate made dimensionless with either the relaxation time of the whole chain, which is the Weissenberg number Wi, or with the relaxation time of a single rod, which is the rod Peclet number Pe. With increasing shear rate, these regimes are as follows. Regime 1: a low shear-rate regime with Wi less than around 100 or so (depending on chain length, where the Wi values are roughly similar to those given in Chapter III) in which the coil elongation in the flow direction R_{gx} increases with shear rate while the coil thickness in the gradient direction R_{gy} remains nearly constant. Regime 2: a modest shear rate regime with Wi > 100 or so and Pe < 1, having a plateau in R_{gx} and a -1/4 power-law decrease in R_{gy} with R_{gy} independent of chain length. Regime 3: an ultra-high shear rate regime with Pe > 1, where the shear is

strong enough to highly orient individual rods and the results are sensitive to the modeling details.

While excluded volume expands the coil size in Regime 1, it has little effect on coil dimensions in Regime 2. However, in the presence of excluded volume, the plateau observed in the results of Chapters III and IV is replaced by a weakly increasing coil elongation. An increase in HI (increase in the bead hydrodynamic diameter) systematically reduces the chain elongation in Regimes 1 and 2, to such an extent that the maximum elongation in Regime 2 is lowered by a factor or roughly two when the bead hydrodynamic diameter equals the length of each rod (or Kuhn step), relative to chains without HI and EV.

In Regime 3, if there is no bead-bead repulsion, the BR chain eventually suffers a decrease in elongation with increasing shear rate even with no HI or excluded volume interactions, and HI strongly exaggerates this tendency, so that the coil elongation R_{gx} even drops below the value it has in the absence of flow, down to a length of roughly a single rod length. This coiled up state in the presence of HI is sustained by the overlap of beads, and even small levels of short-range bead-bead repulsion suppress this coil collapse. This collapse is removed even if the short-range bead repulsion is accompanied by longer-range attraction, such that the coil achieves a theta condition at equilibrium. In the presence of bead-bead excluded volume interactions, Regime 3 is characterized by increasing levels of orientational "locking" in the fully extended state. Here "locking" refers to periods in which the chain remains completely extended with all rods aligned in the flow direction. Our simulations with the FG model, which is resolved to length scales lower than one

Kuhn step, highlights the universality of the chain deformation behavior at high shear rates in the presence of excluded volume interactions. Similar simulations in the presence of HI (without any excluded volume interactions) shows that the chain compression at high shear rates obtained with the BR model is a numerical artifact, and the onset of such decrease in chain stretch will be pushed to arbitrarily high shear rates with increasing model resolution.

References

[1] Smith, D. E.; Babcock H. P.; Chu S. *Science* **283**, 1724-1727 (1999).

[2] Hur, J. S.; Shaqfeh, E. S. G.; Babcock, H. P.; Smith, D. E.; Chu, S. *J. Rheol.* **45**, 421-450 (2001).

[3] Schroeder, C. M.; Teixeira, R. E.; Shaqfeh, E. S. G.; Chu, S. *Phys. Rev. Lett.* **95**, 018301 (2005).

[4] Liu, T. W. *J. Chem. Phys.* 90, 5826-5842 (1989).

[5] Doyle, P. S.; Shaqfeh, E. S. G.; Gast, A. P. *J. Fluid. Mech.* **334**, 251-291 (1997).

[6] Petera, D.; Muthukumar, M. *J. Chem. Phys.* 111, 7614-7623 (1999).

[7] Hur, J. S.; Shaqfeh, E. S. G.; Larson, R. G. *J. Rheol* **44**, 713-742 (2000).

[8] Hsieh, Chih-Chen; Li, Lei; Larson, Ronald G. *J. Non-Newtonian Fluid Mech.* 113, 147-191 (2003).

[9] Sendner, C.; Netz, R. R. *Eur. Phys. J. E* **30**, 75-81 (2009).

[10] Lee, E. C.; Solomon, M. J.; Muller, S. J. *Macromolecules* 1997, 30, 7313-7321.

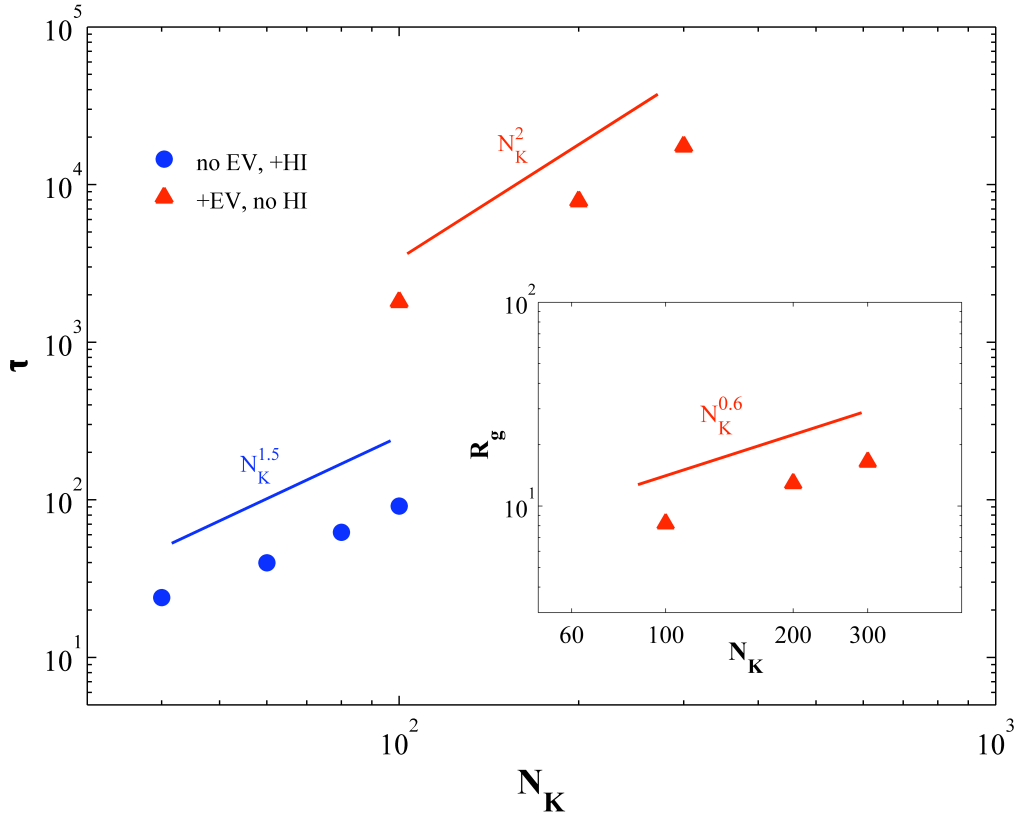

Figure 5.1: Dependence of relaxation time for polymer chains on the number of Kuhn steps, for cases where only excluded volume (EV) and only hydrodynamic interactions (HI) is included. The '+' sign and 'no' indicate the mechanism that is active and not present, respectively. Note that, for results with EV, only the repulsive part of the LJ potential with $\sigma^* = 1$ is used for results presented here. The solid lines indicate that the results follow power laws with exponents of approximately 2 and 1.5 for cases with EV and HI, respectively. The inset shows the variation of the coil radius of gyration at equilibrium with chain length when EV is active. The solid line indicates a power law with an exponent of about 0.6. Note that all these results are obtained using the BR model.

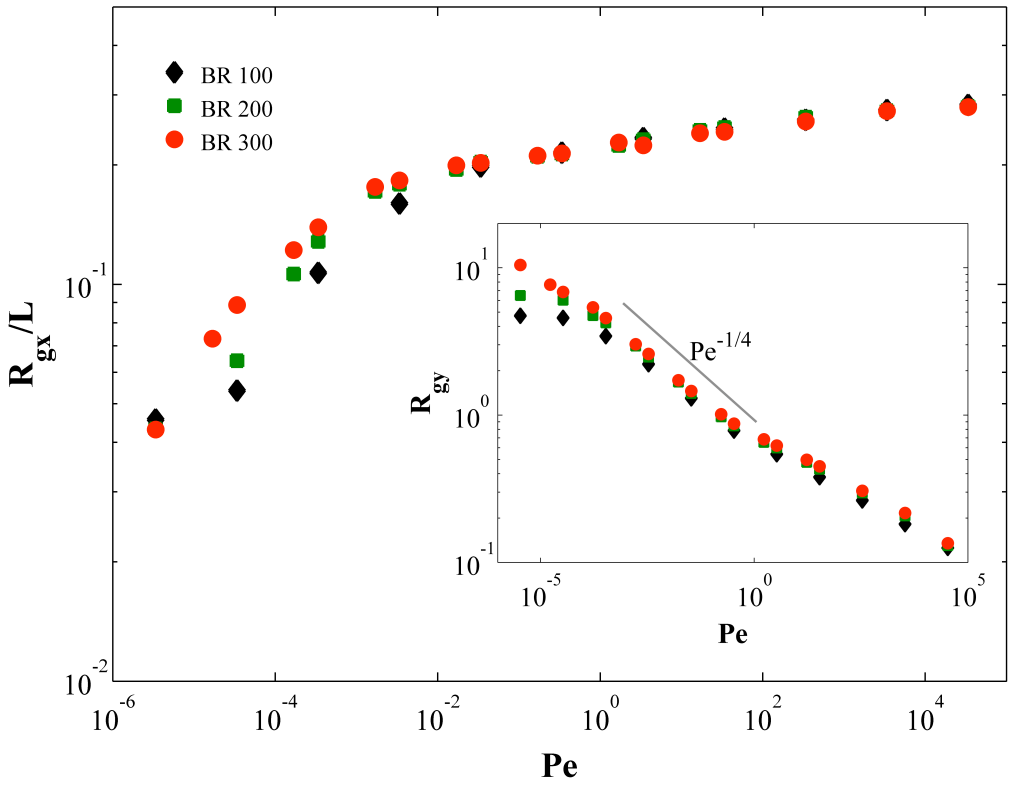

Figure 5.2: Dependence of the chain elongation normalized by chain contour length L on shear rate for chains of different length, when only EV is active between beads. For all results shown here, EV is modeled by the repulsive part of the LJ potential with $\sigma^* = 1$. The inset shows the dependence of the coil thickness R_{gy} on shear rate for chains of different length, when only EV is present. The solid line marks the region of shear rates where R_{gy} follows a power law with an exponent of approximately -1/4.

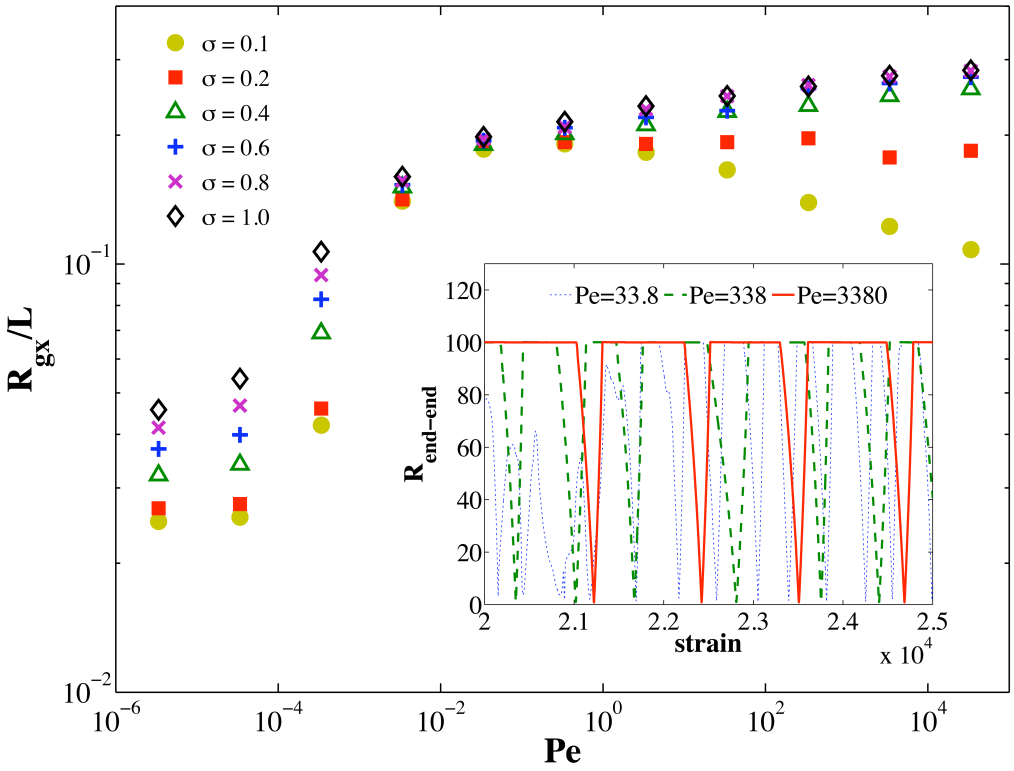

Figure 5.3: Dependence of chain elongation on Peclet number for varying strength of EV, modeled by different values of σ^*, where EV is modeled by the repulsive part of the LJ potential. The results show that chain shrinkage at high shear rates occurs only for $\sigma^* = 0.1$, but the exponent (-0.058) is much smaller than in the case reported in earlier simulations in Chapter III (-0.15) without EV or HI. The inset shows the time variation of the end-to-end distance of a chain of 100 rods at high shear rates, with $\sigma^* = 1$. The 'strain' is the dimensionless time $t\dot{\gamma}$. The plot shows increasing levels of orientational locking at a stretched state at shear rates of $\dot{\gamma} = 10^3$, 10^4 and 10^5, corresponding to Pe = 33.8, 338 and 3380 respectively.

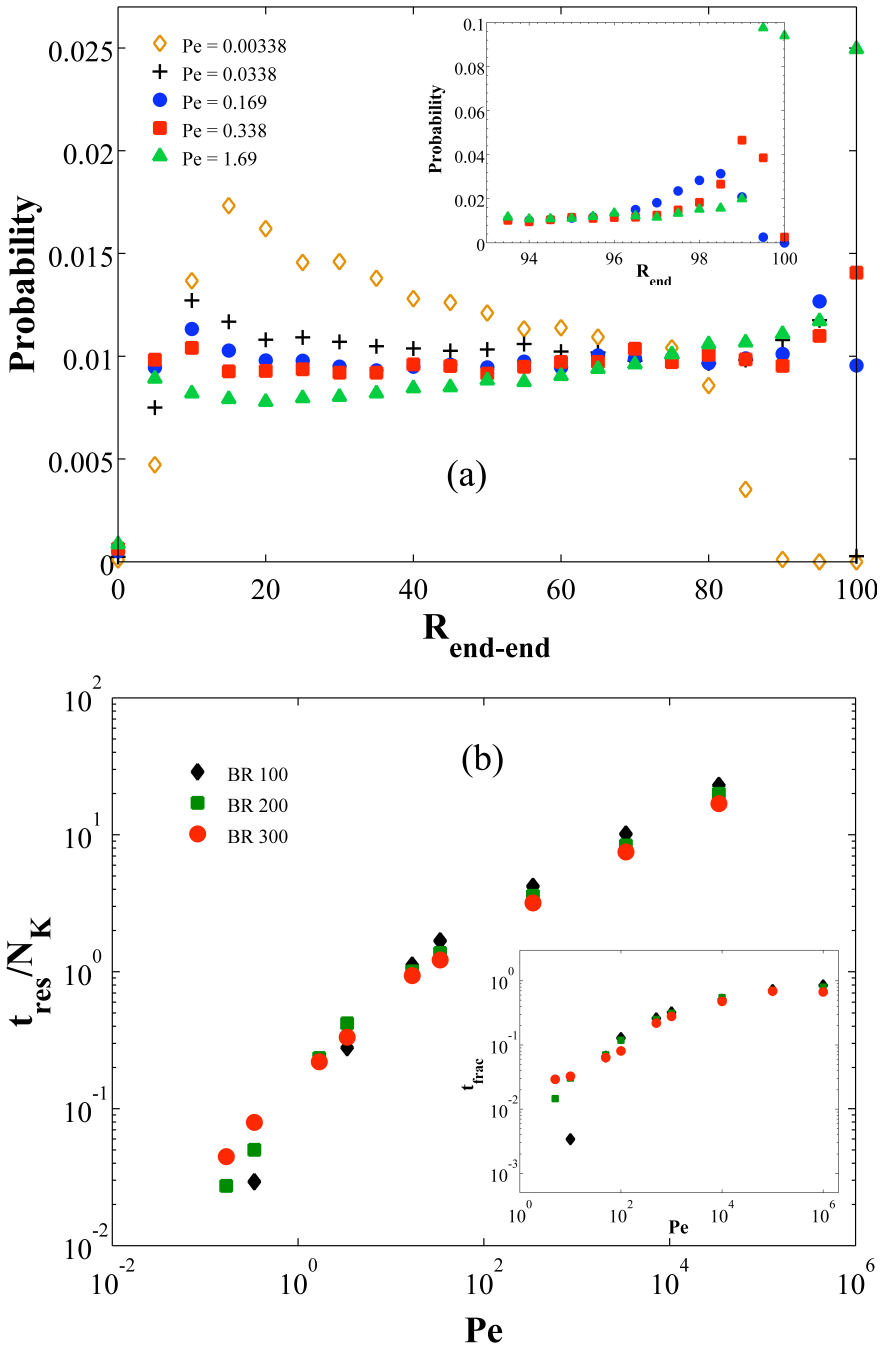

Figure 5.4: (a) Probability distributions of the chain end-to-end distance for a BR chain of 100 rods at different shear rates, denoted by Peclet numbers, calculated using a bin size of 5. The inset shows the same for highly stretched states, using a bin size of 0.5. (b) The Peclet number variation of the average residence time for a chain in a highly stretched state, normalized by the chain length. Inset shows the shear rate dependence fraction of time that the chain spends in a highly stretched state over the whole trajectory. For more details and the definitions of the quantities, see text.

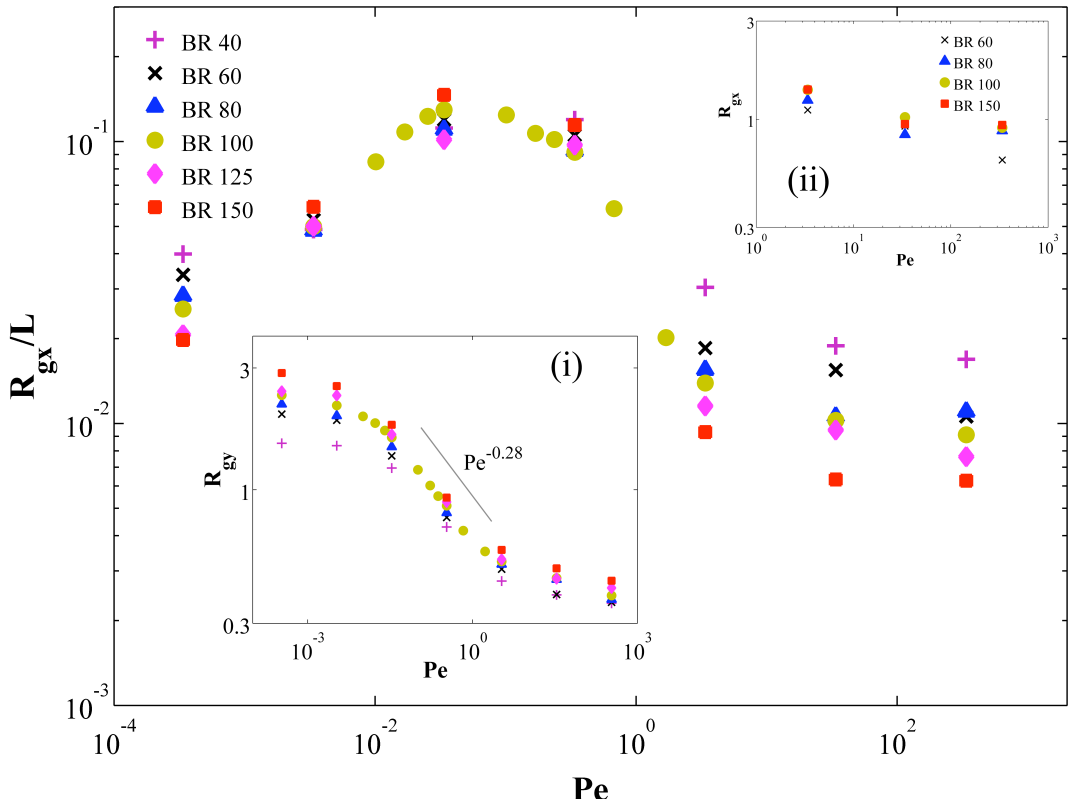

Figure 5.5: Shear rate dependence of the chain elongation R_{gx} normalized by chain contour length L for BR chains of different length, when only hydrodynamic interaction (HI) is active between beads. For all results shown here, the hydrodynamic diameter of beads is equal to one Kuhn length (represented by one rod in the BR model). Inset (i) shows the shear rate dependence of the coil thickness, represented by R_{gy}, for chains of different lengths, when only HI is present. The solid line marks the region of shear rates where R_{gy} follows a power law with an exponent of approximately -1/4. Inset (ii) shows that the chain forms a coil with R_{gx} of roughly one Kuhn length at high shear rates, for all chain lengths considered.

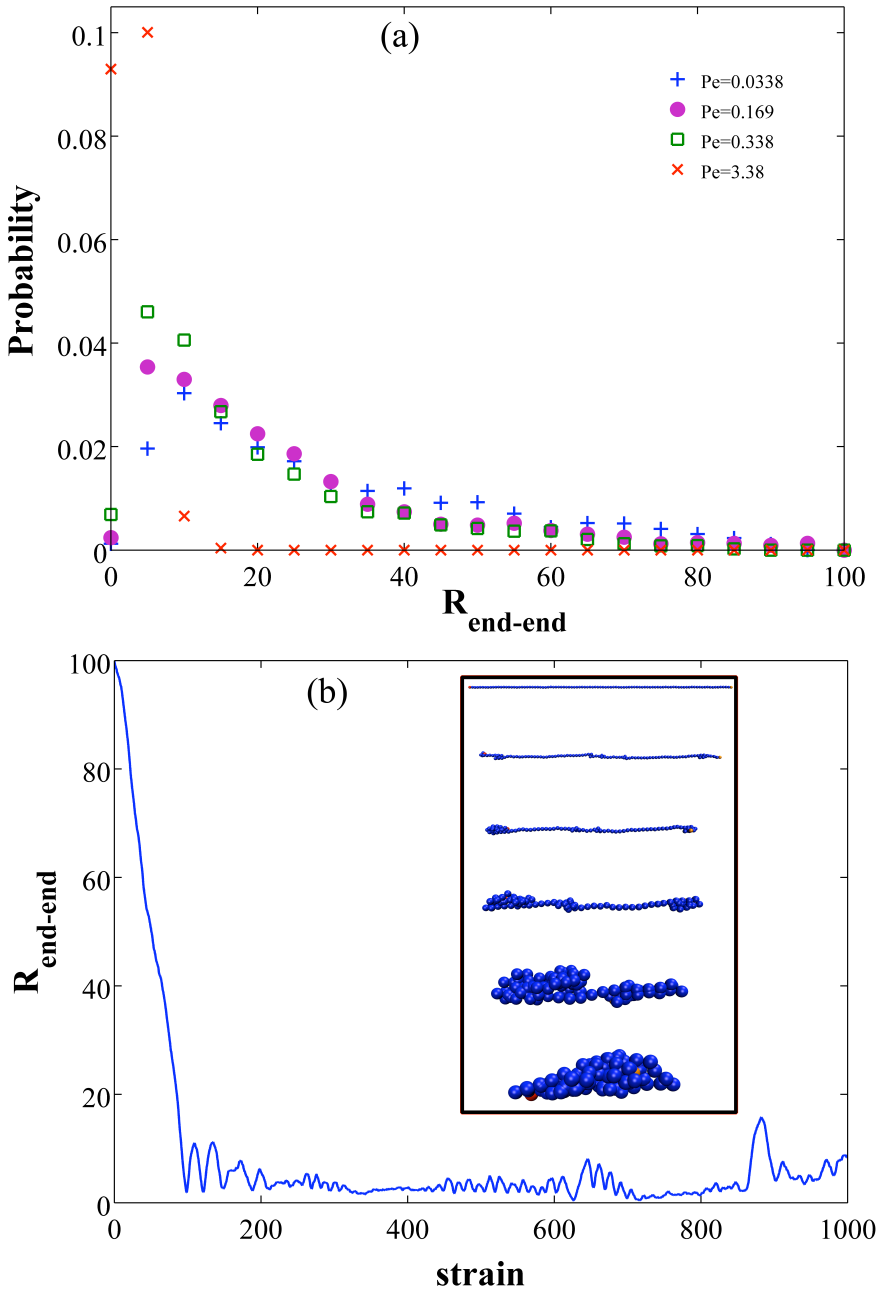

Figure 5.6: (a) The probability distribution of chain end-to-end distance at different shear rates for a BR chain of 100 rods, when only HI is present between beads with a hydrodynamic diameter of one Kuhn length ($h^* = 0.5$). (b) The time variation of the end-to-end distance of a BR chain of 100 rods from a stretched state, with only HI present, at a shear rate with Pe = 3.38 ($\dot{\gamma} = 100$). Inset shows the corresponding sequence of chain configurations to form a coiled state starting from a stretched state, where time increases from top to bottom. Note that the chain shows negligible stretching once a coiled state is attained.

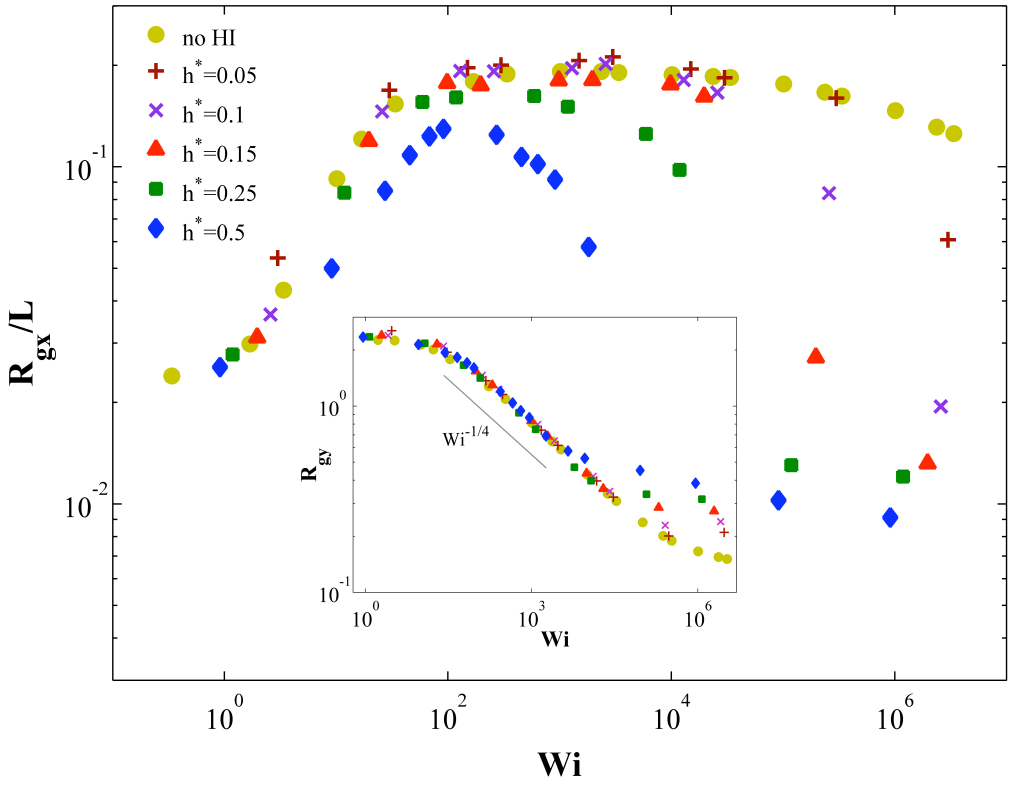

Figure 5.7: Weissenberg number dependence of the chain elongation for varying levels of HI, modeled by different values of the bead hydrodynamic diameter (controlled by the parameter h^* in the simulation). All results shown here are for a BR chain of 100 rods. The inset shows the Weissenberg number dependence of the coil thickness (R_{gy}) for varying levels of HI. The solid line marks the region of shear rates where R_{gy} follows a power law with an exponent of approximately -1/4.

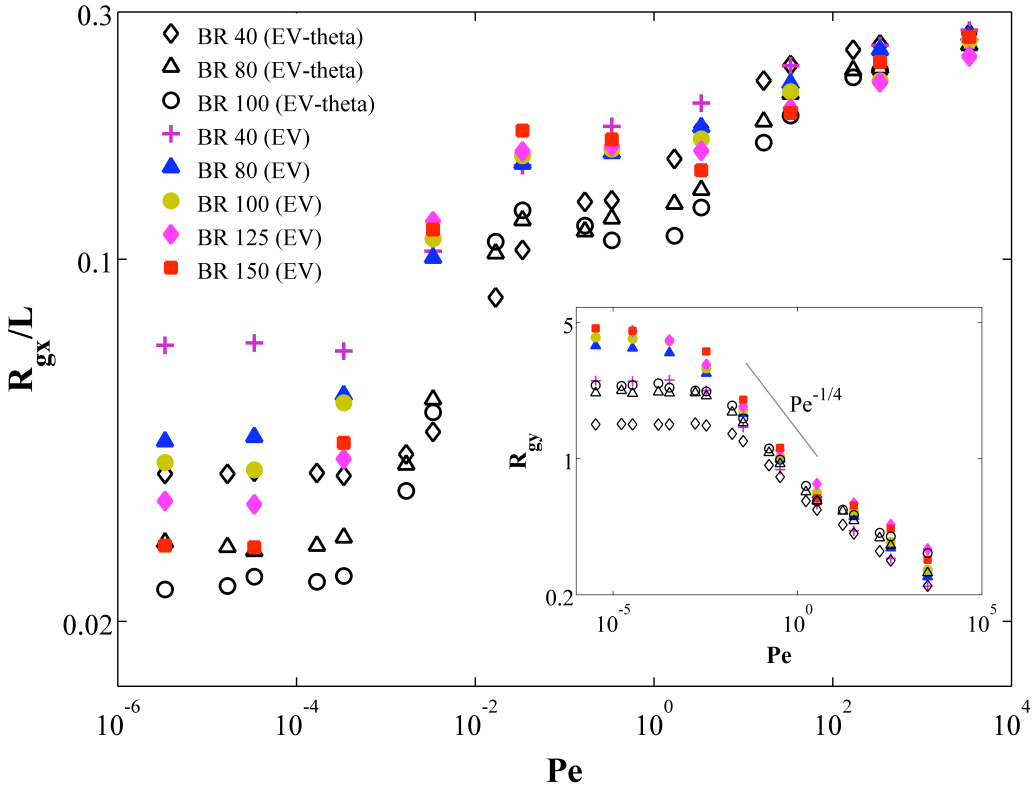

Figure 5.8: Shear rate dependence of the coil elongation normalized by chain length for chains of different length, when both EV and HI are active between beads. EV is modeled in two ways - by the repulsive part of the LJ potential with $\sigma^* = 1$ (denoted by 'EV') and by the full LJ potential with the value of ε^* tuned such that the size of the chain at equilibrium is similar to a theta coil (denoted by 'EV-theta'). The bead hydrodynamic diameter is taken as one Kuhn length for all cases. The inset shows the dependence on Peclet number of the coil thickness R_{gy} for chains of different length, when both EV and HI are active between beads. The solid line marks the region of Peclet numbers where R_{gy} shows a power law with an exponent of approximately -1/4.

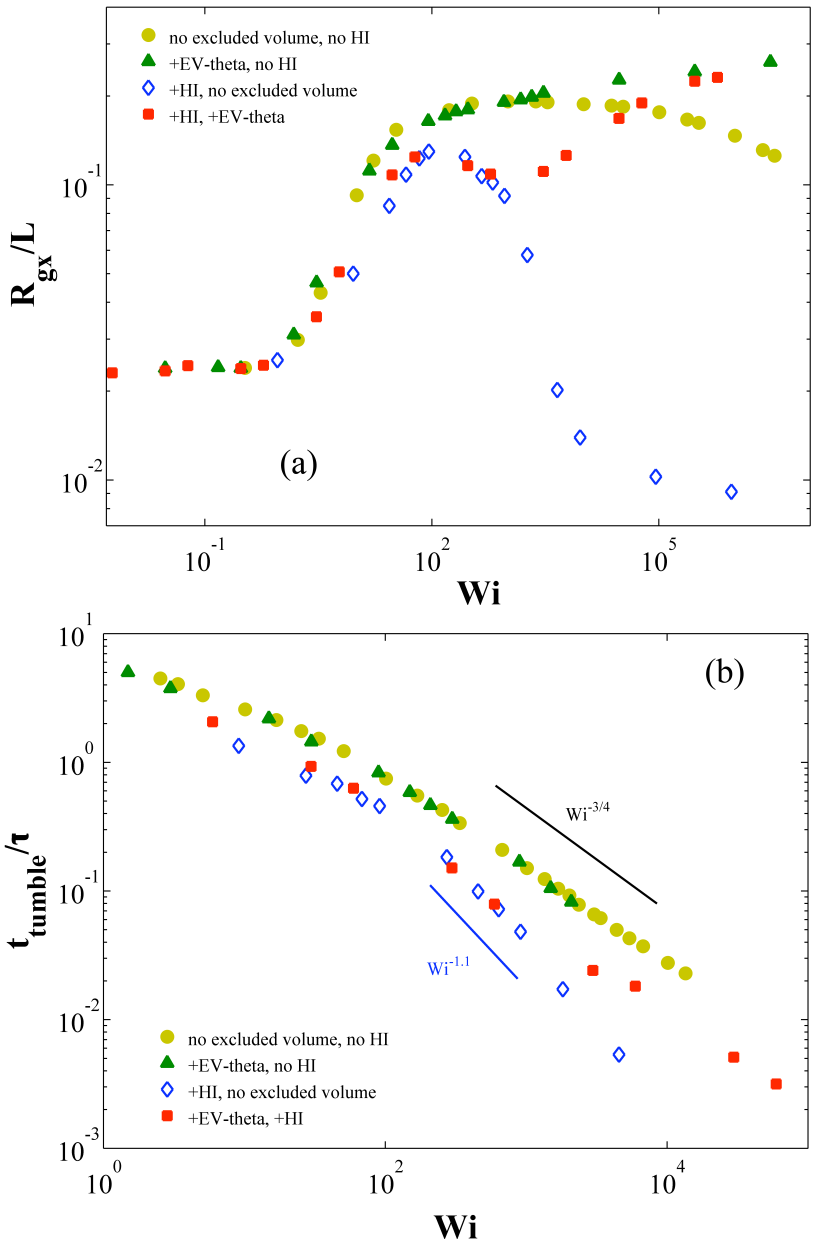

Figure 5.9: Shear rate dependence of (a) the chain elongation and (b) the tumbling time (normalized by the end-to-end relaxation time of the chain) for a BR chain of 100 rods, when EV-theta and HI between beads are present or absent. The '+' sign and 'no' indicate the mechanism that is present and not present, respectively. For all results shown here, EV-theta is modeled by the full LJ potential with $\sigma^* = 1$ and the value of ε tuned such that the coil size at zero shear rate is same as that of a theta coil without excluded volume interactions. The bead hydrodynamic diameter is taken as one Kuhn length for all cases here. The solid lines indicate the different power laws shown in the different cases.

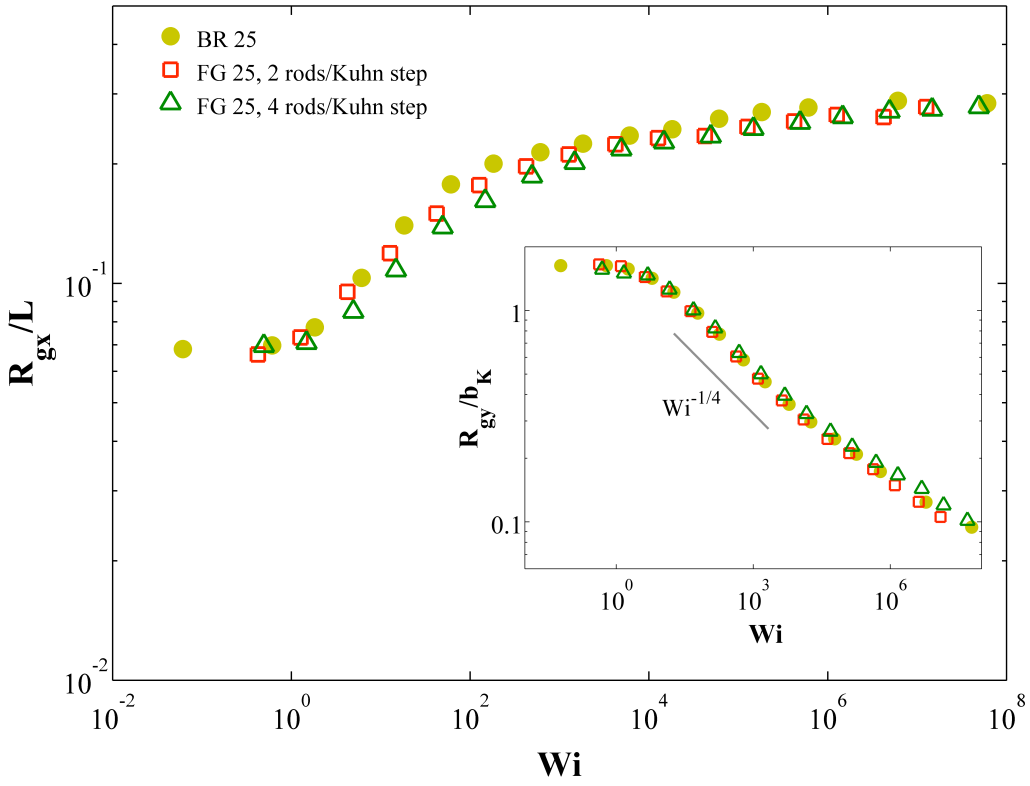

Figure 5.10: Variation of the coil elongation (normalized by the contour length L) with shear rates (represented by Weissenberg numbers) for a chain that consists of 25 Kuhn steps, at different levels of resolution, using the BR and FG models, including EV (no HI). Inset shows the dependence of the coil thickness, normalized by the Kuhn length, on shear rates for the same cases. The solid line indicates the region of shear rates where R_{gy} approximately follows a power law with an exponent of -1/4. The legends indicate the type of model used followed by the number of Kuhn steps. For the FG chains, the number of rods that constitute one Kuhn step is also provided in the legend. For all models used, ε^* is fixed at 1.0 and σ^* is varied so that the coil sizes are similar in the absence of shear flow (σ^* = 0.6 for the BR chain).

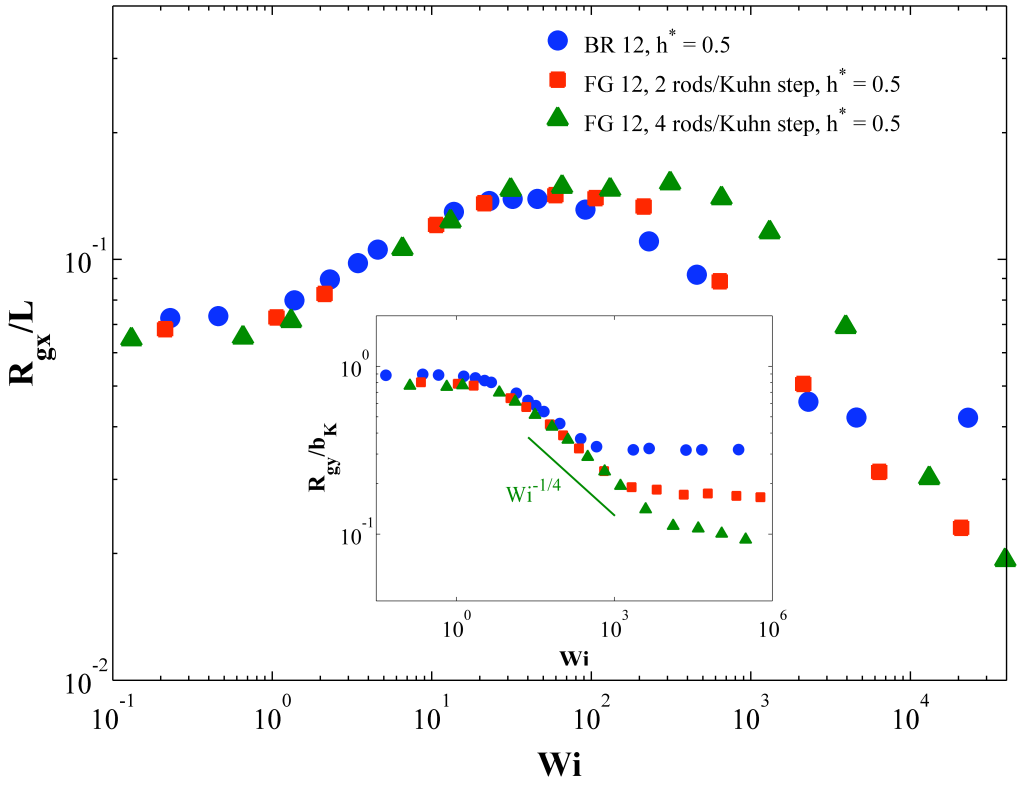

Figure 5.11: Variation of the coil elongation (normalized by the contour length L) with shear rates (represented by Weissenberg numbers) for a chain that consists of 12 Kuhn steps, at different levels of resolution, using the BR and FG models, including HI (without any bead-bead excluded volume interactions). Inset shows the dependence of the coil thickness, normalized by the Kuhn length, on shear rates for the same cases. The solid line indicates the region of shear rates where R_{gy} approximately follows a power law with an exponent of -1/4. As in Figure 5.10, the legends indicate the type of model used followed by the number of Kuhn steps. For the FG chains, the resolution is indicated in the legend by the number of rods that constitute one Kuhn step. For all models used, h^* is fixed at 0.5.

CHAPTER VI

Conclusions and Future Directions

Conclusions

In this dissertation, we have systematically explored the changes induced by the resolution of finer details over a wide range of length scales on various aspects of dynamics of the polymer chain in dilute solutions. For studies in equilibrium, we have employed MD simulations with explicit solvent molecules and BD simulations where the different types of interactions acting between the atoms/beads are introduced one after another. Our results finally help explain the rather surprising experimental observations made by Schrag and coworkers decades ago. The experiments clearly showed that the bead-spring model is in excellent agreement with the experimental results for dilute solutions over a wide range of frequencies, when one spring represents a fairly large subsection of the chain that is approximately 100 backbone bonds in length. In contrast, a satisfactory description of the corresponding behavior in melts require a much smaller minimum sub-chain, about 10 times smaller than that needed for dilute solutions, with the bead-spring model. Our results in Chapter II shows how each additional mechanism causes a slow-down of the relaxation dynamics of the bond vectors in the chain backbone, such that, for a realistic system with

side groups and explicit solvent molecules, the time scales for the relaxation of the bonds and the end-to-end vector for a short chain fragment become similar. Hence, the higher modes in the spectrum are shifted to larger time scales and don't appear on the spectrum, thereby leading to an abrupt cut-off in the relaxation spectrum observed from experiments. The fact that none of the BD simulations, even with all details present on the chain, can predict the single exponential decay for the bond relaxation dynamics highlights the importance of retaining all details (including the explicit solvent molecules) in the system while predicting the correct behavior for the simplest case – that of equilibrium polymer dynamics in the absence of flow. To the best of our knowledge, this is the first study that shows the shift of the time scales of motions at short length scales on a polymer chain due to the various mechanisms that would act on a realistic system. The "reappearing" of the higher modes in the relaxation spectrum with the increase in the size of the molecules in the solvent bath, leading to a melt, will be systematically investigated in a future work.

For our investigations in non-equilibrium conditions, we have employed Brownian dynamics simulations with a variety of models at widely ranging levels of resolution. However, as mentioned earlier, such simulations using an atomistic chain with explicit solvent molecules (using MD simulations) is beyond the scope of this study, owing to the significantly high computational requirements for chains of reasonable length. We have focused on steady shear flows for our non-equilibrium simulations, which is a special case of mixed flow where the extensional and rotational rates are equal. Consequently, the chain doesn't attain a steady state (like chains in purely extensional flows) but undergoes a succession of stretching and coiling events, with end-over-end tumbling. Note that, shear

flows are ubiquitous in nature since any flow near a boundary is approximately a shear flow. The key findings obtained from the results presented in this thesis can be summarized as follows:

(i) The different regimes of deformation for the polymer chain are identified with universal scaling laws and onset points (in terms of flow rates), for simplified models without excluded volume (EV) and hydrodynamic interaction (HI). These form the foundation for studies using both EV and HI (presented in Chapter V), where the changes due to these additional mechanisms are discussed. It is observed that the deformation behavior in terms of Weissenberg numbers is rather similar for weaker shear rates, up to flow rates lower than those of Regime 2. In Regime 2, the chain stretch shows a plateau for simulations without EV, but shows a gradual increase in the presence of EV for the chain lengths considered in our investigations. At high shear rates of Regime 3, chain compression is obtained without EV, which is amplified by the presence of HI, similar to the predictions of some recent similar simulation studies. However, in the presence of EV, even in relatively small amounts, orientational locking in the fully extended state is observed.

(ii) The chain compression at high shear rates, in the presence and absence of HI (and in the absence of EV), is shown to be a numerical artifact of model resolution. For all simulations without EV, our results suggest that the onset of chain compression (i.e. the onset of Regime 3) will be pushed to arbitrarily high shear rates as the chain discretization level is increased. However, the stretch behavior at high shear

rates, where orientational locking is obtained, is almost independent of model resolution in the presence of EV. This implies that the average residence time and the probability of "locked" states are similar across all levels of chain discretization.

(iii) The chain tumbling process is initiated by the formation of loops within which the individual rods follow a random walk. This leads to a simple theoretical model for the tumbling dynamics and the variation of coil width with shear rates in Regime 2, which corrects the previously obtained scaling laws using coarse-grained bead-spring models. At the shear rates of Regime 2, it is observed that the diffusion in the shear-gradient direction is cut off by convection for each bead, whereas this cut off doesn't occur for tumbling in weaker shear rates of Regime 1. A new algorithm to calculate the chain tumbling time from simulation trajectory is also formulated. The estimates of the scaling laws in the presence of HI and EV is also given by simple extensions of our model, but are not validated against simulation results owing to high computational cost.

From our results in Chapter IV, the levels of chain resolution needed to correctly predict the chain behavior at a given shear rate can be estimated. Figure 6.1(a) shows the approximate range of shear rates where a given chain discretization provides accurate predictions. Note that the most coarse-grained model (i.e. the optimal one from the considerations of simulation time) that can be used is shown in each range and it is understood that those with finer resolutions would yield results that are consistent with the optimal one. Also, note that the models using Hookean springs is a subset of the more

general CG model that does not incorporate the effects of finite extensibility, and are expected to be valid only in Regime 1 for shear flow. Although not validated directly, we expect these ranges to provide a rough guide to perform simulations in any general mixed flow. Overall, this is not surprising since high flow rates should excite smaller subsections of the chain away from equilibrium, which can be captured accurately by using models of finer resolutions. However, to the best of our knowledge, such a quantitative relation between the optimal model resolution and the flow rate is not shown in any earlier study. Also, note that for the FG model, the optimal resolution varies with the shear rate, and is shown in Figure 6.1(b). In this figure, the onset Pe for Regime 3 (Pe_{crit}) for chains at various levels of resolution (n_{res}) is shown for simulations without HI and EV (i.e. for results shown in Chapter IV). The power law exponent of about 4 is consistent with that of about ¼ obtained for the coil thickness.

To summarize, we have explored the dynamics of polymer chains, in the presence of excluded volume and hydrodynamic interactions, over a wide range of shear rates and chain lengths. To indicate the relevance of these results to experiments, we provide estimates of the shear rates required for chain scission, in what follows. Note that the rotary relaxation time of a single link in a polymer chain is roughly $\tau_r \approx ab_K^2\eta_s / k_BT$, where b_K is the length of the link, a is the radius of a bead in the chain, η_s is the solvent viscosity, and k_BT is thermal energy. The Peclet number is roughly the product of this relaxation time and the shear rate; i.e., $Pe \approx \tau_r\dot{\gamma}$. At room temperature, a commercial flexible polymer has a Kuhn length of order 1 nm, and the "bead radius" a should be assigned a similar value. For solvents of viscosity 1 Poise or so, this gives $\tau_r \approx 2.5\times10^{-8}$

s. So, shear rates of order 10^8 s^{-1} would be required to achieve Peclet numbers of order unity. This could be achieved in thin lubrication layers between rapidly moving surfaces. Or it could be achieved at modest shear rates if the solvent is brought close to a point of vitrification, where its viscosity can be raised by many orders of magnitude. In principle, using very viscous solvents near their glass transition points, arbitrarily high Peclet numbers could be reached.

However, at high Peclet numbers, the tensions in the polymer chains would also become high, leading eventually to chain scission. Estimates of the force needed to break a carbon-carbon bond range from around 4-14 nN. The drag-induced tension exerted on a dumbbell by a shearing flow can be estimated to be $F_d \approx ab_K \eta_s \dot{\gamma}$. (This rough estimate is obtained from the drag coefficient for a single bead, which is proportional to $a\eta_s$, times the difference in velocity between the two beads, projected in the direction of orientation of the bond. The tension is maximum when the dumbbell is oriented at a 45-degree angle between the flow and the flow gradient directions. This difference in velocity leading to the maximum tension is thus roughly $b_K \dot{\gamma}$, where numerical prefactors of order unity are dropped.) The above force can be re-written as $F_d \approx Pek_B T / b_K$, which works out to be $F_d \approx 4 \times 10^{-5} Pe\ nN$, for b_K = 1 nm. Thus, a force high enough to break the bond in the dumbbell will be achieved at a Peclet number of around 10^5, and this critical Peclet number is independent of solvent viscosity. Thus, for simple synthetic polymers such as polystyrene, Peclet numbers in excess of 10^5 will likely lead to chain scission, even in shear.

In a long chain of connected rods, much higher chain tensions are in principle attainable,

because of accumulation of forces along the backbone of the chain. For this reason, in extensional flows acting on long polymers, Peclet numbers cannot get anywhere near as high as 10^5 without chain scission, and even Weissenberg numbers of unity cannot be achieved in extension without chain scission if the polymer contains millions of backbone bonds. However, in shear, the build-up of tension is strongly limited by the alignment of the chain in the shear flow. If the chain becomes almost perfectly aligned, the tension drops, in principle towards zero for perfect alignment, even at high shear rates. For this reason, polymers are rarely cleaved in a shearing flow, as long as extensional flow components are completely absent. However, in a tumbling event during a shear flow, bonds are rotated out of the flow direction, and the above estimate shows that these bonds in simple synthetic polymers should be cleaved if Pe exceeds around 10^5. They might be cleaved at lower values of the Peclet number, if tumbling events can occasionally cause sufficient rotation of portions of the chain backbone that are longer than a single Kuhn step.

For stiff molecules such as DNA, the Kuhn length is 100 times larger than for ordinary synthetic polymers, and the chain also probably requires a higher force to cleave it, since double-stranded DNA is a duplex of two polymer chains. This implies that much higher Peclet numbers, around 10^7, according to our formula above, might be required to break a very small fragment of DNA. (The actual value of Pe at breakage might be considerably less than this, depending on the details of the tumbling dynamics, as indicated above.) For long DNA polymers, the breakage condition would depend on the tumbling dynamics, as is true for freely jointed polymers. To summarize, large Peclet numbers of the range of

magnitudes studied here can be approached without chain scission.

Thus, in this dissertation, we have investigated the deformation and dynamics behavior of polymer chains over a wide range of shear rates, covering relatively weak to ultra-high shear rates that might be experimentally accessible without encountering chain scission. We have started with a thorough understanding of the simplest case of a chain without HI and EV and then systematically mapped out the additional effects due to resolution, HI and EV. Although a few years ago it seemed that a clear, definitive, picture of polymer chain dynamics in shearing flow up to asymptotically high shear rates had been attained, the recent, puzzling results from other simulation studies (discussed in Chapter III) indicated that this relatively basic problem in polymer physics is not well understood. The results presented here serves to finally completely resolve the entire picture from the standpoint of BD simulations, which is a standard tool to investigate the behavior of polymer chains in flows.

Future directions

There are several other important issues related to the work presented in this dissertation that should be resolved in future investigations, both for equilibrium and non-equilibrium polymer dynamics. Firstly, for equilibrium dynamics, the high frequency modes, which are "missing" for dilute solutions, show up in experiments with melts, even short chain melts for polystyrene. In this dissertation, we have explained how the relaxation dynamics of the individual backbone bonds slow-down with every added mechanism, leading to a single exponential relaxation spectrum for the entire PS chain of 30 monomers. However,

according to the experiments, the relaxation spectrum won't be a single exponential as we make the solution concentrated, thus approaching the melt. Preliminary MD investigations (not shown here) using the same models that are discussed in Chapter II do indicate a similar behavior, as the size of the molecules constituting the solvent bath is increased. Future work will aim towards obtaining a clear physical picture for this change in the breadth of the relaxation spectrum (due to the presence of high frequency relaxation modes) as we approach the melt.

Secondly, the investigations of polymer dynamics in shear flow can be done using MD simulations with all the solvent molecules explicitly treated in the system. The same models for polystyrene in benzene (used in Chapter II) can be used with the SLLOD algorithm that is included in the LAMMPS package to simulate shear flow. Such non-equilibrium simulations have never been done before for highly realistic systems and might provide some clues about the extremely low chain stretch observed in the study by Lee *et al.* [1]. In this context, note that although our BD simulations in this dissertation indicate that the chain stretch decreases with the inclusion of HI, none of our observations show such low coil expansions in shear flow (as given in Ref. [1]). Also, since differences appear even in equilibrium polymer dynamics with the addition of explicit solvent molecules, it is perhaps reasonable to expect some changes in the non-equilibrium dynamics of polymer chains, especially for fast flow rates. Although this will entail a huge computational cost for each shear rate to be investigated (relative to BD simulations), due to technological breakthroughs in recent few years such simulations might be possible by using multiple GPUs instead of CPUs.

Even from the standpoint of BD simulations, there are several interesting problems to be explored in more details. In this dissertation, we have investigated the behavior of chains in shear flows, which is an important member of the more general class of mixed flows that has equal rates of extension and rotation. However, the same models and techniques can be used to study different the dynamics in different types of mixed flows with varying proportions of extension and rotation. A recent article explores this general problem with coarse-grained bead spring chains [2]. However, as observed in this dissertation, these might fail to capture the correct physics at higher flow rates. Thus, it is quite possible that the behavior of chains in a general mixed flow at high flow rates is not known accurately yet, and it can be studied in details using the methods and algorithms discussed here.

Additionally, note that all our simulations presented here are performed on chains that are either at the theta condition (i.e. follows Random Walk statistics) or swollen due to excluded volume interactions (this represents the good solvent condition, where the chain size at equilibrium is larger than that at the theta condition). Several important macromolecules, including proteins, form highly coiled globular structures at their native state (i.e. at equilibrium) and are often exposed to various types of flows in different environments. A polymer chain with long-range attractive interactions is possible model for this class of molecules, which has an equilibrium size much lower than that of a theta coil. A recent example of the modeling of such a macromolecule using BD simulations is found in the study by Sing *et al.* [3]. In this study, and several other related articles by the same authors, the protein von Willebrand Factor (vWF) is modeled by bead-spring models that have attractive interactions. Their study investigates the process of unfolding of the

chain when exposed to high flow rates during the rupture of blood vessels, after which the stretched protein is thought to self-assemble with platelets in the blood stream and starts the blood clotting process. However, this unfolding process that they investigate might be dependent on the chain resolution, as implied from our results in shear flows. Furthermore, BD simulations with strong bending potentials and long-range attraction have shown the existence of configurations referred to as "racquets" and "torus" [4]. The unfolding of these structures in flows is of fundamental importance, and can be studied using the methods and models used in this dissertation.

References

[1] Lee, E. C.; Solomon, M. J.; Muller, S. J. *Macromolecules* **30**, 7313-7321 (1997).

[2] Lee, Joo Sung; Shaqfeh, Eric S. G.; Muller, Susan J. *Physical Review E*. **75**, 040802(R) (2007).

[3] Sing, Charles E.; Alexander-Katz, Alfredo *Biophysical Journal*, **98**, L35-L37 (2010).

[4] Montesi, Alberto; Pasquali, Matteo; MacKintosh, F. C. *Physical Review E*, **69**, 021916 (2004).

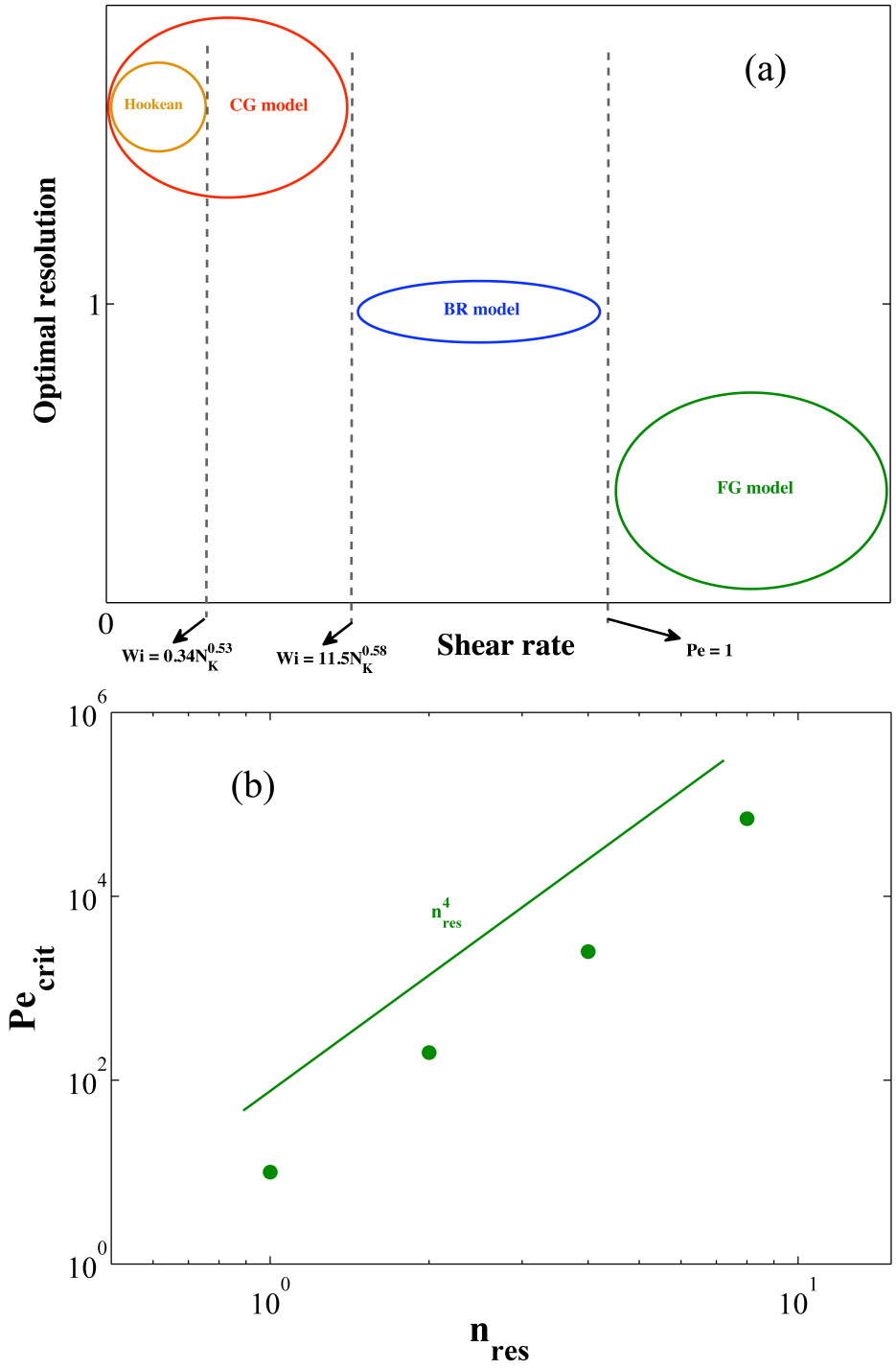

Figure 6.1: (a) The model with the optimal resolution to represent the polymer chain at various regions of shear rates. The dashed lines roughly indicate the zones where each model is expected to be valid. (b) The variation of the Pe for the onset of Regime 3 (Pe_{crit}) for a given model resolution (n_{res}). The green line indicates that the results show a power law exponent of about 4.

APPENDIX A

Additional details on the molecular dynamics and Brownian dynamics simulations of polystyrene in benzene bath

1. Viscosity measurements of benzene bath from the UA and MARTINI models

The most commonly used methods for computing viscosity are summarized and compared in Ref. [1] and the periodic perturbations method was concluded to be the best in terms of efficiency and accuracy. We used GROMACS for our MD simulations, which can implement the periodic perturbation method for non-equilibrium MD calculations. In fact, Zhao *et. al.* [2] has calculated the viscosity of organic liquids using periodic perturbation technique through GROMACS. Since this method has been chosen as the best among the ones investigated in Ref. [1], we use this method to get estimates of the shear viscosity for various benzene models under consideration.

Figure A.1 shows the results from the simulations applying the periodic perturbation technique. The method is described in details in Ref. [3] as well as in Refs. [1] and [2]. The system is perturbed from equilibrium by a force that is periodic in the z-direction (with a certain amplitude) and the viscosity is calculated from the velocity profile generated within the box. The calculations are similar to those reported in Ref. [2], where the experimental viscosity is obtained by the extrapolation of the curve to zero amplitude. The results show

that the Errington-Panagiotopoulos UA model for benzene simulations in Chapter II gives excellent predictions for the experimental viscosity at 293 K (0.652 cP). This potential was originally optimized for the prediction of thermodynamic properties, and to the best of our knowledge, it has never been used to compute the viscosity. In contrast, the CG MARTINI model for benzene predicts a viscosity that is roughly a factor of four higher than the experimental value at 293 K.

2. Variation of density of the benzene bath with system size

For simulations with a benzene bath, it is important to know the thermodynamic limit of the system i.e. the number of molecules in the bath beyond which the predictions from the MD simulations become independent of the system size. Figure A.2 shows the variation of the density for the benzene bath with the number of benzene molecules for the Errington-Panagiotopoulos UA model. Our results clearly indicate that the density predictions become independent of system size for baths containing higher than 800 molecules. Note that although the final predicted density is slightly lower than the experimental predictions (about 2% lower), we consider this model to be adequate for our purposes, when the bath size is larger than 800 benzene molecules.

3. Fits of the bond relaxation dynamics from different models using BD simulations

It is mentioned earlier in the article that only the MD simulations, with explicit solvent molecules, for a short PS chain of 30 monomers, show a single exponential relaxation dynamics of the backbone bonds. In Figure A.3, we show the fits to a single exponential of the relaxation dynamics of the backbone bonds obtained from BD simulations of all the different models listed in Table 2. As observed in Fig. A.3, the behavior in all cases does not agree well with the best-fit single exponential decay, in contrast to the corresponding MD simulation shown earlier (Fig. 2(a) with linear axes and Fig. 7 with log-log axes). However, it is interesting to observe how the dynamics approaches a single exponential decay as the different mechanisms are added (see Figure A.3(a)-(f)), starting from a chain consisting of only beads and stiff springs that mimic inextensible rods. Note that the ACWS model contains all details on the chain but does not account for the explicit solvent molecules, and its relaxation dynamics deviates significantly from a single exponential decay (Fig. A.3(f)), being faster at short times and slower at longer times relative to a single exponential decay.

References

[1] Hess, Berk *J. Chem. Phys*. 2002, 116, 1, 209-217.

[2] Zhao, Lifeng; Wang, Xijun; Wang, Ling; Huai, Sun *Fluid Phase Equilibria*, 2007, 260, 212-217.

[3] Allen, M. P.; Tildesley, D. J., "Computer Simulation of Liquids", Oxford Science Publications (1986).

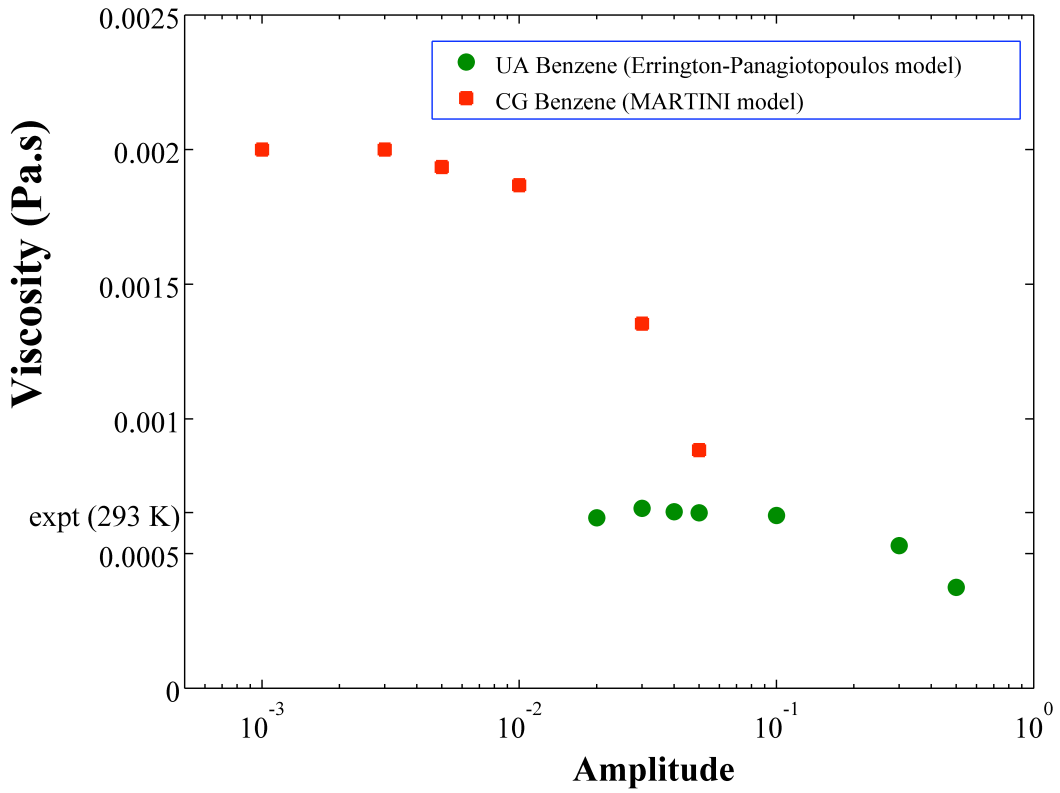

Figure A.1: Variation of the viscosity with the amplitude of periodic perturbation for the UA (Errington-Panagiotopoulos) and the CG (MARTINI) models for benzene. The extrapolation to zero amplitude represents the viscosity prediction for the system. Note that the predictions from the UA model agrees well with the experimental value at 293 K, whereas that from the CG model is about four times larger.

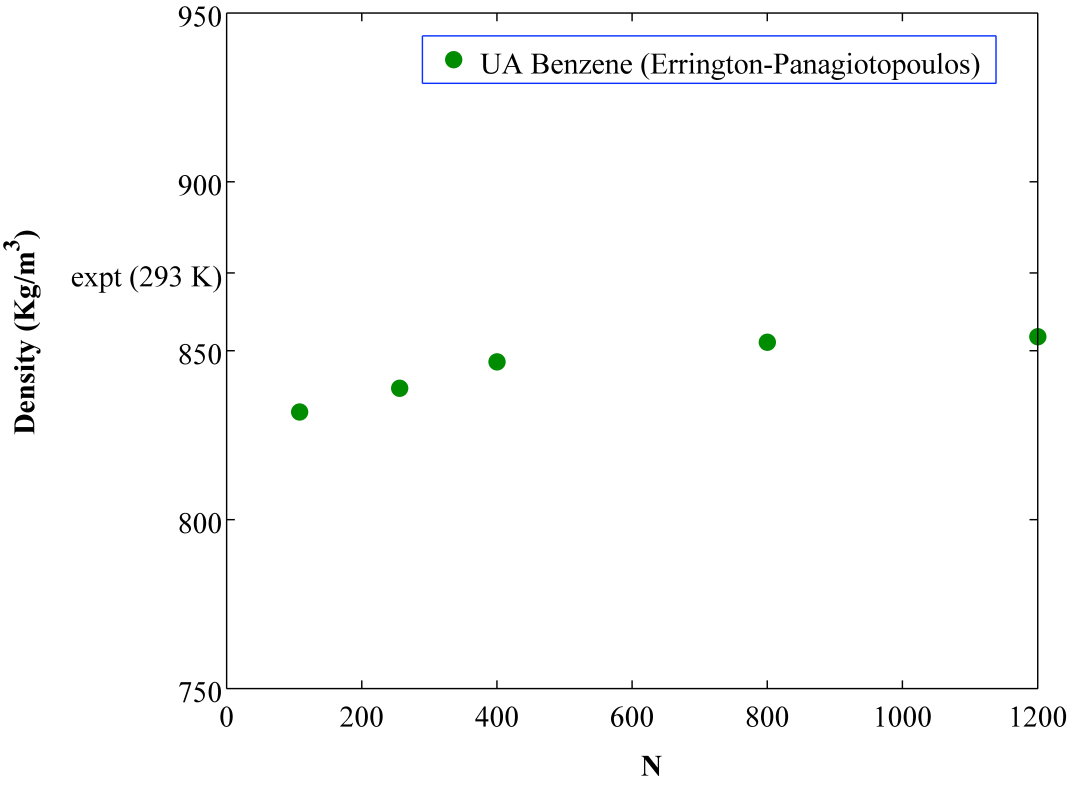

Figure A.2: Variation of computed density with number of benzene molecules in the bath for the Errington-Panagiotopoulos potential. Note that the predicted density for sufficiently large solvent bath is about 2% lower than the experimental value.

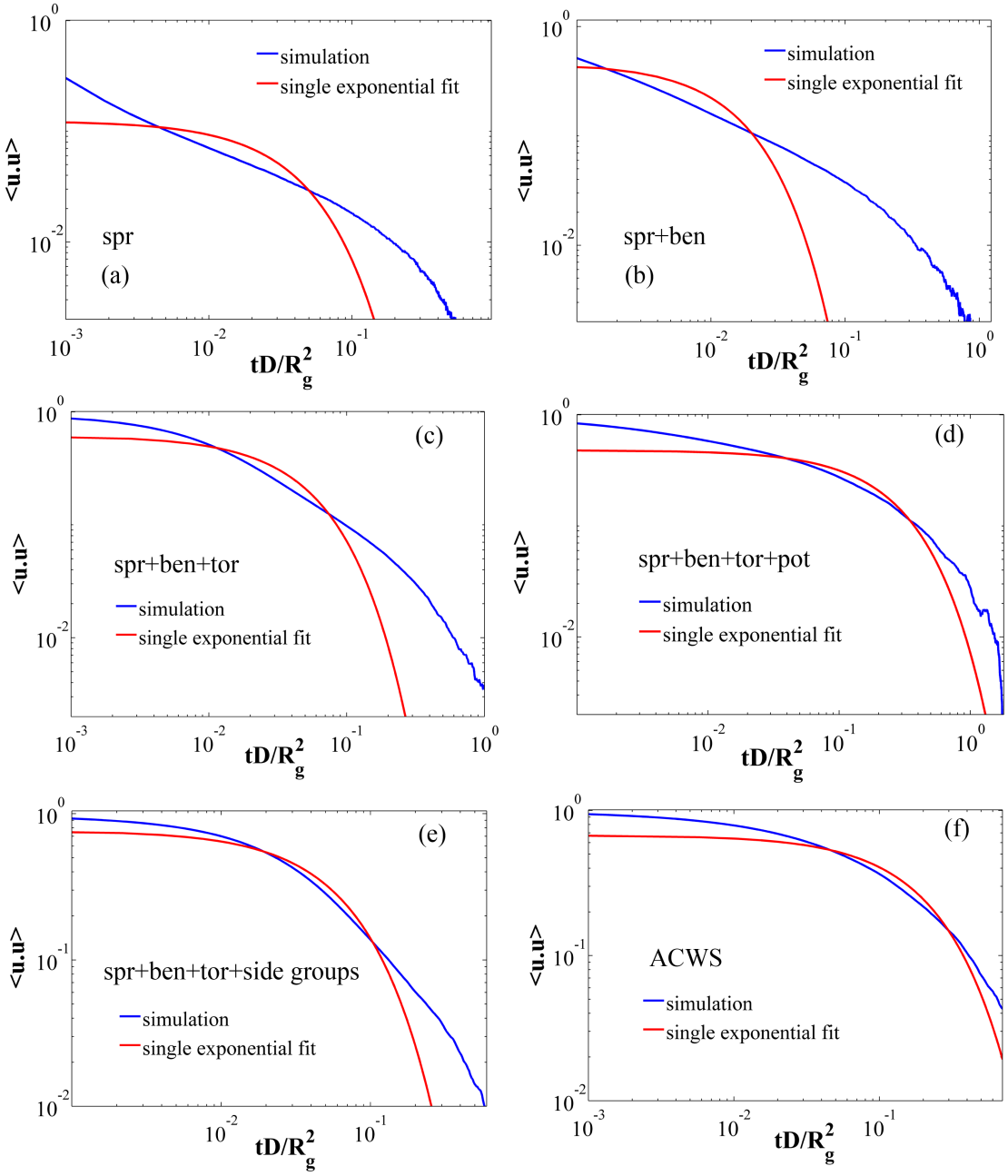

Figure A.3: The relaxation dynamics of the chain backbone bonds and the corresponding fits to a single exponential decay for the following models: (a) spr, (b) spr+ben, (c) spr+ben+tor, (d) spr+ben+tor+pot, (e) spr+ben+tor+side groups and (f) ACWS from BD simulations. Details of the models used for (a)-(f) are provided in text and Table 2.2.

APPENDIX B

Sequences of chain configurations during tumbling in shear flow

Some examples of evolution of configurations for the polymer chain during the tumbling process at high shear rates are shown in Figures B.1, B.2 and B.3. All these sequences of chain configurations for representative pathways of tumbling are for a shear flow with a Peclet number (Pe_K) = 0.15 imposed on a BR chain of 100 rods, in the absence of EV and HI, where the Peclet number represents the product of the shear rate and the rotational time of one Kuhn step. Note that more details for the model and simulations are given in Chapters III and IV. A close inspection of these actual trajectories for shear flows reveals the sequence of diffusion and convection for chain tumbling, where the diffusion in the shear-gradient direction is cut off by convection beyond a certain distance (as explained in Chapter IV). In all these figures, the horizontal (along the chain contour in the extended state) and the vertical directions on the plane of the paper represent the x and y directions respectively, and the shear flow acts along the x-axis with the gradient along the y-axis. As noted from the snapshots shown, for an extended state, diffusion-mediated transport along y-direction typically start at the ends of the chain, with the subsequent tumbling process occurring in various ways. In one pathway, the beads from one end reach the critical y distance before the other end and are carried in x-direction by convection, followed by a similar process for the other end (Figure B.1). However, there are some tumbling events

where the movements of both ends are almost synchronized (Figure B.2). Additionally, some tumbling events occur predominantly due to a group of internal beads reaching the critical y distance ahead of the ends of the chain, which then drag the ends of the chain in the x-direction (Figure B.3).

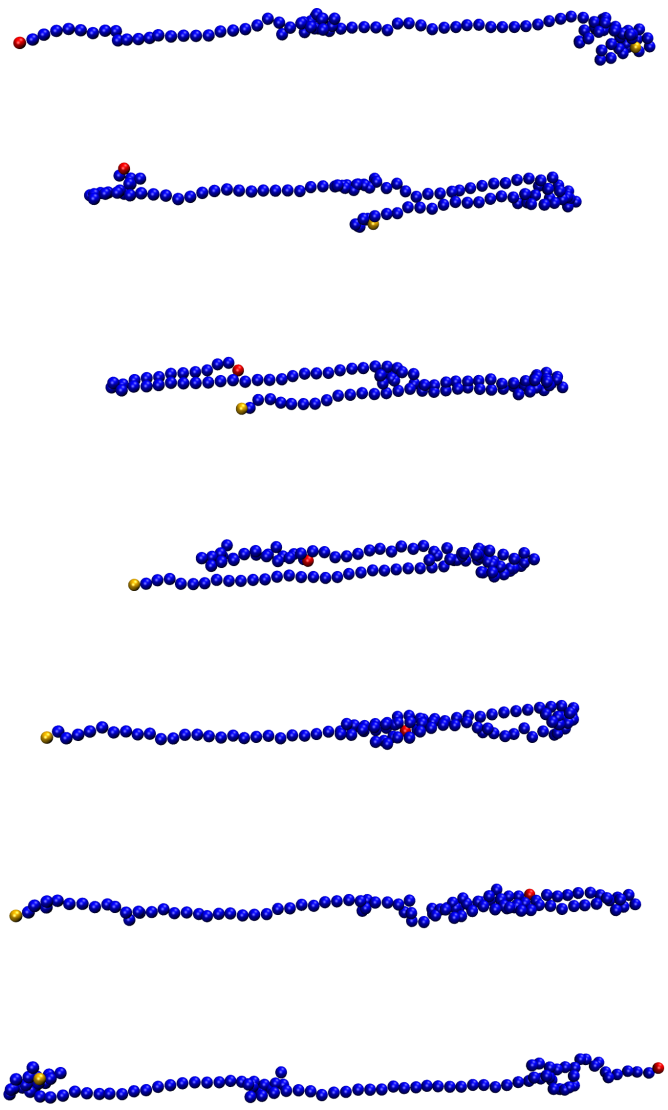

Figure B.1: An example of a tumbling pathway where the beads at one end reach the critical y distance ahead of those at the other end, and are then carried away by convection to reach the other end. The simulations are for a BR chain of 100 rods in the absence of HI and EV, with a $Pe_K = 0.15$, which represents a shear rate in Regime 2. Note that the two end beads on the chain are colored red and yellow, whereas all other beads are colored blue.

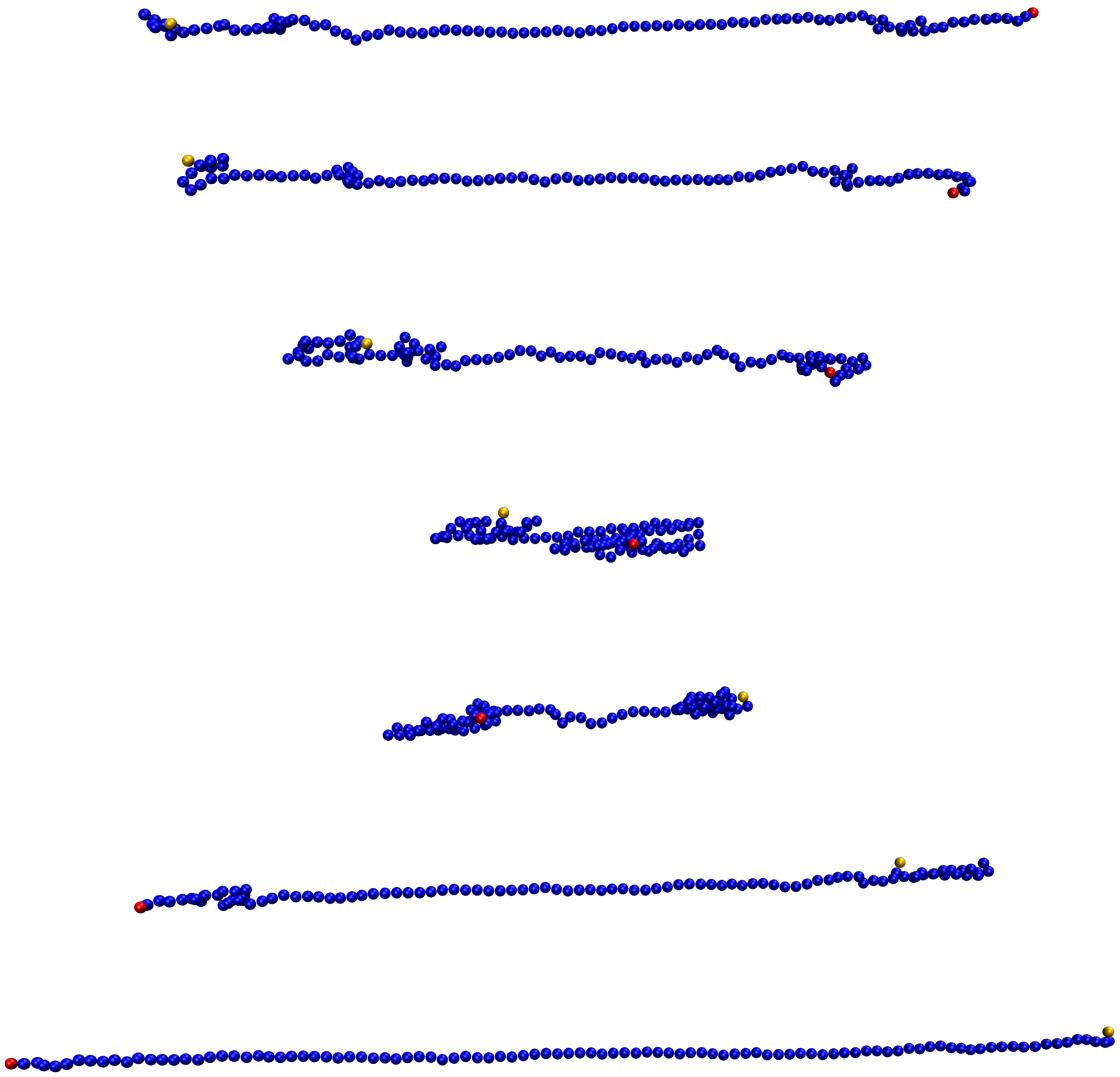

Figure B.2: An example of a tumbling pathway where the motion of the beads at the two ends of the chain are almost synchronized. The simulations are for a BR chain of 100 rods in the absence of HI and EV, with a $Pe_K = 0.15$, which represents a shear rate in Regime 2. Note that the two end beads on the chain are colored red and yellow, whereas all other beads are colored blue.

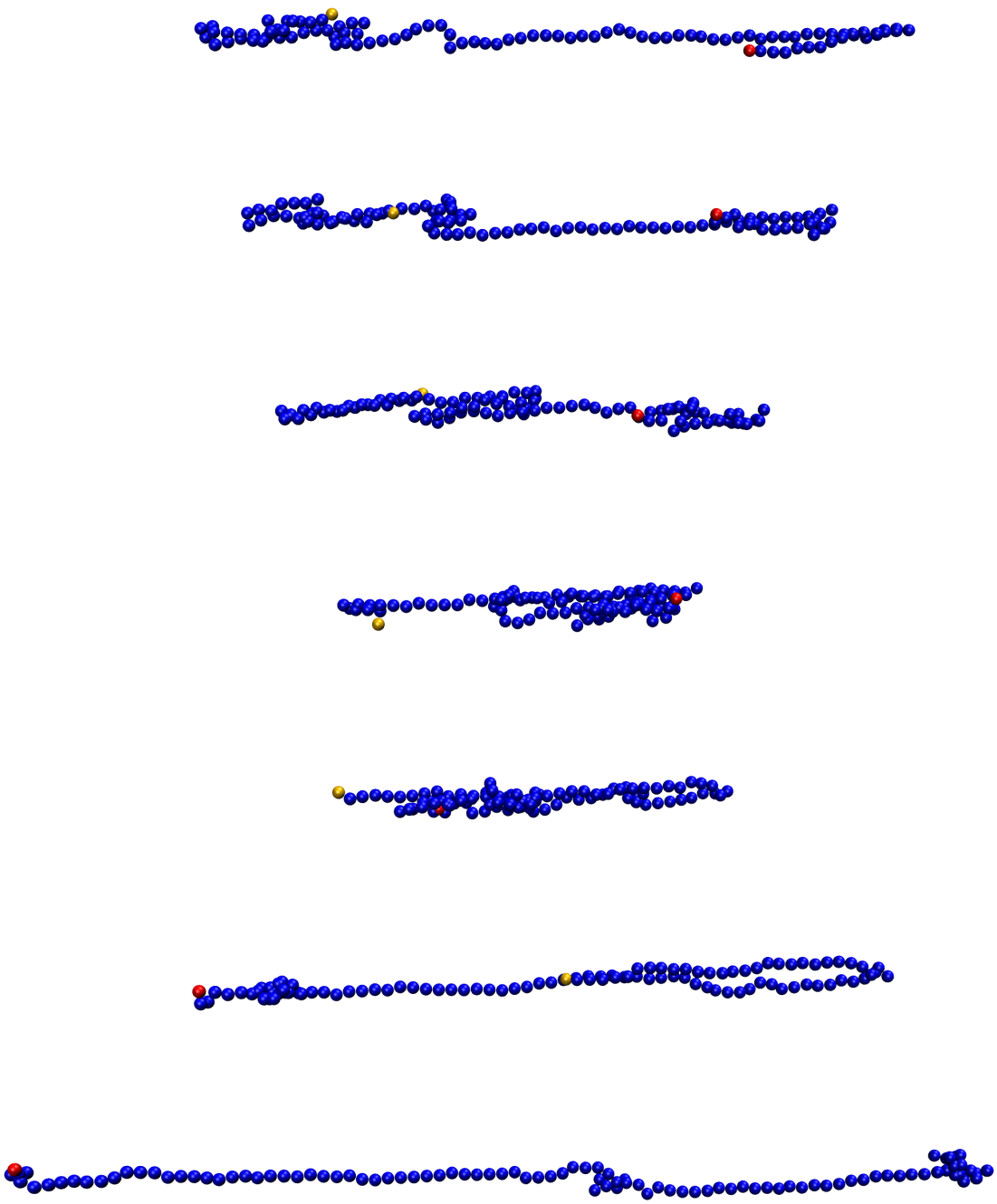

Figure B.3: An example of a tumbling pathway where a group of internal beads reach the critical y distance ahead of those at the ends, and are then dragged away by convection to reach the other end. The simulations are for a BR chain of 100 rods in the absence of HI and EV, with a $Pe_K = 0.15$, which represents a shear rate in Regime 2. Note that the two end beads on the chain are colored red and yellow, whereas all other beads are colored blue.

APPENDIX C

A self-consistent method for the prediction of the deformation behavior of isolated polymer chains in shear flows

Introduction

In the past two decades, several insightful theoretical and simulation studies aimed at understanding the deformation of polymer chains subjected to shear flows [1-9] have been performed. It is well understood from the earlier Brownian dynamics (BD) simulation studies that the stretch (in the shear direction) of a polymer chain increases with increasing shear rates and finally reaches a plateau at strong shear flows [3]. A later study has revealed that, in the absence of excluded volume (EV) and hydrodynamic interaction (HI), the plateau in stretch is indeed the asymptotic response at high shear rates [7]. Among the theoretical ones, Ref. [1] predicts the deformation of chains in shear flow without accounting for the effect of finite extensibility, which is thus successful only for weak shear rates, not far enough from equilibrium. Later studies [2, 9] have attempted to account for the effect of finite extensibility by imposing the constraint of a constant contour length for both extensional and shear flows, but the predictions at strong shear rates are not in good agreement with those obtained from the BD simulations, as highlighted in Ref. [3]

and also shown later in this study. Ref. [4] successfully predicts the asymptotic scaling law for the coil thickness (in the shear-gradient direction) obtained from Brownian dynamics (BD) simulations of coarse-grained bead-spring chains, but over-predicts the chain stretch in the shear direction (predictions are similar to those obtained from the model given in Ref. [2]) for strong shear rates. The effects of incorporating finite extensibility is also investigated in Ref. [8], but a FENE model with a adjustable parameter is used in that study for the individual springs in the chain, which can be tuned to obtain a satisfactory qualitative agreement with experimental results. Thus, it is uncertain whether the spring force law used in Ref. [8] is correct from the standpoint of equilibrium statistical thermodynamics (this predicts an inverse Langevin function for the variation in spring force with extension, and is usually modeled by the Padé approximation), in addition to the fact that it is impossible to estimate the value of the tunable parameter beforehand to predict the behavior of a given polymer chain consisting of certain number of Kuhn steps, unlike the coarse-grained spring laws used in this study. Also, as argued later in this article, the treatment in Ref. [8] will not yield the correct asymptotic value for the chain stretch at strong shear rates, similar to those other studies [2, 4, 9].

In a recent study [7], simple physical arguments are used to model the physics of tumbling at strong shear rates for well-resolved chains. Although the model correctly predicts the scaling laws for the coil thickness and end-over-end tumbling dynamics over a range of shear rates, the knowledge of the variation of the chain stretch with shear rates is obtained from the corresponding BD simulations. At relatively weak shear rates, the tumbling times are predicted by using a Graetz-Lèvêque analysis using an approximate scaling law for the

chain stretch obtained from simulation results. At strong shear, the scaling laws for the coil thickness and tumbling dynamics are derived by assuming a constant average chain stretch, which is also observed from the simulation results. Thus, there is a clear need for an analytical model which will be able to predict the variation in chain stretch and thickness with shear rates. To the best of our knowledge, there are no studies that provide a predictive tool for the deformation of polymer chains over the entire range of shear rates. This article attempts to formulate a simple, self-consistent analytical algorithm that can correctly predict the simulation results for a given polymer chain (consisting of a certain number of Kuhn steps) over the entire range of shear rates. As we show later in the article, the predictions for the chain stretch from our self-consistent model is in very good agreement with those obtained from simulations. Also, the scaling law for the coil thickness at strong shear rates shows an exponent of -1/3, which is consistent with those obtained from BD simulations of similar coarse-grained bead-spring chains (as those used in this study), but not accurate for more finely resolved chains at such strong shear rates that show an exponent of about -1/4 [7].

However, note that this article provides such a predictive tool without the inclusion of hydrodynamic interactions (HI) and excluded volume (EV), and is thus more suitable for semiflexible chains like double stranded DNA, where the effects due to HI and EV are negligible. The incorporation of additional effects due to HI and EV is beyond the scope of this study, but will be investigated in a future work. In this Appendix, we compare the results obtained from our self-consistent method with those given in Chapter III, using BD simulations. We show that such a method works well only when the spring forces are

estimated using the central spring, instead of the contour length of the entire chain that is used in several earlier studies, as mentioned earlier. All the trends obtained using our analytical method agrees very well with those observed earlier in Chapters III and IV, with simulations using the CG model. Furthermore, we refine the estimates of the crossover Peclet numbers given in Chapter III between the different Regimes of deformation (for details, see Chapter III). Interestingly, we note that our method predicts the plateau in chain stretch as the asymptotic response, which is shown to be the case in Chapter IV from simulations with widely ranging chain discretization levels.

Methods and Equations

Most of the equations used in the setup of the self-consistent algorithm are given in Ref. [2]. The dynamics on a polymer chain consisting of N springs (N+1 beads, numbered from n = 0 to N) is described by the following Langevin equation in the long-chain limit that n can be taken to be a continuous variable:

$$\zeta \frac{\partial \vec{R}_n}{\partial t} = k \frac{\partial^2 \vec{R}_n}{\partial n^2} + \zeta \hat{\kappa} . \vec{R}_n + \vec{F}_n^R \qquad (1)$$

with the boundary conditions:

$$\left. \frac{\partial \vec{R}_n}{\partial n} \right|_{n=0} = \left. \frac{\partial \vec{R}_n}{\partial n} \right|_{n=N} = 0$$

Where the vector $\vec{R}_n$ is the position vector of the nth bead on the chain, ζ is the drag coefficient of the beads, k is the spring constant, $\vec{F}_n^R$ is the random force acting on the nth bead and $\hat{\kappa}$ is the velocity gradient tensor for the flow.

Using the following normal coordinates,

$$\vec{X}_p(t) = \frac{1}{N}\int_0^N \cos\frac{p\pi n}{N}\vec{R}_n(t)dn \tag{2}$$

we arrive at the following equation for the evolution of the normal coordinates [1, 2]:

$$\dot{\vec{X}}_p + \frac{k_p}{\zeta_p}\vec{X}_p - \hat{\kappa}.\vec{X}_p = \frac{1}{\zeta_p}\vec{F}_p^R \tag{3}$$

For the Rouse model, we have $\zeta_p = 2N\zeta$ and $k_p = 2k\frac{\pi^2 p^2}{N}$, where $k = Hf$, with H being the spring constant at equilibrium and is given by:

$$H = \frac{3k_B T}{\nu b_K^2}$$

where ν is the number of Kuhn steps modeled by each spring in the chain and b_K is the length of each Kuhn step. For convenience, $b_K = 1$ for this study. The factor f denotes the effect of the finite extensibility on the spring constant, which we will determine by a self-consistent method. It is to be noted that $f = 1$ at equilibrium, so $k = H$.

For a simple shear flow along the x-axis with the gradient along the y-axis and with a shear rate $\dot{\gamma}$, we have

$$\hat{\kappa} = \dot{\gamma}\begin{pmatrix} 0 & 1 & 0 \\ 0 & 0 & 0 \\ 0 & 0 & 0 \end{pmatrix}$$

The solution of Eq (3) is given in Ref. [1]:

$$\left\langle X_p^2 \right\rangle = \frac{3k_BT}{k_p} + \frac{1}{2}\frac{k_BT}{k_p}\left(\frac{\zeta_p\dot{\gamma}}{k_p}\right)^2 \tag{4}$$

The inverse transformation of Eq. (2) yields:

$$\vec{R}_n = \vec{X}_0 + 2\sum_{p=1}^{N}\vec{X}_p\cos\left(\frac{p\pi n}{N}\right)$$

Now, following the approach in Ref. [2], using the "pre-averaging" approximation:

$$\left|X_p\right| \approx \left\langle X_p^2 \right\rangle^{1/2}$$

We get, for the average length of the n^{th} spring:

$$\left|\frac{\partial \vec{R}_n}{\partial n}\right| = 2\left(\sum_{p=1}^{N}\left\langle X_p^2 \right\rangle \frac{p^2\pi^2}{N^2} Sin^2\frac{p\pi n}{N}\right)^{\frac{1}{2}}$$

In a coarse-grained description, the springs in the chain will stretch beyond their equilibrium length in the presence of flow, thereby increasing the contour length of the chain. The contour length of the deformed polymer chain is given as:

$$L_c = \int_0^N \left|\frac{\partial \vec{R}_n}{\partial n}\right| dn = 2\int_0^N \left(\sum_{p=1}^{N}\left\langle X_p^2 \right\rangle \frac{p^2\pi^2}{N^2} Sin^2\frac{p\pi n}{N}\right)^{\frac{1}{2}} dn \tag{5}$$

As mentioned earlier, in the presence of flow, the springs stiffen and f increases as their average length increases. If f were known, and is the same for all springs, we would have:

$$k_p = 2(Hf)\frac{\pi^2 p^2}{N} = f\frac{6\pi^2 p^2 k_B T}{\nu b_K^2 N}$$

When substituted into Eq. (4), this gives:

$$\left\langle X_p^2 \right\rangle = \frac{1}{2}\frac{N\nu b_K^2}{f\pi^2 p^2} + \frac{1}{12}\frac{N b_K^2 \nu}{f^3 \pi^2 p^6}(Wi)^2 \tag{6}$$

Where the Weissenberg number (Wi) is defined as $Wi = \dot{\gamma}\tau$, where τ is the rotational relaxation time of the end-to-end vector and is given as:

$$\tau = \frac{N^2 \nu b_K^2 \zeta}{3\pi^2 k_B T}$$

The radius of gyration of the entire polymer chain is given in Refs. [1] and [2]:

$$\left\langle R_g^2 \right\rangle = 2\sum_{p=1}^{N}\left\langle X_p^2 \right\rangle = \frac{N\nu b_K^2}{6f} + \frac{\pi^4}{5670}\frac{N\nu b_K^2}{f^3}Wi^2 \tag{7}$$

The components of R_g along the x (R_{gx}) and y (R_{gy}) axes that represent the chain stretch and thickness respectively, are given as:

$$\left\langle R_{gx}^2 \right\rangle = \frac{N\nu b_K^2}{18f} + \frac{\pi^4}{5670}\frac{N\nu b_K^2}{f^3}Wi^2 \tag{8}$$

$$\left\langle R_{gy}^2 \right\rangle = \frac{N\nu b_K^2}{18f} \tag{9}$$

Now, since we know the amount of stretch of the springs, we should be able to calculate the spring force (and hence *f*) from their deformations. To calculate *f*, we need a spring law that relates the length of the spring to the spring constant. Throughout this article, we use the Cohen-Padé approximation (details given in Ref. [3] and Chapter III), which is a spring law for a bead-rod chain with finite number of rods:

$$f = \frac{1}{3}\frac{\alpha - \beta\hat{r}^2}{1-\hat{r}^2} \tag{10}$$

where $\hat{r}$ is the fractional extension of the spring, $\alpha = 3$ and $\beta = 1$ for the Cohen-Padé approximation. For the Underhill-Doyle coarse-grained spring law, the parameters α and β are given in Ref. [5] as:

$$\alpha = 3 - \frac{10}{3\nu} + \frac{10}{27\nu^2}$$
$$\beta = 1 + \frac{2}{3\nu} + \frac{10}{27\nu^2}$$

We show later in this article that both the Cohen-Padé approximation and the Underhill-Doyle model yield similar results for our self-consistent model. It has been shown earlier in Chapter III that the results obtained from BD simulations using these two models are in good agreement with one another.

Now, for a given value of *f*, we can calculate $\left\langle X_p^2 \right\rangle$ by Eq. (6), L_c using Eq. (5) and calculate *f* again using a fractional extension obtained by setting the instantaneous spring extension equal to the pre-averaged contour length; i.e., we set $\hat{r} = \frac{L_c}{N\nu b_K}$ in Eq. (10). This

allows calculation of a self-consistent value for f at each shear rate (or Wi) by iteration from an initial guess. For this article, we used a bisection method to calculate the value of f at various Wi where we stop iterations when the "left" and "right" guesses of f differ less than a specified tolerance. Once the suitably accurate value for f is obtained, the chain dimensions are calculated by Eqs. (7)-(9).

As will be clear later in the article, the fractional extension of the contour length ($\hat{r} = \frac{L_c}{N v b_K}$) is not the correct representative for the stretch of the individual springs in the chain. Noting the boundary conditions for Eq. (1), it is clear that the average length of the springs at the ends will be 0, and the length will be higher for the internal springs in the chain, with the maximum average spring length attained for the spring in the middle of the chain. Assuming that this maximum average spring length is a better representative of the spring stretch, and hence of the stiffness of the springs in the chain, we can formulate the same self-consistent method described earlier with a modified $\hat{r}$:

$$\hat{r} = \frac{1}{v b_K} \left| \frac{\partial \vec{R}_n}{\partial n} \right|_{\max} \tag{11}$$

The self-consistent algorithms using the contour length and maximum spring length will be henceforth denoted as 'SC-L_c' and 'SC', respectively.

Results and Discussions

Figure C.1 shows the results for R_{gx} (normalized by $L = N\nu b_K$, which is 500 in this case) calculated using this self-consistent algorithm for a chain of 500 Kuhn steps (also referred to as "rods") with $\nu = 10$. The simulation results are obtained using chain models at two different resolutions, as follows: 1) the BR model uses stiff Fraenkel springs to model each Kuhn step (details given in Chapter IV and also in Ref. [7]), and 2) the CG model uses coarse-grained springs following the Cohen-Padé approximation and the Underhill-Doyle spring law, where ν has the usual meaning. Henceforth, the term 'CG' and 'CG (UD)' will denote coarse-grained bead-spring models using the Cohen-Padé approximation and the Underhill-Doyle spring law in this study, respectively. The results from the self-consistent algorithm clearly predicts a higher asymptotic value for R_{gx} ($\approx 0.3L$) whereas the corresponding value from BD simulations, using the BR and the CG models with both the Cohen-Padé approximation and the Underhill-Doyle spring law, yield approximately $R_{gx} \approx 0.2L$ (details of the set up and results of the BD simulations are given in Chapters III and IV). The inset compares the predictions of R_{gx} obtained the from analytical equations given in Ref. [2] (implementation and equations are also described in Chapter III, with some results shown in Fig. 3.1(c). The legend "theory" is selected for the analytical results to be consistent with the legend used in Fig. 3.1(c)) and those calculated from BD simulations using the BR model, for chains consisting of 300 and 500 rods. Clearly, these analytical predictions at strong shear rates are higher than the simulation results and similar to those obtained from our self-consistent algorithm using the contour length of the chain. Note that this larger asymptotic value for R_{gx} is consistent with the theoretical prediction at $Wi \to \infty$

given in Ref. [4]. Note that the values of R_{gx}/L at high shear rates, where it attains a plateau, are similar for simulations using the BR or the CG models.

In light of the observations in Figure C.1, we argue that the fractional extension of the contour length is not the correct measure of the stretch of the individual springs in the chain. Figure C.2 compares the results obtained with our self-consistent method using the maximum average spring length (i.e. the central spring, Eq. (11)) with simulation results for chains with 500 and 5000 Kuhn lengths. For BD simulations with the CG model, we always use two different values of ν for any given chain to highlight the consistency in the results. Owing to computational limitations, the BR model is not used to simulate the chain with 5000 Kuhn steps. The results clearly demonstrate the success of using the criterion in Eq. (11) as opposed to using the contour length of the chain. In both cases, the results from the self-consistent method agree quite well with the simulation results for the entire range of shear rates investigated, including the asymptotic value of about $R_{gx} \approx 0.2L$ at $Wi \to \infty$ in all cases. As noted later in this article, using different values of ν, while keeping the total number of Kuhn steps in the chain fixed, does not change the predictions obtained from our self-consistent algorithm.

Figure C.3 compares the results for R_{gy} calculated using our method and those calculated from BD simulations of the CG model, for 500 and 5000 Kuhn lengths. This shows that the trends obtained from simulations of the CG model are well captured by our self-consistent method, with R_{gy} remaining a constant at low shear rates and approaching an asymptotic scaling law of $Wi^{-\frac{1}{3}}$ at high shear rates, where R_{gx} shows a plateau. This

exponent of -1/3 at $Wi \to \infty$ is predicted theoretically in Ref. [4] and from earlier BD simulations with coarse-grained bead-spring models [3, 6, 7]. Also, note that the results obtained from the BD simulations are slightly higher than our predictions, but do show an asymptotic scaling of $Wi^{-\frac{1}{3}}$ at high shear rates. Note that no results from BD simulations using the BR model are included in Fig. C.3, since it is already shown in Chapters III and IV that those predict an asymptotic scaling law of $Wi^{-\frac{1}{4}}$, which is different from the predictions of the CG model. It is perhaps not surprising that our self-consistent method is only as accurate as the underlying CG model, and yields results that agree well with the simulations using the CG models.

Figure C.4 shows the predictions of R_{gx} from our self-consistent algorithm for chains of 500 and 5000 Kuhn steps, using CG models at widely different resolutions and also compares the same obtained with the Underhill-Doyle spring law. Clearly, the differences in the results obtained from our calculations, while using different values of ν and different spring laws, are negligible. Similar conclusions are reached for the predictions of R_{gy} (shown in the inset of Figure C.4). Note that, for higher values of ν (i.e. $\nu > 10$), the Underhill-Doyle spring law is expected to yield similar results as the Cohen-Padé approximation (i.e. $\alpha \to 3$ and $\beta \to 1$ for large values of ν in the Underhill-Doyle model). Thus, from the standpoint of our self-consistent method, the results are equivalent for a given chain with a fixed number of Kuhn steps while using different values of ν and different spring force laws, which agrees well with a similar conclusion obtained from results of BD simulations with CG models given in Chapter III.

Figure C.5 shows the variation of R_{gx}/L for a wide range of chain lengths (in terms of the number of Kuhn steps $N_K = N\nu$) with the Weissenberg number. Results are obtained from the self-consistent method described here (solid lines) and compared to those obtained for Gaussian chains without the effects of finite extensibility (dashed lines). The latter are obtained by using Eq. (21) in Chapter III, and are described in details there. The trends are consistent with those seen from BD simulations in Chapter III, where the average chain stretch increases for relatively weaker shear rates (low *Wi* but $Wi > 1$, since otherwise the chain does not stretch appreciably from its equilibrium state) and the reaches saturation, or a "plateau", at strong shear rates. The former constitutes Regime 1, where the Gaussian model (without finite extensibility) holds (and the coil thickness stays constant at its equilibrium value, as shown later in this Appendix), whereas the latter is denoted as Regime 2. Quite interestingly, chain compression is not obtained at even higher shear rates and the plateau in Regime 2 is the asymptotic response obtained at $Wi \to \infty$ from our self-consistent method, for all cases. It is worth noting here that the chain compression observed in some recent simulations (Chapter III and also Ref. [10]) is shown to be a numerical artifact due to insufficient model resolution in Chapter IV. Since our method given here is completely based on theory, it is reasonable to expect that any unrealistic behavior due to inaccuracies in a simulation set-up would not be obtained.

Additionally, our results show that the deviations from the results for Gaussian chains, which denote the end of Regime 1, occur at shear rates where R_{gx} attains a value of about 7% of the chain length L ($L = N\nu b_K$). Interestingly, this is true for all chains considered, for widely varying chain lengths (this is marked by a dashed gray line in Fig C.5). Note

that the end of Regime 1 is estimated to be the shear rates where R_{gx} approximately attains a value of about 5% of the chain length, for BD simulations given in Chapter III, which is probably less refined than the value of 7% deduced from this study. The inset to Figure C.5 highlights the universality for the chain stretch variation in the transition regime between Regimes 1 and 2. Our results show that the approach to the plateau from Regime 1, denoted by $\left(R_{gx,plateau} - R_{gx}\right)$ normalized by $N_K^{1.35}$, where $N_K = N\nu$, shows a universal scaling law of $Wi^{-0.7}$ for all cases considered, in the range of shear rates between Regimes 1 and 2. To the best of our knowledge, such a universal scaling law has never been obtained earlier for this transition regime leading to the stretch saturation.

Figure C.6 shows the variation of R_{gy} for widely varying chain lengths with a Peclet number, $Pe = \frac{Wi}{N_K^2}$. Note that this definition of Pe is equivalent as that used in Chapters III and IV. These results show that the predicted chain thickness at high shear rates are independent of the length of the chain and exhibit a power law exponent of -1/3 when plotted against the Peclet number (or the shear rate). The underlying physics for this N_K-independence of R_{gy} has been discussed in details in Chapter IV (also given in Ref. [7]), where it is also shown that the power law exponent changes from -1/3 to about -1/4 when the chain is resolved at the level of a Kuhn step or finer (i.e. when the BR or the FG models are used in Chapter IV). It is interesting that this independence of R_{gy} on N_K at strong shear rates is also obtained from our self-consistent method for long chains. However, as noted before, this method can only be as accurate as the CG model, and thus shows a scaling law of $Pe^{-1/3}$ at high shear rates, which is consistent with those predicted

from BD simulations using the CG model, instead of the scaling of $Pe^{-1/4}$ obtained from the more finely resolved models given in Chapters III and IV.

Insets (i) and (ii) of Figure C.6 show the chain length variation of the 'crossover' Peclet numbers Pe_{c1} and Pe_{c2}, which mark the shear rates (in terms of Peclet numbers) of the end of Regime 1 and the onset of Regime 2, respectively. As described in Chapter III, Regime 1 denotes the range of shear rates for which the R_{gy} stays constant at its equilibrium value (and the R_{gx} is predicted well by the Gaussian chain model without finite extensibility effects), while Regime 2 is the range of shear rates where the R_{gx} shows a plateau (consequently R_{gy} shows a power law with an exponent of -1/4, or -1/3, depending on the type of model). The approximate values of these crossover Peclet numbers are also given in Chapter III from BD simulations, but the estimates are much more refined here owing to significantly larger number of data points that can be obtained from analytical methods, like the one used here. Interestingly, similar scaling laws are obtained for both the crossover Peclet numbers as $Pe_{c1} \sim N_K^{-3/2}$ and $Pe_{c2} \sim N_K^{-3/2}$, which is in good agreement with the rather approximate estimates of $Pe_{c1} \sim N_K^{-1.5}$ and $Pe_{c2} \sim N_K^{-1.4}$ obtained from BD simulations in Chapter III.

The variation for Pe_{c1} can be explained as follows. Since the Gaussian chain model (Eq. (21) in Chapter III) holds true for shear rates upto the crossover from Regime 1 to Regime 2, we have:

$$\sqrt{\frac{\left(0.07N_K\right)^2}{R_{gx0}^2} - 1} \sim Wi_{c1}$$

where R_{gx0} is the x-component of the radius of gyration of the chain at equilibrium and is given by $R_{gx0} \sim N_K^{1/2}$. Then, assuming that the first term in under the square root is much larger than 1 (which should hold for long chains since the shear rates for this crossover are far away from equilibrium), we have $N_K^{1/2} \sim Wi_{c1}$. Since $Pe_{c1} \sim \frac{Wi_{c1}}{N_K^2}$, we finally get $Pe_{c1} \sim N_K^{-3/2}$, as observed from our results.

For the onset of Regime 2, our earlier universal scaling law for the transition regime should hold. Then, we have:

$$\frac{\left(R_{gx,plateau} - R_{gx}\right)}{N_K^{1.35}} \sim Wi_{c2}^{-0.7}$$

Now, if we define the onset of Regime 2 as the shear rate at which R_{gx} reaches a value that is a certain fraction of the final value at plateau, say 95% of $R_{gx,plateau}$, then we have $\left(R_{gx,plateau} - R_{gx}\right) \sim N_K$, which gives $N_K^{-0.35} \sim Wi_{c2}^{-0.7}$, or $Wi_{c2} \sim N_K^{1/2}$. Since $Pe_{c2} \sim \frac{Wi_{c2}}{N_K^2}$, we finally obtain $Pe_{c1} \sim N_K^{-3/2}$, same as that obtained from our results.

Note that the N_K-independent scaling law of $Pe^{-1/3}$ can also be derived using the Eqs. (8) and (9). At strong shear rates, since the value of f is much larger than 1 as the springs are highly deformed and the values of *Wi* are also large, the first term on the right hand side in Eq. (8) becomes negligible relative to the second term. Also, our results suggest that R_{gx} is a constant (dependent on chain length, but not on shear rates) at large shear rates, i.e.

$R_{gx} \sim N\nu$. Hence, for a given bead-spring chain, Eq. (8) gives $f \sim \left[\frac{Wi^2}{N\nu}\right]^{1/3} = \frac{Wi^{2/3}}{(N\nu)^{1/3}}$ for strong shear flows. If this is substituted in Eq. (9), we get $R_{gy}^2 \sim (N\nu) f^{-1} \sim (N\nu)^{4/3} Wi^{-2/3}$, or $R_{gy} \sim (N\nu)^{2/3} Wi^{-1/3}$, irrespective of the spring force law used. Hence, as $Wi \sim Pe(N\nu)^2$, we finally obtain $R_{gy} \sim Pe^{-1/3}$, which is N_K-independent. Note that, the scaling law $R_{gy} \sim Wi^{-1/3}$ for the coil thickness has been reported from all earlier BD simulations of coarse-grained bead-spring chains [3, 6, 7]. Then, at high shear rates, since $R_{gx} \sim N\nu$ and $R_{gy} \sim Pe^{-1/3}$, the aspect ratio of the two varies as $N\nu Pe^{1/3}$, which means that the tumbling time would follow a scaling law of $N\nu Pe^{-2/3}$, which agrees with the result given in Ref. [6].

Summary

In this study, we have shown a new self-consistent method to estimate the deformation of isolated polymer chains in shear flows, in the absence of excluded volume (EV) and hydrodynamic interactions (HI). Our results clearly indicate that the self-consistent algorithm has to be formulated using the length of the central spring, and not the contour length of the entire chain as done earlier in multiple studies, to correctly predict the behavior over all ranges of shear rates (treated here in terms of Weissenberg numbers). This analytical method is based on the usual coarse-grained spring force laws, and yields

results that agree remarkably well with those obtained from BD simulations using similar CG bead-spring models (explained earlier in Chapters III and IV). Interestingly, our results don't show the existence of Regime 3 at any range of shear rates, where the chain gets compressed with increasing shear rates, as observed in some BD simulation studies recently. However, as we explained in Chapter IV, chain compression in Regime 3 is a numerical artifact of the model resolution, and hence perhaps it is not too surprising that a completely theoretical model, as the one described here, does not predict the existence of such a regime. Note that the incorporation of the effects of HI and EV in the self-consistent method is beyond the scope of this study, and will be explored in future. To summarize, the method described here can be a very useful analytical tool to quickly, and accurately, estimate the deformation behavior for a given polymer chain at a given shear rate.

References

[1] Bruns, Wolfgang; Carl, Wilfried *Macromolecules* **26**, 557-558 (1993).

[2] Carl, W. *Maromol. Theory Simul*. **3**, 705-713 (1994).

[3] Saha Dalal, Indranil; Hoda, Nazish; Larson, Ronald G. *J. Rheol* **56**, 305 (2012)

[4] Winkler, Roland G. *Phys. Rev. Lett.* **97**, 128301 (2006).

[5] Underhill, P. T.; Doyle, P. S. *J. Rheol.* **49**, 963-987, (2005).

[6] Schroeder, C. M.; Teixeira, R. E.; Shaqfeh, E. S. G.; Chu, S. *Phys. Rev. Lett.* **95**, 018301 (2005).

[7] Saha Dalal, Indranil; Albaugh, Alex; Hoda, Nazish; Larson, Ronald G. *Macromolecules* 2012, 45, 9493-9499.

[8] Wang, Xiaoling; Chatterjee, Avik P. *Macromolecules* **34**, 1118-1121 (2001).

[9] Carl, W. *Rheol Acta* **36**, 197-201 (1997).

[10] Sendner, C.; Netz, R. R. *Eur. Phys. J. E* **30**, 75-81 (2009).

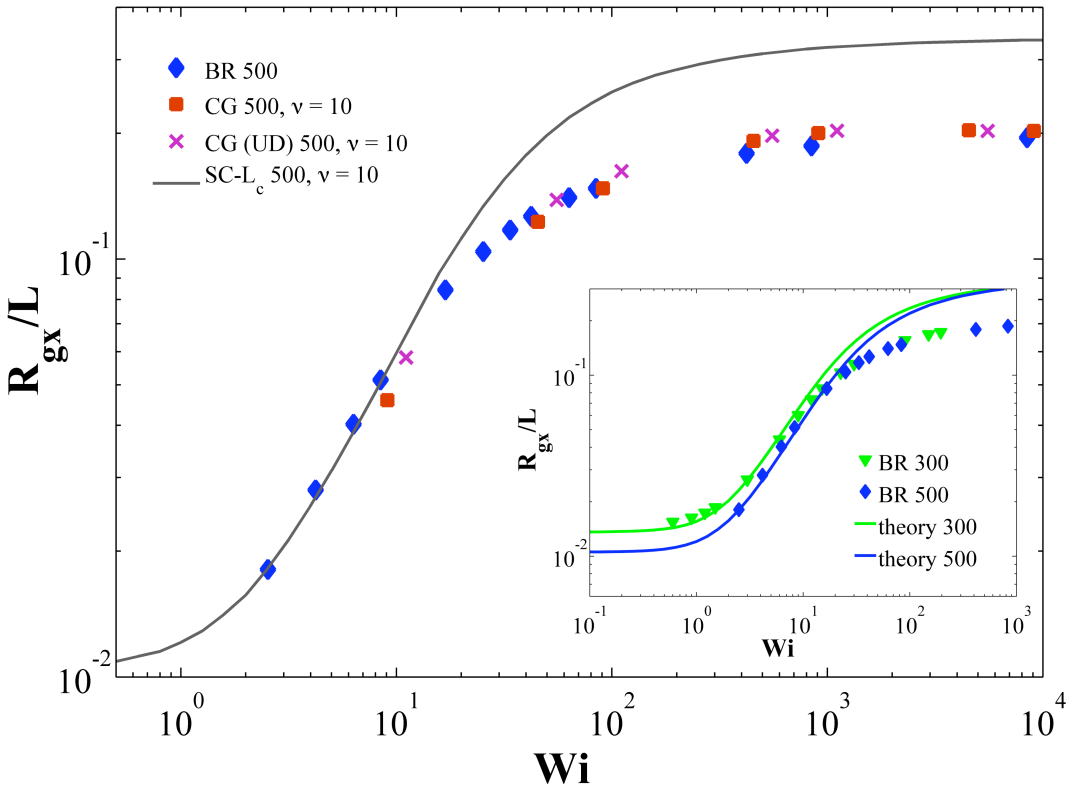

Figure C.1: Comparison of the variation of R_{gx}/L with Wi obtained from the self-consistent method using the fractional extension based on the pre-averaged contour length of the whole chain and those obtained from BD simulations. The first term in the legend denotes either the model used for BD simulations or the method used for the self-consistent algorithm, which is followed by the chain length in terms of the number of Kuhn steps and the number of Kuhn steps mimicked by each spring. 'BR' and 'CG' denote bead-rod and bead-spring chains in BD simulations, respectively. The term 'UD' indicates the case where the Underhill-Doyle spring force law is used. The inset compares the results obtained from an analytical model given in Ref. [3] (implementation is discussed in details in Chapter III) and BD simulations with the bead-rod chain model.

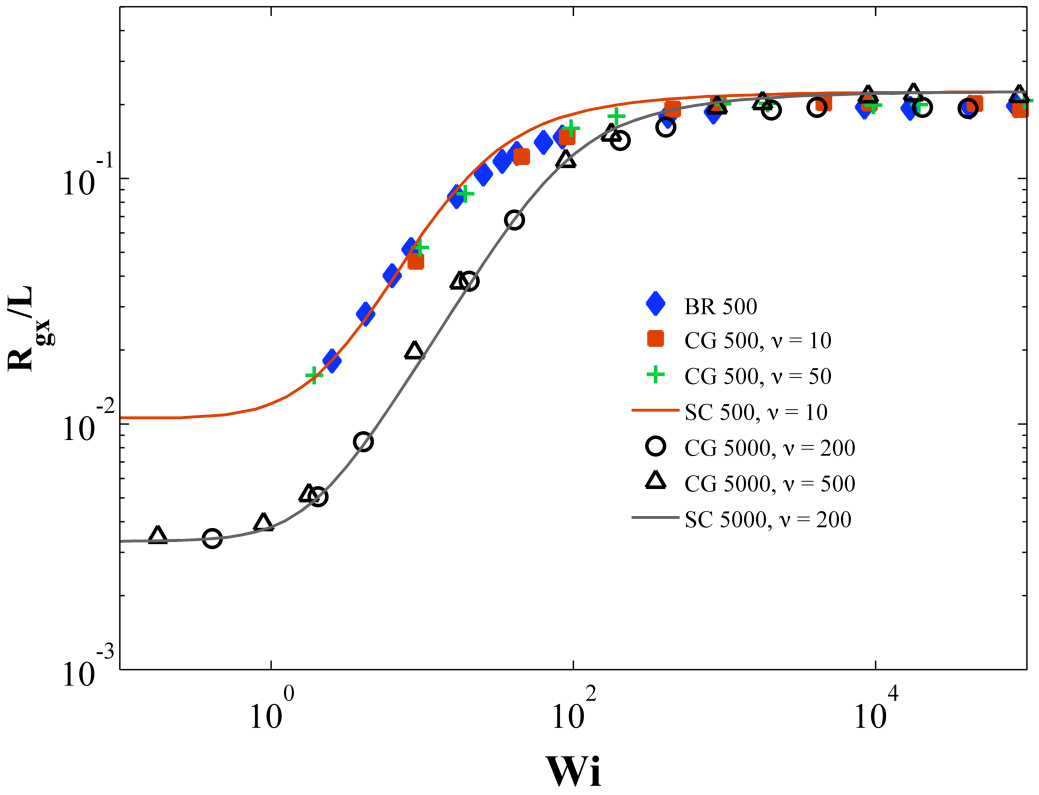

Figure C.2: Comparison of the variation of R_{gx}/L with *Wi* obtained from the self-consistent method using the fractional extension based on the maximum average spring length in the chain (i.e. the length of the central spring, see Eq. (11)) and those obtained from BD simulations. The legends have similar meaning as those in Figure C.1. Note that the results from the self-consistent method agree well with those from simulations for the chain lengths considered here.

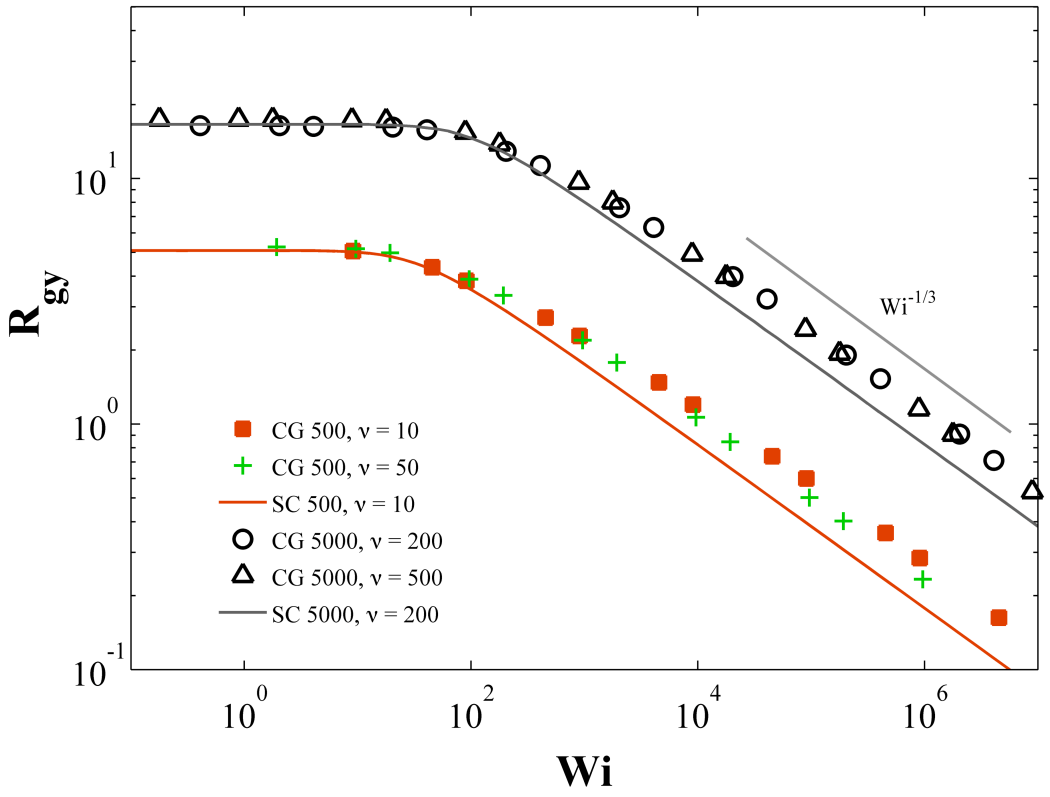

Figure C.3: Comparison of the shear rate variation of R_{gy} obtained from the self-consistent method using the fractional extension given in Eq. (11) and those obtained from BD simulations. The legends have usual meanings (as described in the caption of Figure C.1). The solid gray line indicates a power law with an exponent of -1/3 at high shear rates.

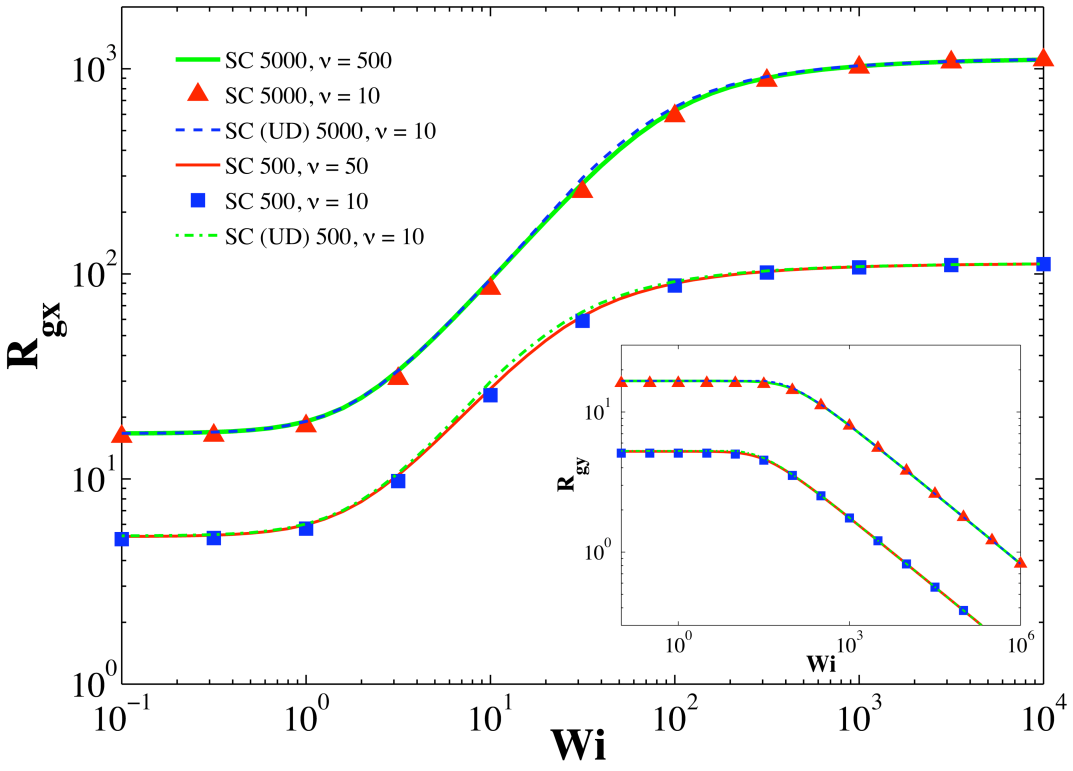

Figure C.4: Comparison of the shear rate dependence of R_{gx} from the self-consistent method with different spring force laws and different number of Kuhn steps mimicked by one single spring, for chain lengths of 500 and 5000 Kuhn steps. Inset shows the same for R_{gy}. The legends have usual meanings.

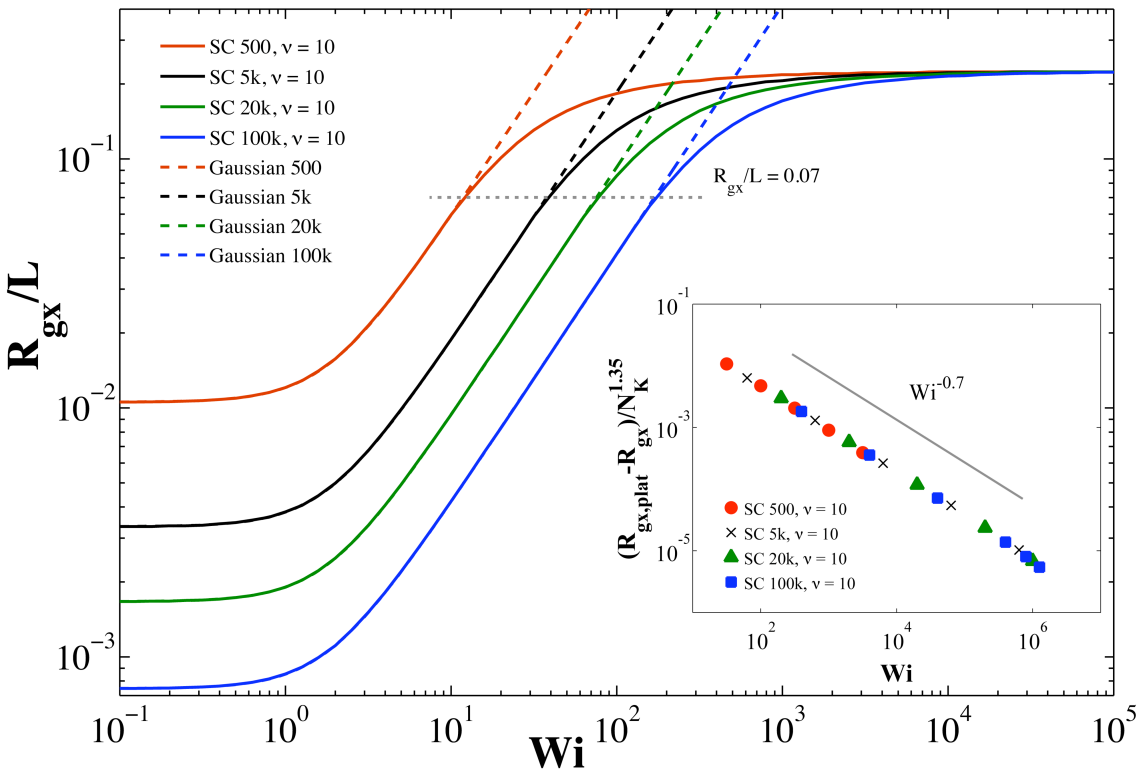

Figure C.5: The variation of chain stretch (R_{gx}) normalized by the chain length (number of Kuhn steps) with *Wi* for widely varying chain lengths, from the self-consistent method and from the model for Gaussian chains without the effects of finite extensibility (see text for details). The gray dotted line indicates the values of *Wi* where the results from the two models start to deviate (i.e. end of Regime 1). Note that, for all chain lengths investigated here, this deviation starts when R_{gx} attains a value of about 7% of the chain length. The inset highlights the universality in the variation of the quantity $\frac{\left(R_{gx,plat} - R_{gx}\right)}{N_K^{1.35}}$ with *Wi* in the transition Regime, between Regime 1 and Regime 2. Here $R_{gx,plat}$ is the saturation value of R_{gx} at high shear rates (i.e. at the plateau, about 0.2L). The solid line indicates a power law with an exponent of -0.7.

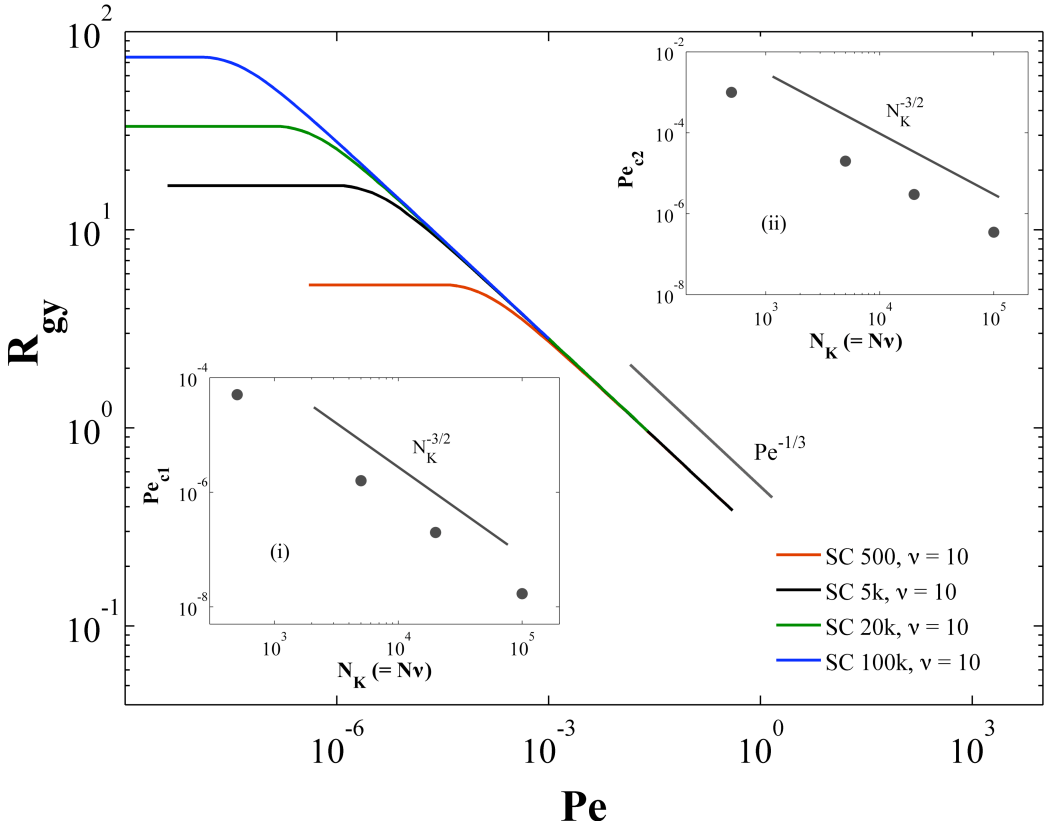

Figure C.6: The Peclet number dependence of R_{gy} for widely varying chain lengths from the self-consistent method. The Peclet number is defined as Wi/N_K^2. The solid line indicates a power law with an exponent of -1/3 at high shear rates. Note that the results are independent of chain length at high shear rates of Regime 2, consistent with the simulation and theoretical predictions in Chapters III and IV. Insets (i) and (ii) show the variation of the crossover Peclet numbers Pe_{c1} (denotes the end of Regime 1) and Pe_{c2} (denotes the onset of Regime 2) with chain length. In both cases, the solid line indicates a power law with an exponent of -3/2.